Magnetic Domain Wall Motion and Switching under Microwave Excitation

Dissertation

Zur Erlangung des Doktorgrades der Naturwissenschaften
(Dr. rer. nat.)

der

Naturwissenschaftlichen Fakultät II
Chemie, Physik und Mathematik

der Martin-Luther-Universität
Halle-Wittenberg

vorgelegt von

Herrn Lukas Fischer

Gutachter:
Prof. Dr. Stuart S. P. Parkin
Prof. Dr. Georg Woltersdorf
Prof. Dr. Dirk Grundler

Tag der öffentlichen Verteidigung:
26.01.2026

Declaration

Hiermit erkläre ich, dass ich die vorliegende Arbeit selbstständig verfasst und keine anderen als die angegebenen Quellen und Hilfsmittel benutzt habe. Alle Stellen der Arbeit, die wörtlich oder sinngemäß aus anderen Quellen übernommen wurden, sind als solche kenntlich gemacht. Ich habe keine vergeblichen Promotionsversuche unternommen und keine Dissertation an einer anderen wissenschaftlichen Einrichtung zur Erlangung eines akademischen Grades eingereicht. Ich bin weder vorgestraft noch sind gegen mich Ermittlungsverfahren anhängig.

Halle (Saale), den 19.06.2025,

Lukas Fischer

Acknowledgements

The path towards this thesis has been an incredible journey that would not have been possible without the company and support of many people. First and foremost, I would like to express my deepest gratitude to Prof. Stuart Parkin. He gave me a lot of freedom in my research and I am greatly thankful for the scientific guidance I received from him. Our meetings were very refreshing and I felt motivated to think beyond existing literature and perform novel experiments. I am also very grateful to Prof. Georg Woltersdorf for his support in developing my research project and discussing the results. Especially in the beginning of my PhD, these meetings greatly strengthened my confidence in my scientific results. Furthermore, this endeavor would not have been possible without Jae-Chun Jeon. From day one, I have enjoyed his mentoring and profited from his technical and scientific knowledge that was essential to conduct my research. He has always been available to answer countless questions and I am very thankful for our productive teamwork. Moreover, I would like to mention the Max-Planck Gesellschaft and our International Max-Planck Research School.

Special thanks belongs to Rouven Dreyer and Prof. Georg Woltersdorf for our productive cooperation and the many fruitful discussions. In particular, I would like to thank Rouven Dreyer for his great measurements at the SNS-MOKE and for always being so optimistic and cheerful.

Thanks also belong to numerous colleagues: Many thanks to everyone who revised this thesis. Special thanks to Yicheng Guan, Jae-Chun Jeon, Jiho Yoon and Andrea Migliorini for their kind training in measurement and fabrication techniques as well as many discussions about domain wall dynamics. Many thanks belong to Berthold Rimmler, Pedram Bassirian and Jiho Yoon for initially welcoming me at MPI and having countless discussions and joyful laughs together. I am also greatful to Antje Paetzold, Michael Strauch, Martha Schulz, Ann-Kristin Flieger for their organizational support and their very productive cooperation in countless projects. Thanks should also go to Ilya Kostanovski, Mindaugas Silinskas, Daniel Meyer, Mike Borrmann, Dirk Sander, Detlef Proske, Michael Oppelt, Tim Gärtner and Kay Wrobel.

During my time in Halle, I enjoyed our daily lunch groups and frequent coffee gatherings. Thanks should also go to my fellow PhD representatives Guanmin, Pedram, Kajal and Chris and to all members of the PhD Committee and the PhD Stammtisch. I am grateful for my office mates Pedram, Tobias and Renata, whose company I greatly enjoyed. Moreover, I'd like to thank Tobias and Simon for our occasional Schafkopf ses-

sions. Many thanks to André, Andrea and Jae-Chun for many spontaneous wine tastings and the delicious Korean barbecues.

Words can not express my gratitude to my family and friends. I am extremely grateful to my parents and my brother for encouraging and supporting me for all these years. This would not have been possible without you. I am also very thankful to my friends Berthold, Svenja, Valerie, Martin, Daniel, Prajwal, Anvesh, Ivan, Sasha, Guanmin.

Abstract

Magnetic domain wall (DW) motion and magnetization switching in atomically-thin magnetic films with perpendicular magnetic anisotropy are of significant importance for high performance spintronic devices. The excitation of magnetization precessions is mostly avoided in such devices to reduce energy losses due to magnetic damping. Nevertheless, the resonant excitation of magnetization has been demonstrated to facilitate field-induced magnetic switching. Strikingly, the corresponding excitation of DWs and its impact on current-induced DW motion and magnetization switching has not yet been explored. In this work, it is demonstrated that DWs may be resonantly excited by a radio-frequency (RF) magnetic field or an RF electrical current and that this excitation has a pronounced impact on the DW's motion. First, the excited DWs exhibit current-free, long-range self-propulsion in the sole presence of an RF excitation and a symmetry-breaking, transverse magnetic field. The direction of the DW during self-propulsion is determined by the transverse field. Second, when triggering DW motion by a nanosecond-long current pulse, the resonant RF excitation of the DW allows for its sustained motion along its initial direction of motion. This sustained motion is stable for several microseconds after the initial current pulse ends and only requires the additional presence of a weak longitudinal magnetic field. In addition to exciting magnetic resonances for DW motion, this work also focuses on RF-assisted magnetic switching. It is shown that the current-induced spin-orbit torque (SOT) switching, being composed of domain nucleation and subsequent expansion by DW motion, is significantly facilitated by the excitation of the DW resonance. This demonstrates that DW motion plays a key role during SOT switching. Moreover, RF-assisted field switching by an RF SOT and a purely RF-induced demagnetization are achieved by exciting the ferromagnetic resonance mode of the magnet. Overall, the results of this thesis demonstrate that the excitation of magnetic resonances has versatile impacts on DW motion and magnetic switching and thereby advances the fundamental understanding and the technological applicability of spintronics.

Zusammenfassung

Die Bewegung einer magnetischen Domänenwand (DW) und das Schalten der Magnetisierung in atomar dünnen magnetischen Filmen mit senkrechter magnetischer Anisotropie sind von großer Bedeutung für leistungsstarke spintronische Bauelemente. Die Anregung von Präzessionen der Magnetisierung wird in solchen spintronischen Geräten meist vermieden, um Energieverluste durch magnetische Dämpfung zu reduzieren. Allerdings wurde bereits gezeigt, dass die resonante Anregung der Magnetisierung das Feld-induzierte Schalten der Magnetisierung erleichtert. Jedoch wurde die entsprechende Anregung einer DW und ihre Auswirkung auf die strominduzierte DW-Bewegung sowie das Schalten der Magnetisierung noch nicht erforscht. In dieser Arbeit wird gezeigt, dass eine DW durch ein hochfrequentes (HF) Magnetfeld oder einen elektrischen HF-Strom resonant angeregt werden kann und dass diese Anregung einen deutlichen Einfluss auf die DW Bewegung hat. Erstens bewegt sich die angeregte DW automatisch über große Distanzen fort. Dies geschieht in alleiniger Anwesenheit der HF-Anregung und eines symmetriebrechenden, transversalen Magnetfeldes, aber in Abwesenheit eines antreibenden elektrischen Stroms. Die Richtung der DW während des automatischen Fortbewegung wird durch das transversale Feld bestimmt. Zweitens, wenn die DW-Bewegung durch einen nanosekundenlangen Strompuls ausgelöst wird, ermöglicht die resonante HF-Anregung der DW eine anhaltende Bewegung entlang ihrer ursprünglichen Bewegungsrichtung. Diese anhaltende Bewegung ist für mehrere Mikrosekunden nach dem Ende des anfänglichen Strompulses stabil und erfordert nur das zusätzliche Vorhandensein eines schwachen, longitudinalen Magnetfeldes. Neben der Anregung magnetischer Resonanzen für DW-Bewegungen konzentriert sich diese Arbeit auch auf HF-unterstütztes Schalten der Magnetisierung. Es wird gezeigt, dass das Schalten durch ein Spin-Orbit Drehmoment (SOD), das sich aus dem lokal begrenzten Schalten einer Domäne und anschließender Domänenexpansion durch DW-Bewegung zusammensetzt, durch die Anregung der DW-Resonanz erheblich erleichtert wird. Dies zeigt klar die Bedeutung der DW Bewegung während des Schaltprozesses. Darüber hinaus werden ein HF-unterstütztes Feld-induziertes Schalten durch ein HF SOD sowie eine rein HF-induzierte Entmagnetisierung durch Anregung der ferromagnetischen Resonanz des Magneten erreicht. Insgesamt zeigen die Ergebnisse dieser Arbeit, dass die Anregung von magnetischen Resonanzen vielseitige Auswirkungen auf die DW-Bewegung und das Schalten der Magnetisierung hat und dadurch das grundlegende Verständnis und die technologische Anwendbarkeit der Spintronik vorantreibt.

Glossary

Terms	
CPW	Co-planar waveguide
DL	Damping-like
DMI	Dzyaloshinskii-Moriya interaction
DW	Domain wall
FL	Field-like
FM	Ferromagnet
FMR	Ferromagnetic resonance
HDD	Hard-disk drive
HM	Heavy metal
IBD	Ion-beam deposition
IP	In-plane
iSGE	Inverse spin-galvanic effect
LCP	Left-circularly polarized
LLG	Landau-Lifshitz-Gilbert
LLGS	Landau-Lifshitz-Gilbert-Slonczewski
L-MOKE	Longitudinal MOKE
MAMR	Microwave-assisted magnetic recording
MAS	Microwave-assisted switching
MCA	Magneto-crystalline anisotropy
MOKE	Magneto-optical Kerr effect
MRAM	Magnetic random access memory
OOP	Out-of-plane
PMA	Perpendicular magnetic anisotropy
P-MOKE	Polar MOKE
RCP	Right-circularly polarized
RF	Radio-frequency
RTM	Racetrack memory
SNS-MOKE	Super-Nyquist samping MOKE
SOC	Spin-orbit coupling
SOT	Spin-orbit torque
STT	Spin-transfer torque
SWM	Stoner-Wohlfarth model
TR-MOKE	Time-resolved MOKE
VNA	Vector-network analyzer
VSM	Vibrating sample magnetometry

Contents

Part I

Introduction

Chapter 1

Motivation and scope

Spintronics represents a broad research field focusing on the utilization of the electron spin to realize nano-electronic devices for memory storage, logic application or neuromorphic computing [1,2]. Some spintronic applications, such as spin-valves in the read-heads of magnetic hard-disk drives (HDDs) or spin-transfer torque based magnetic random access memory, are already in use in today's technology. Another proposed concept called *racetrack memory* (RTM) represents a promising approach to realize a magnetic memory architecture that combines non-volatility, high bit-density and high operation speed [3–6]. RTM is a type of magnetic shift register where information is encoded by the orientation of small magnetic domains and these domains are moved along the register by an electrical current [3]. Two neighboring magnetic domains with opposite orientation are separated by a magnetic domain wall (DW). Hence, the success of RTM relies on both the motion of DWs and the writing of magnetic domains in ferromagnets.

With respect to the DW motion, an electrically induced spin-orbit torque (SOT) is highly efficient [7–11]. Most experimental and numerical studies have focused on DW motion using a pulsed current because it induces a steady state DW motion. A magnetization precession during DW motion is usually avoided since it causes additional energy dissipation and thereby reduces the efficiency of DW motion. However, the Walker precession of a DW during field or current-driven DW motion clearly shows the connection between DW motion and the precession of the DW [12, 13]. This connection is well known from the set of differential equations from the collective-coordinate model that connect the DW position and the angular DW orientation [14, 15]. Interestingly, the effect of an externally excited DW precession on the DW motion, has not yet been explored. The efficient excitation of a DW requires both a radio-frequency (RF) field or an RF-current and also the correct, resonant frequency. It should be noted that the resonance of localized magnetic textures, such as DWs, is fundamentally different from that of the uniform magnetic domain [16]. Moreover, the dynamic response of a DW is highly affected by the magnetic material properties such as Dzyaloshinskii-Moriya interaction [13].

This work aims at bridging the gap between a high frequency excitation of magnetic DWs and its motion. In order to do so, a suitable excitation geometry is first required. Furthermore, the frequencies to which the DW is susceptible, e.g. the DW resonance, are

investigated. Finally, the impact of an RF excitation on the DW itself and during current-induced DW motion is studied. This work focuses on chiral Néel DWs in perpendicularly magnetized conduits, commonly used for cutting-edge DW-based spintronic devices.

In this work, a novel approach is demonstrated to achieve the RF excitation of a magnetic DW with RF fields by integrating a magnetic conduit on top of a co-planar waveguide. Super-Nyquist-Sampling magneto-optical Kerr (SNS-MOKE) imaging is then used to measure the dynamic susceptibility of both DWs and unfiorm domains. These measurements reveal that the DWs are susceptible to RF fields at significantly lower frequencies than the ferromagnetic resonance (FMR) and exhibit a resonance at approximately $f = 640$ MHz.

Exciting the DW at its resonant frequencies is shown to strongly impact the DWs in various ways: Firstly, the DW is shown to self-propel by the action of a resonant RF field and a symmetry-breaking static transverse magnetic field, i.e. the DW moves by itself without the need of electrical current pulses. The effective speed during self-propulsion is rather slow with $v \sim 1$ m/s which lies not in the flow regime of DW motion but in the depinning regime. Additionally, the DW excitation by an alternative mechanism using RF electrical currents is demonstrated and similarly exhibits self-propulsion. However, the latter does not occur at a resonance but instead its strength diverges towards low frequencies.

Furthermore, when the DW motion is initiated by a sufficiently strong current pulse, the DW excitation by resonant RF fields leads to the sustained motion of the DW after the end of the initial current pulse. This sustained motion requires the presence of a longitudinal magnetic field and is surprisingly stable over several microseconds. Overall, the results indicate that an RF excitation of a DW indeed impacts its motion in various ways and thereby extends the toolbox for DW manipulation.

In addition to the motion of DWs, the efficient writing of magnetic domains, better described as magnetization reversal or switching, is a key requirement for RTM and other spintronic applications [1, 2]. Herein, SOT switching represents an efficient method for current-induced magnetization switching [17–19]. In many cases, it involves not only the nucleation of a switched domain but also the subsequent expansion of the latter [20]. Since this domain expansion involves DW motion, the excitation of a DW resonance will supposedly affect the SOT switching. Indeed, the results in this work will show that the RF-excitation at the DW resonance will significantly facilitate switching of a magnet.

Moreover, when exciting not the DW resonance but instead the uniform FMR mode in the domains, microwave-assisted switching (MAS) has been demonstrated [21, 22]. However, so far no MAS has been shown in ultra-thin films that are suitable for current-induced DW motion or SOT switching. Further on, the demonstration of MAS that is induced by current-induced RF spin torques such as SOT is still missing. These missing points will be addressed in the last chapter of this work where microwave-assisted field

switching is investigated. An RF SOT exhibits a strong MAS effect, thereby reduces the switching field by almost 100% and is capable of causing a purely RF-induced demagnetization of the magnet.

The thesis is structured as follows: In addition to introducing the field of research and the particular research questions here, part I lays the theoretical and methodical groundwork. The fundamentals of magnetism and the concepts of magnetic domain wall motion and switching are established in chapter 2. Chapter 3 shows the details of sample and device fabrication as well as the magneto-optical measurement techniques. Part II is about the excitation of a DW resonance and starts with the SNS-MOKE measurements on DWs in chapter 4. Chapter 5 demonstrates the self-propulsion of a DW by both RF magnetic fields and RF electrical currents. Chapter 6 shows the sustained DW motion by a resonant RF field excitation after the end of an initial current trigger. Part III explores the field of microwave-assisted switching. Herein, chapter 7 presents the facilitated SOT switching by excitation of the DW resonance. Moreover, chapter 8 reveals the assisted field switching by RF-fields and currents. Part IV provides the summary of this work and gives a perspective on future research as well as the implications for the field of spintronics.

Chapter 2

Background

The field of spintronics exploits the electron spin in predominantly magnetic materials to realize advanced electronics such as non-volatile memory. This thesis focuses on the phenomena of magnetic DW motion and magnetization reversal in metallic ferromagnets (FMs). In particular, it is shown how the excitation of spin precessions impacts these phenomena.

This chapter first introduces the fundamentals of ferromagnetism by introducing the relevant energy terms and equations of motion. The emergence of magnetic DWs and the mechanisms behind field- and current-driven DW motion are discussed next. Finally, different methods to reverse the magnetization of a magnet are reviewed.

2.1 Magnetic domains and domain walls in ferromagnets

The electrons in any material may possess a magnetic dipole moment $\mathbf{m}$ that arises due to the angular momentum $\mathbf{l}$ and spin momentum $\mathbf{s}$ of the electron wave-function [23, 24].

$$\mathbf{m} = -\frac{\mu_B}{\hbar}\left(\mathbf{l} - g_{\mathrm{S}}\mathbf{s}\right) \tag{2.1}$$

Here, $\mu_B = \frac{e\mu_0\hbar}{2m_{\mathrm{e}}}$ is the Bohr magneton and $g_{\mathrm{S}} \approx 2$ is the spin g-factor. In a FM material, nearby magnetic moments start to order parallel to each other below a certain temperature, the so-called Curie-temperature. The material thus exhibits a finite spontaneous magnetization $\mathbf{M}$ that corresponds to the average magnetic moment per volume V [25].

$$\mathbf{M} = \frac{1}{V}\int_{\mathrm{V}} \mathbf{m} \tag{2.2}$$

For the metallic FMs discussed here, this ordering of the moments originates from the Heisenberg exchange interaction between itinerant conduction electrons that aligns the magnetic moments parallel to each other [1, 24, 26]. In terms of a macroscopic magnetization $\mathbf{M}$, the exchange energy density (i.e. in units of energy per volume) E_{ex} is determined by the exchange stiffness A_{ex} and the inhomogeneity of the magnetization,

expressed by $\nabla \mathbf{M}$ [25]. M_S denotes the saturation magnetization, i.e. the magnetization value when all moments are fully aligned.

$$E_{ex} = A_{ex} \frac{(\nabla \mathbf{M})^2}{M_S^2} \tag{2.3}$$

The magnetic anisotropy determines the equilibrium orientation that is preferred by the magnetization. Herein, the magneto-crystalline anisotropy (MCA) plays a crucial role. It arises from the spin-orbit interaction that couples the electron spin to an anisotropic lattice environment. Such MCA is induced in a crystallographically anisotropic or a strained lattice but also in layered films [1,23]. In this work, a Pt/$[Co/Ni]_N$/Ni multilayer achieves a strong uniaxial MCA perpendicular to the film surface due to interface anisotropy at the Pt/Co and Co/Ni interfaces [27–32] (see also chapter 3.1.2). The uniaxial anisotropy energy is expressed as

$$E_{ani} = K_u \sin^2(\theta) + \mathcal{O}\left(\sin^4(\theta)\right) \tag{2.4}$$

where K_u is the anisotropy constant, θ is the polar angle of $\mathbf{M}$ with respect to the anisotropy axis (i.e. to the plane normal). Note that terms of higher order than $\sin^2(\theta)$ were not considered in the equation. In ultrathin magnetic films, demagnetizing effects (also referred to as shape anisotropy) tries to align $\mathbf{M}$ in-plane (IP). The demagnetizing field $\mathbf{H}_d$ arises from the change in magnetization at the boundaries of the magnetic material ($\nabla \cdot \mathbf{M} = -\nabla \cdot \mathbf{H}$) and heavily depends on the sample dimensions and shape. $\mathbf{H}_d$ is determined by the orientation of the magnetization and the demagnetizing tensor $\widehat{N}$ and gives rise to the corresponding energy density E_{demag} [25].

$$\mathbf{H}_d = -\widehat{N}\mathbf{M} \tag{2.5}$$

$$E_{demag} = -\mu_0 \mathbf{M} \cdot \mathbf{H}_d \tag{2.6}$$

If the uniaxial anisotropy exceed the shape anisotropy, perpendicular magnetic anisotropy (PMA) is achieved and the magnetization points normal to the film plane.

The Zeeman energy density E_{Zeeman} describes the effect of an applied magnetic field $\mathbf{H}_a$ on the magnetization $\mathbf{M}$ [25].

$$E_{Zeeman} = -\mu_0 \mathbf{M} \cdot \mathbf{H}_a \tag{2.7}$$

In addition to the Heisenberg exchange interaction, an antisymmetric exchange exist that is commonly referred to as the Dzyaloshinskii-Moriya interaction (DMI) [33–35]. It requires both a broken inversion symmetry, e.g. at the interface between two different materials, and spin-orbit coupling (SOC). At the interface of a bilayer composing of a metallic FM and a heavy metal (HM), the SOC scattering of conduction electrons by nonmagnetic atoms gives rise to the DMI interaction [36, 37]. The DMI-term in the Hamiltonian $\hat{\mathcal{H}}_{DMI} = \mathbf{D}_{ij} \cdot \left(\mathbf{S}_i \times \mathbf{S}_j\right)$ favors the canting of the spins $\mathbf{S}_i$, $\mathbf{S}_j$ in the plane nor-

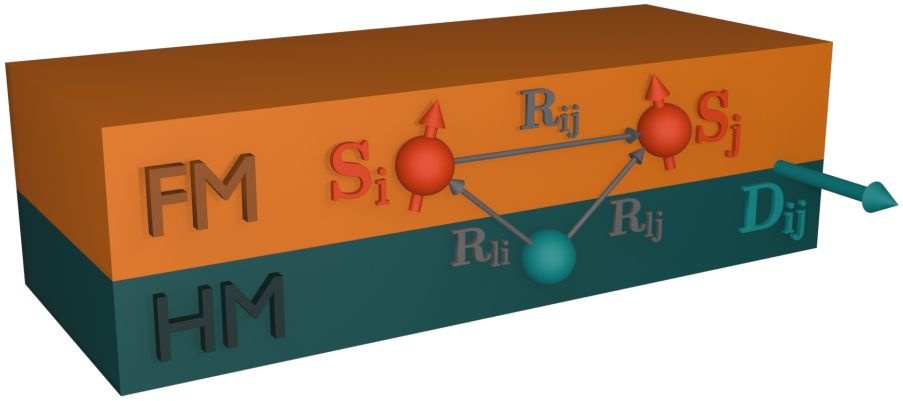

Figure 2.1: **Schematic of the Dzyaloshinskii-Moriya Interaction.**

mal to the DMI vector $\mathbf{D}_{ij}$. It has been shown that the orientation of the DMI vector is determined by $\mathbf{D}_{ij} \sim -\left(\mathbf{R}_{li} \times \mathbf{R}_{lj}\right)$ where $\mathbf{R}_{li,lj}$ are the distance vectors between the magnetic ions *i, j* and the non-magnetic scattering center *l* (see Fig. 2.1). The micromagnetic energy density of the interfacial DMI-energy density in ultrathin films reads [25, 38]:

$$E_{\mathrm{DMI}} = \frac{D}{M_{\mathrm{S}}^2}\left[M_{\mathrm{x}}\frac{\partial M_{\mathrm{z}}}{\partial x} - M_{\mathrm{z}}\frac{\partial M_{\mathrm{x}}}{\partial x} + M_{\mathrm{y}}\frac{\partial M_{\mathrm{z}}}{\partial y} - M_{\mathrm{z}}\frac{\partial M_{\mathrm{y}}}{\partial y}\right] \tag{2.8}$$

Here D denotes the DMI constant in units of J/m² [25]. As can be directly seen from the previous equations, the DMI favors a canted spin arrangement and will be particularly relevant with respect to non-uniform spin arrangement such as for DWs as shown later.

The total magnetic energy density can then be expresses by the sum of exchange, anisotropy, demagnetization, Zeeman and DMI energies:

$$E = E_{\mathrm{ex}} + E_{\mathrm{ani}} + E_{\mathrm{demag}} + E_{\mathrm{Zeeman}} + E_{\mathrm{DMI}} \tag{2.9}$$

Magnetic materials do not only exist with uniform magnetization throughout the sample but can host regions with different orientations of $\mathbf{M}$. These regions are called magnetic domains and the transition region between two domains is called a magnetic domain wall. For instance, a magnet with perpendicular anisotropy along $\pm z$ hosts 180° DWs transitioning from an up-domain ($\mathbf{M} \parallel +z$) to a down-domain ($\mathbf{M} \parallel -z$) or vice versa. A DW that transitions from an up- to a down-domain when moving along the $+x$ direction is uniquely defined as a $\uparrow\downarrow$ DW. For the reverse case, it is dubbed a $\downarrow\uparrow$ DW. The emergence of DWs increases the magnetic energy due to the increased exchange and anisotropy energies [24–26]. The spatial profile of such a DW is mainly determined by the trade-off between exchange, favoring a wide DW, and anisotropy, preferring a narrow DW. The

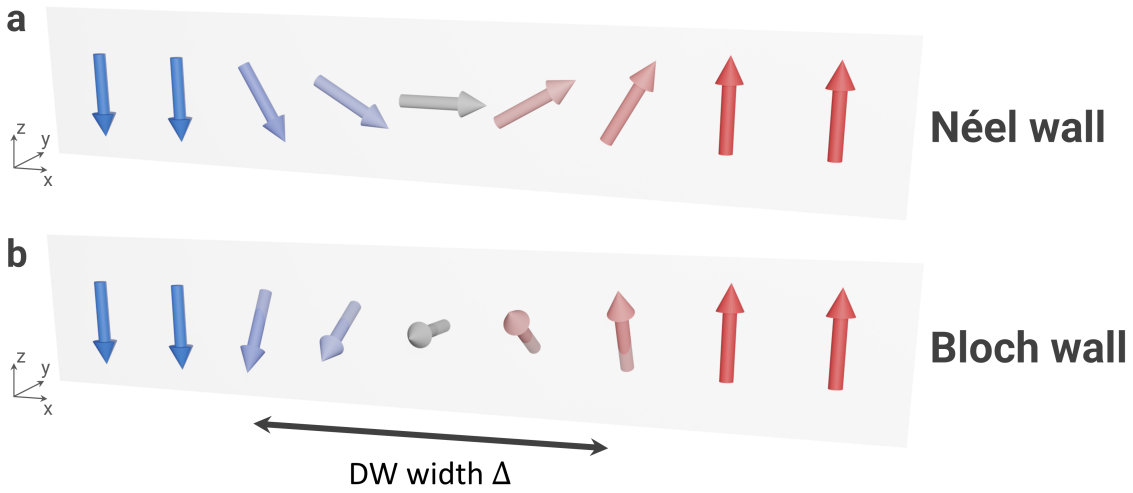

Figure 2.2: **Domain wall configuration types.** Schematic of a ↓↑ magnetic domain wall in **(a)** Néel configuration and **(b)** Bloch configuration.

z-component of magnetization $M_z(x)$ reverses over a distance Δ, dubbed the DW width (Fig. 2.2) [26].

$$\frac{M_z(x)}{M_S} = \pm \tanh\left(\frac{x-q}{\Delta}\right) \tag{2.10a}$$

$$\Delta = \sqrt{\frac{A_{ex}}{K_u}} \tag{2.10b}$$

The parameter q denotes the DW position. There are two possible configurations of a 180° DW: Either it exists in a Néel configuration with the magnetization rotating perpendicular to the DW-plane (in the xz-plane) or it exists in a Bloch configuration with the magnetization rotating in the DW-plane (in the yz-plane) (Fig. 2.2). DWs in ultrathin films with PMA are usually Bloch walls due to shape anisotropy. However, the DW turns into a Néel wall when sufficient DMI is present to overcome the shape anisotropy. Additionally, the DMI makes the Néel wall chiral, i.e. it fixes a rotational sense.

2.2 Magnetization dynamics

The interpretation and prediction of the magnetization response to external perturbations requires the equations of motion for $\mathbf{M}$, i.e. the Landau-Lifshitz-Gilbert (LLG) equations [25, 26]:

$$\frac{\partial \mathbf{M}}{\partial t} = -\gamma \mathbf{M} \times \mathbf{H}_{eff} - \frac{\alpha_L}{M_S} \mathbf{M} \times (\mathbf{M} \times \mathbf{H}_{eff}) \tag{2.11}$$

Here, the effective field $\mathbf{H}_{eff} = -\frac{1}{\mu_0}\frac{\delta E}{\delta \mathbf{M}}$ determines the equilibrium orientation of $\mathbf{M}$ where the torque $\frac{\partial \mathbf{M}}{\partial t}$ vanishes. $\gamma = \mu_0 \gamma_e = \mu_0 \frac{g_e \mu_B}{\hbar}$ denotes the Gilbert gyromagnetic ratio where g_e is the electron g-factor. $\alpha_L = \gamma \alpha_G$ is the phenomenological damping constant that relates to the dimensionless Gilbert damping parameter α_G. When $\mathbf{M}$ does not align with $\mathbf{H}_{eff}$, the first term on the right hand side of eq. (2.11) induces the precession of $\mathbf{M}$ around

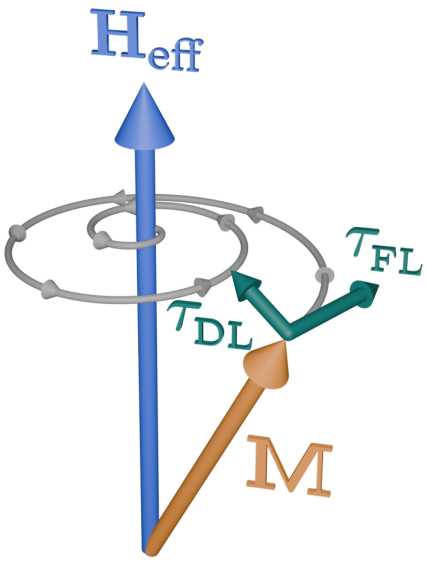

Figure 2.3: **Schematic of field-like and damping-like torques from the LLG-equation.**

$\mathbf{H}_{\text{eff}}$ and is called the field-like (FL) torque $\tau_{\text{FL}} = -\gamma \mathbf{M} \times \mathbf{H}_{\text{eff}}$. The second term on the right side of the equation accounts for magnetization relaxation and gradually dampens magnetization precessions and aligns $\mathbf{M}$ along the equilibrium orientation (Fig. 2.3). It is thus called a damping-like (DL) torque $\tau_{\text{DL}} = \frac{\alpha_{\text{L}}}{M_{\text{S}}} \mathbf{M} \times (\mathbf{M} \times \mathbf{H}_{\text{eff}})$.

An alternating magnetic field $\mathbf{h}_{\text{rf}}$ that drives the magnetization at radio-frequency (RF) frequency f may compensate the energy losses due to damping and achieve a stable precession of $\mathbf{M}$. A uniform magnetization precession throughout the FM is called *ferromagnetic resonance* (FMR). At the FMR resonance frequency f_{FMR}, the precession can be excited most efficiently. This resonance condition strongly depends not only on the magnetic material parameters but also on the shape of the magnet because the shape determines the demagnetizing tensor $\widehat{N}$. The well-known Kittel eq. (2.12b) [39] gives the general resonance condition for a diagonal $\widehat{N}$ where $\mathbf{M}$ is aligned along the axis ξ:

$$\widehat{N} = \begin{pmatrix} N_\mu & 0 & 0 \\ 0 & N_\nu & 0 \\ 0 & 0 & N_\xi \end{pmatrix} \tag{2.12a}$$

$$\omega_0 = \gamma\mu_0 \left[H_{\text{a}} + \left(N_\mu - N_\xi\right) M_{\text{S}}\right]^{1/2} \left[H_{\text{a}} + \left(N_\nu - N_\xi\right) M_{\text{S}}\right]^{1/2} \tag{2.12b}$$

For IP magnetized thin films with $N_\mu = N_\xi \approx 0$ and $N_\nu \approx 1$, eq. (2.12b) returns $\omega_0 = \gamma\mu_0 \sqrt{H_{\text{a}} \left(H_{\text{a}} + M_{\text{S}}\right)}$ where the external field is aligned IP along the initial orientation of $\mathbf{M}$.

In perpendicularly magnetized magnetic thin films, $N_\mu = N_\nu \approx 0$ and $N_\xi \approx 1$ holds and the FMR occurs at $\omega_0 = \gamma\mu_0 \left(H_{\text{a}} - M_{\text{S}}\right)$ for an external field $\mathbf{H}_{\text{a}}$ normal to the film plane.

Adding the effective anisotropy field $H_{\mathrm{ani}} = \frac{2K_{\mathrm{u}}}{\mu_0 M_{\mathrm{S}}}$ increases the resonance frequency accordingly:

$$f = \frac{\gamma}{2\pi}\mu_0 \left(H_{\mathrm{a}} + H_{\mathrm{ani}} - M_{\mathrm{S}}\right) \tag{2.13}$$

Aside from knowing the resonance condition, information on the complex magnetic susceptibility $\chi = \chi' + i\chi''$ is required to determine the FMR lineshape and the excitation efficiency of the FMR mode by alternate magnetic fields $\mathbf{h}_{\mathrm{rf}}(t)$. An equilibrium magnetization $\mathbf{M}_0 \parallel z$ is assumed here [39, 40].

$$\begin{pmatrix} m_{\mathrm{x}} \\ m_{\mathrm{y}} \end{pmatrix} = \mathbf{m}_{\mathrm{rf}}(t) = \chi \cdot \mathbf{h}_{\mathrm{rf}}(t) = \begin{pmatrix} \chi_{\mathrm{xx}} & \chi_{\mathrm{xy}} \\ \chi_{\mathrm{yx}} & \chi_{\mathrm{yy}} \end{pmatrix} \cdot \begin{pmatrix} h_{\mathrm{x}} \\ h_{\mathrm{y}} \end{pmatrix} \tag{2.14a}$$

$$\chi'_{\mathrm{xx}} \sim \frac{H_{\mathrm{a}} - H_{\mathrm{FMR}}}{\left(H_{\mathrm{res}} - H_{\mathrm{a}}\right)^2 + \Delta H^2} \tag{2.14b}$$

$$\chi''_{\mathrm{xx}} \sim \frac{-\Delta H}{\left(H_{\mathrm{res}} - H_{\mathrm{a}}\right)^2 + \Delta H^2} \tag{2.14c}$$

Here, $\Delta H \sim \alpha_{\mathrm{L}}$ originates from the magnetization relaxation mentioned before and determines the width of the resonance. The real part of the susceptibility χ'_{xx} follows an asymmetric Lorentzian shape while the imaginary part χ''_{xx} has a symmetric Lorentzian shape. The latter determines the RF power that is absorbed by the magnet $\mathrm{P} = \mu_0 \pi f \chi''_{\mathrm{xx}} h^2_{\mathrm{RF,x}}$ that is placed in an RF field $h_{\mathrm{RF,x}}$ along x [39]. The experimental realization of FMR and the data analysis is explained in chapter 3.1.4.

Measuring the FMR of a magnet enables the extraction of important magnetic parameters such as the gyromagnetic ratio γ, the damping constant α and the effective magnetic anisotropy.

2.3 Domain wall motion

2.3.1 Collective coordinate model

The dynamics of magnetic domain walls may be accurately described by solving the full LLG equations. Nevertheless, the LLG equations may be simplified by describing the DW only as a set of two variables, the position q and the azimuthal angle ψ of the magnetization at the DW center (i.e. the orientation of the DW magnetization in the xy plane where $\psi = 0°$ corresponds to an alignment along $+x$) as shown in Fig. 2.4. The resulting model is know as the q-ψ-model or the collective coordinate model and describes the DW as a point-like object that is moving in a one-dimensional space.

The model uses the LLG equation in spherical coordinates (ϕ, θ) that are integrated along the DW-axis x. The DW-profile from eq. (2.10a) is used to perform this integration.

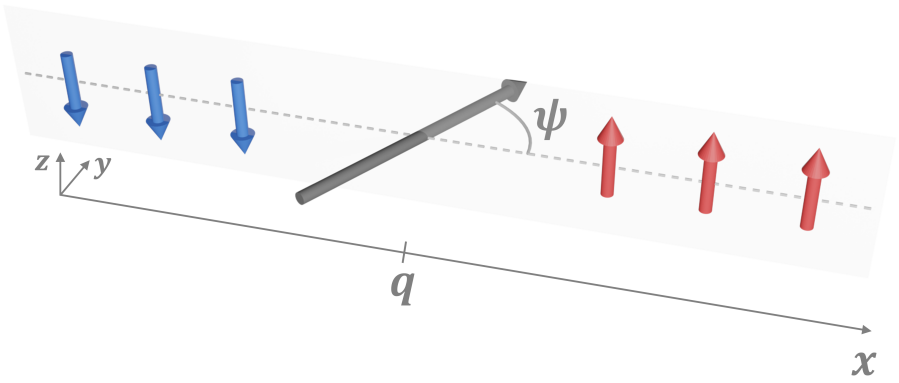

Figure 2.4: **Definition of the domain wall position q and its azimuthal angle ψ in the collective coordinate model.**

The full derivation of the model is given in the appendix A. This provides a set of differential equations for the position q and angle ψ.

$$\frac{\gamma}{2M_S}\frac{\partial\sigma}{\partial q} = \pm\dot{\psi} - \frac{\alpha\dot{q}}{\Delta} \tag{2.15a}$$

$$\frac{\gamma}{2M_S}\frac{\partial\sigma}{\partial\psi} = \mp\dot{q} - \alpha\Delta\dot{\psi} \tag{2.15b}$$

$$\tag{2.15c}$$

Here, $\sigma(q,\psi)$ denotes the area energy density of the DW and the $\pm(\mp)$ signs correspond to the DW type (cf. eq. (2.10a)). Re-arranging these equations returns the following expressions for $\dot{q}$, $\dot{\psi}$.

$$\dot{\psi} = \frac{1}{1+\alpha^2}\left[-\frac{\gamma}{2\mu_0 M_S}\left(\frac{\partial\sigma}{\partial q} + \frac{\alpha}{\Delta}\frac{\partial\sigma}{\partial\psi}\right)\right] \tag{2.16a}$$

$$\dot{q} = \frac{1}{1+\alpha^2}\left[\frac{\gamma}{2\mu_0 M_S}\left(-\alpha\Delta\frac{\partial\sigma}{\partial q} + \frac{\partial\sigma}{\partial\psi}\right)\right] \tag{2.16b}$$

2.3.2 Field-induced motion

In order to calculate the DW motion using eq. (2.16), the energy density E and the corresponding DW area energy density σ have to be known. Assuming a magnetic field H_a along the easy axis of a magnet with PMA, an IP field H_{ip} at an angle ψ_{ip}, an effective IP demagnetizing field at the DW position due to the difference of demagnetization factors along the wall axis N_x and along the wire width N_y, the area energy density of the DW can be derived (also see appendix A):

$$\sigma = \int_{-\infty}^{\infty} E\,dx = \int_{\theta(-\infty)}^{\theta(+\infty)} E\frac{\partial x}{\partial\theta}\,d\theta = \int_0^{\pi} E\frac{\Delta}{\sin(\theta)}d\theta \tag{2.17a}$$

$$= 2\frac{A}{\Delta} + 2K_{u,\mathrm{eff}}\Delta + 2\Delta\mu_0 M_S^2\left(N_x - N_y\right)\cos^2(\psi) \tag{2.17b}$$

$$\pm\left(2\mu_0 M_S H_a\right)q - \pi\mu_0 M_S H_{ip}\Delta\cos\left(\psi - \psi_{ip}\right) \tag{2.17c}$$

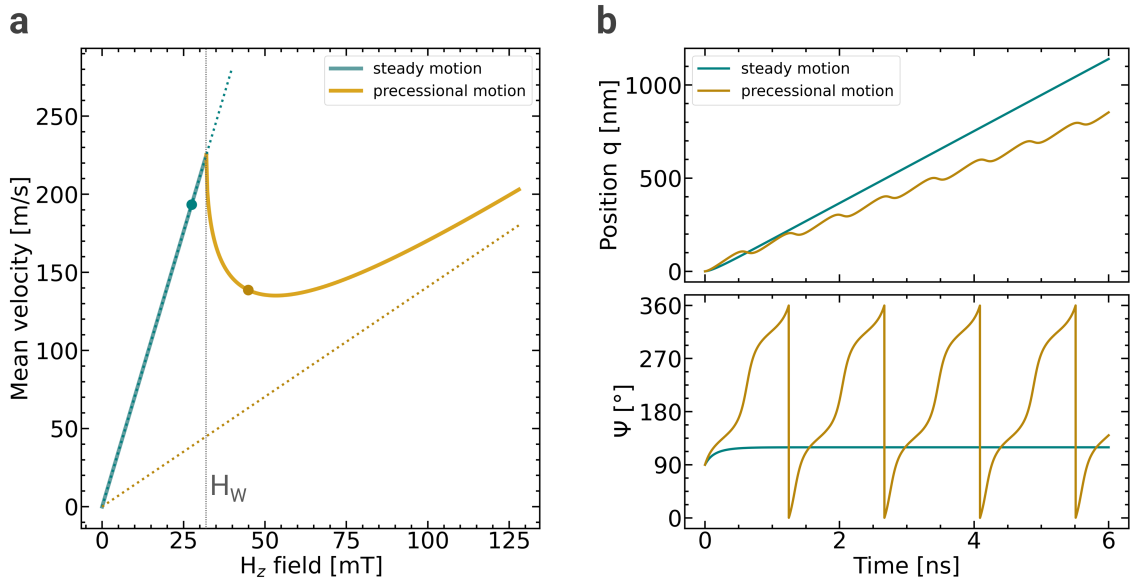

Figure 2.5: **Field-induced domain wall motion. (a)** Numerical solution of the q-ψ-model showing the Walker-breakdown. The mobility in the steady motion regime is significantly higher than the one in the precessional regime. **(b)** Simulations of the time-resolved position q (top graph) and angle ψ (bottom graph) of the DW. The corresponding fields for the simulations are indicated in **(a)** by large dots.

Note, that the DW configuration (e.g. $\downarrow\uparrow$ vs. $\uparrow\downarrow$) affects the DW energy as seen by the term that scales with $\pm H_a q$. Using the previous equation and eq. (2.16), the final expressions for $\dot{\psi}$, $\dot{q}$ are obtained.

$$\dot{\psi} = \frac{\gamma}{1+\alpha^2}\left[H_a + \alpha M_S\left(N_x - N_y\right)\sin(2\psi) - \frac{\alpha\pi H_{ip}}{2}\sin\left(\psi - \psi_{ip}\right)\right] \tag{2.18a}$$

$$\dot{q} = \frac{\gamma}{1+\alpha^2}\left[\mp\alpha\Delta H_a \pm \Delta M_S\left(N_x - N_y\right)\sin(2\psi) \mp \frac{\Delta\pi H_{ip}}{2}\sin\left(\psi - \psi_{ip}\right)\right] \tag{2.18b}$$

Starting with a Bloch-wall configuration ($\psi_0 = 90°$) in an easy-axis magnetic field H_a, the DW shows two propagation regimes as shown in Fig. 2.5a. Below a critical field, the so-called Walker breakdown field H_W, the DW moves in a steady state where $\dot{\psi}$ eventually becomes zero and $\dot{q}$ is constant. For $H_W < H_a$ however, the DW moves in a precessional regime, i.e. the DW orientation ψ is continuously rotating while the DW position q is oscillating back-and-forth with a net propagation in one direction [12] (see Fig. 2.5b). Looking at eq. (2.18a) for $\dot{\psi}$, it can be clearly seen that the H_a term increases the $\dot{\psi}$ while the second, demagnetizing term opposes $\dot{\psi}$ once ψ tilts away from 90°. For low H_a, the angle eventually stabilizes and $\dot{\psi}$ becomes zero. The DW then moves with $\dot{q} = \mp\frac{\gamma H_a \Delta}{\alpha} = \text{const.}$. However, once H_a exceeds the critical value of $H_W = \alpha M_S\left(N_x - N_y\right)$, the demagnetization term in $\dot{\psi}$ can not stabilize the field-induced tilting of ψ. The DW angle ψ is thus continuously rotating and $\dot{q} \neq \text{const.}$. The DW thus shows a net motion in one direction but superimposed with a back-and-forth oscillation at a frequency $f_W = \frac{\gamma}{2\pi}\frac{1}{1+\alpha^2}\sqrt{H^2 - H_W^2}$.

It can be clearly seen from Fig. 2.5a that the mean DW velocity $\langle \dot{q} \rangle$ significantly drops for $H > H_{\mathrm{W}}$ and follows $\langle \dot{q} \rangle = \frac{\gamma \Delta}{\alpha} \left(H - \frac{1}{1+\alpha^2} \sqrt{H^2 - H_{\mathrm{W}}^2} \right)$ [15]. The significantly lower slope in the precessional regime may be interpreted with respect to the energy dissipation $\dot{E}$ from magnetic relaxation [14, 26].

$$\dot{E} = -\frac{M_S \alpha}{\gamma} \left[\dot{\theta}^2 + \dot{\phi}^2 \sin^2(\theta) \right] \tag{2.19}$$

A moving DW, i.e. a variation of the spatial $\theta(x)$-texture with time, always causes energy losses due to $\dot{\theta}$. However, when the IP component of $\mathbf{M}$ is also varying in time, i.e. when $\dot{\phi} \sin(\theta) \neq 0$, this causes additional energy dissipation. It is thus intuitive that a precessing DW dissipates more energy and thus propagates slower. It should be noted that the collective-coordinate approach gives a simplified picture of DW motion whereas micromagnetic simulations are able to present a detailed two-dimensional picture of DW dynamics. Micromagnetic simulations revealed that the precessional DW motion in the Walker regime corresponds to the continous nucleation and annihilation of antivortices (also known as vertical Bloch lines) at the DW [41, 42].

2.3.3 Current-induced domain wall motion by spin-transfer torque

In addition to a magnetic field, magnetic DWs can also be moved by electrical currents. The impact of a spin-polarized electrical current on a FM has been first proposed by Berger [43, 44] and Slonczewski [45]. The mechanism herein lies in the s-d exchange between spin-polarized 4s conduction electrons and the localized 3d magnetic moments. Zhang et al. introduced this current-induced spin-transfer torque (STT) in the LLGS equations (the added letter S stands for Slonczewski) [46, 47]. As spin-polarized conduction electrons enter a FM with a local magnetization $\mathbf{M}$ that is not parallel to the orientation of spin polarization $\mathbf{M}_{\mathrm{p}}$ of the current, itinerant electron spins and local spins exchange momentum. This gives rise to the so-called adiabatic STT $\mathbf{T}_{\mathrm{a}}$.

$$\mathbf{T}_{\mathrm{a}} \sim \mathbf{M} \times \left(\mathbf{M} \times \mathbf{M}_{\mathrm{p}} \right) \tag{2.20}$$

In case of a current flowing accross a DW where $\mathbf{M}$ is slowly varying in space, this torque may be expressed by the magnetization gradient along the direction of electron flow (along $+x$) [47, 48].

$$\mathbf{T}_{\mathrm{a}} = -u \left(\mathbf{e}_{\mathrm{x}} \cdot \nabla \right) \mathbf{M} = -u \frac{\partial \mathbf{M}}{\partial x} \tag{2.21}$$

$$u = -\frac{g \mu_{\mathrm{B}} P j}{2 e M_{\mathrm{S}}} \tag{2.22}$$

Here, $\mathbf{e}_{\mathrm{x}}$ is the unit vector along $+x$, g is the g-factor and the parameter u mainly depends on the electrical current density j and the spin-polarization P. However, another kind of STT exists when the spin-polarization of the conduction electrons can not quickly adjust to the local magnetization. This leads to so-called non-adiabatic conduc-

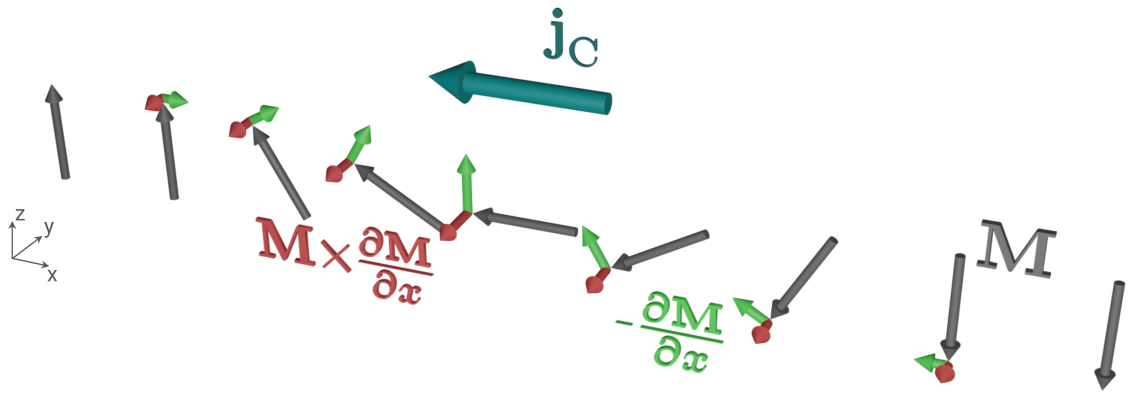

Figure 2.6: **Adiabatic and non-adiabatic STT acting on a domain wall.** A spin-polarized electron flow along $+x$ (opposite to the charge current flow $\mathbf{j}_C$) exerts both an adiabatic torque $\mathbf{T}_a$ (green) and a non-adiabatic torque $\mathbf{T}_{na}$ (red) on the DW.

tion electrons that induce a secondary STT torque, the non-adiabatic torque $\mathbf{T}_{na}$ [49]. The introduction of $\mathbf{T}_{na}$ successfully predicts the experimentally observed low threshold current-density for DW motion by STT that could not be explained by a purely adiabatic torque [49, 50].

$$\mathbf{T}_{na} = \frac{\beta u}{M_S}\mathbf{M}\times\left[(\mathbf{e}_x\cdot\nabla)\,\mathbf{M}\right] = \frac{\beta u}{M_S}\mathbf{M}\times\frac{\partial \mathbf{M}}{\partial x} \tag{2.23}$$

Complementing the LLG-equations with the adiabatic and non-adiabatic torques yield:

$$\frac{\partial \mathbf{M}}{\partial t} = -\gamma\mathbf{M}\times\mathbf{H}_{eff} + \frac{\alpha_G}{M_S}\mathbf{M}\times\frac{\partial \mathbf{M}}{\partial t} - u\frac{\partial \mathbf{M}}{\partial x} + \frac{\beta u}{M_S}\mathbf{M}\times\frac{\partial \mathbf{M}}{\partial x} \tag{2.24}$$

Based on eq. (2.24), the differential equations for q, ψ can be derived similar to chapter 2.3.1 (also shown in the appendix A).

$$\dot{\psi} = \frac{1}{1+\alpha^2}\left[\gamma H_a + \alpha\gamma M_S\left(N_x - N_y\right)\sin(2\psi) - \frac{1}{2}\alpha\gamma H_{ip}\pi\sin\left(\psi-\psi_{ip}\right) \pm \frac{\alpha u}{\Delta} \mp \frac{\beta u}{\Delta}\right] \tag{2.25}$$

$$\dot{q} = \frac{1}{1+\alpha^2}\left[\mp\alpha\Delta\gamma H_a \pm \gamma M_S\left(N_x - N_y\right)\Delta\sin(2\psi) \mp\frac{1}{2}\gamma H_{ip}\pi\Delta\sin\left(\psi-\psi_{ip}\right) + u + \alpha\beta u\right] \tag{2.26}$$

DW motion in the presence of $\mathbf{T}_a$ and $\mathbf{T}_{na}$ is summarized in Fig. 2.7 for different ratios of β/α. Similar to the field-induced DW motion, the motion by STT can also be divided in steady-state motion and precessional motion. The threshold for precessional motion u_W depends on the ratio β/α [15].

$$u_W = \frac{\alpha}{|\alpha-\beta|}\gamma M_S\Delta\left(N_x - N_y\right) \tag{2.27}$$

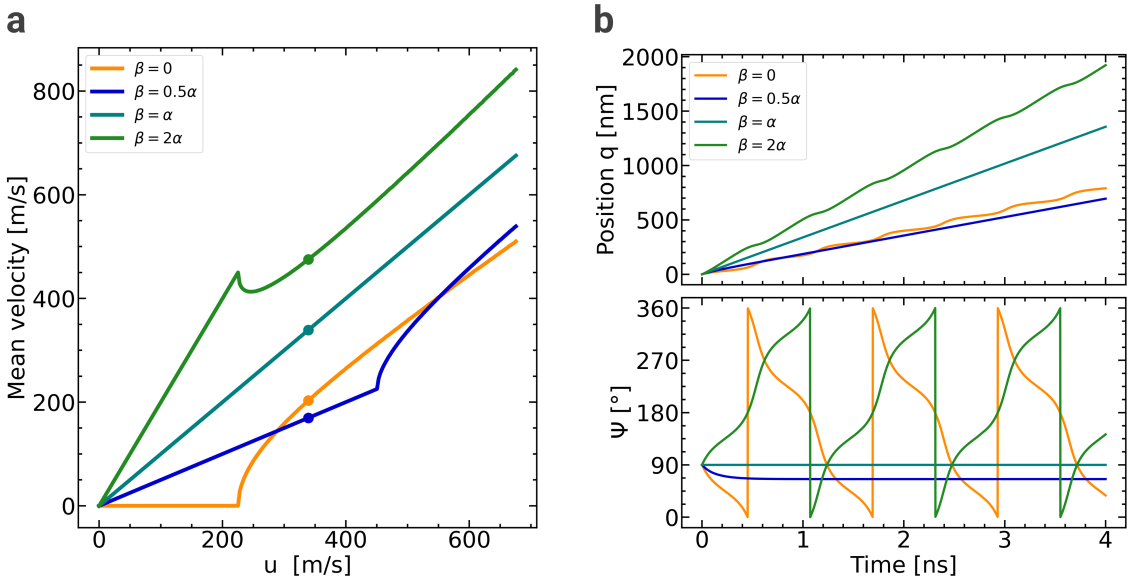

Figure 2.7: **Domain wall motion by current-induced STT.** Numerical solution of the q-ψ-model. **(a)** The average DW velocity for various values of the non-adiabatic torque coefficient β is shown. A Walker breakdown occurs for all β except for $\beta = \alpha$. **(b)** Simulations of the time-resolved position q (top graph) and angle ψ (bottom graph) of the DW for each value of β from **(a)**. The corresponding simulation parameter u is indicated in **(a)** by large dots.

In this regard, the case $\beta = \alpha$ is special since the DW never exhibits a Walker precession.

Below the threshold, i.e. for $u < u_W$, the DW moves at costant velocity $\dot{q}$.

$$\dot{q}\,(u < u_W) = \frac{\beta}{\alpha} u \tag{2.28}$$

Consequently, for $\beta = 0$, the DW does not move ($\dot{q} = 0$) below the threshold $u < u_W$. A finite β is thus required to move the DW also at low current densities.

2.3.4 Current-induced domain wall motion by spin-orbit torque

In addition to the previously mentioned STT, another kind of spin torque has been proven to be particularly effective in driving the motion of magnetic domain walls. The so-called spin-orbit torque (SOT) requires an additional layer, interfaced with the magnetic layer, so that an electrical current flow through the layers layers and along interface generates a spin-accumulation at the interface. In general, the spin Hall effect (SHE) and the inverse spin galvanic effect (iSGE, also referred to as Rashba-Edelstein effect) fulfill this requirement and are introduced in the following.

Spin-Hall effect and spin-orbit torque

The spin Hall effect essentially describes that a transverse spin current density $\mathbf{j}_S$ is created as a result of a longitudinal (and unpolarized) charge current density $\mathbf{j}_C$ [51–53] as seen in Fig. 2.8. The conversion efficiency between charge and spin current density j_C and j_S, is expressed by the Spin Hall angle (SHA) $\theta_{SHE} = \frac{j_S}{j_C}\frac{2e}{\hbar}$. The polarization σ_{SHE} of

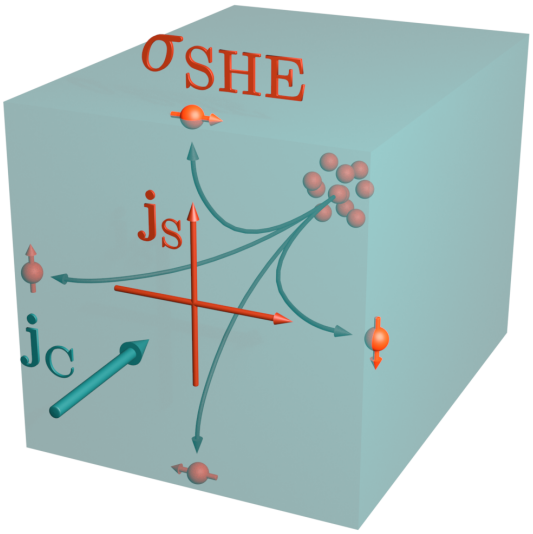

Figure 2.8: **Schematic of the spin Hall effect.** A unpolarized charge current density j_C causes a spin-dependent deflection of the moving electrons (orange balls). As a result, a spin accumulation builds up at each surface of the material whereby the unit vector of the spin moment polarization σ_{SHE} at each surface is parallel to its surface and perpendicular to j_C. This process can be described by a pure spin-current density j_S between the surfaces of the spin Hall material.

the accumulated spin moment at the surface of the spin-Hall material is a unit vector perpendicular to both $\mathbf{j}_S$ and $\mathbf{j}_N$.

$$\sigma_{SHE} \sim \mathbf{j}_C \times \mathbf{j}_S \tag{2.29}$$

The SHE leads to the spin-accumulation at the boundaries of the spin Hall (SH) material but it does not lead to a charge accumulation. The microscopic origins of the SHE lie in the relativistic SOC of the material. One differentiates between intrinsic and extrinsic mechanisms [53]. The intrinsic contribution to the SHE is linked to a topological property of the band structure of the material, called the Berry curvature, that causes a spin-dependent deflection of electrons [52, 53]. The extrinsic contributions are linked to the spin-dependent (Mott) scattering at impurities or a disorder potential [51,53,54]. Materials that have been observed to exhibit a strong SHE, i.e. a large charge-to-spin conversion efficiency, are heavy metals such as Pt, W, Ta due to their large intrinsic SHE. For completeness it should be noted that in case of a system with broken inversion symmetry and SOC the iSGE also causes the current-induced spin-accumulation at the interface [55–58].

The observable effects of the SHE and iSGE may not be straightforward to disentangle [59,60] but their combined effects are generalized as follows: An electrical current density in the plane of the normal metal (and along the interface) generates a spin accumulation at the interface of metal and FM. Moreover, this spin-density may diffuse into the FM layer.

This will exert a FL torque $\mathbf{T}_{\mathrm{FL}}^{\mathrm{SOT}}$ and a DL torque $\mathbf{T}_{\mathrm{DL}}^{\mathrm{SOT}}$ on the nearby magnetization. These torques are referred to as spin-orbit torques (SOTs).

$$\mathbf{T}_{\mathrm{DL}}^{\mathrm{SOT}} = -\frac{\tau_{\mathrm{DL}}}{M_{\mathrm{S}}^2}\mathbf{M}\times(\mathbf{M}\times\sigma_{\mathrm{SHE}}) \tag{2.30}$$

$$\mathbf{T}_{\mathrm{FL}}^{\mathrm{SOT}} = -\frac{\tau_{\mathrm{FL}}}{M_{\mathrm{S}}}\mathbf{M}\times\sigma_{\mathrm{SHE}} \tag{2.31}$$

Here, τ_{DL} and τ_{FL} are the magnitude of the DL and FL torques whose magnitude and sign are determined by the spin mixing conductance at the interface [59–61]. The torque $\mathbf{T}_{\mathrm{DL}}$ results in the alignment of $\mathbf{M}$ along σ_{SHE} while $\mathbf{T}_{\mathrm{FL}}$ causes a precession of $\mathbf{M}$ around σ. Considering the SHE-dominated Pt/Co bilayer system that is used in this work, the DL-torque is strongest with $\left|\frac{\tau_{\mathrm{FL}}}{\tau_{\mathrm{DL}}}\right| < 1$ [59, 62]. The extended LLGS equations with SOTs are shown in the following:

$$\begin{aligned}\frac{\partial\mathbf{M}}{\partial t} =& -\gamma\mathbf{M}\times\mathbf{H}_{\mathrm{eff}} + \frac{\alpha_{\mathrm{G}}}{M_{\mathrm{S}}}\mathbf{M}\times\frac{\partial\mathbf{M}}{\partial t} - u\frac{\partial\mathbf{M}}{\partial x} + \frac{\beta u}{M_{\mathrm{S}}}\mathbf{M}\times\frac{\partial\mathbf{M}}{\partial x}\\ &- \frac{\tau_{\mathrm{DL}}}{M_{\mathrm{S}}}\mathbf{M}\times(\mathbf{M}\times\sigma_{\mathrm{SHE}}) - \tau_{\mathrm{FL}}\mathbf{M}\times\sigma_{\mathrm{SHE}}\end{aligned} \tag{2.32a}$$

Mechanism of domain wall motion by SOT

In the following, the impact of the predominant DL-SOT on DW motion will be outlined: For a current injection along the DW-axis, the DL-SOT does not induce DW motion in FMs hosting Bloch walls. However, in a static magnetic field that rotates the DW towards the Néel configuration, a DL-SOT results in fast DW speeds [11, 13, 63]. Such a Néel configuration is stabilized also in the absence of any static magnetic fields when an interfacial DMI is present. This DMI does not only induce the Néel character of the DW, but also makes it chiral, i.e. the rotational sense of the magnetization along the DW-axis is determined by the sign of the DMI constant. As mentioned in chapter 2.1, such DMI exists at HM/FM interfaces in the presence of strong SOC and is also present at the typical Pt/Co interface used throughout this work. The micromagnetic DMI constant D is negative at the Pt/Co interface so that it favors an anti-clockwise rotation of the magnetization. Next, the DL-SOT and the DMI are integrated into the equations of motion from the q-ψ model deduced from the LLGS eq. (2.32a) (also see the full derivation in the appendix A):

$$\begin{aligned}\dot{\psi} = \frac{1}{1+\alpha^2}\Bigg[&\gamma H_{\mathrm{a}} + \alpha\gamma M_{\mathrm{S}}\left(N_{\mathrm{x}}-N_{\mathrm{y}}\right)\sin(2\psi) - \frac{1}{2}\alpha\gamma H_{\mathrm{ip}}\pi\sin\left(\psi-\psi_{\mathrm{ip}}\right)\\ &\pm\frac{\alpha\gamma D\pi\sin(\psi)}{2\Delta\mu_0 M_{\mathrm{S}}} \pm \frac{\alpha u}{\Delta} \mp \frac{\beta u}{\Delta} + \frac{\pi\cos(\psi)}{2}\left(-\tau_{\mathrm{DL}} - \alpha\tau_{\mathrm{FL}}\right)\Bigg]\end{aligned} \tag{2.33}$$

$$\begin{aligned}\dot{q} = \frac{1}{1+\alpha^2}\Bigg[&\mp\alpha\Delta\gamma H_{\mathrm{a}} \pm \gamma M_{\mathrm{S}}\left(N_{\mathrm{x}}-N_{\mathrm{y}}\right)\Delta\sin(2\psi) \mp \frac{1}{2}\gamma H_{\mathrm{ip}}\pi\Delta\sin\left(\psi-\psi_{\mathrm{ip}}\right)\\ &+\frac{\gamma D\pi\sin(\psi)}{2\mu_0 M_{\mathrm{S}}} + u + \alpha\beta u + \frac{\Delta\pi\cos(\psi)}{2}\left(\pm\alpha\tau_{\mathrm{DL}} \mp \tau_{\mathrm{FL}}\right)\Bigg]\end{aligned} \tag{2.34}$$

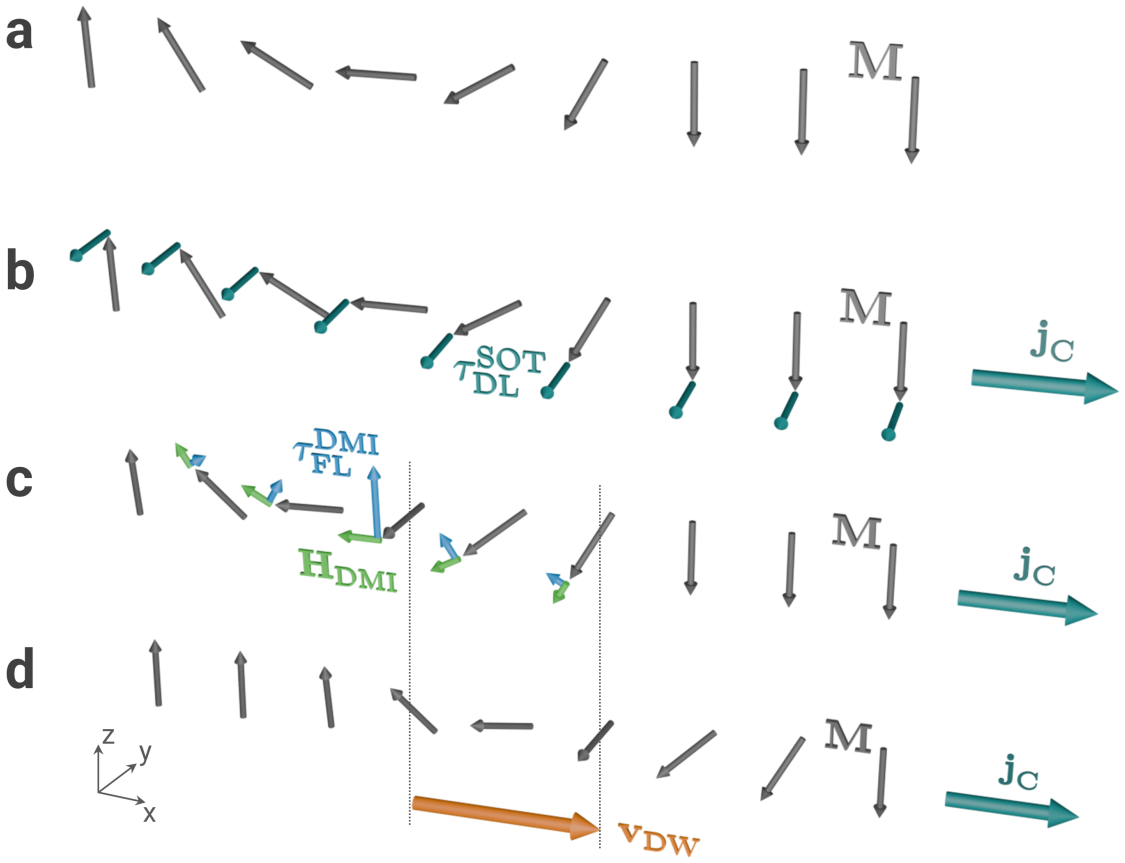

Figure 2.9: **Domain wall motion by a damping-like spin-orbit torque.** **(a)** Static configuration of a Néel DW in $\uparrow\downarrow$ configuration. **(b)** An applied charge current density along $+x$ in the neighboring heavy metal layer causes a DL-SOT in the FM tilting the magnetization towards $-y$. **(c)** The magnetization tilting out of the xz plane results in a field-like torque τ_{FL}^{DMI} from the effective DMI-field H_{DMI}. **(d)** The combined action of τ_{DL}^{SOT} and τ_{FL}^{DMI} lead to the propagation of the DW along $+x$.

Starting from a $\uparrow\downarrow$ Néel configuration ($\psi = 180°$), a positive current density causes a DL-SOT along $-y$ that has a strong impact on $\dot{\psi}$ (see $-\frac{\pi\cos(\psi)}{2}\tau_{DL}$ term) so that ψ tilts towards $\psi = 270°$. As soon as ψ deviates from 180°, a term $\frac{\gamma D\pi\sin(\psi)}{2\mu_0 M_S}$ in $\dot{q}$ accelerates the DW along the current flow (note that $D < 0$ here).

Figure 2.9 visualizes the aforementioned mechanism: The current-induced DL-SOT τ_{DL}^{SOT} alone tilts the DW magnetization towards a Bloch configuration (Fig. 2.9b-c). The effective DMI field H_{DMI} (preferring a Néel configuration) subsequently creates a field-like torque τ_{FL}^{DMI}(Fig. 2.9c). The strength of this torque is maximal at the DW center and points along $+z$ there. The latter torque thus rotates the magnetization such that the whole DW effectively moves along $+x$ (Fig. 2.9d). By this mechanism a DW can be moved along $+x$ ($-x$) by applying positive (negative) current pulses. This method of DW motion works the same for both $\downarrow\uparrow$ and $\uparrow\downarrow$ DWs.

The SOT moves the DW along the electrical current flow and is thus opposite to the STT-induced motion and typically dominates the latter for ultra-thin films. For thicker films, the strength of the SOT, originating from the interface, ceases and the DW mo-

tion is eventually STT-dominated again. The advantages of the SOT-driven DW motion are (a) the vanishing intrinsic threshold current density and (b) the fact that the Walker breakdown is heavily suppressed by the DMI so that higher energy dissipation is avoided and the DW moves in a steady-state [13]. Nevertheless, the DW velocity saturates at $\dot{q}_{\mathrm{sat}} = \frac{\gamma D \pi}{2\mu_0 M_{\mathrm{S}}\left(1+\alpha^2\right)}$ so that a large DW speed requires a large D. An important difference to the field-induced DW motion in chapter 2.3.2 is that the steady-state DW velocity is now independent of the DW width Δ. Altogether, the integration of a DL-SOT and the DMI yields highly efficient current-induced motion of DWs [7, 9, 10, 13].

Magnetic field dependence of DW motion

The eqs. (2.33) already show that an IP magnetic field H_{ip} at an angle ψ_{ip} to the DW axis impacts the DW's equation of motion. In contrast to an out-of-plane (OOP) magnetic field, the IP field itself can not cause the DW to move steadily but it only modifies the DW's equilibrium magnetic state for instance by changing ψ. Nevertheless, the impact of an IP field during current-induced DW motion by SOT is significant. In the following, the effect of a longitudinal field H_{x} ($\psi_{\mathrm{ip}} = 0°$, $180°$) and a transverse field H_{y} ($\psi_{\mathrm{ip}} = \pm 90°$) will be outlined [10]:

A longitudinal H_{x} field is either aligned along or opposite to the effective DMI-field H_{DMI} and acts similarly in the equations of motion. As previously explained, the presence of DMI (in the field-free case) is a necessity to induce DW motion by a DL-SOT. Hence, H_{x} will either reinforce the DW motion when it is parallel to the H_{DMI} or slow down the motion when it is opposite to H_{DMI}. Consequently, when $H_{\mathrm{x}} = -H_{\mathrm{DMI}}$, the impact of both fields cancel and the DW does not move under the action of SOT. In particular, when H_{x} is opposite to H_{DMI} and exceeds the magnitude of the latter, the DW reverses its direction of motion, i.e. it now moves *opposite* to the current pulse whereas conventionally it used to move *along* the pulse. Moreover, since $\downarrow\uparrow$ and $\uparrow\downarrow$ DWs have opposite internal DMI-fields, i.e. $H_{\mathrm{DMI}}(\downarrow\uparrow) \parallel +x$ and $H_{\mathrm{DMI}}(\uparrow\downarrow) \parallel -x$, they react oppositely to an externally applied field H_{x}. Altogether, the impact of an H_{x} field on DW motion is shown in Fig. 2.10a [10].

Note that both in the field-free case and in presence of an H_{x} field, the DW motion is symmetric to the current polarity, i.e. the DW moves at equal speed along $+x$ or $-x$ when a positive or negative current pulse is applied. This symmetry is not preserved when a transverse magnetic field H_{y} is applied. The presence of H_{y} induces asymmetry to the DW motion, i.e. for $H_{\mathrm{y}} > 0$ the DW moves slightly faster along $+x$ and significantly slower along $-x$. This asymmetry reverses for $H_{\mathrm{y}} < 0$ where DW motion along $-x$ is favored. These H_{y}-induced effects are seen in Fig. 2.10b [10]. This behavior is equal for both DW configurations $\downarrow\uparrow$ and $\uparrow\downarrow$. The H_{y} field is thereby inducing a directionality to the DW motion, i.e. DW propagation along one direction is favored while it is suppressed along the other. In contrast to H_{x}, however, the H_{y} field is not capable of significantly speeding up to maximum attainable DW speed.

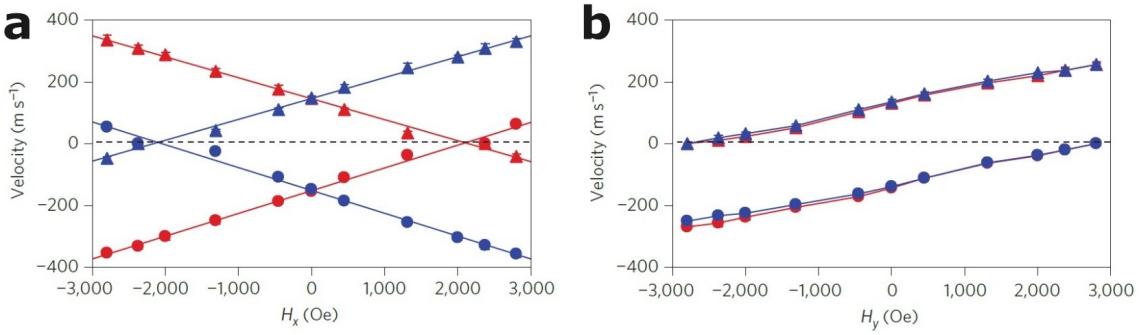

Figure 2.10: **Magnetic in-plane field dependence of current-induced DW motion by SOT.** Current-induced DW motion in Pt/Co/Ni/Co multilayers using 5 ns long current pulses. Longitudinal (H_x, **(a)**) and transversal (H_y, **(b)**) magnetic IP fields are applied during DW motion. The blue and red color of the symbols corresponds to ↓↑ and ↑↓ DWs, respectively. The triangular and circular shape represents a positive and negative current polarity that is passed through the conduit. Figures are taken with permission from [10].

2.4 Magnetization switching mechanisms

In addition to DW motion, the magnetization reversal is also addressed in this work. In the following, the general reversal mechanisms will be introduced, i.e. field-induced switching and current-induced SOT switching. In general, the terms magnetization *switching* and magnetization *reversal* will be used synonymously.

2.4.1 Field-induced switching

The most intuitive means to reverse a FM is a magnetic field. Using the simplifying assumptions of having a single-domain FM with volume V and uniaxial anisotropy K_u in an static external magnetic field H_a, the reversal may be predicted with the Stoner-Wohlfarth model (SWM) [64]. The potential energy E_{SWM} landscape exhibits two degenerate minima in zero field and is altered by H_a until one of these minima becomes unstable and switching occurs.

$$\frac{E_{SWM}}{V} = K_u \sin^2(\phi) - \mu_0 H_a M_S \cos(\theta - \phi) \tag{2.35}$$

Here, ϕ and θ are the angles of the magnetization and the magnetic field relative to the easy axis, respectively. Figure 2.11a shows the hysteretic magnetization switching for different orientations of H_a and the easy axis of the magnet. This angular dependence of the required switching field is visible in the Stoner-Wohlfarth astroid [65] seen in Fig. 2.11b and given by the following equation [66] where $h_i = H_i/H_{an}$ denote the fields normalized to the effective anisotropy field H_{an}.

$$h_x^{2/3} + h_z^{2/3} = 1 \tag{2.36}$$

The SWM is based on a uniform rotation of the magnetization of a magnet without any spin textures or waves and in many cases predicts higher switching fields than exper-

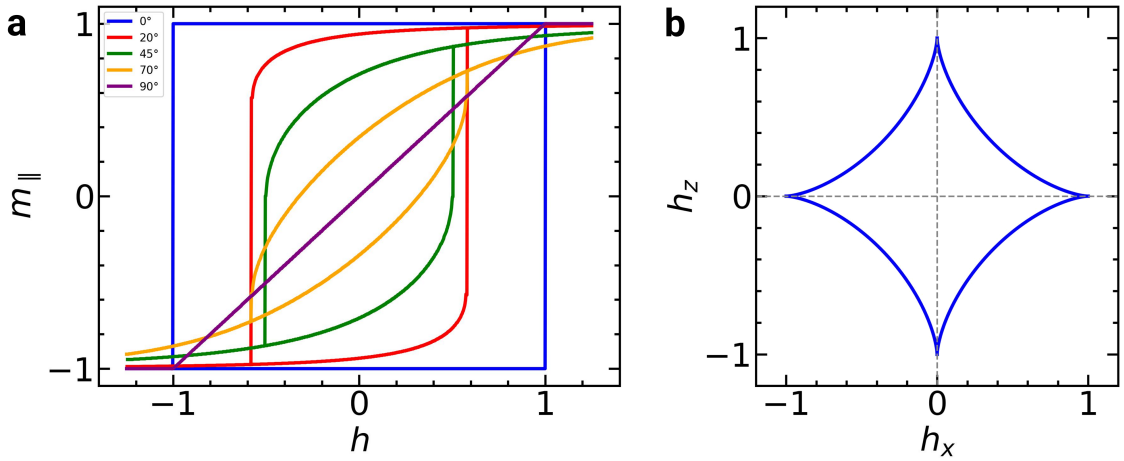

Figure 2.11: **Stoner-Wohlfarth magnetization reversal.** (**a**) Normalized magnetization component parallel to the applied magnetic field. The field variable h is the magnetic field normalized to the anisotropy field. The magnetization reversal is shown for different angles θ between field and easy axis. (**b**) The Stoner-Wohlfarth astroid displays the x- and z-components of the normalized switching field.

imentally observed. In an experiment, switching often occurs at much lower fields owing to domain nucleation and subsequent DW propagation. This alternative switching mechanism occurs in macroscopic samples with sizes exceeding the single-domain diameter and is assisted by temperature. The initial domain nucleation takes place at magnetic defects with lower anisotropy [67] or at the edges of the magnet if DMI is present [68].

2.4.2 Microwave-assisted field-induced switching

Applying an additional microwave/RF magnetic field has been shown to significantly facilitate the field-switching of many different classes of FM [22, 69, 70]. This concept is called microwave-assisted switching (MAS) or microwave-assisted magnetic recording (MAMR). Considering a FM with perpendicular anisotropy that is exposed to a static easy-axis field H_z and a circularly-polarized RF-excitation field with magnitude h_{rf}, the RF-field excites the FMR when at resonance. A coordinate transform to the rotating frame of the precessing magnetization shows that the magnetic field in the rotated frame H^{R} is now static in time and reads as follows [22, 71]:

$$H^{\mathrm{R}} = \begin{pmatrix} 0 \\ h_{\mathrm{rf}} \\ H_{\mathrm{z}} + H_\omega \end{pmatrix} = \text{const.} \tag{2.37}$$

Here, $H_\omega = \frac{\omega}{\gamma}$ is a static field pointing opposite to the effective anisotropy field. In the rotated frame, the magnetization experiences two additional static fields, namely the z-field H_ω and the transverse field (h_{rf}), that are both assisting reversal. The enhanced

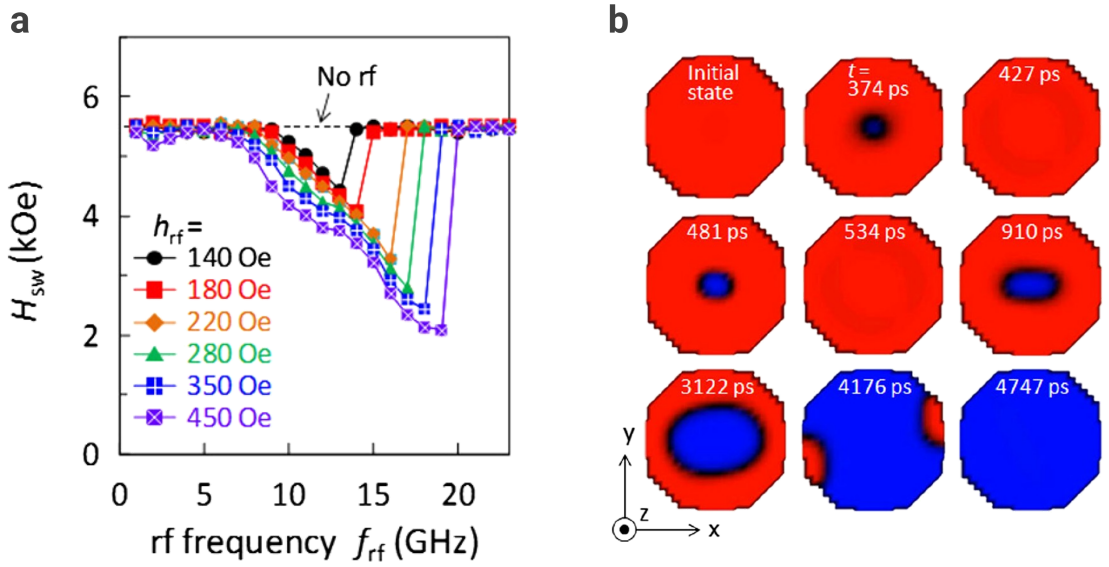

Figure 2.12: **Microwave-assisted switching of Co/Pt nanodots.** **(a)** Frequency-dependence of MAS for various RF field amplitudes h_{rf}. H_{sw} decreases linearly with frequency until a critical frequency is reached. **(b)** Snapshots of the z-component of the magnetization of a Co/Pt nanodot based on micromagnetic simulations. Red (Blue) corresponds to a magnetization along $-z$ ($+z$). The excitation of concentric standing spin waves in the nanodot eventually leads to domain nucleation at the center and induce MAS. Figures is taken with permission from [22].

reversal (i.e. the reduction of the required switching field $H_{z,sw}$) is particularly obvious when revisiting the SWM astroid eq. (2.36) and inserting H_ω and h_{rf} [72, 73].

$$H_{z,sw} = \left(H_k^{2/3} - h_{rf}^{2/3}\right)^{3/2} - H_\omega \tag{2.38}$$

In contrast to magnetization switching by domain nucleation and propagation, the FM reverses uniformly during MAS. This results in a much narrower distribution of switching fields since the stochasticity of the temperature-assisted nucleation is not required for switching anymore [22].

While eq. (2.38) within the SWM provides a very intuitive picture to explain the occurrence of MAS, calculations of the steady precession states, using the LLG-equations, provide a more rigorous understanding of MAS. For instance, the frequency dependence and the occurrence of a maximum frequency (see Fig. 2.12a) can be theoretically explained by investigating the number of allowed steady-state solutions for magnetization precessions that are stable at a certain frequency and field [71, 73]. The switching occurs at the transition from a field that allows for two stable precession states to a field that only allows for one such state. At high frequencies exceeding the FMR, the magnetization can not follow the RF field anymore and the MAS thus disappears [73].

Furthermore, a MAS mechanism exists that goes beyond the MAS effect in the SWM. In samples with sufficiently large diameter, perpendicular standing spin-wave modes [74] may exist close to the FMR frequency. The strong excitation of these modes leads to a MAS (see Fig. 2.12b) with much stronger reductions of the reversal field and much larger

maximum frequency exhibiting the MAS-effect (compared to the MAS in the macrospin picture of the SWM) [22].

2.4.3 Spin-orbit torque switching

The previously mentioned switching mechanisms exclusively involved magnetic fields to induce the switching. However, an electrically induced SOT can also switch the magnetization. For this, a current-induced DL-SOT (cf. chapter 2.3.4) in presence of a longitudinal magnetic field H_x (see Fig. 2.13) deterministically switches the magnetization between its two equilibrium states along $\pm z$. While H_x alone does not favor one of these states, it breaks the symmetry of the magnetization response to the SOT and thereby determines the outcome of a switching process [75]. One needs to differentiate between two mechanisms of magnetization reversal: (a) coherent reversal in single-domain magnets and (b) incoherent reversal by domain nucleation and DW propagation.

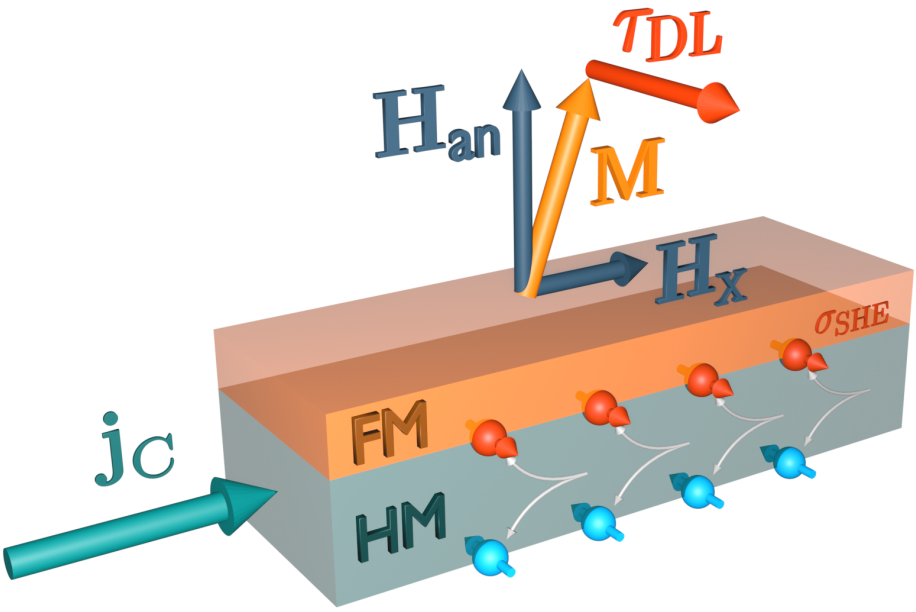

Figure 2.13: **Schematic of spin-orbit torque switching.** A charge current density j_c creates the accumulation of spin momentum with the polarization σ_{SHE} at the HM/FM interface and causes a damping-like torque τ_{DL}. In presence of a longitudinal field H_x, SOT switching occurs.

Firstly, in very small magnets it is energetically unfavorable to host multiple domains [25,76]. During switching, the magnetization in these single-domain magnets is expected to rotate coherently throughout the sample. SOT switching in this framework requires the following ingredients: a damping-like spin-orbit torque τ_{DL}, an effective anisotropy field $H_{eff,an}$ and a longitudinal field H_x. Figure 2.14 visualizes the switching trajectory and the relevant torques during the up-to-down switching of **M**. Starting from the initial magnetization, determined by $H_{an,eff}$ and H_x, the DL-SOT tilts **M** towards the y-axis. This tilting from the former equilibrium state induces the field torques τ_{an} and τ_x that rotate **M** towards the x-axis. If the current-induced τ_{DL} is too weak, the magnetization

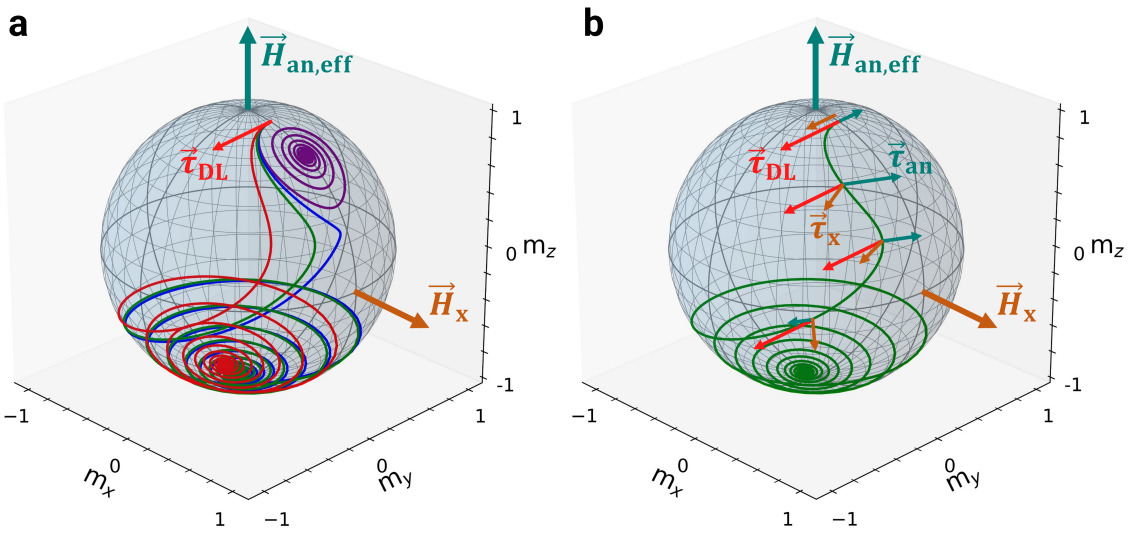

Figure 2.14: **Trajectory of magnetization during SOT switching.** (**a**) The orientation of the reduced magnetization is displayed on a unit sphere. Starting from an equilibrium state on the upper hemisphere with $m_z > 0$, a DL-SOT with variable strength is applied. The SOT-strength gradually increases from purple (no switching) to blue, green and red (successful switching). (**b**) The orientation and magnitude of the different torques acting on the magnetization during a switching process is schematically indicated. The underlying data for the trajectories in (**a,b**) was generated using Mumax3 [78]

stabilizes at a new equilibrium position with $m_z > 0$ and no switching occurs (see purple curve in Fig. 2.14a). When sufficient current is applied, τ_{DL} forces $\mathbf{M}$ on a trajectory that crosses the equator ($\theta = 90°$), reverses the chirality of precession and stabilizes in a down-magnetized state (see blue, green and red curves). Note that H_{an} reverses sign when crossing the equator and thereby causes the opposite precession chirality. A finite H_x enables the switching by forcing $\mathbf{M}$ accross the equator. In a simplified model, the required switching current density $j_{sw,crit}$ relates to H_x as follows [77]:

$$j_{sw,crit} = \frac{2eM_S d_{FM}}{\hbar \theta_{SHE}} \left(\frac{H_{an,eff}}{2} - \frac{H_x}{\sqrt{2}} \right) \tag{2.39}$$

Herein, d_{FM} and θ_{SHE} denote the FM thickness and the spin Hall angle, respectively.

An alternative switching mechanism occurs in larger samples which can form a multi-domain state. Magnetization reversal in such samples occurs by domain nucleation and subsequent DW propagation. Local (non-uniform) nucleation of a reverse domain may occur at magnetic defects with low anisotropy [67], by thermal fluctuations [79] or by the presence of DMI [68, 80]. Once a reverse domain exists, the surrounding DW will move by the SOT as shown in chapter 2.3.4 and propagate and annihilate at the sample edge. Ultimately, the magnetization throughout the sample volume is reversed (see Fig. 2.15a). This two step mechanism usually requires a lower current density than in eq. (2.39) but the total switching time depends on the DW propagation time and thus on the size of the magnetic element [19].

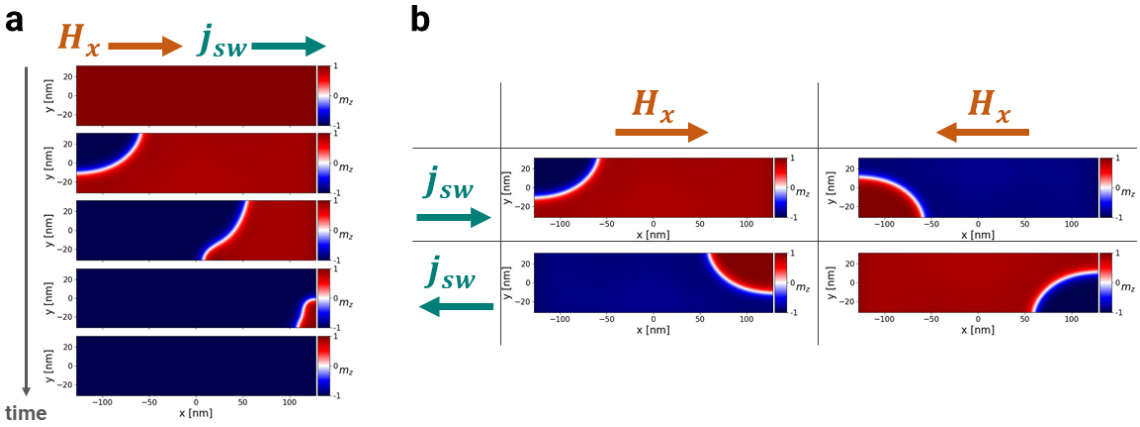

Figure 2.15: **SOT switching by domain nucleation and propagation.** (**a**) The up-to-down switching process by SOT occurs by domain nucleation in the top left corner of the FM, followed by a domain propagation along the current. The DW annihilates at the right end of the sample. (**b**) Overview of the H_x, j_{sw} configuration for the four different switching configurations. The images each show the magnetization 180 ps after the application of j_{sw} and shows the deterministic domain nucleation in different corners of the FM. The data shown in (**a,b**) was generated using Mumax3 [78].

As shown in Fig. 2.15b, a domain deterministically nucleates at one corner for HM/FM systems with finite DMI (that are under investigation in this work). Since the DMI tilts **M** at the sample edges, the additional presence of H_x favors the nucleation at one of the edges that are normal to H_x and explains the left/right asymmetry [20, 68, 80]. Furthermore, the top/down asymmetry of the nucleation site has been ascribed to a DMI-induced tilting at the top/bottom edges that leads to an effective z-field favoring/opposing the switching [81]. Regarding this two-step switching mechanism, the stability and the dynamics of DWs thus play a crucial role for the switching.

Chapter 3

Methods

3.1 Deposition and characterization of magnetic thin films

3.1.1 Magnetron sputtering

The magnetic thin films were grown by DC magnetron sputtering, a physical vapour deposition technique schematically represented in Fig. 3.1. It consists of a material target, a magnetron source and a substrate, all of which are placed in a vacuum chamber [1, 82]. The target consists of the material that is to be deposited as a thin film and is located on top of the magnetron source. The latter consists of an arrangement of permanent magnets, a water-cooling and a voltage source. When a high negative voltage is applied to the source and the target and a flow of inert gas atoms such as Argon is applied, a DC plasma discharge is ignited. The magnetron magetic field confines the plasma to the region near the target. The plasma constantly recreates positively charged gas ions Ar^+ by ionization. The large electric field accelerates these ions towards the target. This results in a collision cascade between Ar^+-ions and the target surface. This process can eject atoms from the target into the chamber, where they will move towards the substrate. This process is called *sputtering*. While a sputtered atom moves towards the substrate it collides with the Ar-gas multiple times and therefore reduces its kinetic energy to typically a few eV when it reaches the substrate and adsorbs there. To ensure uniform composition and thickness of the deposited film, the substrate is usually rotated during deposition. The intricate details and requirements for the choice of substrate, temperature, buffer/seed layers and the growth mode are beyond the scope of this introduction and are described elsewhere [1].

To grow the magnetic thin films used throughout this work, a home-built deposition system with a base pressure of below 10^{-9} Torr is used. The deposited film structure is: 20 TaN / 50 Pt / d_{Ta} / 3 Co / [7 Ni / 3 Co]$_{\mathrm{N}}$ / 30 TaN (the numbers indicate the thickness in Å). Different multilayer repetitions N are used. While films with $N = 1$ are deposited for domain wall motion and SOT-switching purposes, multilayers with $N = 3, 4, 5$ are deposited for MAS. Note that the Tantalum thickness d_{Ta} is varied to modify the magnetic anisotropy of the film which strongly depends on the Pt/Co interface (chapter 3.1.2). A

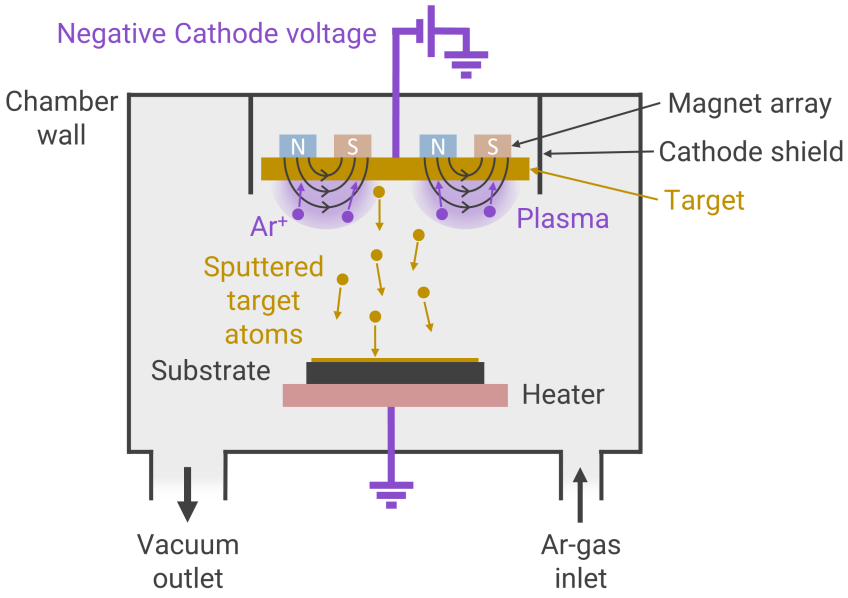

Figure 3.1: **Schematic of magnetron sputtering.**

different repetition number N of the Co/Ni multilayers also impact the effective anisotropy of the film. During deposition, a typical Argon pressure of 3 mTorr is applied and plasma powers of 30 W are used for the deposition of Pt, while 20 W are used for the deposition of Co, Ni, Ta. For the TaN, reactive sputtering is used. Here, a mixture 85% Ar and 15% N_2 serves as the sputter gas and the reaction of Ta to TaN takes place in the plasma at the target surface. The sputter deposition takes place at room temperature, at a substrate rotation rate of 10 rpm.

3.1.2 Role of the interfaces in Pt/[Co/Ni]$_N$ multilayers

This chapter serves to elaborate on the importance of the Pt/Co and the Co/Ni interface and the impacts of its interface modification. Not only is the Pt underlayer required to generate a strong SOT in the FM (c.f. chapter 2.3.4), but it also significantly affects the magnetic properties of the film.

The interface between Pt and Co in (111) orientation exhibits a strong hybridization of electronic 3d and 5d states of Co and Pt, respectively, as shown by XMCD [27]. On the one hand this induces an orbital magnetic moment in Co that is typically quenched in the bulk. This orbital moment is oriented perpendicular to the surface and induces PMA due to the SOC in Co. On the other hand, the electronic hybridization also induces an orbital moment in Pt. The latter translates into a spin magnetic moment in Pt, due to the strong SOC in Pt. This effect is commonly referred to as proximity induced magnetization [83].

The interface in (111)-oriented Co/Ni also exhibits significant PMA due to SOC-induced energy splitting of the 3d-electron states with x^2-y^2- and xy-character at the Fermi level [28]. This effect is strongly dependent on the exact band-filling and thus varies depending on the ratio of the Co and Ni thicknesses. Moreover, a (111) growth orientation is crucial to obtain a strong PMA [29, 30].

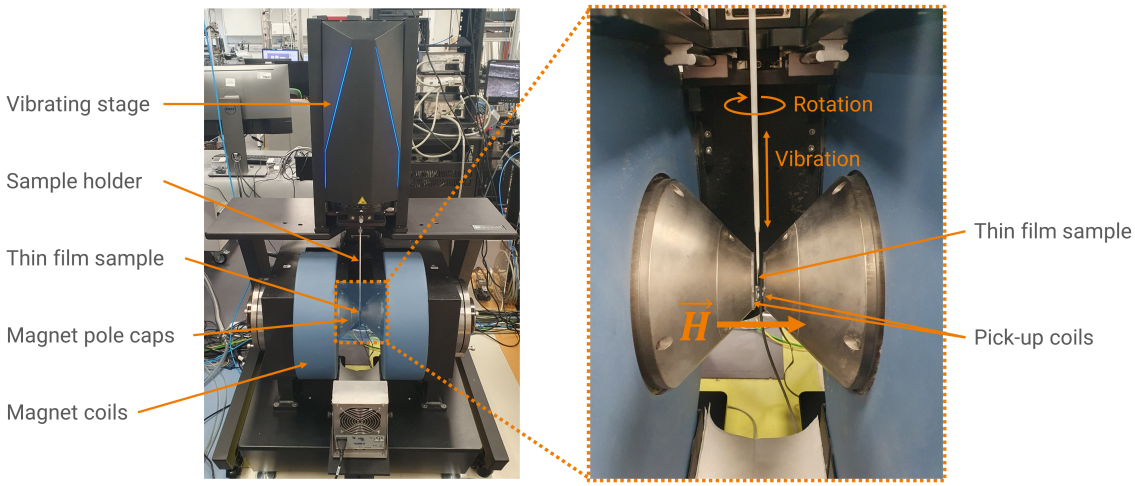

Figure 3.2: **Vibrating Sample Magnetometry.**

While the strong dependence of the observed PMA on the electronic structure at the interface has been clearly shown [27, 28, 30], it should be noted that magnetoelastic anisotropy due to mechanical strain in the thin film may also give a contribution to PMA. This can be hard to disentangle from electronic effects at the interface [31, 32].

In this work, the Pt/Co interface is precisely modified by inserting a thin Ta layer, dubbed a *dusting layer*, in between. It has been shown that such interface modifications have a pronounced impact on magnetic anisotropy, DMI and consequently impacts also the effectivity of spin torques [84]. The dusting layer of Ta considered here, typically ranges up to 1.25 Å and significantly reduces the perpendicular magnetic anisotropy and the DMI strength. The Ta thickness is thus used to tune the FMR resonance frequency that scales with the PMA strength according to eq. (2.13).

3.1.3 Vibrating sample magnetometry

The static magnetic properties of the magnetic films were measured using vibrating sample magnetometry (VSM) (Fig. 3.2). Note that these measurements were performed at room temperature with unpatterned samples with an area of $A = (5\ \text{mm})^2$. The VSM setup (Lakeshore VSM 8600) consists of a large electromagnet capable of producing a magnetic field of up to 3.5 Tesla. A magnetic sample is attached to a vibrating rod and is placed between the pole caps of the electromagnet. The magnetic field either points along the normal of the sample plane (Out-of-plane mode, OOP) or parallel to the plane (In-plane mode, IP). To detect the sample's magnetization, VSM makes use of the stray field of the magnetized sample. This stray field creates a magnetic flux in small pick-up coils that are placed close to the sample at the pole caps. The vibration of the sample periodically modulates the magnetic flux at the pick-up coils and thus creates a periodic voltage signal in the coils according to Faraday's law. This periodic voltage is then de-

tected using a lock-in amplifier and can be converted into the samples magnetization.

3.1.4 Ferromagnetic resonance

A home-built FMR setup (see Fig. 3.3) is used to measure the dynamic magnetic properties such as resonant magnetic fields and linewidths for different frequencies. This allows to determine for instance the effective magnetic anisotropy and the Gilbert damping constants of the thin film. In order to perform the measurement, the sample is placed face-down on a co-planar waveguide (CPW). Passing microwaves with gigahertz frequencies through the CPW generates a high-frequency in-plane magnetic field above the signal line of the CPW, where the magnetic thin film is placed. The CPW and the sample are positioned inside a static magnetic field that is generated by an electromagnet. The normal of the magnetic film is parallel to the static field. The high-frequency magnetic field is thus perpendicular to the static field. If the frequency of the microwaves applied to the CPW matches the FMR condition, RF power is absorbed by the magnetic sample. The magnitude of the transmitted RF power is detected using a rectifying RF-diode that translates the RF-amplitude into a DC voltage.

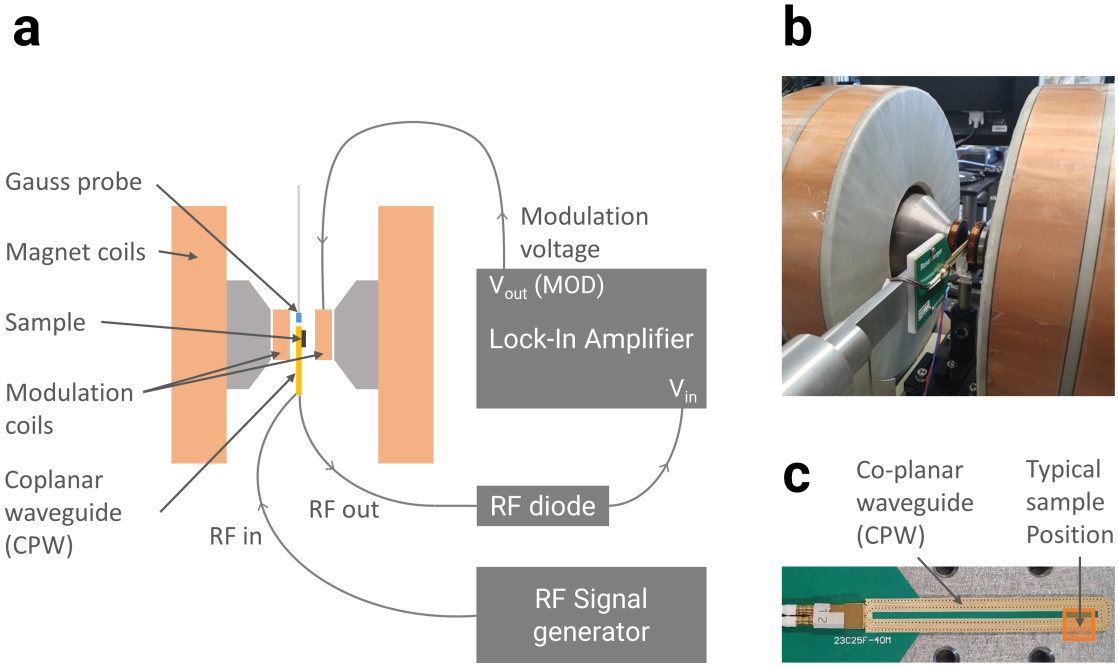

Figure 3.3: **Ferromagnetic resonance setup.** Schematic **(a)** and picture **(b)** of FMR setup. **(c)** Close-up picture of the CPW where the sample is placed.

Since the changes in the microwave absorption at the FMR are quite low, a lock-in technique is used to enhance the signal-to-noise ratio. For this purpose, the static field is weakly modulated at a frequency of a few tens of Hertz by using a set of modulation coils near the pole caps of the electromagnet. This field modulation translates into a modulation of the FMR resonance frequency and consequently modulates the absorbed RF power. To avoid perturbing the measurement, the modulation field needs to be small compared

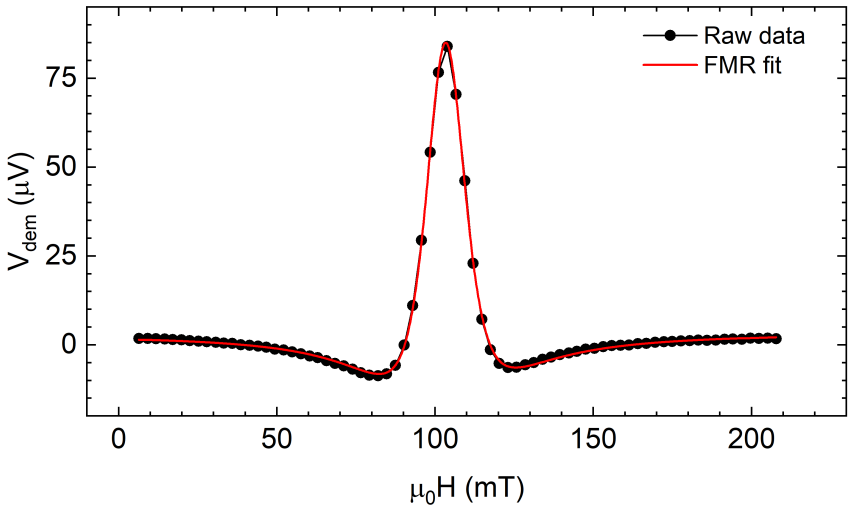

Figure 3.4: **Lineshape of FMR resonance.** This resonance is measured on a TaN(20)/Pt(50)/Ta(1)/Co(3)/[Ni(7)/Co(3)]$_3$/TaN(30) (numbers in Å) magnetic film at an RF frequency of 10 GHz with the static magnetic field pointing along the film normal. The fit corresponds to eq. (3.1).

to the FMR linewidth. After rectification of the RF signal, the modulated RF power is fed into a lock-in amplifier and is demodulated. Because of the lock-in detection, the measured signal corresponds to the field-derivative of the dynamic susceptibility χ_{xx}, as shown below. This technique significantly enhances the signal-to-noise ratio and enables the detection of FMR in ultra-thin magnetic films with thicknesses down to 1.3 nm.

During a typical measurement, a fixed RF frequency is applied and the static magnetic field is varied. The demodulated voltage signal $V_{\mathrm{dem}}(H)$ obtained at the lock-in amplifier is fitted with the following function to determine the resonance field H_{res} and the linewidth ΔH [85].

$$\begin{aligned} V_{\mathrm{dem}}(H) &\sim \frac{d}{dH_{\mathrm{a}}}\left(\cos(\varepsilon)\chi''_{xx} + \sin(\varepsilon)\chi'_{xx}\right) \\ &\sim -\frac{2\Delta H\,(H_{\mathrm{a}} - H_{\mathrm{res}})\cos(\varepsilon)}{\left[(H_{\mathrm{a}} - H_{\mathrm{res}})^2 + \Delta H^2\right]^2} + \frac{\left(\Delta H^2 - (H_{\mathrm{a}} - H_{\mathrm{res}})^2\right)\sin(\varepsilon)}{\left[(H_{\mathrm{a}} - H_{\mathrm{res}})^2 + \Delta H^2\right]^2} \end{aligned} \tag{3.1}$$

The imaginary and real parts of the dynamic susceptibility χ''_{xx}, χ'_{xx} (see eq. (2.14b)-(2.14c)) both contribute to the detected signal due to a mixing angle ε that describes the coupling between the waveguide and the magnetic sample [40, 85].

The measurement of the FMR at many different frequencies allows to determine the effective anisotropy of the film using eq. (2.13) and fitting the resonance fields accordingly. The development of the resonance linewidths with frequency allows to determine

the magnetic damping constant α using the following equation [26, 40] if no significant non-linear processes or two-magnon scattering are present [39]:

$$\mu_0 \Delta H(f) = \alpha \frac{2\pi f}{\gamma} + \mu_0 \Delta H_0 \tag{3.2}$$

The damping constant determines the linear slope of the linewidth with frequency while ΔH_0 is the inhomogeneous linewidth broadening that is independent of the frequency and arises due to inhomogeneities of the magnetic film [40].

3.2 Device fabrication

3.2.1 Devices for domain wall motion measurements

To measure the current-induced motion of DWs in the presence of microwaves, two different device designs were used:

- Design A: RF current flows through CPW → RF magnetic field acts on magnet
- Design B: RF current flows through magnet → RF SOT acts on magnet

Design A: The images of the final device and their electrical connection are shown in Fig. 3.5. The magnetic conduit is placed on top of a CPW, separated by an insulating Al_2O_3 layer. The electrical RF current is injected into the CPW and flows below the magnetic conduit. The RF current thus creates an RF magnetic field at the conduit that is perpendicular to the RF current direction.

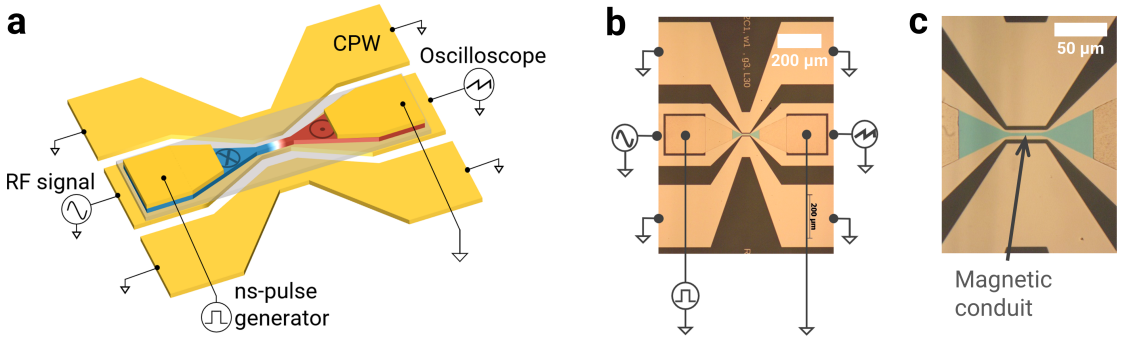

Figure 3.5: **Design A: Schematic and microscopy pictures of final device.** **(a)** Schematic of final device. **(b)** Microscopy picture showing the electrical connections during a DW motion measurement. **(c)** Close-up microscopy picture showing the magnetic conduit on top of the CPW.

The fabrication process of these devices is shown in Fig. 3.6: First, 5 nm Ti and 220 nm Au is deposited on a Sapphire substrate with 001-cut by ion beam deposition (IBD). Then, the CPW is patterned by a negative tone photoresist and etched by Argon ion milling. The gaps are subsequently filled by Al_2O_3 (in-situ IBD). For the exemplary device shown in Figs. 3.5b-c, the signal line of the CPW has a width $w_S = 10$ µm, a gap $g = 3$ µm in the center and an ohmic resistance of ~ 10 Ω. The dimensions laterally increase towards the outside region where the wirebonds are placed. These length scales vary depending on the measurment requirements. Secondly, a lift-off technique was used to deposit an 80 nm Al_2O_3 layer using IBD in order to electrically isolate the CPW from the conduit. Thirdly, using photo-lithography for a double-layer resist, a mask with undercut was formed. Then the magnetic thin films were deposited and lifted-off to form a magnetic nanowire on top of the CPW. Lastly, after the deposition of the magnetic microstructures, a lift-off technique was used to deposit electrical contact pads by IBD (5 nm Ti / 60 nm Au).

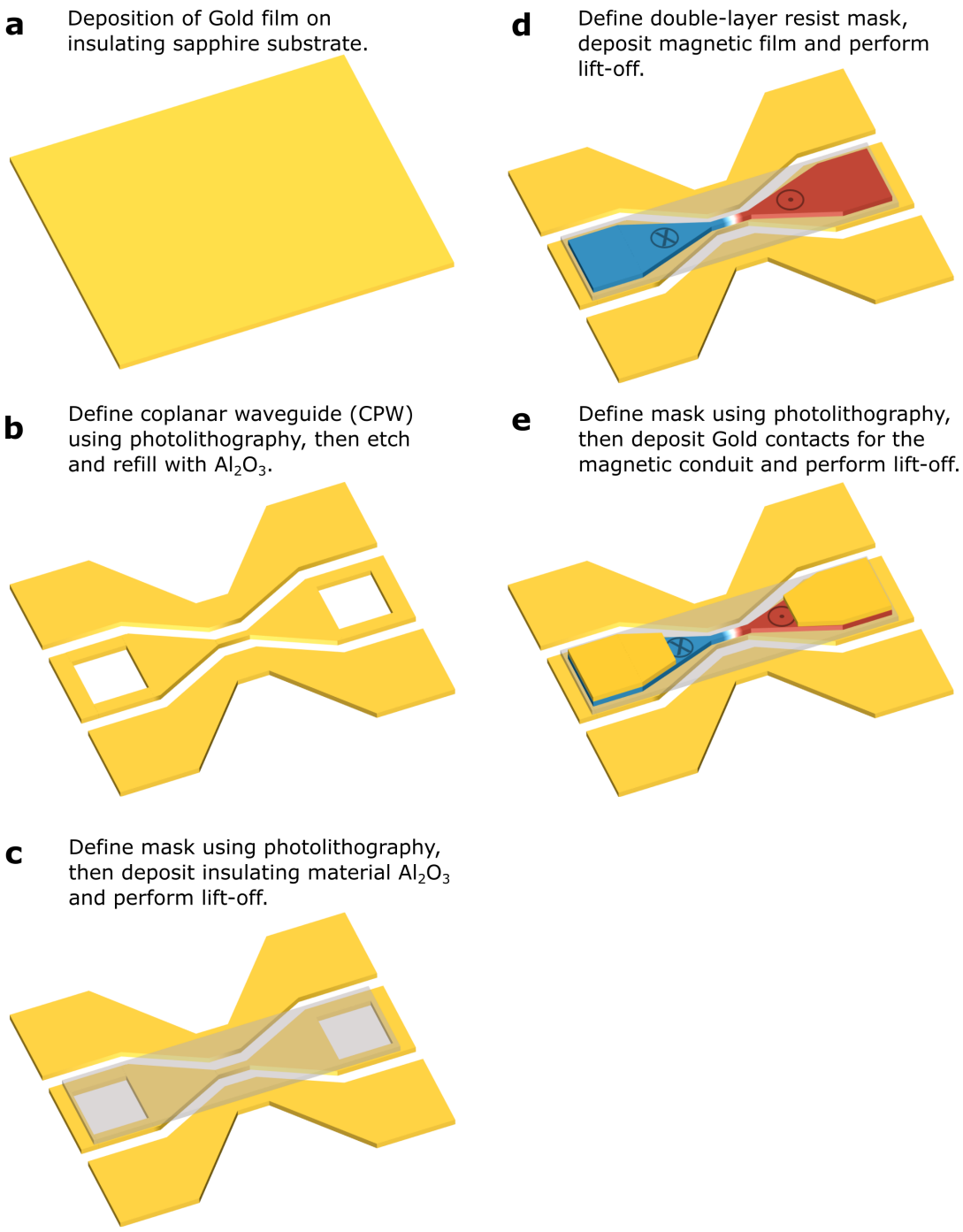

Figure 3.6: **Design A: Sample fabrication procedure.**

Design B: The images of the final device and their electrical connection are shown in Fig. 3.7. Instead of passing the microwaves through a CPW, they are directly transmitted through the magnetic conduit itself. Therefore, an electrical RF current flows through the conduit and creates an RF SOT.

The fabrication process of these devices is shown in Fig. 3.8: First, the magnetic film is deposited on a Sapphire substrate with 001-cut by IBD. Then, the magnetic conduit is patterned by a negative tone photoresist and etched by Argon ion milling. For the exemplary device shown in Figs. 3.7b-c, the central, straight part of the magnetic stripe has

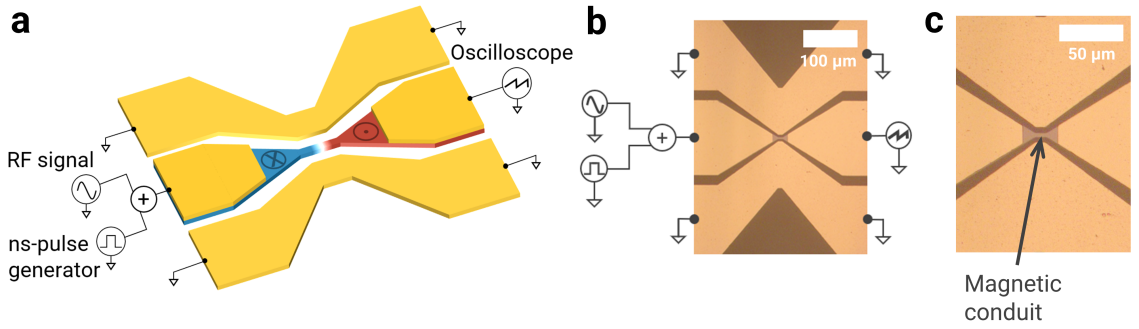

Figure 3.7: **Design B: Schematic and microscopy pictures of final device.** **(a)** Schematic of final device. **(b)** Microscopy picture showing the electrical connections during a DW motion measurement. **(c)** Close-up microscopy picture showing the magnetic conduit.

a width $w_S = 3$ µm and a length $L = 10$ µm. The ohmic resistance lies, depending on the specific device dimensions, in the range of $\sim 200 - 500\ \Omega$. The gap to the ground planes is $g = 3$ µm in the center. These length scales may vary depending on the measurment requirements. Again, the dimensions laterally increase towards the region where the wirebonds are placed. Finally, a lift-off technique is then used to deposit electrical contact pads by IBD (5 nm Ti / 60 nm Au).

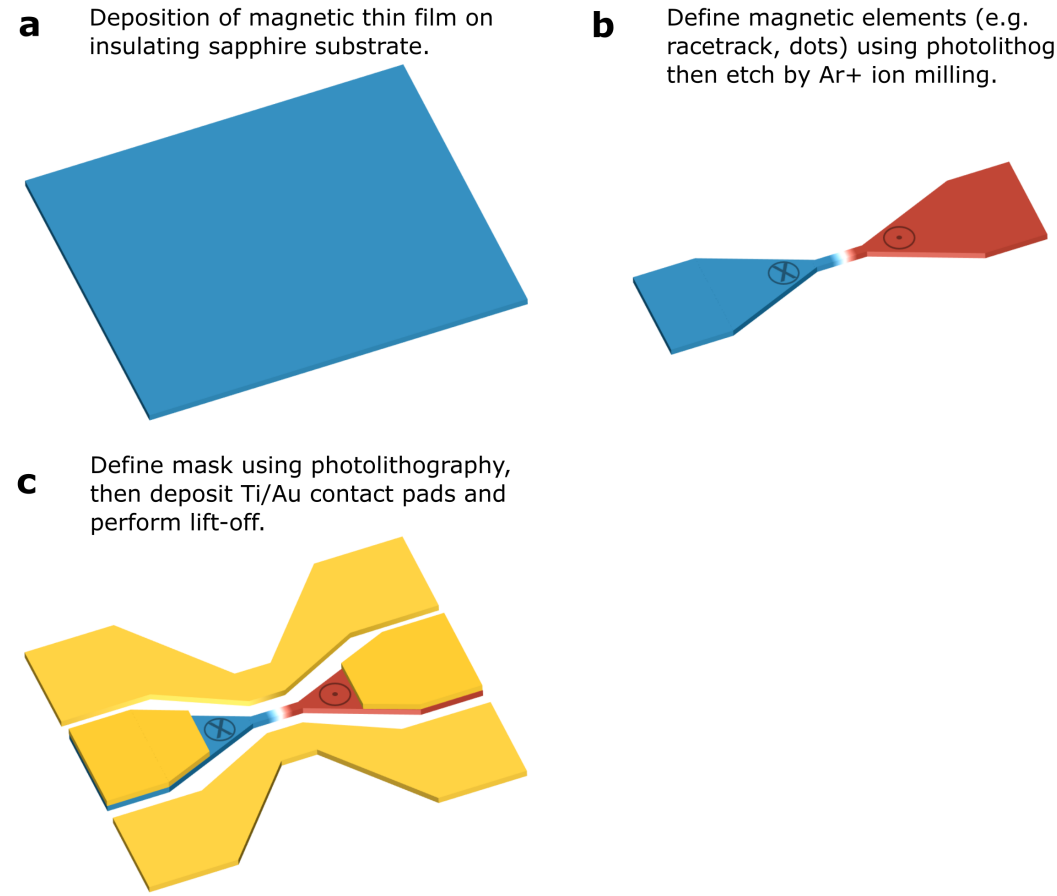

Figure 3.8: **Design B: Sample fabrication procedure.**

3.2.2 Devices for microwave-assisted switching measurements

Two different switching mechanisms are investigated in this work. Firstly, current-induced SOT switching (see chapter 2.4.3) in the presence of microwave magnetic fields is investigated and the previously shown device design A (Fig. 3.5) is used for these measurements.

Secondly, microwave-assisted field-switching is studied (see chapter 2.4.2) in the presence of either an RF SOT or an RF magnetic field. To achieve MAS using RF SOT, the device design B (as shown previously in Fig. 3.7) is used, though with different dimensions. Furthermore, the device design and fabrication for MAS measurements using an RF magnetic field is outlined in the following.

Design C: The images of the final device and their electrical connection are shown in Figs. 3.9. A magnetic dot is placed on top of a CPW, separated only by a thin Al_2O_3 layer. An RF current passing through the CPW will generate an RF magnetic field at the magnetic dot.

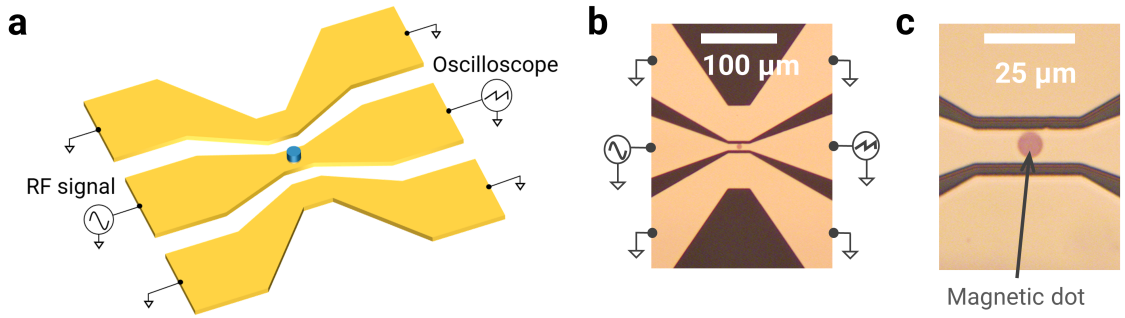

Figure 3.9: **Design C: Schematic and microscopy pictures of final device.** **(a)** Schematic of final device. **(b)** Microscopy picture showing the electrical connections during microwave-assisted field-switching measurement. **(c)** Close-up microscopy picture showing the magnetic dot on top of the CPW.

The fabrication process of these devices is seen in Fig. 3.10: First, 5 nm Ti and 220 nm Au is deposited on a Sapphire substrate with 001-cut by IBD. Then, a 5 nm thin layer of Al_2O_3 is deposited by IBD, followed by the deposition of the magnetic thin film. A magnetic dot is patterned by a negative tone photoresist and etched by Argon ion milling. The exemplary device shown in Figs. 3.9b-c has a dot radius of 4 µm. These length scales may vary depending on the measurment requirements. Lastly, the CPW is patterned by a negative tone photoresist and etched by Argon ion milling.

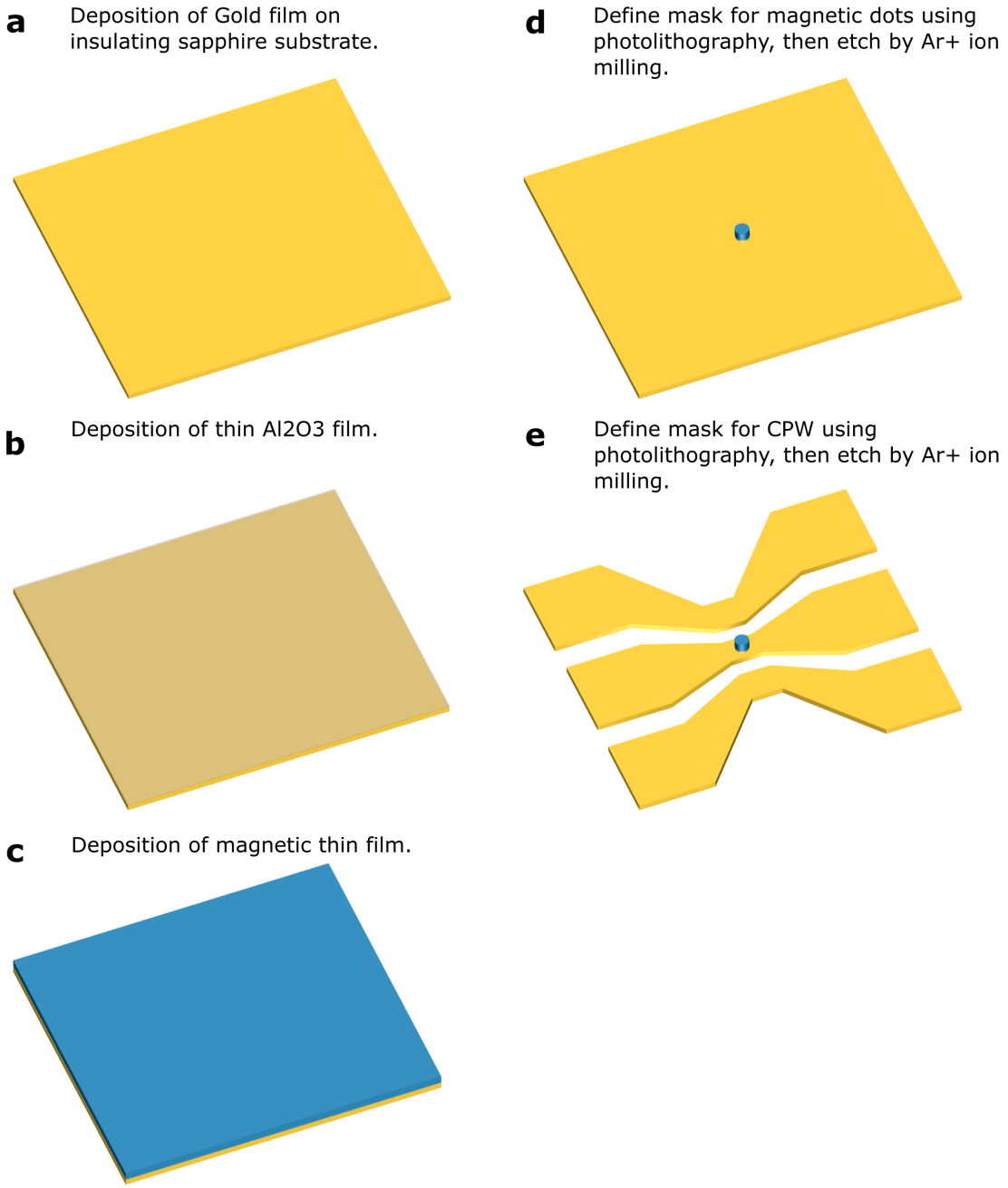

Figure 3.10: **Design C: Sample fabrication procedure.**

3.3 Magneto-optical Kerr effect (MOKE) measurements

3.3.1 Magneto-optical theory

A powerful optical technique to characterize the magnetism of magnetic thin films on a local scale is the magneto-optical Kerr effect (MOKE). Figure 3.11a shows that for linearly polarized light that reflects from a magnetic sample at an incidence angle θ_i, the Kerr effect both leads to a rotation of the main polarization axis as well as a finite ellipticity of the polarization.

Macroscopically, the MOKE can be described by a non-symmetric dielectric tensor $\hat{\varepsilon}$ that modifies the refractive index of right and left circularly polarized (RCP/LCP) light $n_{\mathrm{R,L}}$ [86].

$$\hat{\varepsilon} = \varepsilon \begin{pmatrix} 1 & iQ_{\mathrm{z}} & -iQ_{\mathrm{y}} \\ -iQ_{\mathrm{z}} & 1 & iQ_{\mathrm{x}} \\ iQ_{\mathrm{y}} & -iQ_{\mathrm{x}} & 1 \end{pmatrix} \tag{3.3}$$

$$n_{\mathrm{R,L}} = n(1 \pm \frac{1}{2}\mathbf{Q} \cdot \mathbf{e}_{\mathrm{k}}) \tag{3.4}$$

$$\mathbf{Q} = (Q_{\mathrm{x}} \;\; Q_{\mathrm{y}} \;\; Q_{\mathrm{z}})^{\mathrm{T}} \tag{3.5}$$

Here, $n = \sqrt{\varepsilon}$ is the average refraction index and $\mathbf{e}_{\mathrm{k}}$ is the unit vector along the propagation of the light. The Voigt vector $\mathbf{Q}$ is approximately proportional to the sample magnetization [87] and is usually a complex value. Since linearly polarized light is a superposition of RCP and LCP light, the different refraction index $n_{\mathrm{R,L}}$, which is in general a complex value, will lead to different phase shifts and attenuations of the circularly-polarized components of the refected beam. This translates into a slight rotation ϕ_{K} and a finite ellipticity η_{K} of the reflected beam (see Fig. 3.11a) [88].

$$\phi_{\mathrm{K}} + i\eta_{\mathrm{K}} = \frac{inQ_{\mathrm{z}}}{n^2 - 1} \tag{3.6}$$

There exist different geometries to measure the magnetization using MOKE as seen in Fig. 3.11b-c. First, the perpendicular/polar MOKE (P-MOKE) is strongest for light at normal incidence (i.e. at $\theta_{\mathrm{i}} = 0$) and probes the magnetization component along the film normal. Second, the longitudinal MOKE (L-MOKE) requires a finite incidence angle θ_{i} and probes the planar magnetization component that is parallel to the plane of incidence.

Since the previous description of the Kerr effect is solely macroscopic, the microscopic origin of the effect will be outlined in the following. To explain the gyrotropy of $\hat{\varepsilon}$, i.e. the presence of its non-diagonal components, one may use the Lorentz-force that is induced by an effective magnetic field acting on the electrons in the magnetic material [87]. The electric field of the linearly polarized incoming light $\mathbf{E}_{\mathrm{i}}$ induces a vibrational motion of the electrons, i.e. an oscillating electron dipole moment or polarization $\mathbf{P}_{\mathrm{f}}$. The local magnetic field due to the magnetization of the film leads to a Lorentz

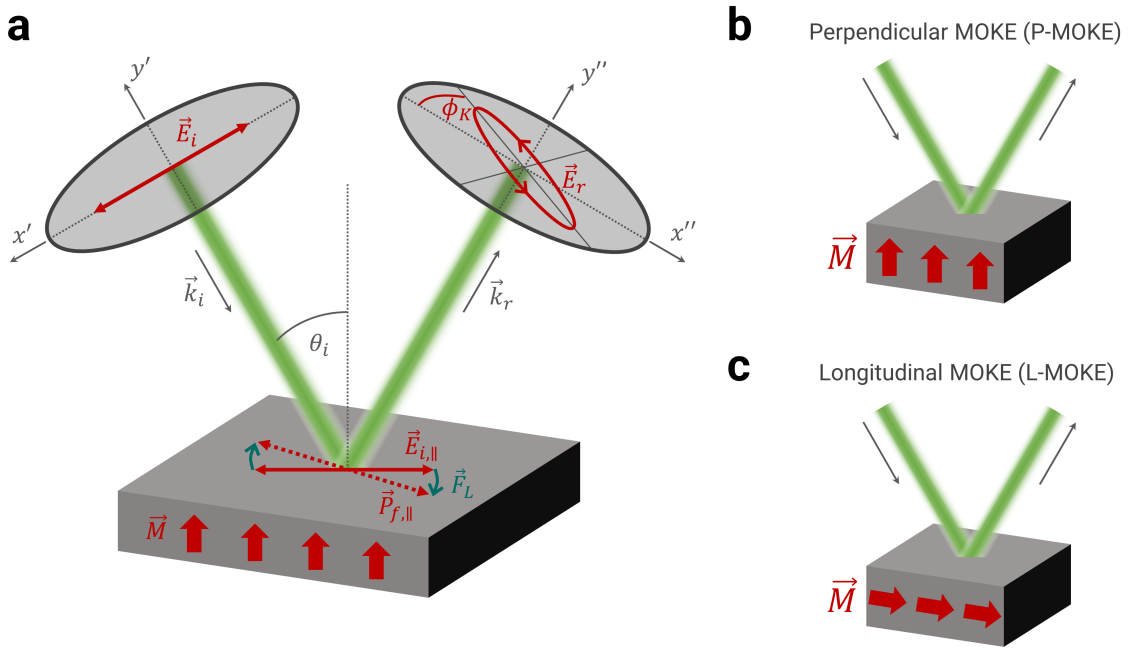

Figure 3.11: **Magneto-optical Kerr effect. (a)** Linearly polarized light that reflects from an perpendicularly magnetized sample exhibits a rotation ϕ_K of the polarization and a finite ellipticity. The shown rotation originates from the Lorentz force F_L acting on the oscillating electron polarization P_f. **(b-c)** The P-MOKE occurs for sample magnetization perpendicular to the plane whereas the magnetization for the L-MOKE lies in-plane and parallel to the plane of incidence.

force $\mathbf{F}_L \sim \mathbf{E}_i \times \mathbf{M}$ that rotates the path of $\mathbf{P}_f$ slightly. The secondary radiation emerging from this vibrational motion (both transmitted and reflected light) thus exhibits a slightly rotated polarization axis (see Fig. 3.11a). The experimentally observed Kerr effect in ferromagnets is very large and can be explained by the strong Heisenberg exchange field but only when spin-orbit coupling is taken into account. By coupling the magnetic moment with the electron motion, the SOC connects the magnetic and optical properties of a FM [86, 89]. To predict the magneto-optical properties of a itinerant FM such as Nickel or Cobalt, the dielectric tensor can be calculated from the band structure of the magnet by taking spin-orbit interaction and exchange-split bands into account [88–90]. In this framework, intra-band electric dipole transitions significantly contribute to the Kerr effect at low photon energies (< 2 eV) while inter-band transitions dominate at larger photon energies [88]. Note that heavy metals such as Pt in proximity to the FM may contribute to the Kerr effect by hybridizing with the band structure of the FM and modulating the effective SOC of the HM/FM bilayer.

3.3.2 Wide-field P-MOKE microscopy setup

The P-MOKE can be exploited to visualize oppositely magnetized domains in a FM with PMA and thus enables to track the position of a DW over time. A wide-field microscopy setup is used for this purpose (see Fig. 3.12). White LED light is first linearly polarized at

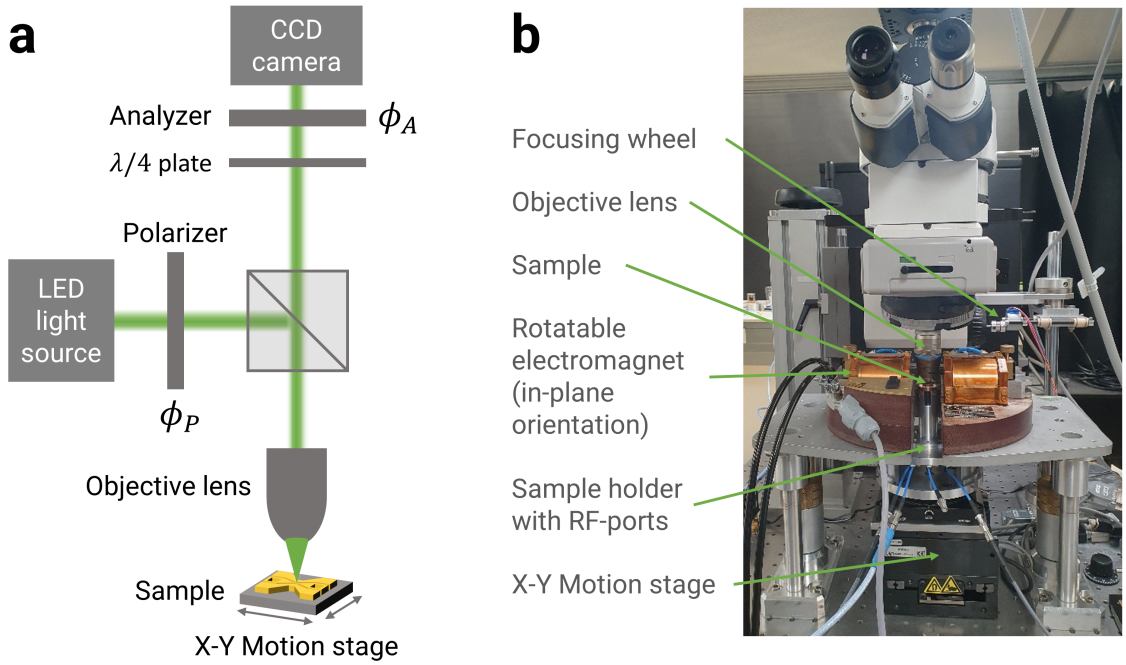

Figure 3.12: **Kerr microscopy setup. (a)** Schematic of setup. **(b)** Picture of the microscopy setup used throughout this work.

an angle ϕ_P and reaches the sample at normal incidence. The reflected beam first passes through a $\lambda/4$ compensator and secondly through an analyzer. The compensator changes the phase difference between the p (parallel) and s (perpendicular) components of light and allows to adjust the ellipticity of light [90]. Here, it is used to minimize the ellipticity of the reflected light. The analyzer subsequently allows to detect small rotations of the light polarization due to the Kerr effect. Usually, the analyzer angle ϕ_A is slightly detuned from the extinction point (where polarizer and analyzer are perpendicular to each other and no light passes through). In that case, a positive (negative) Kerr rotation will for instance result in a signal increase (decrease) at the detector behind the analyzer. Up (down) domains will thus appear with dark (bright) contrast. To enhance the domain contrast, differential mode imaging is used. Herein, by taking a background image and digitally subtract it from the live image, any change to the previous magnetization state is highlighted (Fig. 3.14).

This optical setup allows for the measurement of DW motion and magnetization switching in micro-structured magnetic devices. For this purpose, external magnetic fields are often required and are generated by electromagnets (see Fig. 3.12b as an example). In addition to the application of magnetic fields, the measured samples are electrically connected by wirebonding. An RF signal generator and subsequent RF amplifier allows to inject a high-frequency electrical signal into the sample. This RF-signal may either be injected into the CPW below the magnetic element to generate a high-frequency magnetic field at the conduit (Fig. 3.13a). Alternatively, the RF signal may directly be injected into the magnetic conduit (Fig. 3.13b) to generate radiofrequency spin-torques. The transmitted RF signal is monitored at a digital oscilloscope. In order to precisely tune the effect

of the RF signal on the spintronic device, bursts of RF-power may be applied instead of continuous-wave RF. For this, an RF mixer and a burst pulse generator are used to chop the RF signal into RF bursts. An additional, nanosecond-long SOT current pulse can be sent through the magnetic conduit to induce DW motion or switching. The timing between this pulse and RF burst is adjustable. In most cases, the SOT pulse was sent through the magnetic conduit a few nanoseconds after the beginning of the RF burst. Note that due to the timing uncertainty of a few nanoseconds between SOT pulse and RF burst, the timing of the SOT pulse with respect to the phase of the RF-signal was not investigated. A schematic of the electrical setup is shown in Fig. 3.13.

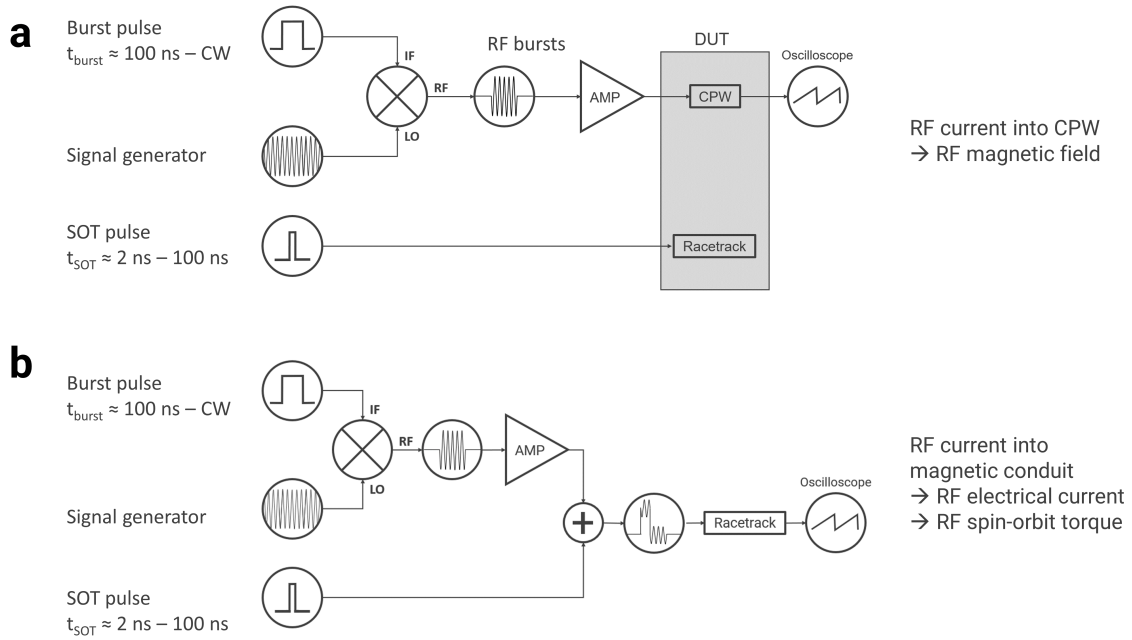

Figure 3.13: **Schematic of electronic circuitry. (a)** The injection of an RF current into CPW generates a transverse, high-frequency magnetic fields at the magnetic conduit. The ns-long current pulse is injected directly into the magnetic conduit which is isolated from the CPW. **(b)** Direct injection of RF electrical current into the magnetic conduit to induce a high-frequency SOT. A power combiner is used to add the RF-signal with a ns-long current pulse.

3.3.3 Domain wall motion measurement

For the measurements of DW motion, the previously mentioned wide-field Kerr microsopy is used. A single DW is first isolated in the magnetic conduit. Current-induced DW motion is obtained by applying a series of current pulses with current density j and widths t_{pulse} of typically 5 ns or 10 ns through the magnetic conduit. Note that the SOT is the major source for current-induced DW motion in the thin films under consideration here and induces a DW motion opposite to the electron flow (Fig. 3.14). The effective DW velocity $v_{\mathrm{eff}} = d_{\mathrm{p}}/t_{\mathrm{pulse}}$ is then determined from the wall displacement per pulse d_{p} and the pulse time t_{pulse}. This procedure to measure the DW velocity is repeated several times to obtain a statistical measurement error.

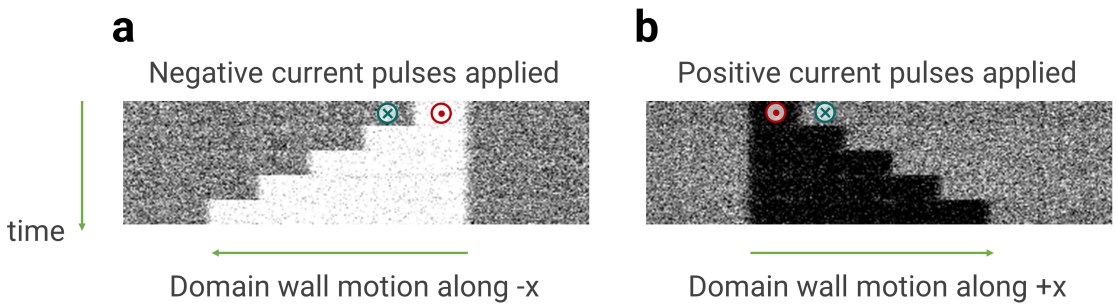

Figure 3.14: **Current-induced motion of an ↑↓ DW.** White contrast corresponds to the change in the local magnetization from an ↑ to a ↓ state and vice versa for black contrast as indicated in the image. The DW is moved by an SOT and thus propagates along the electrical current density. After taking a background image, a train of electrical current pulses is applied to the conduit and snapshots of the conduit are taken. The image shows the DW motion by five pulse trains (from top to bottom).

When current-induced DW motion is measured in the additional presence of RF magnetic fields, the DW can move after the end of the current pulse, as will be shown later in this thesis. This complicates the determination of a unique DW velocity since the DW velocities generally differ when motion is induced by a current pulse or an RF field. Therefore, the DW displacement per current pulse d_p will be shown as the more suitable variable.

3.3.4 Magnetization switching experiments

In addition to DW motion, the wide-field Kerr microscope is used to measure the magnetization switching under assistance of RF fields or RF currents. As outlined already in chapter 3.2.2, both the microwave-assisted SOT-switching and the microwave-assisted field-switching are investigated in this work. The typical procedures of both experiments are outlined below:

SOT switching:

1. Remove any domain walls e.g. by DW annihilation or saturating the FM in a magnetic field.
2. Apply a static longitudinal magnetic field H_x.
3. Apply both an electrical current pulse through the magnetic conduit and an RF burst that are synchronized to each other.
4. If the magnet switched, a contrast change is visible in the Kerr image.

Microwave-assisted field-switching: The microwave-assisted field-switching investigates switching by a magnetic field H_z in the additional presence of RF fields or currents. The measurements were performed on devices with design B (Fig. 3.7) or design C (Fig. 3.9). The typical measurement procedure is as follows:

1. Saturate the FM in a large H_z field.
2. Apply a weak magnetic field in the reverse direction (opposite to the initial magnetization) and apply an RF burst to the device.
3. Record the Kerr contrast I_K of the FM.
4. Repeat the previous two steps for increasing field magnitude until the magnetic element switches.
5. Measure such a resulting contrast curve $I_K(H_z)$ several times for statistics.

3.3.5 Super-Nyquist sampling magneto-optical Kerr microscopy (SNS-MOKE)

To investigate the magnetic response at the DWs and adjacent uniform domains, a variant of time-resolved magneto-optical Kerr (TR-MOKE) microscopy is used, commonly referred to as *Super-Nyquist sampling magneto-optical Kerr microscopy* [91] (see Fig. 3.15). In this approach, an RF-current at GHz frequencies passing through a CPW generates an RF magnetic field which excites magnetization dynamics within the microstructured magnetic sample (cf. device design A in chapter 3.2.1). As a probe, a short-pulsed laser system is employed that operates at 515 nm with a repetition frequency of $f_{rep} = 80$ MHz. By means of a high-numerical aperture microscope objective, the laser beam is focused to a diffraction limited spot size of approximately 300 nm. A balanced photo-detector converts the optical signal into an electrical one which is first amplified and then detected at a lock-in amplifier. The obtained signal corresponds to a change of the light's polarization state under reflection via MOKE within the diffraction limited area of the laser spot. In contrast to conventional TR-MOKE experiments, this approach does not require additional external modulation techniques. To achieve this, an external master clock (i.e. a synchronizer) stabilizes the laser's repetition rate, the frequency generator as well as the lock-in amplifier. Herein, a phase-locked loop detects variations of the laser's repetition rate and adjusts the latter by varying its resonator length. The synchronization allows the lock-in to directly demodulate at alias frequency components $|n \cdot f_{rep} - f_{RF}|$, where n is an integer number representing the comb lines of the frequency comb of the ultra-short laser pulses. These alias frequencies originate from an under-sampling of GHz magnetization dynamics with the 80 MHz sampling frequency of the laser pulses. However, since all frequency components are stabilized to the external clock, the exact position of the alias frequency is predetermined and can be used for demodulation, without the need of any additional modulation. This case of under-sampling allows to reconstruct the amplitude and phase information at arbitrary frequencies.

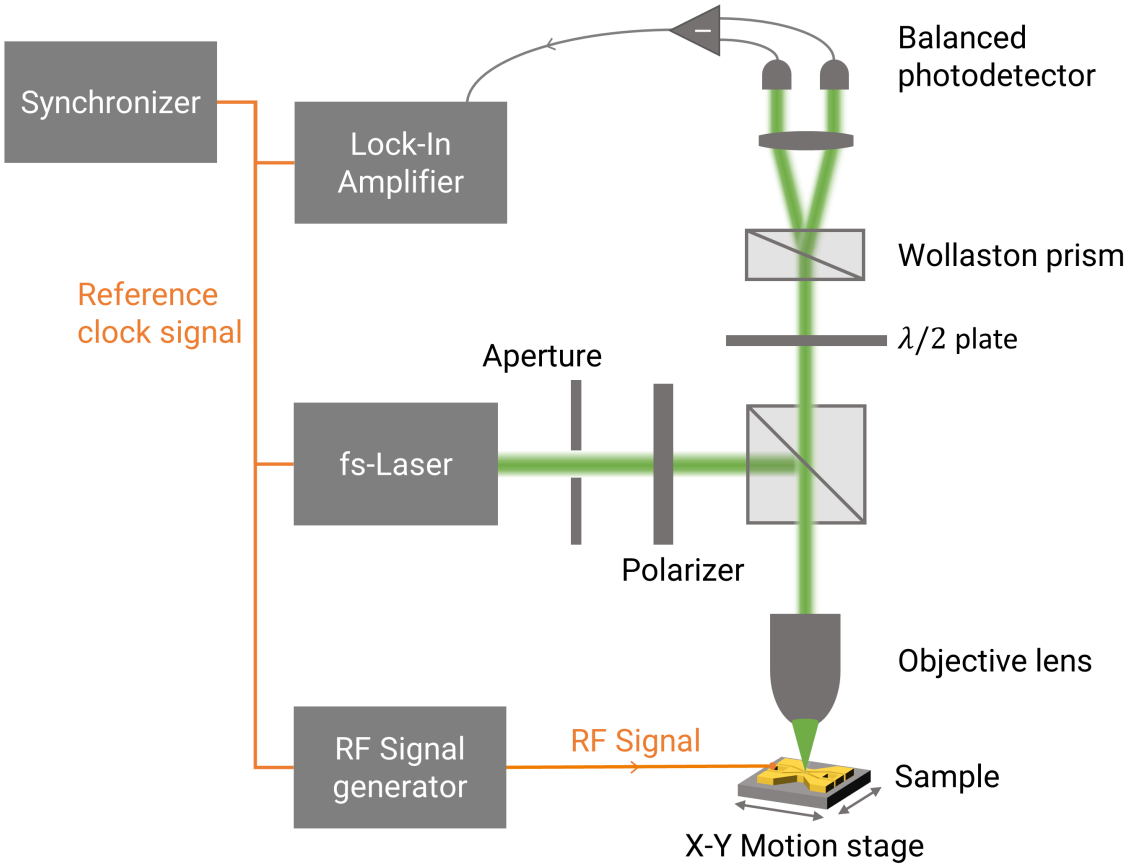

Figure 3.15: **Super-Nyquist samping MOKE.**

Two different MOKE geometries are used for the SNS-MOKE measurements in this work: First, P-MOKE measurements probe magnetization precessions having a z-component. It should be pointed out that the SNS-MOKE technique does not probe the static but only the dynamic magnetization components. Because of this, the uniform magnetic domains of OOP magnetized samples, i.e. the $\uparrow$ and $\downarrow$ domains, are invisible to the P-MOKE in the SNS-measurement since the magnetization along the z-axis is static and insensitive to the measurement. Spin precessions in the domains have only components in the xy plane and are thus also insensitive to this dynamic P-MOKE (Fig. 3.16b). This situation changes for the region of the domain wall. Here, the static magnetization at the DW is rotated towards the IP direction (e.g. parallel to the x-axis for a Néel wall). Hence, a spin precession of a Néel DW will mostly occur in the yz plane. The finite z-component of the precession is thus accessible with P-MOKE in SNS configuration.

Second, the SNS-setup becomes sensitive to the L-MOKE by blocking half of the incoming laser beam and cutting half of the wave-vector spectrum provided by the microscope objective. However, this also halves the detected light intensity and deteriorates the spatial resolution in one direction. Nevertheless, by this procedure, the longitudinal components of the Kerr rotation will not average to zero anymore and can be obtained by means of lock-in detection. The L-MOKE probes the dynamic longitudinal component of the magnetization along x-direction (i.e. along the magnetic wire). It allows to image

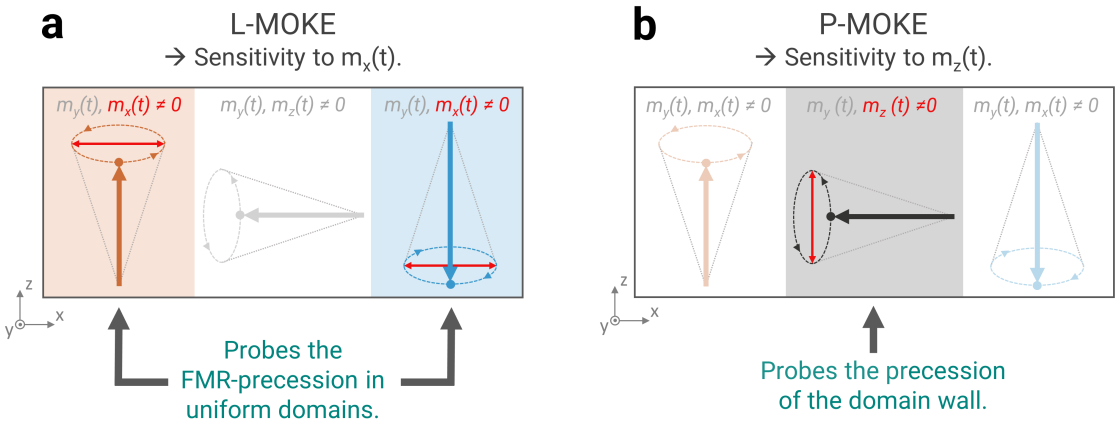

Figure 3.16: **Sensitivity of SNS-MOKE to uniform domains and domain walls.**

the spin precession in the uniform domains where precession occurs in the *xy*-plane (Fig. 3.16a). In contrast to the L-MOKE sensistivity to the uniform domains it yields zero signal at the DW position. At the DW, the magnetization statically points along *x*-direction, while its precession will only provide a dynamic *y*- and *z*-component.

Part II

Resonant excitation of domain wall precession

The following part of this thesis focuses on the dynamics of magnetic DWs in the presence of RF fields or RF electrical currents. Firstly, in chapter 4, it is shown that a DW exhibits a resonant response to external RF fields at significantly lower frequencies than the FMR. Secondly, the DW's motion is investigated in the combined presence of RF fields (or RF currents) and pulsed electrical currents. In chapter 5, it is shown that an RF magnetic field induces self-propulsion of a DW, i.e. the DW propagates over long distances in the absence of any pulsed driving currents. Herein, the direction of the DW's self-propulsion is determined by a weak transverse magnetic field. The experimental results also show the different actions of both RF magnetic fields and RF electrical currents during self-propulsion. Lastly, as shown in chapter 6, a nanosecond-long electrical current pulse can be used to trigger DW motion that is subsequently sustained by the resonant RF field. The directional of this sustained DW motion follows the motion that is induced by the initial current pulse.

Chapter 4

SNS-MOKE measurements of a domain wall resonance

Super-Nyquist sampling MOKE is a powerful technique to optically detect phase-resolved magnetization dynamics. The spatial resolution of approximately 300 nm allows to spatially differentiate between the dynamic magnetization response of a uniform magnetic domain and a DW. Additionally, the choice of the MOKE operation, i.e. L-MOKE or P-MOKE, determines if the technique is either sensitive to the domains or the DWs. Altogether, this allows not only to localize the DWs but also to probe the distinct resonances of uniform domains and DWs and to identify their precession modes.

4.1 Thin film characterization

Magnetic thin films with the following structure were used throughout this chapter: 20 TaN / 50 Pt / 1 Ta / 3 Co / [7 Ni / 3 Co]$_{N=1}$ / 30 TaN (the numbers indicate the thickness in Å). Following the notation from chapter 3.1.1, this corresponds to thin films with $d_{Ta} = 1.0$ Å and $N = 1$ multilayer repetitions. The magnetic characteristics of the films were measured using VSM. Note that all measurements in this thesis were performed at room temperature. Fig. 4.1a shows the OOP field scan with a coercive field of $\mu_0 H_c = 2.5$ mT and a rectangular shaped hysteresis loop. This confirms the PMA of the film. The IP measurement, shown in Fig. 4.1b, reveals the non-hysteretic magnetization tilting towards the sample plane until saturation is reached. This saturation field corresponds to the effective anisotropy field $\mu_0 H_{ani,eff}^{VSM} = \frac{2K_u}{M_S} - \mu_0 M_S$ and equals 325 ± 10 mT.

The dynamic magnetic properties of the film were measured with the FMR setup. Fig. 4.2a displays the linear increase of f_{FMR} with the OOP magnetic field as expected according to eq. (2.13). The linear fit yields an extrapolated zero-field FMR frequency of $f_0 = f_{FMR}(H = 0) = 9.9 \pm 0.1$ GHz. The latter corresponds to an effective anisotropy field $\mu_0 H_{ani,eff}^{FMR} = \frac{2\pi}{\gamma} f_0 = 294 \pm 4$ mT and matches well to the effective anisotropy field obtained from VSM. The linewidth dependence with frequency is displayed in Fig. 4.2b. Using eq. (3.2), a linear fit returns the damping constant $\alpha = 0.0455 \pm 0.0002$.

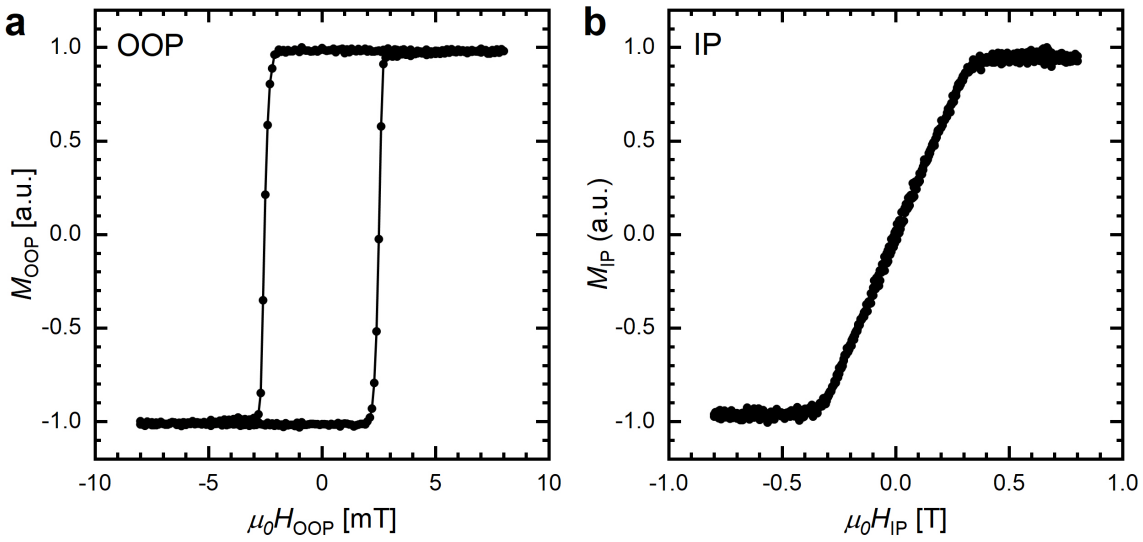

Figure 4.1: **Vibrating sample magnetometry.** **(a)** Out-of-plane and **(b)** in-plane magnetization of the magnetic film. The OOP-scan shows the square like hysteretic switching and the IP-scan shows the effective anisotropy field. The data is normalized to the saturation value.

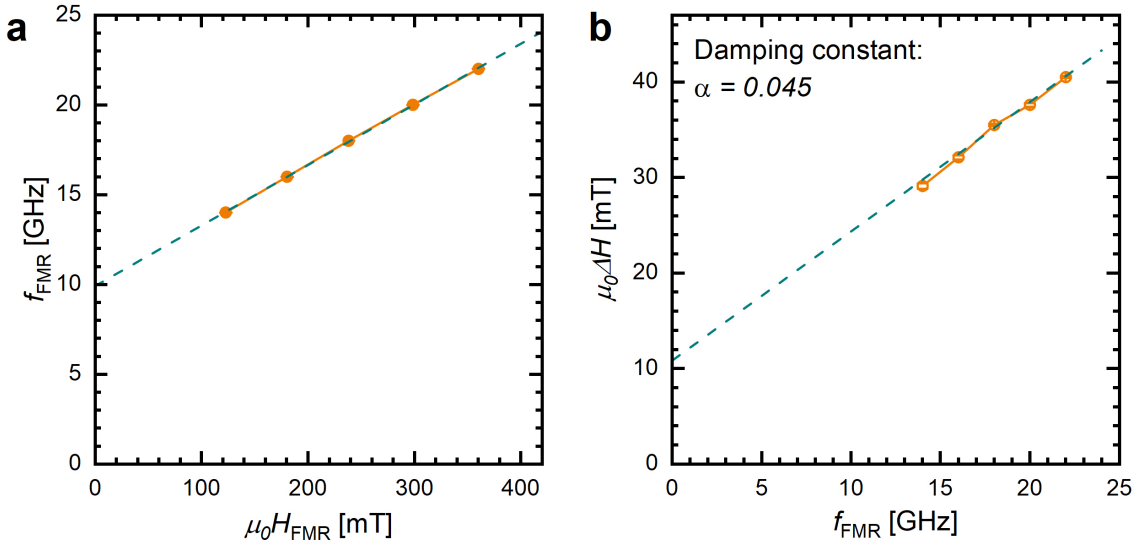

Figure 4.2: **Ferromagnetic resonance.** **(a)** The linear dependence of the FMR frequency with an OOP-field is shown. **(b)** The resonance linewidth as a function of f_{FMR} allows to determine the damping constant α.

4.2 Measurement setup

In order to perform an SNS-MOKE measurement, devices with the design A (chapter 3.2.1) were fabricated and electrically connected by wirebonding (Fig. 4.3a). An RF signal generator is connected to the device and injects an RF current to the CPW. The transmitted RF power is detected at a vector network analyzer (VNA) or an RF power meter. The RF current in the CPW generates a high-frequency magnetic field at the position of the magnetic conduit with transverse orientation relative to the CPW (see Fig. 4.3b). The narrow, straight part of the conduit has has the dimensions 3×30 µm^2.

The frequency-dependent transmission of RF power through the CPW is measured with a VNA and shown in Fig. 4.4. The figure displays the S-parameter S_{21}, that indicates the RF power transmission (see appendix chapter B.1 for details on S-parameters), and the corresponding RF field amplitude $h_{\mathrm{RF,y}}$. The calculation of $h_{\mathrm{RF,y}}$ is based on the analytical solution of the Biot-Savart law based on an input power of $P_{\mathrm{in}} = 0$ dBm.

While the transmission is relatively high in the frequency range below 5 GHz, a pronounced absorption dip appears between 5 GHz and 6.5 GHz. This dip is probably caused by RF losses due to the CPW design or the RF circuitry of the sample holder. Beyond the dip, the transmission then slowly decreases from -7 dB at 6.5 GHz to -24 dB at 10 GHz.

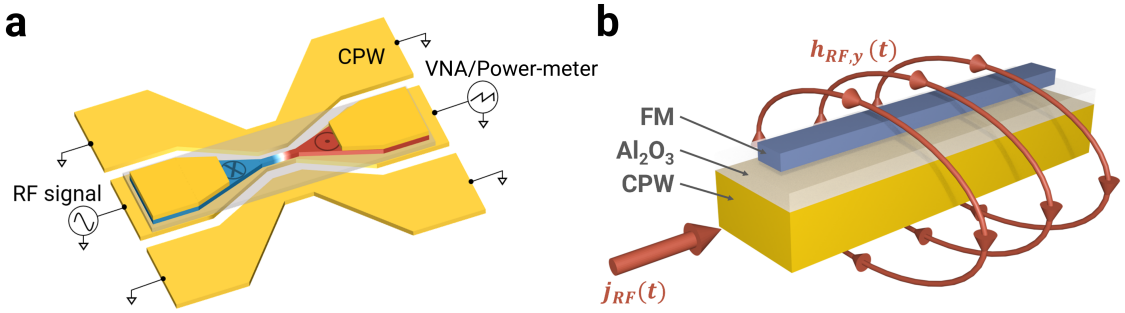

Figure 4.3: **Schematic of device geometry and RF field generation. (a)** Schematic of the device geometry and electrical connections used in the SNS-MOKE measurements. Note that the magnetic conduit sitting on top of the CPW is not wirebonded and hence not in any direct electrical contact. **(b)** Schematic of RF field generation at the conduit position. An RF current density $j_{\mathrm{RF}}(t)$ flowing through the CPW generated a high-frequency Oersted-field $h_{\mathrm{RF}}(t)$ at the conduit position. This RF-field is transverse to the current flow in the CPW.

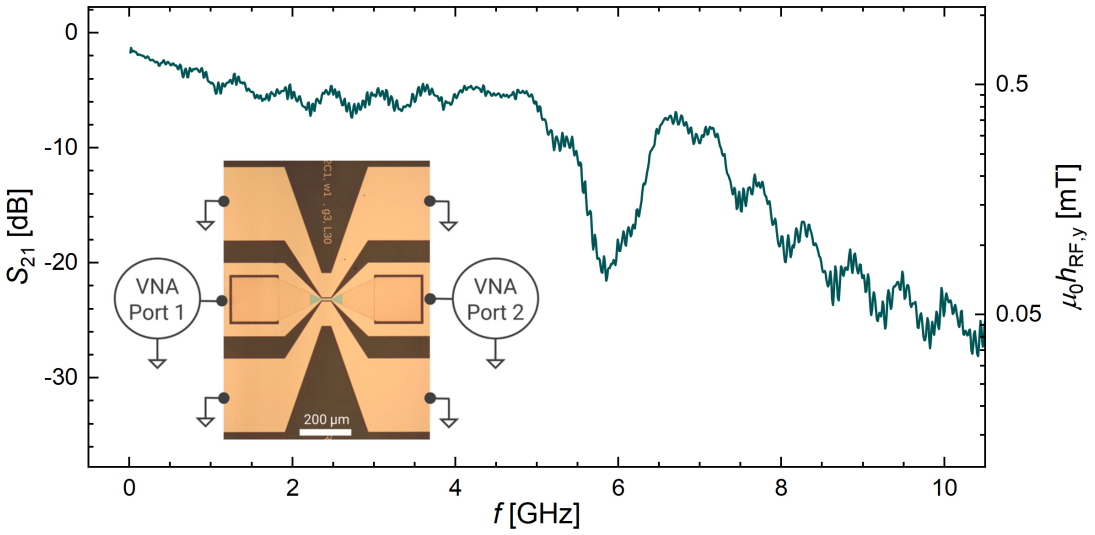

Figure 4.4: **RF transmission through the CPW.** The frequency-dependent CPW transmission S_{21} (left axis) is measured using a VNA and converted into the RF-field amplitude at the conduit position $h_{\mathrm{RF,y}}$ (right axis). The conversion uses the analytical solution of the Biot-Savart equations to calculate $h_{\mathrm{RF,y}}$ and uses an input power $P_{\mathrm{in}} = 0$ dBm. The inset shows the microscope picture of the measured device with schematically shown electrical connections.

4.3 L-MOKE measurements

In order to investigate the difference in the magnetization dynamics between uniform domains and DWs, two DWs were initially placed in the magnetic conduit. This results in a ↑↓↑ domain configuration (going from left to right). Consequently, the DW on the left (right) side of the conduit has an ↑↓ (↓↑) configuration. Since the material exhibits DMI, the DWs are chiral Néel walls, i.e. their static magnetic moments rotate perpendicular to the DW plane with a fixed rotational sense (cf. Fig. 2.2).

Next, an RF signal at a power of $P_{\mathrm{in}} = 0$ dBm is applied to the CPW and creates an RF magnetic field at the conduit. The RF frequency is varied from from 160 MHz to 10 GHz in steps of 80 MHz. The magnetization dynamics at these frequencies are now optically measured using the SNS-MOKE microscopy. Starting with L-MOKE, the setup probes the dynamic x-component, $m_{\mathrm{x}}(t)$, of the magnetization precession in the magnetic conduit (cf. methods chapter 3.3.5). The magnetization precessions are illustrated in Fig. 4.5a: The three sections of this illustration correspond to the precession at the uniform domains around $\pm z$ (left and right) and the precession of the DW around $-x$ (center). When exciting the FMR mode in the domains, the magnetization precesses around the z-axis with a significant x-component $m_{\mathrm{x}}(t)$ (red arrow). This allows to detect the FMR in the domains using L-MOKE. In contrast, the magnetization of a Néel DW precesses around the $-x$-axis and only its y- and z-components are oscillating at the excitation frequency. Since the x-component $m_{\mathrm{x}}(t)$ at the DW remains static, the L-MOKE measurement gives zero signal there.

The L-MOKE map in Fig. 4.5b, experimentally confirms the precession around $\pm z$ happening in the uniform domains. Herein, the Kerr intensity and phase are visualized

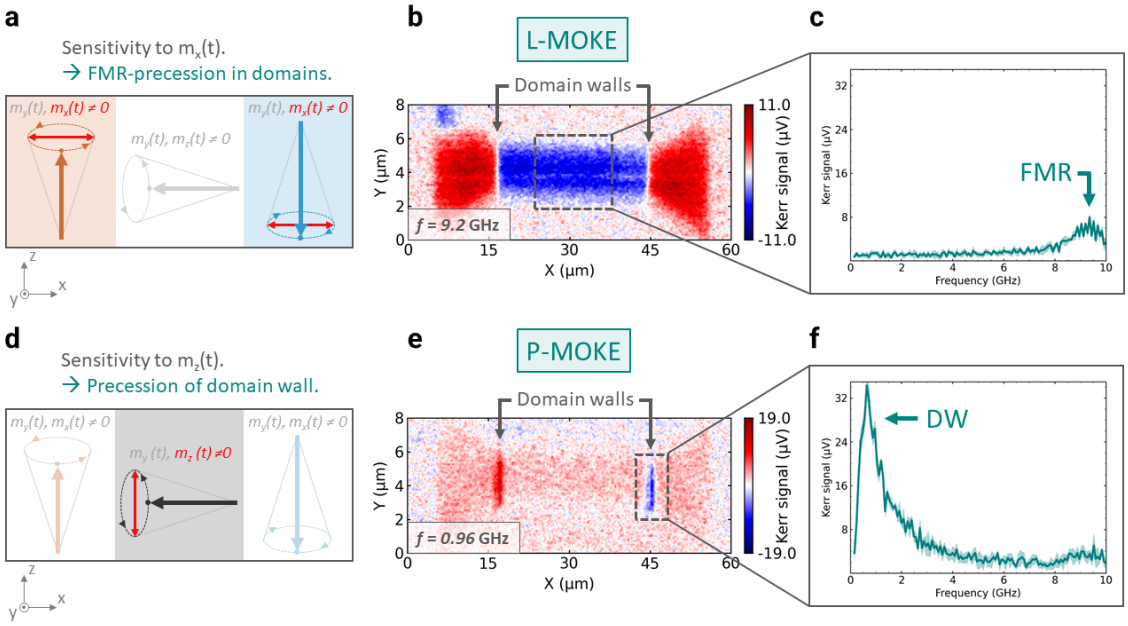

Figure 4.5: **Magneto-optic microscopy of domain and DW dynamics.** SNS-MOKE data of a magnetic conduit hosting two chiral Néel DWs. Top row: L-MOKE (**a**) In this configuration, the setup is sensitive to the x-component of the magnetization precession and probes the FMR mode in the uniform, OOP-magnetized domains. (**b**) The L-MOKE map shows a strong signal in the domains but yields zero signal at the DW itself. The signal exhibits a sign change (phase shift of 180°) when crossing a DW. The DW is visible as a narrow white line with zero signal. (**c**) The frequency scan has been measured in the domain at the center. The shaded area in (**c**) and (**f**) indicates the standard deviation determined from multiple measurements at each frequency. Bottom row: P-MOKE. (**d**) This configuration probes the z-component of the magnetization precession and is insensitive to the FMR mode in the uniform domains and only detects a precession or oscillation of the DW. (**e**) Hence, the P-MOKE data only returns a signal at the DW position. (**f**) Frequency scan of the P-MOKE response at the DW position.

by the image intensity and color, respectively. The clear presence of the uniform FMR mode at $f = 9.20$ GHz is seen in the $\uparrow$ and $\downarrow$ domains while the DW gives zero signal. As expected, the FMR precession exhibits a 180° phase shift (visualized by the color change from red to blue) on either side of any DW due to the opposite static magnetization in the up- and down-domains, respectively.

The L-MOKE frequency scan in Fig. 4.5c clearly shows that the FMR response is centered at approximately 9.5 GHz. As shown in the previous section, the extrapolated zero-field FMR frequency of the magnetic films measured with a conventional FMR set-up lies at $f_0 = 9.9 \pm 0.1$ GHz with a linewidth $\Delta f(H = 0) = \frac{\partial f}{\partial H}\Delta H_0 = \frac{\gamma}{2\pi}\mu_0 \Delta H_0$ $= 0.82 \pm 0.07$ GHz and matches reasonably well with the SNS-MOKE data.

4.4 P-MOKE measurements

Different from the L-MOKE configuration, the P-MOKE configuration is highly sensitive to the z-component of magnetization precession. The schematic in Fig. 4.5d clearly shows that only a magnetization precession at the DW has such a finite z-component and is sensitive to the P-MOKE measurement. The spin precession in the uniform domains occurs in the xy-plane so that it is insensitive to the P-MOKE.

Indeed, the P-MOKE map in Fig. 4.5e shows a strong, localized response only at the positions at which DWs are placed. The map shows a similar intensity but different phases (visualized by different colors) at both DWs. In contrast to the previous L-MOKE map, the P-MOKE map was acquired at a frequency of $f = 0.96$ GHz, i.e. at much lower frequency than the FMR. This clear distinction to the FMR is also visible in the frequency dependence of this DW precession in Fig. 4.5f. The SNS-MOKE signal at the DW exhibits a pronounced maximum at $f = 640$ MHz which is significantly lower than the FMR mode ($f \approx 9.5$ GHz). It should be noted that the frequency scan shows a weak background signal at the FMR frequency that is, however, independent of the DW and is also present when measuring P-MOKE in the uniform domains. Overall, these experiments clearly visualize that the uniform domains and the chiral Néel DWs exhibit distinct precession dynamics. Herein, the DW exhibits a resonant excitation spectrum at frequencies that are significantly lower than the FMR.

The asymmetric DW resonance shape in Fig. 4.5f can be accounted for by a superposition of numerous standing spin wave modes along the width of the magnetic conduit. It is highly unlikely that the asymmetry is caused by a hybridization of the DW and FMR modes since the only available band of the forward-volume spin-waves in the uniform domains has no overlap with the low-frequency DW mode [92].

Lastly, the out-of-phase response of the two neighboring DW resonances in Fig. 4.5e can be explained by their oppositely orientated static, in-plane magnetization. Since the DW's chirality is fixed, the DW's IP component points along $-x$ for an $\uparrow\downarrow$ DW while it points along $+x$ for a $\downarrow\uparrow$ DW. Fig. 4.6 shows how this affects the magnetic precession and the measured SNS-signal of the DWs: Because of the oppositely oriented IP orientation M_x of two neighboring DWs, they precess in an opposite sense of rotation when they are excited by an RF field $h_\mathrm{RF,y}$. Since the dynamic magnetization component $m_\mathrm{z}(t)$ is probed by P-MOKE, the SNS-MOKE signal arising from both DWs is phase shifted by 180°. Moreover, the out-of-phase $m_\mathrm{z}(t)$ response of two neighboring Néel walls will equally appear when no DW precession, but a periodic DW motion (oscillation) is excited.

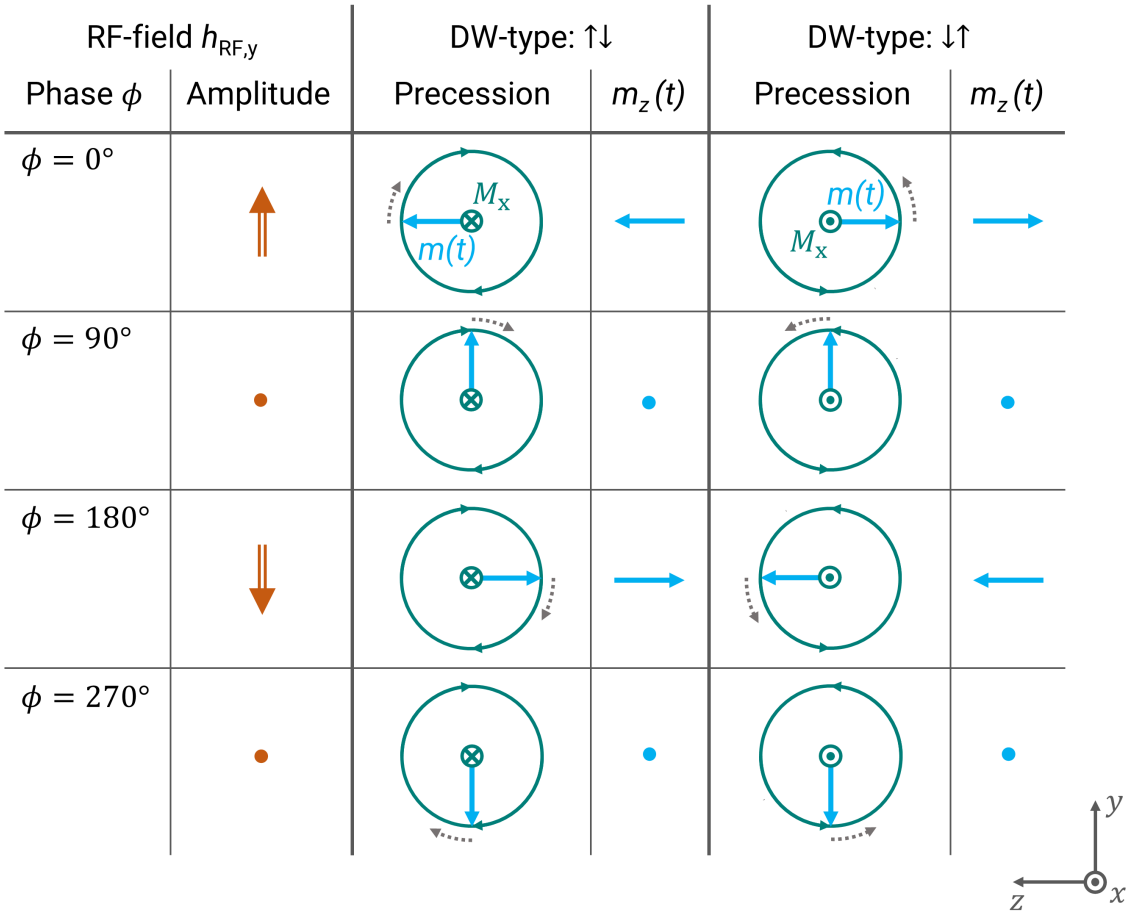

Figure 4.6: **Explanation of the out-of-phase SNS-MOKE response for two precessing neighboring DWs.** The orientation of the RF magnetic field $h_{RF,y}$ along $\pm y$ is shown in the left two columns for the phases $\phi = 0°$, 90°, 180° and 270° of the periodic RF signal. The corresponding precession of the ↑↓ DW (center two columns) and ↓↑ DW (right two columns) is shown at resonance. Note that the schematic depicts the projection of the time-dependent magnetization $m(t)$ to the yz plane and the static DW magnetization M_x points along $-x$ (↑↓ DW) or $+x$ (↓↑ DW). In this projection, the two DWs precess with an opposite sense of rotation. Because of this, the $m_z(t)$ variations for the ↑↓ and ↓↑ DWs are out-of-phase. Since SNS-MOKE is only sensitive to periodic $m_z(t)$ variations, the SNS-MOKE signal of the two DWs will be out-of-phase as well according to this model.

Chapter 5

Self-propulsion of a magnetic domain wall

In this chapter, the current-induced DW motion is investigated in the presence of RF magnetic fields or RF currents. The chapter is structured as follows: The general measurement setup and the measured device geometries will be introduced first. Next, the effect of a static, transverse H_y field on the DW motion will be briefly revisited. Afterwards, the DW motion in the presence of both a resonant RF-field and a static H_y field will be demonstrated and the RF-induced effects such as DW rectification and self-propulsion will be introduced. Finally, the equivalent measurements using an RF-current (instead of an RF-field) will be shown and compared with the RF-field measurements.

5.1 RF-field excitation of a magnetic domain wall

The current-induced DW motion is now measured in the presence of RF magnetic fields. Note that the results are presented both as the DW displacement per current pulse d_p as well as the effective velocity $v_{eff} = d_p/t_{pulse}$ that is deduced from the current pulse length t_{pulse}. Since the calculation of v_{eff} is based only on t_{pulse}, any DW motion that takes place after the current pulse will thus overestimate v_{eff}.

5.1.1 Measurement setup

The same device design and magnetic films as in the previous chapter 4 are used here, i.e. devices with the design A (chapter 3.2.1) were fabricated and electrically connected by wirebonding. An RF signal generator is connected to the device and injects an RF current to the CPW. The transmitted RF power is detected by a digital oscilloscope. In addition to the wirebonding used for the SNS-MOKE measurements in chapter 4, the magnetic conduit is wirebonded here and electrically connected to the pulse generator (Fig. 5.1a). The narrow, straight part of the conduit has the dimensions 3×30 µm^2. Fig. 5.1b summarizes all elements acting on the DW: An electrical current with current density j_{SOT} flows directly through the conduit and induces an SOT that drives the DW

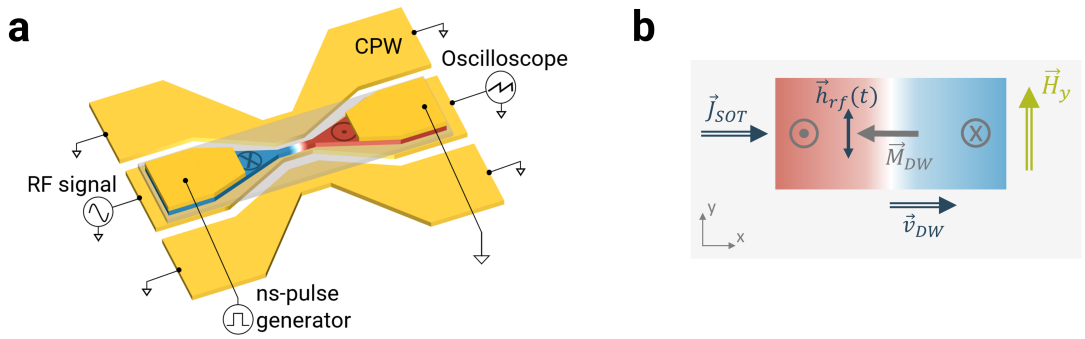

Figure 5.1: **Schematic of device geometry and measurement configuration using RF-magnetic fields. (a)** Schematic of the device geometry and electrical connections used in the DW motion measurements using the device design A. **(b)** Schematic illustration of the magnetic fields and currents acting on the magnetic DW.

along j_{SOT} with a velocity v_{DW}. With respect to magnetic fields, both a static transverse field H_{y} and an RF-field $h_{\mathrm{rf}}(t)$ will be applied for the measurements in this chapter. Note that the RF current in the CPW generates $h_{\mathrm{rf}}(t)$ at the position of the magnetic conduit. As explained in Fig. 3.13, the RF-signal can be either sent as a continuous-wave or as a bursted signal with a length t_{burst}.

5.1.2 RF-induced unidirectional domain wall motion

According to the collective coordinate model introduced in section 2.3.4, a static IP magnetic field such as H_{x} or H_{y} induces no steady-state DW motion. Such static fields can cause a slight distortion of the DW, e.g. a DW tilting, but do not cause a continuous movement of the DW. Similarly, it is not expected that the periodic time-varying RF-field may cause a net motion in any preferential direction by symmetry considerations. This is experimentally seen in Fig. 5.2b which shows the measurement of current-induced DW motion without and with an additional RF-field. The DW displacement d_{p} versus current density j is unaffected by the RF-field. It is also seen that the current-induced DW motion in zero magnetic field is symmetric, i.e. the DW moves an equal distance to the right (left) when a positive (negative) current pulse with equal current density is applied.

The previous symmetry considerations break down however, when a static magnetic field modifies the DW energy. As discussed in section 2.3.4, a transverse magnetic field H_{y} induces a directionality to the DW propagation (see Fig. 5.1 for the coordinate of the system). This makes the current-induced DW motion asymmetric, i.e. the DW displacement for a positive current-density, d_{p}^{+}, and a negative one, d_{p}^{-}, are not equal. If H_{y} is positive, $d_{\mathrm{p}}^{+} > |d_{\mathrm{p}}^{-}|$ and vice versa. Such asymmetric $d_{\mathrm{p}}^{\pm}(j, H_{\mathrm{y}} \neq 0)$ curves in the presence of a weak field $\mu_0 H_{\mathrm{y}} = 18$ mT are shown in Fig. 5.2a when comparing the two gray curves with open ($H_{\mathrm{y}} = 0$) and closed ($\mu_0 H_{\mathrm{y}} = 18$ mT) symbols.

The application of an RF-field at $f = 475$ MHz, referred to as *resonant*, yields a significant enhancement of this asymmetry in the DW propagation. The threshold for DW motion at a positive current-density, j_{th}^{+}, lowers further while the one at a negative

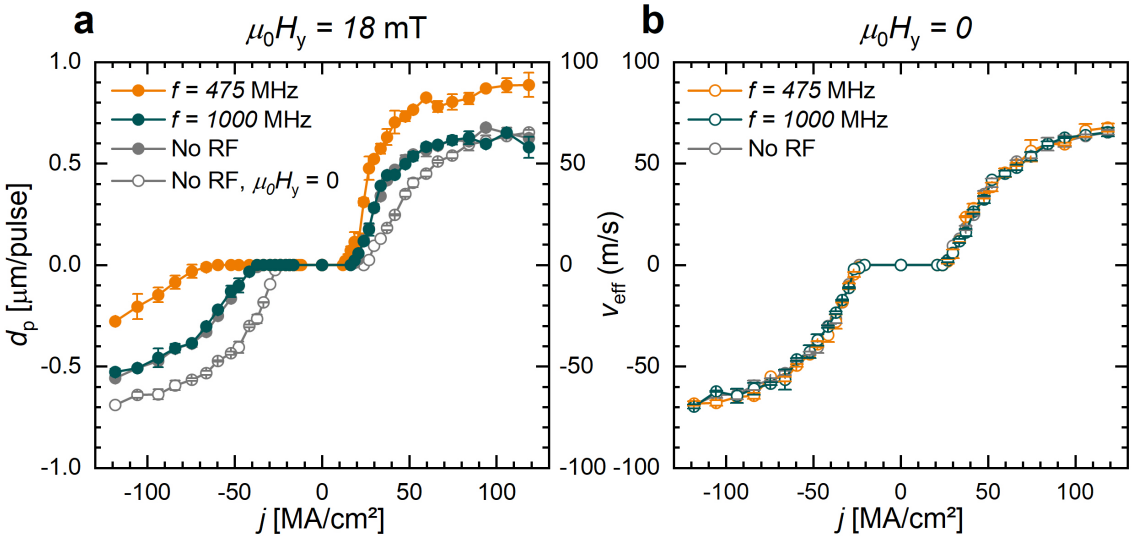

Figure 5.2: **Current-density dependence of the current-induced DW motion in the presence of an RF-field.** Electrical current pulses with $t_{\mathrm{pulse}} = 10$ ns cause the displacement d_{p} of a magnetic DW. The latter is also expressed as an effective velocity v_{eff}. The measurements are performed in the presence of a continuous-wave RF-magnetic field where the transmitted power reads $P_{\mathrm{RF}}^{out}(f = 475\ \mathrm{MHz}) = -12.7$ dBm and $P_{\mathrm{RF}}^{out}(f = 1000\ \mathrm{MHz}) = 0.7$ dBm. The RF-field only shows an impact for $f = 475$ MHz and in the presence of a static, transverse magnetic field H_{y} **(a)** but not in zero static field **(b)**. The inset of **(a)** schematically shows the orientation of the DW and magnetic fields and electrical currents.

current-density, $|j_{\mathrm{th}}^{-}|$, increases further. In addition, the maximum d_{p}^{+} increases from 0.65 µm/pulse (no RF) to 0.88 µm/pulse ($f = 475$ MHz). The resonant microwaves appear to create an additional torque on the DW in the preferential direction of motion. Note that this preferential direction reverses when H_{y} is reversed. In the absence of a preferential direction, i.e. at $\mu_0 H_{\mathrm{y}} = 0$, this torque vanishes due to symmetry, as shown in Fig. 5.2b. Note that for $f = 475$ MHz, the RF power $P_{\mathrm{RF}}^{\mathrm{out}} = -12.7$ dBm transmitting the CPW amounts to a peak RF field amplitude, $\mu_0 h_{\mathrm{RF}} = 0.389$ mT. For $f = 1.0$ GHz, referred to as *off-resonant*, despite a higher transmitted power of $P_{\mathrm{RF}}^{\mathrm{out}} = 0.7$ dBm (corresponding to $\mu_0 h_{\mathrm{RF}} = 0.91$ mT), no RF-induced torque is visible. Fig. 5.3 shows the Kerr microscope images of these results.

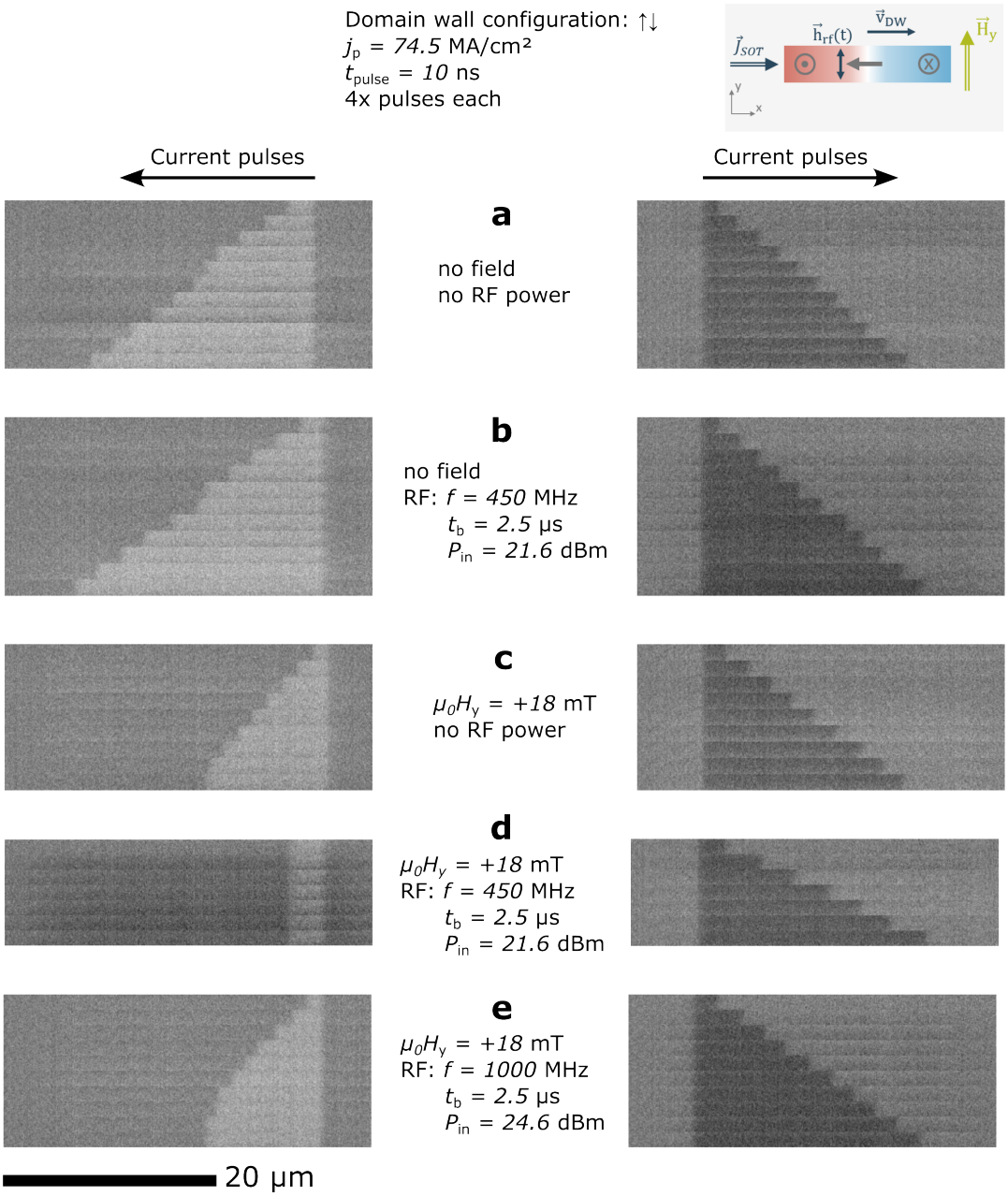

Figure 5.3: **DW motion in the presence of a static H_y field and (off-)resonant RF fields.** Subsequent snapshots of the differential Kerr image showing the current-induced DW propagation along the electrical current flow are recorded in various configurations. White (black) contrast indicates that the up-down DW is moving to the left (right). DW motion is measured in the following configurations: (**a**) Zero static field and no RF-power. (**b**) Zero static field and resonant RF-bursts with $t_{burst} = 2.5$ µs. (**c**) $\mu_0 H_y = +18$ mT but no RF-power. (**d**) $\mu_0 H_y = +18$ mT and resonant RF-bursts are applied and show the complete rectification of DW motion towards the right (along $+x$). (**e**) An off-resonant RF-field at $f = 1000$ MHz shows no modified DW motion at $\mu_0 H_y = +18$ mT compared to (**c**).

To further understand the role of the H_y field on this RF-induced torque, Fig. 5.4a shows the dependence of the current-induced DW motion on H_y, without and with an RF field at frequencies below, at, and above the resonance. For simplicity, $\Delta d_p = d_p^+ - |d_p^-|$ is defined as the difference in displacement for a positive and a negative current pulse. In the absence of a resonant RF-field, Δd_p increases slowly with H_y. However, a resonant RF field at $f = 550$ MHz dramatically increases the asymmetry Δd_p at low H_y, so that, at positive fields, d_p^+ reaches significantly higher values than in the absence of RF-fields. The maximum displacement reaches a peak value of $d_p^+ = 1.97$ µm/pulse ($|d_p^-| = 1.95$ µm/pulse) at $\mu_0 H_y = 18$ mT ($\mu_0 H_y = -20$ mT), respectively, which is more than 3 times higher than at off-resonance. $|d_p^\pm|$ then decreases and approaches the off-resonant curve at high field ($|\mu_0 H_y| \sim 70$ mT).

The emergence of the peaked $d_p(H_y)$ data for resonant RF-fields will be discussed in the following: One possible explanation for the $d_p(H_y)$ behavior is the trade-off between the asymmetry of DW motion and the coupling of the DW magnetization $\vec{M}_{DW}$ with the RF field $\vec{h}_{rf}$. As shown in the Fig. 5.4b, H_y rotates $\vec{M}_{DW}$ by the angle Φ from x to y. This rotation gradually induces the asymmetry of the DW motion. At the same time the coupling between $\vec{M}_{DW}$ and $\vec{h}_{rf}$ scales with $\cos(\Phi)$ and decreases with H_y. However, an unidirectional RF-induced torque on the DW occurs only when both the DW motion is asymmetric and the RF-field couples well to the DW. Hence, for $\mu_0 H_y = 0$, there is no RF-induced torque since the DW motion is still symmetric. In contrast, a finite H_y provides the DW asymmetry and enables unidirectional motion of the DW. Nevertheless, at high H_y, despite the highly asymmetric DW motion, the coupling between $\vec{M}_{DW}$ and $\vec{h}_{rf}$ reduces and the efficiency of RF-induced torque decreases.

A second important aspect for the discussion of the $d_p(H_y)$ data is the H_y-induced DW tilting (schematically shown in Fig. 5.4c). In zero magnetic field, the DW exhibits a tilt of the DW plane during current-induced motion by an SOT [8, 93]. This tilt is caused by a combination of DMI and the DL-SOT. When a magnetic H_y field is applied and the DW is moved by a current pulse along the preferred direction of motion (induced by the polarity of H_y), the tilting angle is first reduced by H_y. A further increase in H_y then leads to an increase of the tilting angle but in the reverse direction. Experimentally, large DW tilting angles can be detrimental for DW motion since the DW is increasingly stretched and is more susceptible to extrinsic pinning sites (especially at the conduit edges). Zero DW tilting is thus optimal for DW motion. Altogether, the H_y-induced transition from the initial DW tilt, to zero DW tilt and finally to a large and reverse DW tilt could explain some features of the $d_p(H_y)$ data: Firstly, it illustrates the existence of an optimal H_y-field where the DW tilting is zero and the DW mobility is least affected by pinning. At this field, the RF-induced torque can most efficiently drive the DW. Secondly, the low efficiency of the RF-induced torque for large H_y can be explained by the large DW tilting and the large impact of extrinsic pinning sites.

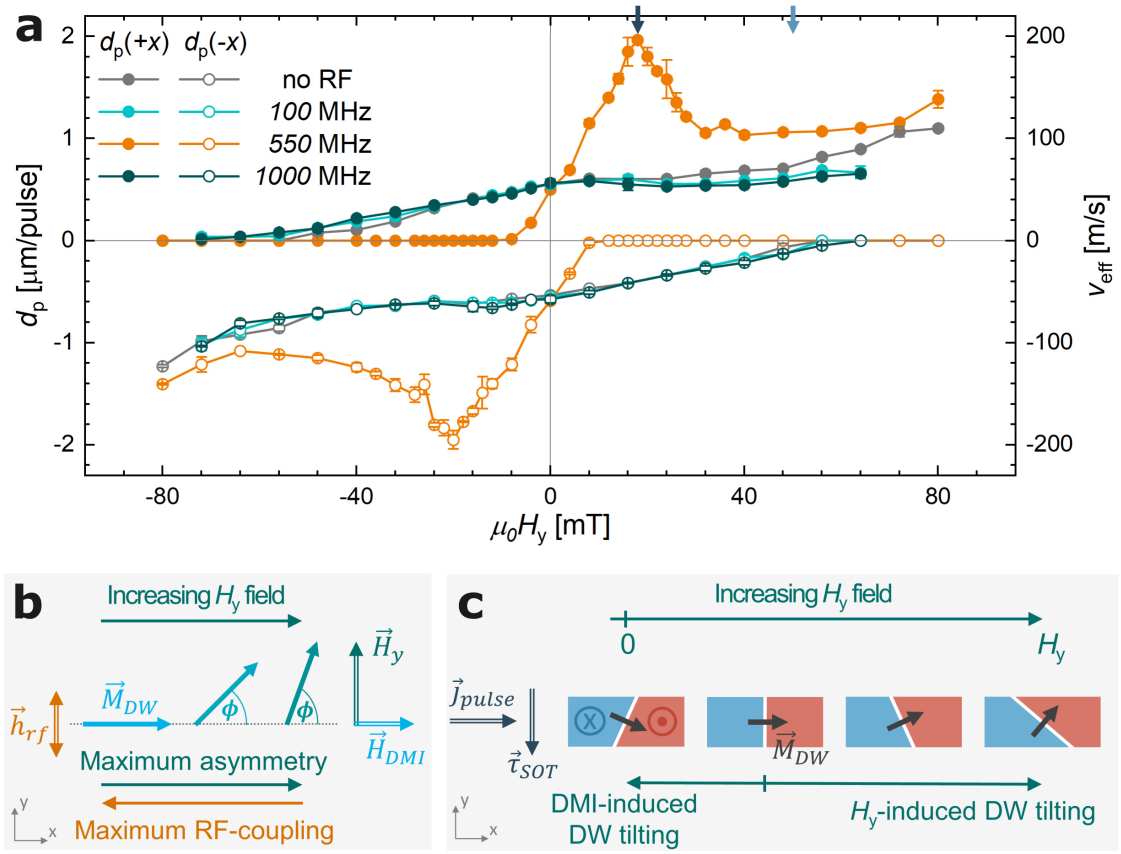

Figure 5.4: **Magnetic field-dependence of the current-induced DW motion in the presence of an RF-field.** **(a)** The DW motion is induced by current pulses with $j = 74.5$ MA/cm² and $t_p = 10$ ns while a static magnetic field H_y is applied transverse to the magnetic conduit. Filled (Open) symbols represent the DW displacement for a positive (negative) applied current pulse. An additional continuous-wave RF-magnetic field is present during the current-induced DW motion where the transmitted RF-power through the CPW is kept constant at $P_{RF}^{out} = 0.7$ dBm. Two blue arrows at the top axis at $\mu_0 H_y = 18$ mT and $\mu_0 H_y = 50$ mT indicate the field at which frequency-scans are later-on performed. **(b)** Schematic on the rotation of the static DW magnetization with increasing H_y. With increasing field magnitude, the asymmetry of DW motion increases while the coupling between the RF-field and the DW magnetization decreases. **(c)** Schematic on the DW tilt during current-induced DW motion for different H_y. Large tilting angles for large H_y makes the DW more susceptible to extrinsic pinning. The depicted mechanisms in **(b-c)** could potentially cause the emergence of the $d_p(H_y)$ peak at 550 MHz.

5.1.3 Self-propulsion of magnetic domain wall

The frequency-dependence of this unidirectional DW displacement in Fig. 5.5a shows that $|d_p^{\pm}|$ is clearly unaffected by the microwaves at low and high frequencies. However, when approaching a range of resonant frequencies that lies between $f = 400$ MHz to $f = 550$ MHz, the unidirectional DW displacement sets in, i.e. d_p^+ increases and $|d_p^-|$ decreases. Remarkably, for excitation frequencies within this resonant frequency range, the DW moves without current pulses but solely due to the resonant RF field in the presence of a static H_y field. This motion is therefore dubbed *self-propulsion* or *automotion* of the DW. As before, the polarity of H_y defines the directionality of this self-propulsion, i.e. for $H_y > 0$ ($H_y < 0$) the DW moves along the positive (negative) x-direction. Note

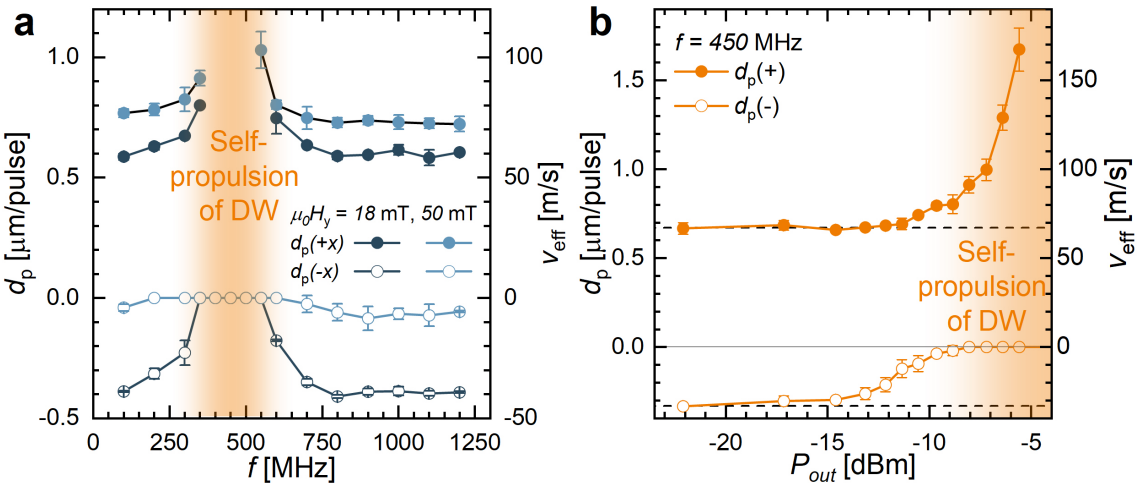

Figure 5.5: **Frequency and power dependence of RF-induced unidirectional DW motion.** The DW motion is initiated by current pulses with $j = 74.5$ MA/cm² and $t_p = 10$ ns while a transverse H_y field is present. **(a)** Dependence of the DW-displacement on the frequency of the RF-field. Two different H_y fields are compared that are indicated in Fig. 5.4 by small blue arrows. The transmitted RF-power is kept constant at $P_{RF}^{out} = 0.7$ dBm. In the region between 400 MHz and 550 MHz the DW displacement diverges and the DW exhibits weak self-propulsion, i.e. it moves without the action of a current pulse. **(b)** Power-dependence of the RF-induced rectification of the DW motion at $f = 450$ MHz and $\mu_0 H_y$ = 16 mT . The transmitted RF power P_{RF}^{out} is plotted here and the typical RF-attenuation at this frequency is approximately 18 dB.

that the applied RF-power determines the strength of the self-propulsion (Fig. 5.5b). For moderate powers (e.g. $P_{RF}^{out} = -10$ dBm), only an enhanced asymmetry in the current-induced DW motion is visible while a higher RF-power (e.g. $P_{RF}^{out} \geq -5$ dBm) allows the self-propulsion to overcome pinning points so that the DW visibly moves over micron distances without any electrical current pulse. The frequency-dependence in Fig. 5.5a is each measured at $\mu_0 H_y = 18$ mT and $\mu_0 H_y = 50$ mT. These values correspond to H_y-fields at and above the $d_p(H_y)$-maximum in Fig. 5.4 and are indicated by small blue arrows there. Interestingly, no significant H_y-induced shift of the resonance region is visible. However, the self-propulsion efficiency at the resonance is highest at $\mu_0 H_y = 18$ mT and decreases at $\mu_0 H_y = 50$ mT. For instance, at $f = 400$ MHz, the self-propulsion at $\mu_0 H_y = 18$ mT drags the DW along the entire conduit for more than 30 µm without pinning whereas at $\mu_0 H_y = 50$ mT the maximum self-propulsion distance between two pinning points is approximately 6.4 µm.

This agrees well with the previous observation of the marked maximum of d_p^+ at $\mu_0 H_y = 18$ mT in Fig. 5.4 and moreover implies that the $d_p(H_y)$-maximum is not caused by a frequency-shift of the DW resonance condition. Furthermore, for large fields of $\mu_0 H_y = 50$ mT, i.e. when the DW magnetization is almost aligned along y, the frequency scan reveals no signature of a parametric excitation of the DW. The parametric excitation geometry requires the pumping field h_{rf} to be parallel to the magnetization (i.e. along y) and the precession to be elliptical. In this geometry, a magnetization precession at twice the original frequency would be excited. The excitation efficiency strongly depends on the

ellipticity and vanishes for circular precession [39]. Despite the fact that the FMR mode of the considered PMA magnets has zero ellipticity, the precession mode of the DW is expected to be elliptic due to its in-plane configuration. However, no parametric excitation at twice the resonant frequency is observed in Fig. 5.5a. Either no such excitation takes place or because of a low excitation efficiency its impact on the DW motion is negligible.

In the previous measurements, continuous-wave RF-fields h_{rf} were applied. However, for RF-fields at resonant frequencies that are sufficiently strong, the self-propulsion of the DW prohibits a quantitative measurement of the DW speed. In the following, the RF-signal will be chopped into short RF-bursts by using an RF mixer (as outlined in section 3.3.2). This allows to limit the distance that the DW moves during self-propulsion and enables to quantify the true DW velocity during the self-propulsion. The frequency scan $d_{\mathrm{p}}(f)$ using RF-bursts with length t_{burst}= 5 µs is displayed in Fig. 5.6a. The bursts are synchronized to the current pulse and reach the device $20-30$ ns before the current pulse. The figure shows the frequency scans for two RF power modes: constant output power $P_{\mathrm{RF}}^{\mathrm{out}} = const.$ and constant input power $P_{\mathrm{RF}}^{\mathrm{in}} = const.$. The resonance for $P_{\mathrm{RF}}^{\mathrm{out}} = const.$ is very narrow and centered at 475 MHz and follows the trend in Fig. 5.5a where the same power mode was used for CW-microwaves. For the $P_{\mathrm{RF}}^{\mathrm{in}} = const.$ mode, the resonance is significantly wider with a maximum at 350 MHz.

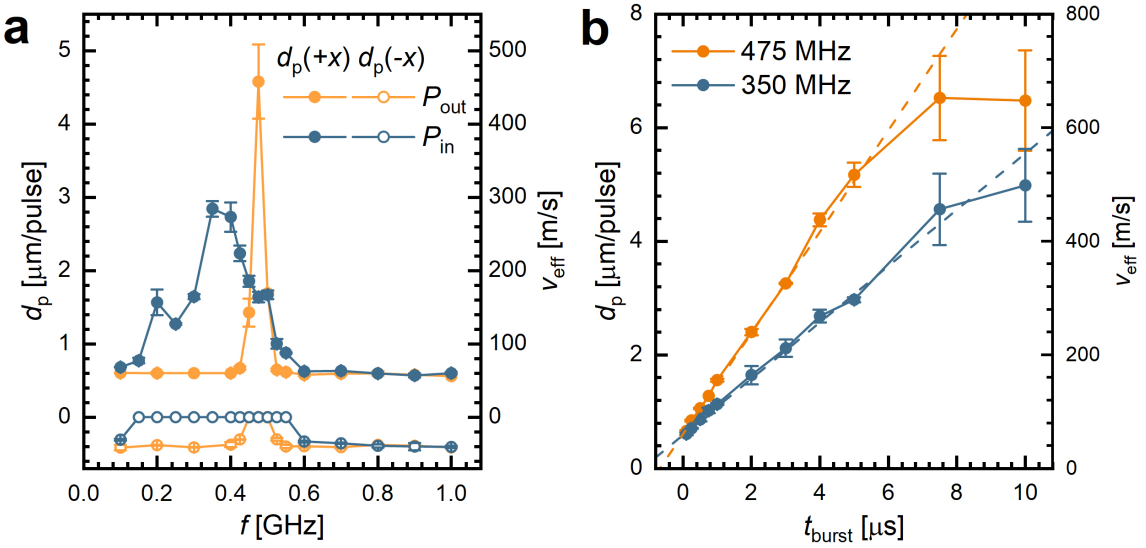

Figure 5.6: **Frequency scan and burst-time dependence of unidirectional DW motion.** RF magnetic fields with bursts length t_{burst} are applied to the CPW. The bursts are synchronized with the electrical current pulses with j = 74.5 MA/cm² and t_{pulse}= 10 ns. The bursts start shortly before the current pulse acts on the DW. All measurements are taken in a transverse magnetic field $\mu_0 H_{\mathrm{y}}$= 18 mT. **(a)** Frequency scan of the DW displacement d_{p} with t_{burst}= 5 µs. The displacement d_{p} for a positive (negative) current pulse is indicated by filled (open) symbols. RF bursts are applied at two power modes, either at constant output power $P_{\mathrm{RF}}^{\mathrm{out}} = 1.0(1)$ dBm or for constant input power $P_{\mathrm{RF}}^{\mathrm{in}} \approx 23.5(5)$ dBm. **(b)** At the maxima of the $P_{\mathrm{RF}}^{\mathrm{out}}$ and $P_{\mathrm{RF}}^{\mathrm{in}}$ scans in part (a), i.e. at 475 MHz and 350 MHz, the burst time dependencies are measured. The dashed lines are linear fits to the linear slope for $t_{\mathrm{burst}} \leq$ 5 µs.

Before discussing this crucial importance of the power settings in the next section (chapter 5.1.4), the velocity during self-propulsion will be investigated first. To determine the speed of the RF-induced self-propulsion, the increase of the DW displacement d_p with the bursting time t_{burst} is measured as shown in Fig. 5.6b. For $t_{burst} = 0$, the DW displacement is purely driven by the SOT-pulse and acts as an offset to the data. For finite burst times, d_p increases linearly for $t_{burst} \leq 5$ µs. This linear slope corresponds to the DW velocity during self-propulsion v_{self} and amounts to $v_{self} = 0.9 \pm 0.1$ m/s ($f = 475$ MHz) and $v_{self} = 0.50 \pm 0.15$ m/s ($f = 350$ MHz). Compared to the SOT-driven DW motion, where the DW velocities are on the order of tens of meters per second (Fig. 5.2b), the values of v_{self} are allocated in the depinning regime where the DW exhibit enhanced mobility as compared to the creep regime, but is still affected by microscopic pinning sites [94]. The different DW speeds during the SOT pulse and during self-propulsion are schematically shown in Fig. 5.7.

The self-propulsion's sensitivity to pinning sites may be seen from two further aspects: First, the $d_p(t_{burst})$ curve deviates from its linear slope and levels off for longer burst times. This suggests that after a few micrometers of propagation the DW is likely to stop at a pinning site since the RF-induced torque is not sufficient to overcome the pinning potential. Second, all previous measurements applied RF-signals in addition to an initial current pulse. This initial current pulse provides a strong SOT and serves to initiate the DW motion and to overcome occasional pinning sites. The RF-burst subsequently propels the DW at a much lower speed and might be insufficient to overcome some pinning sites. This measurement protocol has been chosen because a solely RF-driven DW is easily pinned and impedes repeated measurements. The current pulses are thus a key requirement to overcome an initial DW pinning. Note that to a large extent, pinning arises due to extrinsic effects such as magnetic defects or edge roughness. While SOT-driven DW motion is only affected by such extrinsic pinning, the possibility of an additional intrinsic pinning for the self-propulsion mechanism remains to be studied.

Finally, Fig. 5.8 displays the sequences of DW motion during self-propulsion: Fig. 5.8a shows the burst-time dependence of pulse-assisted self-propulsion while Fig. 5.8b displays the self-propulsion of a DW in the absence of current-pulses, i.e. solely by RF-bursts.

To put these results into perspective, the automotion of magnetic bubbles with a specific magnetic configuration was accomplished many decades ago by Argyle *et al.* by using a pulsed $h_z(t)$ field and a static in-plane field [95]. While their use of an in-plane magnetic field to define the directionality of the automotion is similar to this work, there are several important differences to it as well. The reported automotion relied on rather long rectangular field-pulses along the easy-axis of the magnet while only resonant RF fields in the magnetic hard-plane achieve automotion in this work. Furthermore, magnetic bubbles are two-dimensional textures and their internal configuration crucially affects the automotion. In contrast, this work reports the self-propulsion of straight DWs that is independent of their configuration (i.e. $\uparrow\downarrow$ or $\downarrow\uparrow$ DW).

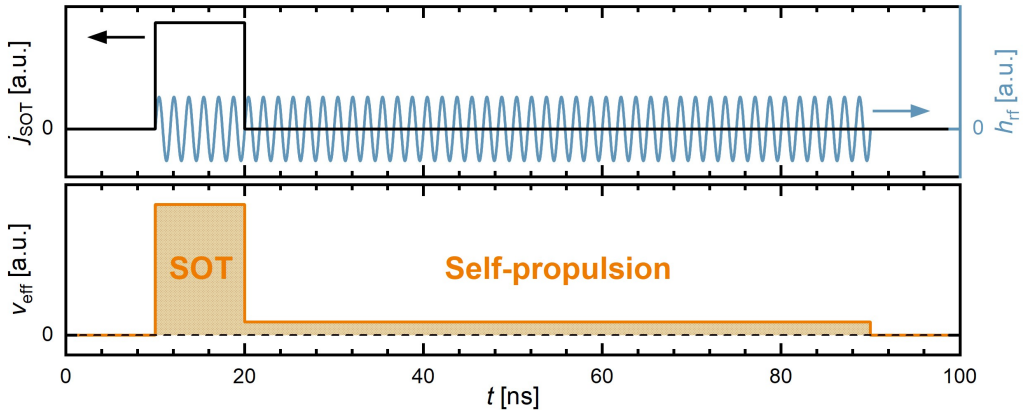

Figure 5.7: **Schematic of DW velocities during an SOT-pulse and self-propulsion.** While an SOT pulse is acting on the DW, the DW is moving in the flow regime at a high speed. After the end of the SOT-pulse, when resonant RF-fields h_{rf} are present and the DW is self-propelling, the effective DW speed is significantly lower.

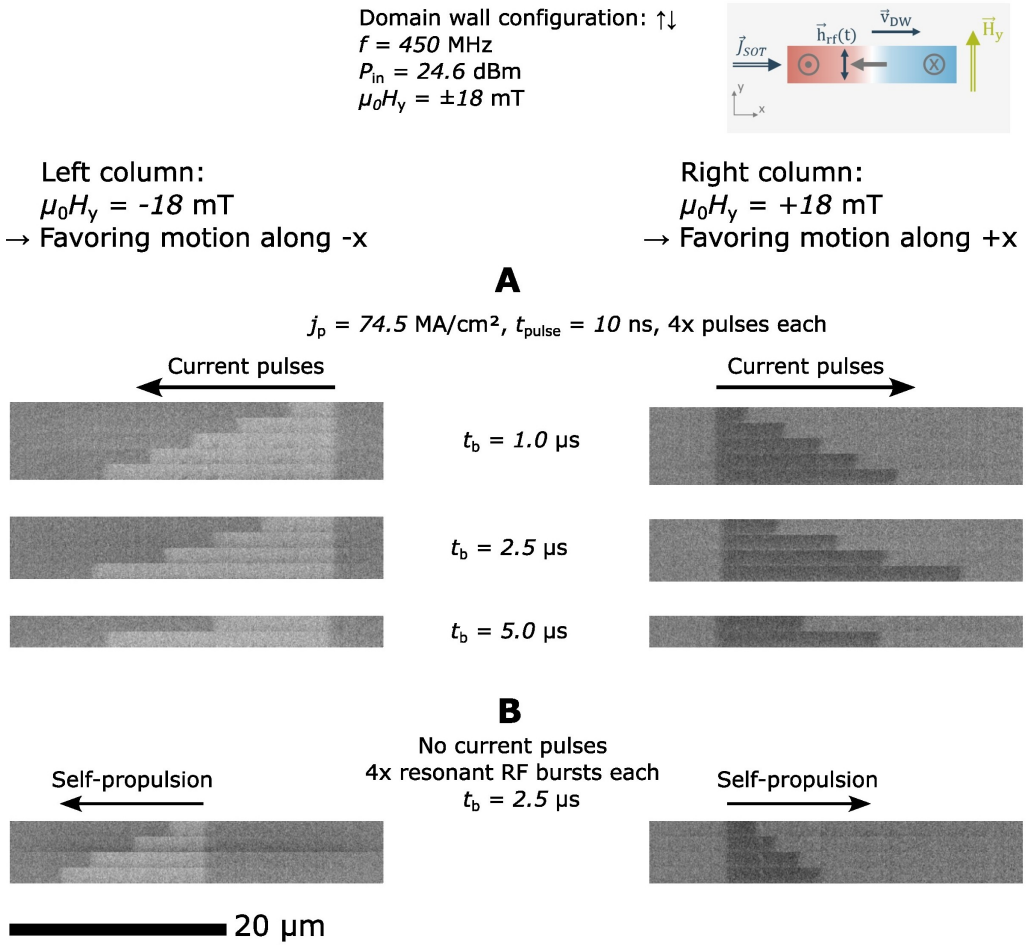

Figure 5.8: **Burst time dependence and self-propulsion in the presence of a static H_y field and resonant RF fields.** The same measurement setup and image contrast as in fig. 5.3 applies here. In the left (right) column a negative (positive) H_y field is applied.(**a**) Burst time dependence of the RF-enhanced current-induced DW motion. (**b**) Self-propulsion of the DW solely by the application of RF bursts and without any current pulses.

5.1.4 Discussion of the frequency and power dependence of the self-propulsion

In the previous sections, the SNS-MOKE microscopy has revealed the presence of a DW resonance (Fig. 4.5f) and the static MOKE has revealed the self-propulsion of the DW by resonant RF-fields (Figs. 5.5, 5.6). Nevertheless, even though both resonances overlap in frequency space, they do not perfectly match regarding center frequency, linewidth and shape as shown in Fig. 5.9a. The SNS-MOKE signal is maximum at 640 MHz, has an approximate width of 500 MHz (half-width half-maximum) and an asymmetric resonance shape. In contrast, the self-propulsion frequency scans are centered at significantly lower frequencies of 350 MHz or 475 MHz (depending on the power mode) and are much narrower. The strong impact of the power mode, i.e. constant $P_{\mathrm{RF}}^{\mathrm{out}}$ or $P_{\mathrm{RF}}^{\mathrm{in}}$, on the frequency-dependence of self-propulsion adds to this complexity. A systematic discussion of this complex behavior will be provided in the following:

To understand the impact of the power mode on the frequency dependence of self-propulsion, the frequency-dependent transmission coefficient S_{21} and reflection coefficient S_{11} of the CPW are measured using a VNA (see Figs. 5.9b-c). These measurements are performed for several different configurations of electrical connections which are shown in Figs. 5.9d-f. Note that the frame of the depicted configuration and the corresponding data are matching in color.

The configuration 5.9d is used for the SNS-MOKE measurements and only the CPW, but not the magnetic conduit, is electrically connected here. From 10 MHz to 3.25 GHz, the transmission S_{21} gradually decreases by -4 dB while the reflection S_{11} increases from -20 dB to a plateau at -6 dB. Nevertheless, the S_{21} parameter changes drastically, when in addition to the CPW the magnetic conduit is electrically connected (Fig. 5.9e-f). Such an experimental configuration is used during a DW motion measurement where a pulse generator is connected to the conduit. Here, the CPW transmission S_{21} (light blue line in Fig. 5.9b) exhibits a pronounced dip at $f \sim 480$ MHz where S_{21} drops to a value that is almost 22 dB less than for previous configuration in Fig. 5.9d. This transmission dip aligns very well to the maximum in self-propulsion for the $P_{\mathrm{RF}}^{\mathrm{out}} = const.$ mode in Fig. 5.9a. In the $P_{\mathrm{RF}}^{\mathrm{out}} = const.$ mode, the input power is controlled such that the transmitted RF power remains constant. Since the transmission reads $S_{21} = \frac{P_{\mathrm{out}}}{P_{\mathrm{in}}}$, a dip in S_{21} causes the input power to peak at the same frequency. It is therefore likely, that the $P_{\mathrm{RF}}^{\mathrm{out}} = const.$ mode artificially causes the strongest self-propulsion at the transmission dip by increasing the input RF power. Consequently, the transmitted power does not seem to be the only parameter to determine the strength of the RF-torque.

Aside from the RF-transmission through the CPW, the configuration in Fig. 5.9f allows to measure the power transmission from the CPW to the magnetic conduit (light green line in Fig. 5.9b). Such a coupling arises due to the capacitive and inductive coupling between CPW and conduit and is schematically shown in Fig. 5.10. A current flowing through the CPW may thus induce a current through the magnetic conduit, depending on the frequency-dependent coupling strength. This coupling is very low at 10 MHz due to the dielectric spacer between CPW and conduit (i.e. the DC resistance is

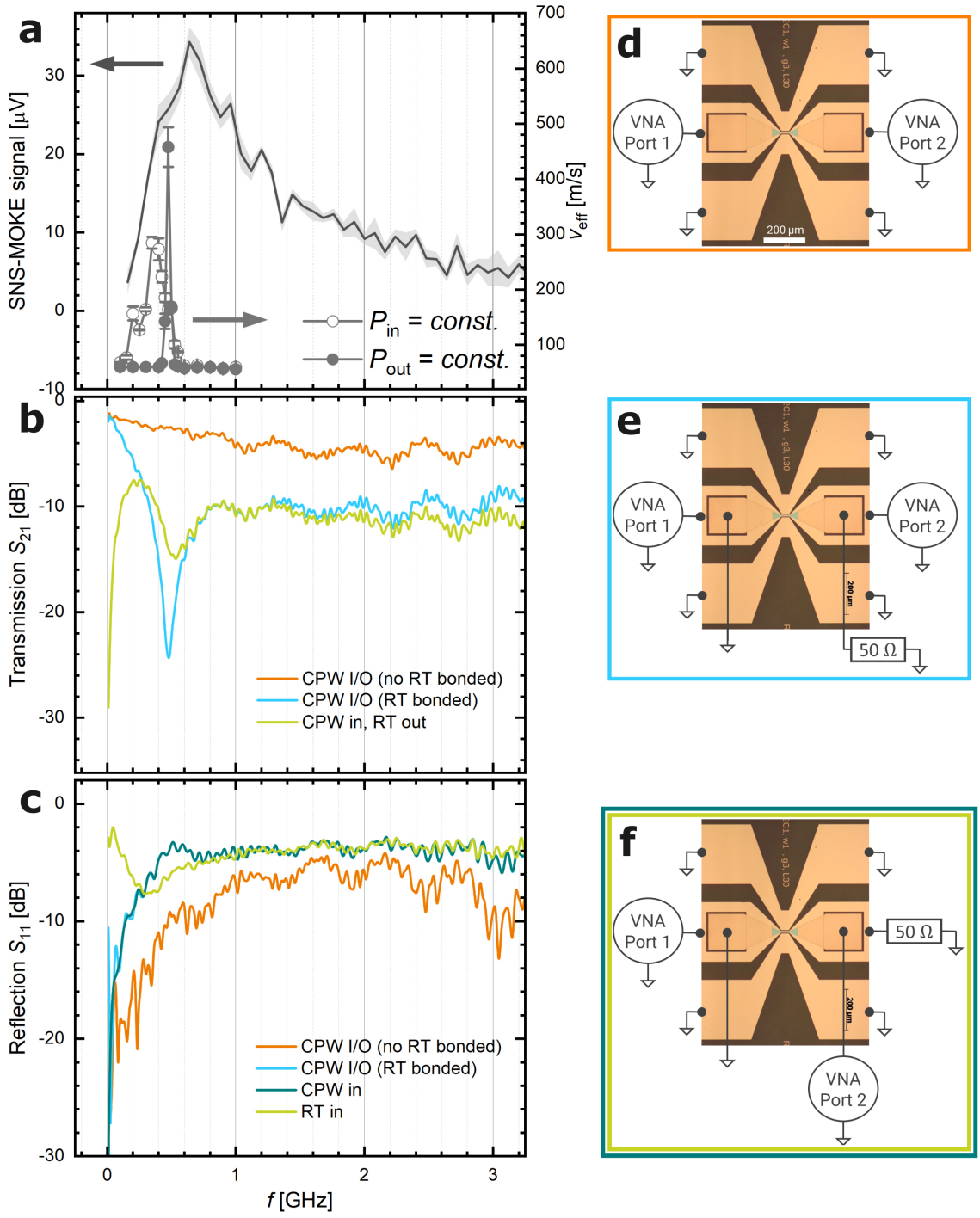

Figure 5.9: **RF transmission and reflection for different device configurations.** **(a)** Left axis: DW resonance observed in the SNS-MOKE. Right axis: frequency-scan of the RF-enhanced DW velocity for $\mu_0 H_y = 18$ mT. The previous graph is compared with the RF transmission S_{21} **(b)** and reflection S_{11} **(c)** properties of the CPW that were measured using a VNA. The VNA data for three differently contacted devices was measured: **(d)** Only the CPW is wirebonded and connected to the VNA. This setup is identical to the SNS-MOKE measurement. **(e)** Similar to **(d)**, the transmission and reflection of the CPW is measured. Nevertheless, the magnetic conduit on top of the CPW is electrically contacted as well and terminated using a 50 Ω load. **(f)** Here, the coupling between CPW and conduit is measured. The unmeasured RF-port of the CPW is 50 Ω terminated.

very high ≥ 50 MΩ) but rapidly increases to -7.5 dB at 250 MHz. Beyond 330 MHz it decreases and for $f > 600$ MHz it matches the CPW transmission (light blue line). Overall, the transmitted RF-power between CPW and magnetic conduit is therefore significant and even exceeds the power transmission through the CPW in the frequency range from 280 MHz to 600 MHz. This means that, in a certain frequency range, significant RF-currents can be flowing through the magnetic conduit, thereby affecting the magnetic DW through SOT and STT.

Interestingly, the frequency range with highest CPW-to-conduit coupling (light green line in Fig. 5.9b) approximately matches with the frequency range of self-propulsion for the $P_{\mathrm{RF}}^{\mathrm{in}} = const.$ mode (Fig. 5.9a). In the $P_{\mathrm{RF}}^{\mathrm{in}} = const.$ mode, the RF input power is kept constant and thus the transmission parameters S_{21} in Fig. 5.9b directly indicate the RF-powers that either flow through the CPW or through the magnetic conduit. The fact that strong self-propulsion coincides with a large coupling between CPW and conduit, and not with a large CPW transmission, further corroborates that the RF magnetic field (mainly determined by the current through the CPW) is not the exclusive driver or possibly not even the main driver of the DW's self-propulsion. The electrical RF current that is induced in the magnetic conduit by coupling to the CPW appears as a possible origin of self-propulsion. In order to comprehend the effect of an RF current, the DW motion and self-propulsion in the exclusive presence of RF currents are investigated in the following section 5.2.

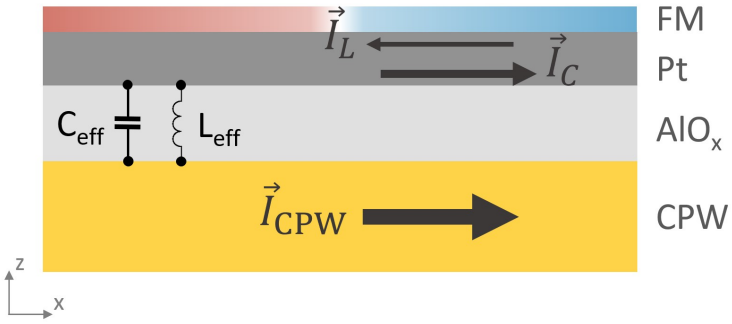

Figure 5.10: **Schematic of the capacitive and inductive RF-coupling between magnetic conduit to CPW.** The schematic illustrates how the dielectric layer (AlO_x) between CPW and magnetic conduit introduces the effective capacitance C_{eff} and inductance L_{eff}, which lead to the induction of currents I_{C} and I_{L} in the top magnetic conduit.

In addition to the previously discussed reflection and transmission of microwaves, the dissipation of RF power in the circuitry needs to be considered as well. The dissipated power P_{diss} is calculated from the input power P_{in}, the reflected power P_{refl} and the transmitted power P_{trans}:

$$P_{\mathrm{diss}} = P_{\mathrm{in}} - P_{\mathrm{refl}} - P_{\mathrm{trans}} \tag{5.1}$$

The VNA data allows to calculate the fraction $P_{\mathrm{diss}}/P_{\mathrm{in}}$ of the dissipated power at each frequency. In the frequency range considered here, between 30% and 70% of the input power is dissipated. This gives rise to the question if the DW resonance and the self-propulsion are influenced by heat dissipated from the microwaves. In order to determine the extent of RF-induced heating in the circuitry, the longitudinal resistance of the magnetic conduit, R_{xx}, is investigated in the presence of RF currents in the CPW. Any RF-induced heating will induce a measurable increase in R_{xx}. To relate a change in R_{xx} to temperature, the calibration measurement of $R_{\mathrm{xx}}(T)$ in Fig. 5.11a is used where the temperature T is varied in a physical properties measurement system and no microwaves are applied. Fig. 5.11b shows the heating of the magnetic conduit with increasing RF power. The microwaves are applied to the CPW (similar to the configuration in Fig. 5.9e) and the R_{xx} increase of the magnetic conduit is measured at ambient room temperature. The corresponding effective temperature increase of the magnetic conduit, ΔT_{eff}, is shown on the right axis. The microwave-heating is measured for 470 MHz and 1000 MHz. In this measurement, 470 MHz corresponds to the frequency where the CPW transmission is minimum (i.e. at the transmission dip in Fig. 5.9b) while the measurement at 1000 MHz serves as a reference with normal RF-transmission. At the highest RF-powers, comparable to typical RF-powers during DW motion measurements, the RF-induced heating reaches $\Delta T \sim 49.0$ K for $f = 470$ MHz and $\Delta T \sim 13.7$ K for $f = 1000$ MHz. Indeed the RF-induced heating is highest at the frequency with minimum RF transmission (i.e. at 470 MHz for this measurement). The significant difference in conduit heating for different frequencies suggests that temperature might play a role in the DW's self-propulsion, particularly regarding the frequency-dependence of the latter. The stochasticity of temperature itself, however, can not account for the unidirectional character of the self-propulsion. Moreover, it is questionable if the moderate temperature increase of ~ 50 K is sufficient for a drift of the DW position. Nevertheless, the RF-induced heating might assist other torques acting on the DW that are unidirectional and lead to self-propulsion, e.g. torques due to the RF-field or due to induced RF-currents that were previously discussed. This temperature-assistance is particularly important because the observed self-propulsion is rather slow and takes place in the depinning regime. In this depinning regime, temperature plays a crucial role to facilitate the DW depinning [94,96], i.e. to overcome the extrinsic pinning potential of the DW [97].

In conclusion, a magnetic DW exhibits unidirectional self-propulsion when microwaves at resonant frequencies are applied. The previous experiments used the device design A, where the magnetic conduit was placed on top of a CPW. In addition to the RF-field that is generated by the RF-current flowing through the CPW, it is highly likely that RF-currents are also flowing in the magnetic conduit because of a CPW-conduit-coupling. The RF-currents through the conduit are thereby inducing RF SOTs at the DW. Lastly, RF-induced heating of the conduit needs to be taken account with regard to temperature-assisted DW depinning. Table 5.1 summarizes these impacts on the DW and indicates

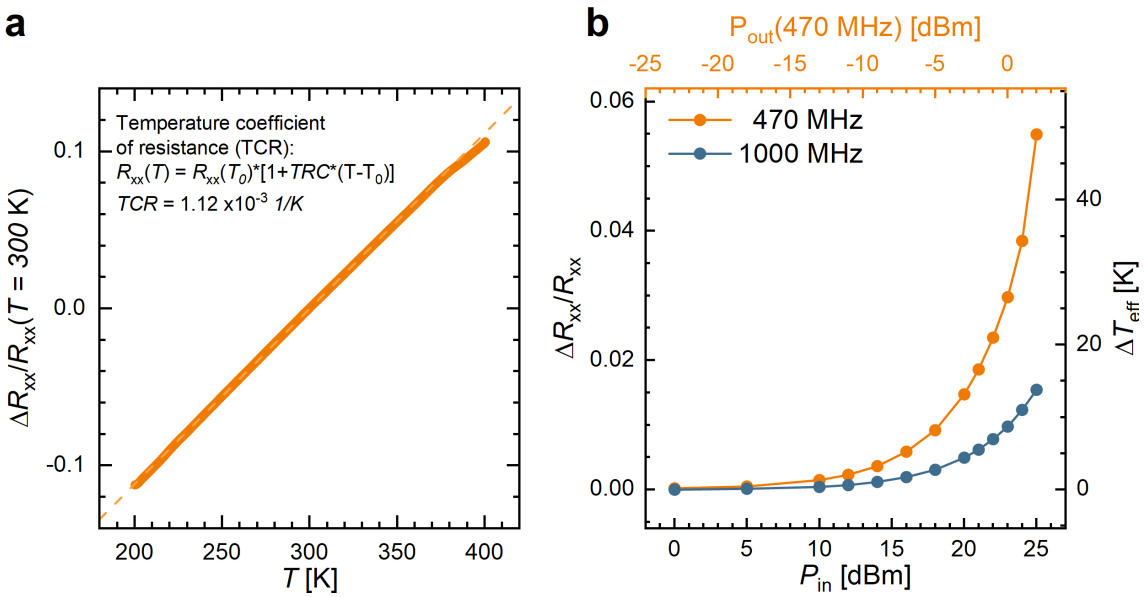

Figure 5.11: **Conduit heating due to dissipation of RF-power. (a)** The temperature coefficient of resistance (TCR) of the magnetic conduit is determined by a linear fit to the relative resistance change $\Delta R_{xx}(T)/R_{xx}(T = 300\ \text{K})$ from 200 K to 400 K. The resistance R_{xx} was measured using a 2-point resistance measurement technique by using a constant current bias of 10 μA and simultaneously measuring the voltage accross the conduit. A physical properties measurement system (PPMS) from Quantum Design was used for the temperature-dependent measurements. **(b)** At ambient room-temperature, the R_{xx} of the conduit increases with increasing RF power through the CPW. The TCR allows to translate the relative resistance increase $\Delta R_{xx}/R_{xx}(P_{in} = 0\ \text{W})$ into a temperature increase ΔT_{eff}. Microwaves at frequencies of 470 MHz and 1000 MHz are applied and the top axis displays the transmitted RF-power for 470 MHz. In the measured sample, the attenuation through the CPW is highest at 470 MHz with $S_{21} = -23.0$ dB and moderate at 1000 MHz with $S_{21} = -8.2$ dB. Note that the frequency with highest attenuation may vary slightly from sample to sample.

their dependencies on experimental parameters. Since many of these parameters, such as the RF power that is directly flowing through the magnetic conduit, P_{conduit}, are local entities that are hard to precisely determine experimentally, the interpretation of the previous results remains challenging. In order to disentangle the complicated interplay of RF-magnetic fields and RF-electrical currents that affect the DW, the following section of this chapter investigates the DW's self-propulsion in the mere presence of an RF-current.

Impacts on DW	**Relevant parameter**	**Dependencies**
RF field h_{rf}	I_{CPW}	P_{CPW}, Z_{CPW}, CPW transmission S_{21}
RF spin-orbit torque	I_{Conduit}	P_{Conduit}, Z_{Conduit}, CPW-conduit coupling
Heat dissipation	P_{diss}	S_{11}, S_{21}

Table 5.1: **Overview of various impacts on magnetization dynamics.** Note that all listed entities are frequency dependent.

5.2 RF-current excitation of a magnetic domain wall

The results of the previous section indicate a complicated interplay between RF magnetic fields, RF electrical currents and temperature. In contrast, this section investigates the DW motion in the sole presence of RF electrical currents. Most importantly, the questions arise whether a pure RF current can induce self-propulsion, and what the frequency dependence of such self-propulsion would be. This chapter consequently complements the experimental observations on self-propulsion, despite the qualitatively different means of excitation.

5.2.1 Measurement setup

The device design used in this section is shown in Fig. 5.12a and the fabrication details are provided in the methods section 3.2.1. Instead of placing a magnetic conduit on top of a CPW, the magnetic conduit is now integrated into the waveguide such that the electrical RF-currents flow directly through the conduit. The narrow, straight part of the conduit has the dimensions 4×20 µm^2. The schematic of all electrical currents and magnetic fields is schematically shown in Fig. 5.12b. In such a device structure, a pulsed current density j_{SOT} is applied along with an RF-current density $j_{\mathrm{SOT,rf}}(t)$ to manipulate the DW by damping-like SOTs. The occurence of self-propulsion will, as before, be investigated in a static transverse magnetic field H_{y}. Previously, the CPW and the magnetic conduit served as independent electrical lines to conduct the RF-current and the pulsed current, respectively. This is different for the devices here, where the RF-signal and the pulsed signal need to be combined into the same transmission line. An RF-power combiner is used to superimpose both electrical signals (see methods section and Fig. 3.13 for more details.).

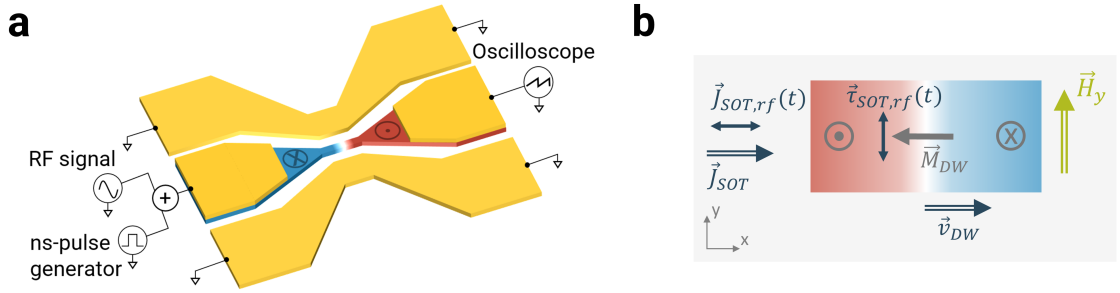

Figure 5.12: **Schematic of device geometry and measurement configuration using RF-currents. (a)** Schematic of the device geometry and electrical connections used in the DW motion measurements using the device design B. **(b)** Schematic illustration of the magnetic fields and currents acting on the magnetic DW. Note that the electrical RF-current $J_{\mathrm{SOT,rf}}(t)$ induces damping-like RF-torques $\tau_{\mathrm{SOT,rf}}$.

The film stack used for the measurements in this section is as follows: 20 TaN / 50 Pt / 0.75 Ta / 3 Co / [7 Ni / 3 Co]$_{\mathrm{N=1}}$ / 30 TaN (the numbers indicate the thickness in Å). Compared to the previous experiment, the interfacial Tantalum thickness d_{Ta} is slightly decreased from $d_{\mathrm{Ta}} = 1.0$ Å to $d_{\mathrm{Ta}} = 0.75$ Å. This d_{Ta} decrease slightly enhances the

PMA and the DMI but qualitatively leaves the current-induced DW motion and its H_y-dependence unchanged. Furthermore, the thinner Tantalum enhances the field-stability of the DW such that a weak misalignment of the external magnetic field does not have a large impact on the measurements. For magnetic thin films with different d_{Ta}, a detailed characterization by VSM and FMR is shown in the appendix in Figs. B.1, B.2.

The RF-transmission S_{21} and reflection S_{11} parameters of this device, measured by a VNA, are shown in Fig. 5.13a. The overall transmission is significantly lower than the transmission through a CPW due to the higher impedance mismatch and the higher ohmic losses. Nevertheless, the frequency dependence does not exhibit resonant absorption features, and S_{21} increases with frequency in the region of interest here. This moderate frequency dependence represents a major improvement compared to the complex VNA data in Fig. 5.9.

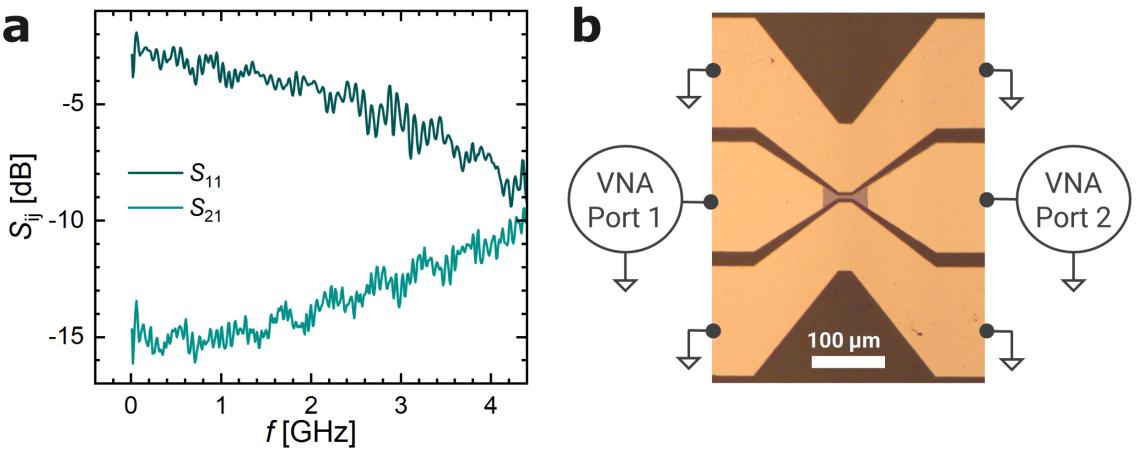

Figure 5.13: **Direct RF transmission through the magnetic conduit.** The RF transmission S_{21} and reflection S_{11} through the conduit are measured using a VNA. The inset shows a microscope picture of the device and schematically indicates the wirebonding and electrical connection to the VNA. Note that this device does not use a CPW but instead guides the microwaves through the conduit as an electrical current.

5.2.2 RF-induced unidirectional motion and self-propulsion of a DW

In analogy to chapter 5.1, the combined action of a short current pulse and an RF electrical current on DW motion is measured here. The typically microsecond-long RF current arrives at the DW a few nanoseconds before the current pulse. The current pulse has a much higher amplitude than the RF current and enables the DW to overcome local pinning potentials and to start moving. If the DW keeps moving after the end of the short current pulse, i.e. when only RF-current is present, this will be dubbed *self-propulsion* or *automotion* as before.

Fig. 5.14a displays the dependence of the DW displacement on the electrical current density of the initial current pulse. The open (closed) gray circles represent the DW displacement without (with) a transverse magnetic field H_y when no RF-current is applied. The positive H_y field induces asymmetry to the current-induced DW motion and favors

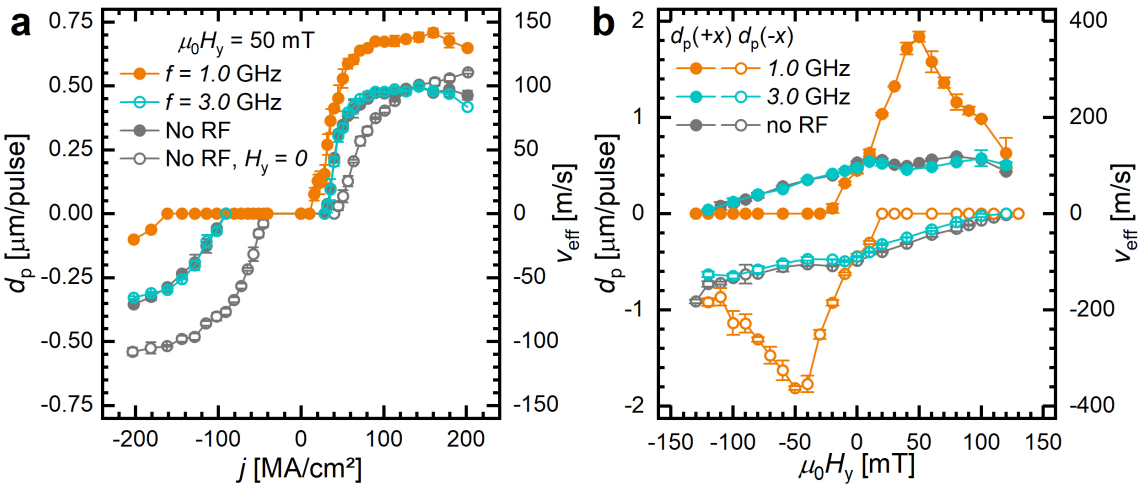

Figure 5.14: **Rectification of the current-induced domain wall motion in the presence of an electrical RF-current.** Electrical current pulses with $t_{\mathrm{pulse}} = 5$ ns cause the displacement d_{p} of a magnetic DW. The latter is also indicated as an effective velocity v_{eff}. In addition to the current pulses, a static transverse magnetic field H_{y} and an RF-current are present. **(a)** Dependence of d_p on the current density j showing the impact of the static H_{y} and a dynamic RF-current at frequency f. Herein, the transmitted power is $P_{\mathrm{RF}}^{out} = +1$ dBm at all frequencies and RF-bursts with a burst duration of $t_{\mathrm{burst}} = 2\ \mu$s are used. **(b)** H_{y}-field dependence of the current-induced DW motion for current pulses with $j = 162$ MA/cm². The RF-power is increased to $P_{\mathrm{RF}}^{out} = +4$ dBm at all frequencies and RF-bursts with $t_{\mathrm{burst}} = 1\ \mu$s are being sent. Note that the gray *'No RF'* data and the turquoise data for $f = 3.0$ GHz are very similar and often overlap in **(a-b)**.

DW motion along $+x$. While this asymmetric DW motion remains unchanged in the presence of an additional RF-current at $f = 3.0$ GHz (turquoise-colored curve), the asymmetry of the DW motion is significantly enhanced when an RF-current at $f = 1.0$ GHz (orange-colored curve) is applied. In the latter case, the threshold current densities for DW motion along $+x$ ($-x$) are further reduced (increased) and the maximum DW displacement along $+x$ is enhanced from 0.55 µm/pulse to 0.71 µm/pulse compared to the situation without RF-current. Overall, this graph is qualitatively very similar to Fig. 5.2a and is thus the first indicator that RF-currents may similarly be employed as RF-fields to rectify the current-induced DW motion or cause self-propulsion.

Moreover, the H_{y}-field dependence in Fig. 5.14b also shows strong similarities to Fig. 5.4 where an RF-field was used instead of an RF-current. Again, the H_{y}-induced asymmetry of the current-induced DW motion remains unchanged in the presence of RF-currents at a high frequency of $f = 3.0$ GHz while for $f = 1.0$ GHz this field-induced asymmetry is significantly enhanced and a $d_{\mathrm{p}}(H_{\mathrm{y}})$ maximum emerges. Note that this maximum is now located at significantly higher fields, i.e. at $\mu_0 H_{\mathrm{y}} = 50$ mT instead of the previously observed maximum at $\mu_0 H_{\mathrm{y}} = 18$ mT. However, this is caused by the fact that the magnetic films here are slightly different as mentioned above. The reduced interfacial Ta-layer yields a larger DMI here. Consequently a larger H_{y} field is required to rotate the DW magnetization towards $\pm y$.

The frequency-dependence of this RF-induced unidirectional DW motion is shown in Fig. 5.15a for two power modes, i.e. for $P_{\mathrm{RF}}^{\mathrm{out}} = const.$ and for $P_{\mathrm{RF}}^{\mathrm{in}} = const.$. Surprisingly, the RF-induced $d_{\mathrm{p}}(+x)$ enhancement (i.e. along $+x$) diverges towards low frequencies and almost vanishes for $f \geq 2.25$ GHz. The DW displacement $d_{\mathrm{p}}(+x)$ decays monotonously for $P_{\mathrm{RF}}^{\mathrm{out}} = const.$ from 10 MHz to 0.8 GHz. From 0.8 to 1.0 GHz a local maximum in $d_{\mathrm{p}}(+x)$ is seen beyond which $d_{\mathrm{p}}(+x)$ decays to the dashed baseline (see inset). While the $P_{\mathrm{RF}}^{\mathrm{in}} = const.$ data qualitatively shows the same decrease of $d_{\mathrm{p}}(+x)$ with f, it is less monotonous and exhibits many narrow maxima. Note that this fluctuation in d_{p} for the $P_{\mathrm{RF}}^{\mathrm{in}} = const.$ mode might arise due to the frequency-dependency of the power transmission through the conduit that is, in contrast to the $P_{\mathrm{RF}}^{\mathrm{out}}$ mode, not being corrected for.

This frequency-dependence for RF-currents is strikingly different from the corresponding data using RF-fields (cf. Figs. 5.5a, 5.6a), where a resonant frequency range was observed, i.e. a strong response to RF-fields existed only in a defined frequency range. Nevertheless, RF-currents cause the strongest unidirectional DW displacement (along $+x$ in this case) at lowest frequencies. For instance, when only the initial current pulse is present, the DW moves by $d_{\mathrm{p}}(+x) \approx 0.5$ µm/pulse, but by $d_{\mathrm{p}}(+x) \approx 8.2$ µm/pulse when an additional RF-current at $f = 10$ MHz and a burst length of $t_{\mathrm{burst}} = 1.0$ µs is present.

Fig. 5.15b shows that the d_{p} linearly increases with the burst length t_{burst} of the RF-current. Herein, the slope of $d_{\mathrm{p}}(t_{\mathrm{burst}})$ corresponds to the effective velocity during self-propulsion. At the frequencies of 10 MHz, 200 MHz and 1.0 GHz, this effective velocity amounts to 8.6(1) m/s, 1.84(3) m/s and 0.223(8) m/s, respectively. A visual representation of these results is given in Fig. 5.16 that shows the t_{burst}-dependence and the f-dependence of the DW motion.

Finally, Fig. 5.15c displays the increasing displacement of d_{p} on the SOT pulse length t_{pulse}. Without RF-current (gray datapoints), d_{p} increases linearly with t_{pulse} which corresponds to a constant DW velocity. For pulses with $t_{\mathrm{pulse}} \geq 10$ ns, Joule heating of the conduit could play a significant role and the slope of $d_{\mathrm{p}}(t_{\mathrm{pulse}})$, i.e. the effective DW velocity, decreases. Because of this, d_{p} lowers below the dashed line, i.e. below the linear fitting performed for $t_{\mathrm{pulse}} \leq 10$ ns. In the presence of an additional RF-current, d_{p} is vertically displaced, but the linear slope perfectly matches the slope of the gray curve where no RF was applied. This vertical displacement corresponds to the DW displacement during self-propulsion. The fact that the slope in $d_{\mathrm{p}}(t_{\mathrm{pulse}})$ does not change with RF-current implies that no threshold in t_{pulse} is required for the self-propulsion.

In conclusion, the Figs. 5.15b-c offers important insights into the mechanism of the DW's self-propulsion during the application of an RF-current. The t_{burst}-dependence in Fig. 5.15b shows that the increase in d_{p} is linear in t_{burst} and Fig. 5.15c shows that the RF-induced self-propulsion is independent of the current pulse width. The two processes of (a) SOT-driven DW motion by a current pulse and (b) RF-current induced self-propulsion are thus mostly independent of each other.

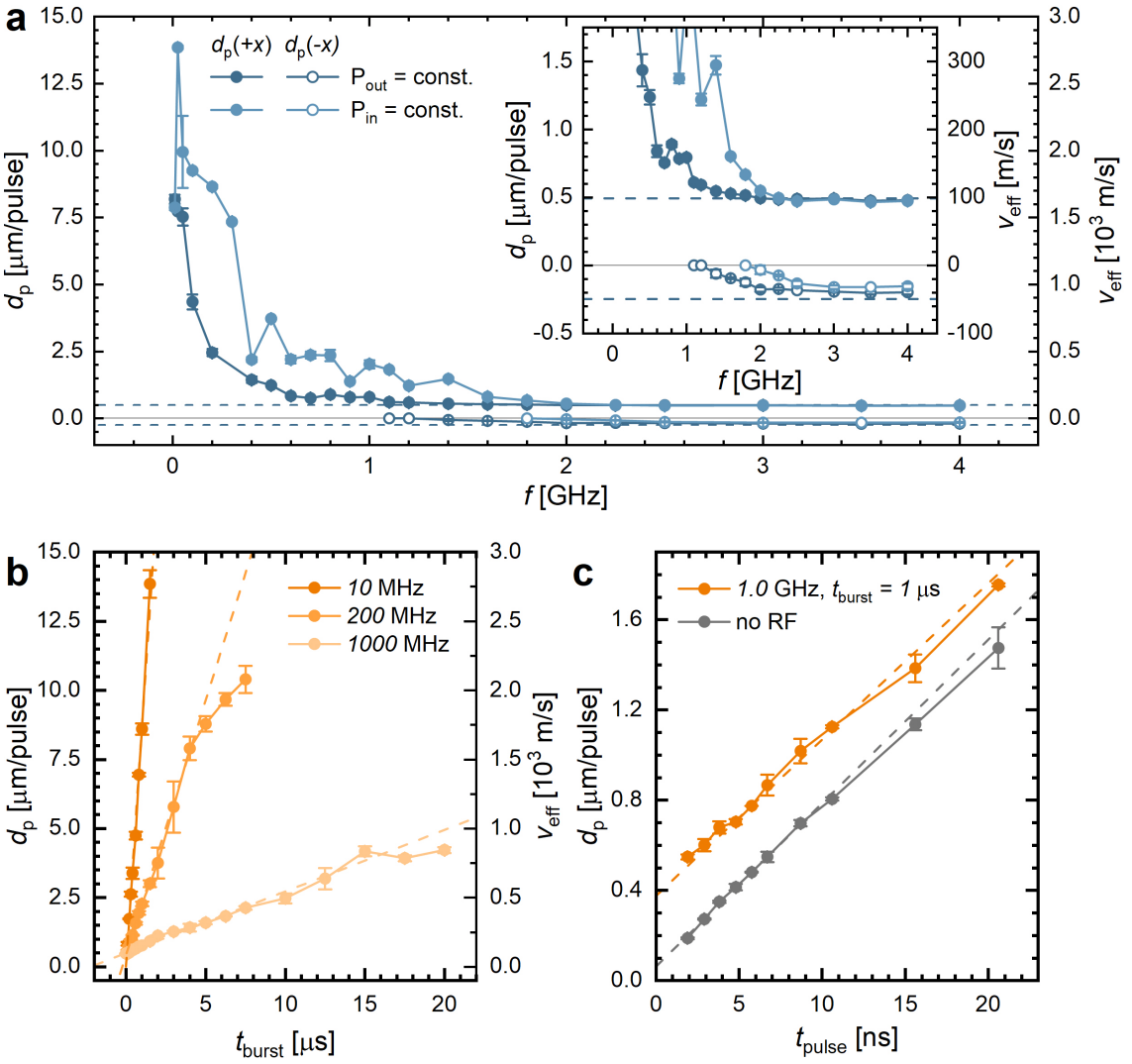

Figure 5.15: **Frequency- and time-dependence of the DW rectification.** Electrical current pulses with current density $j = 162$ MA/cm² ns cause the displacement d_p of a magnetic DW. The latter is also indicated as an effective velocity v_{eff}. In addition to the current pulses, a static transverse magnetic field $\mu_0 H_y = 50$ mT and an RF-current is present in all graphs. **(a)** Frequency dependence of the rectification of current-induced DW motion by the RF-current. A diverging DW displacement is found towards the lower frequency bound of 10 MHz. The comparison between constant input RF-power $P_{RF}^{in} \approx +15$ dBm and constant output power $P_{RF}^{out} = +2$ dBm is shown. These two power modes are identical at the reference point of 10 MHz. The inset in **(a)** shows a weak local maximum in d_p at $f \approx 0.8$ GHz (when looking at the $P_{RF}^{out} = const.$ curve). RF-bursts with $t_{burst} = 1$ µs are used in **(a,c)**. In **(a,b)**, current pulses with $t_p = 5$ ns are used. **(b)** Burst-time dependence of d_p for a positive current pulse. The linear increase with t_{burst} shows the stable self-propulsion of the DW under the action of the RF-current. In both **(b)** and **(c)** a constant transmitted RF-power $P_{RF}^{out} = +2$ dBm is used. **(c)** Pulse-time dependence of the electrical current pulses to initiate the DW displacement d_p. The linear slope corresponds to the DW speed due to the SOT-driven DW motion. The slope remains unchanged in presence of RF-currents that cause the self-propulsion of the DW but instead d_p is vertically displaced.

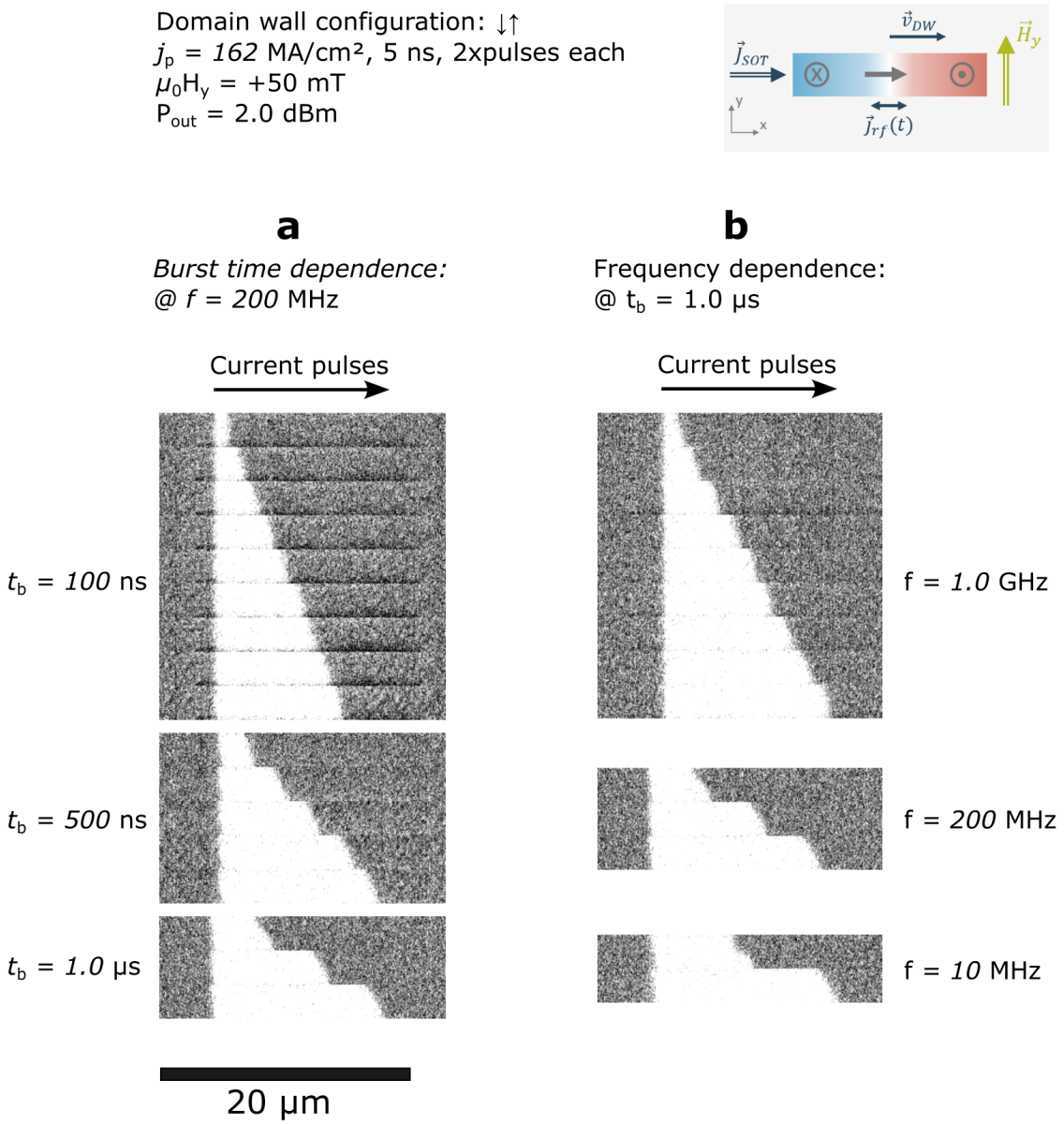

Figure 5.16: **DW motion in the presence of a static H_y field and electrical RF-currents.** Subsequent snapshots of the differential Kerr image showing the current-induced DW propagation along the electrical current flow are recorded in various configurations. White contrast indicates that the ↓↑ DW is moving to the right. The same experimental settings were used as in Fig. 5.15a-b and the $P_{RF}^{out} = const.$ power mode was applied. **(a)** The left column shows the burst time dependence of d_p according to 5.15b. **(b)** The right column shows the frequency dependence of d_p according to 5.15a.

5.2.3 Discussion of the origin of self-propulsion during RF-current application

The frequency-dependence of a DW's self-propulsion is significantly different in the presence of an RF-current (cf. Fig. 5.15a) or an RF-field (cf. Figs. 5.5a, 5.6a). To understand the underlying physics, the key differences between the RF-currents and RF-fields need to be pointed out. The LLG equation (2.32a) and the collective coordinate model (eq. (2.33)) in the theory chapter 2.3.4 clearly show that a magnetic field acts on the magnetization mainly as a field-like torque whereas an electrical current mainly induces a damping-like spin-orbit torque (DL-SOT). A magnetic field and a current-induced DL-SOT are fundamentally different as seen from DW motion: A static magnetic field along $-y$, i.e. transverse to the magnetic conduit, slightly tilts the DW but does not lead to an ongoing motion (cf. eqs. (2.18a), (2.18b)). In contrast, a DL-SOT along $-y$ leads to highly efficient and fast DW motion [7, 9, 10, 13]. For completeness, it should be noted that an electrical current induces an FL-SOT here as well, despite being weaker than the DL-SOT in the considered Pt/Co system [59, 62]. Moreover, the RF current flowing through the conduit, i.e. the Pt/Co/Ni/Co multilayer, induces an Oersted RF magnetic field at the FM. Therefore, a weak effective RF *magnetic field* is acting on the DW here as well. Nevertheless, the following interpretation of the data relies on the (supposedly stronger) impact of the DL-SOT.

In analogy to the directional DW motion that is induced by a (DC) current pulse, a time-varying (RF) current causes the DW to oscillate back and forth. However, the current-induced DW motion by SOT is symmetric with respect to the current polarity and the RF-current is sinusoidally varying in time. This would cause a periodic DW oscillation but does not lead to a net DW motion. This situation changes in the presence of a transverse magnetic field H_y. As shown theoretically in chapter 2.3.4 and experimentally in Figs. 5.4, 5.14b, the DW motion becomes asymmetric in presence of H_y. A sinusoidal RF-current $j_\mathrm{rf}(t)$ in a positive H_y field would consequently cause a larger DW displacement along $+x$ while $j_\mathrm{rf}(t) > 0$ than along $-x$ while $j_\mathrm{rf}(t) < 0$. The DW will consequently oscillate back and forth with a net motion along $+x$. In other words, the H_y field *rectifies* an RF-driven DW oscillation. This theoretical reasoning matches nicely with the experimental findings in this section. Nevertheless, two questions arise in regard to this theory. First, the electrical current density of the RF-current appears to be much below the threshold current density observed in Fig. 5.14a. Secondly, the theory does not predict any dependence of the rectified DW motion on the frequency of the RF-current. In the following, these two questions are addressed in detail:

The threshold current-density for DW motion in Fig. 5.14a reads as $j_\mathrm{th} \approx 40$ MA/cm² in zero field. For $\mu_0 H_\mathrm{y} = 50$ mT, this changes to $j_{\mathrm{th},+\mathrm{x}} \approx 28$ MA/cm² and $|j_{\mathrm{th},-\mathrm{x}}| \approx 91$ MA/cm². Considering the transmitted RF-power $P_\mathrm{trans} = +2$ dBm $= const.$ through the magnetic conduit, this amounts to an RF-current density $j_\mathrm{rf} = 7.9$ MA/cm² which is well below $j_{\mathrm{th},+\mathrm{x}}$. It has already been discussed in section 5.1.4, however, that the total power at the magnetic conduit is not given exclusively by the transmitted power P_trans but also a large fraction of the input power is dissipated at the conduit. This dissipated power P_diss

might arise due to ohmic losses of the RF-current at the conduit. When an RF signal propagates along the conduit, it is attenuated along the conduit's length, mostly due to ohmic losses. The local electrical current density along the conduit thus needs to take a fraction of this dissipated power P_{diss} into account, in addition to P_{trans}. Despite the difficulty of determining the exact current density, a lower and upper bound as well as an intermediate value of j_{rf} are presented in table 5.2. While the lower (upper) bound of j_{rf} assume that 0% (100%) of P_{diss} contributes to j_{rf}, the intermediate estimate assumes a fraction of 50% of P_{diss}. Using this intermediate estimate, j_{rf} increases to 22.2 MA/cm² and is already close to $j_{\mathrm{th},+\mathrm{x}} \approx 28$ MA/cm².

Estimation	**Formula**	j_{rf} [MA/cm²]
Upper bound	$P_{\mathrm{dev}} = P_{\mathrm{trans}} + P_{\mathrm{diss}}$	30.4
Intermediate estimate	$P_{\mathrm{dev}} = P_{\mathrm{trans}} + 0.5 \cdot P_{\mathrm{diss}}$	22.2
Lower bound	$P_{\mathrm{dev}} = P_{\mathrm{trans}}$	7.9

Table 5.2: **Estimate of the RF current density in the magnetic conduit.** The j_{rf} calculation for the upper bound and the realistic estimate are based on the VNA data in Fig. 5.13 that are generally frequency dependent. The dissipated power is calculated using P_{diss} = P_{in} - P_{refl} - P_{trans}. The indicated value for j_{rf} is based on the respective calculation formula for P_{dev} and uses the average between 10 MHz and 4.0 GHz, i.e. the region frequency region that was previously investigated.

Furthermore, when comparing threshold values j_{th} for DW motion, the respective timescale of the current application needs to be taken into account. In general, j_{th} varies with the current pulse length and typically exhibits at least two different scaling regimes [19, 97–100]. For short timescales in the order of nanoseconds, j_{th} scales with $1/t_{\mathrm{pulse}}$. But for microsecond or millisecond-long times, j_{th} decreases logarithmically due to the thermal-assistance to the DW motion. Fig. 5.17 shows the measured decrease of j_{th} with t_{pulse}. Fits to the short and long t_{pulse} regime are indicated by dashed lines. The threshold current density monotonously decreases from $j_{\mathrm{th}} = 57$ MA/cm² at $t_{\mathrm{pulse}} = 1.7$ ns to $j_{\mathrm{th}} = 3.6$ MA/cm² at $t_{\mathrm{pulse}} = 1.0$ µs. As a reference, the range of approximate RF-current densities j_{rf} from table 5.2 is indicated by an orange shading. The data shows that this range of j_{rf} is below j_{th} for $t_{\mathrm{pulse}} \leq 20$ ns but above j_{th} for $t_{\mathrm{pulse}} \geq 10$ µs. The crossing point has a large uncertaintly due to the imprecise value of j_{rf}. Assuming the intermediate estimate $j_{\mathrm{rf}} = 22.2$ MA/cm² from table 5.2, the crossing point is close to $t_{\mathrm{pulse}} = 75$ ns. In order to compare this pulse time t_{pulse} with the frequency of an RF-current, it needs to be converted into an effective frequency $f = 1/(2t_{\mathrm{pulse}})$ as shown at the top axis. As a result, the crossing point of $t_{\mathrm{pulse}} \geq 75$ ns corresponds to a frequency of $f_{\mathrm{eff}} \leq 6.7$ MHz.

In conclusion, this estimate suggests that the RF-current is able to oscillate the DW for $f \leq 6.7$ MHz. This oscillation in the presence of an H_{y} field leads to a rectification of DW motion and would lead to self-propulsion. If the frequency is too high, however, the RF-current density is not sufficient with $j_{\mathrm{rf}} < j_{\mathrm{th}}$ and the DW does not move at all. Hence, the DW requires low frequencies, corresponding to long effective pulse widths, such that the RF-current density j_{rf} exceeds j_{th} and is sufficient to overcome the DW pinning and move

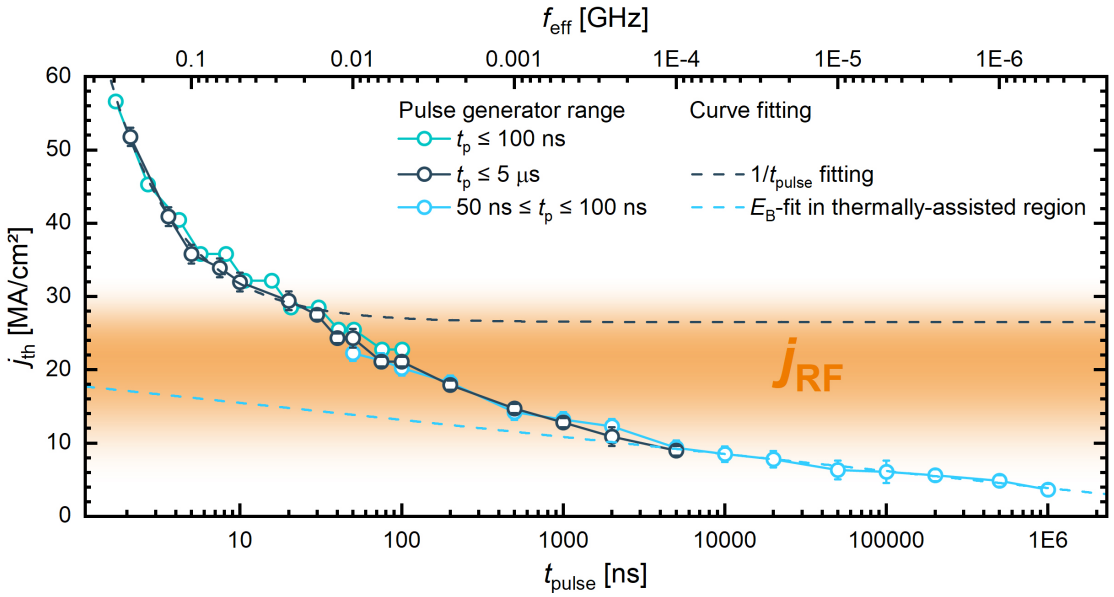

Figure 5.17: **Threshold current density for DW motion.** The required current-density for current-induced DW motion j_{th} monotonously decreases with increasing the pulse time t_{pulse}. Different pulse generators were used to cover longer t_{pulse} ranges. In the short time range with $t_{pulse} \leq 20$ ns, a $1/t_{pulse}$ fit applies (dark dashed line) while the equation $j_{th}(t_{pulse}) = j_{th,0}\left[1 - 1/\beta \cdot \ln(t_{pulse} f_0)\right]$ was fitted to the long pulse region (thermally assisted DW motion) [97] with $t_{pulse} \geq 5$ µs (bright dashed line). $f_0 = 10^{10}$ 1/s denotes the used attempt frequency and $\beta = E_B/(k_B T)$ is the thermal stability factor that is determined by the extrinsic energy barrier E_B for DW motion and the thermal energy $k_B T$. To compare the current pulses used here with RF-currents, the corresponding frequency $f = 1/(2t_{pulse})$ is indicated at the top axis. Moreover, the orange-shaded region marks the approximate current density of the RF-current that was applied in Fig. 5.15a for $P_{RF}^{out} = const.$.

the DW. Fig. 5.17 thus provides a *qualitative* explanation of the frequency-dependence in Fig. 5.15a, i.e. for the decrease in self-propulsion efficiency with increasing frequency.

Besides the previous explanation of the frequency dependence of self-propulsion, an additional qualitative understanding can be gained by considering the inertia of the DW. Due to its finite inertia, the DW requires a finite amount of time, typically up to a few nanoseconds, to accelerate and decelerate when subjected to a driving current [101, 102]. While this behavior is typically negligible under pulsed current excitation, it becomes critical in the case of RF currents, as employed here. If the oscillation period of the RF current becomes shorter than the characteristic acceleration/deceleration time of the DW, the DW can no longer follow the alternating drive effectively and thus remains largely immobile. This limitation by the DW's inertia provides a plausible explanation for the observed decrease in self-propulsion efficiency with increasing frequency. However, verifying this interpretation requires to quantify the acceleration and deceleration times of the DW in this specific system.

In addition to the monotonous decrease of d_p with increasing frequency in Fig. 5.15a, the inset of the figure shows a weak side maximum in $d_p(+x)$ between 0.8 GHz and 1.0 GHz. This maximum does not match with the previous explanation of the self-propulsion, but matches quite well with the maximum observed in the SNS-MOKE mea-

surements on a similar sample in Fig. 4.5f. Despite the weak signature of the side maximum, the excitation of a *resonant* DW excitation between 0.8 GHz and 1.0 GHz cannot therefore be disregarded.

Lastly, RF-current induced Joule heating of the conduit is shown in Fig. 5.18. A constant output power $P_{\mathrm{RF}}^{\mathrm{out}} = +2$ dBm $= const.$ which was previously used in Fig. 5.15 corresponds to a temperature increase of approximately 19 K, 14 K and 12 K for 10 MHz, 200 MHz and 1000 MHz, respectively (see orange dashed line in Fig. 5.18). This heating decreases with increasing frequencies and correlates with the decrease in d_{p} with frequency in Fig. 5.15a. Therefore, a thermal contribution to the self-propulsion cannot be fully disregarded. However, it seems unlikely that this temperature increase of only 20 K fully accounts for the self-propulsion of the DW since the latter is usually stable under such moderate temperature increases.

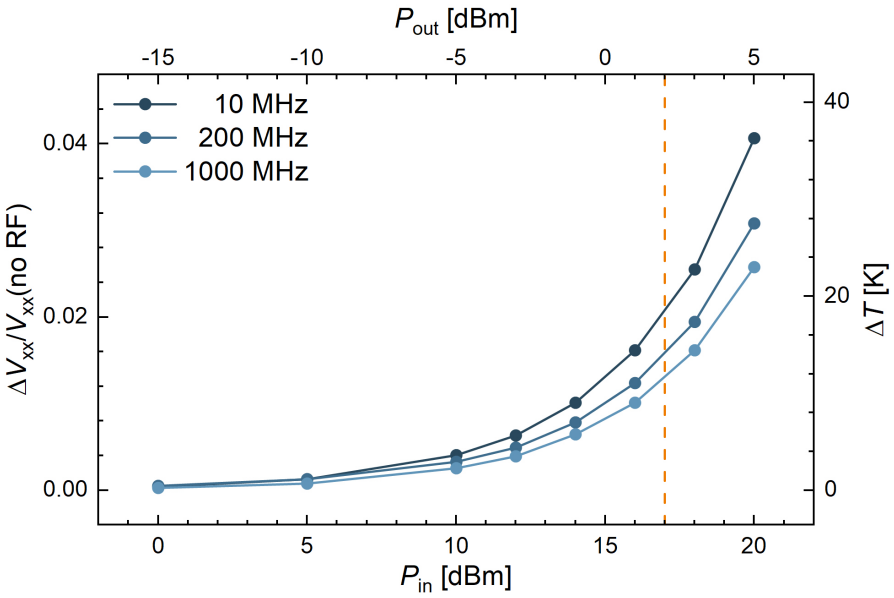

Figure 5.18: **Conduit heating due to dissipation of RF-power.** At ambient room-temperature, the R_{xx} of the conduit increases with increasing RF power through the magnetic conduit. The temperature coefficient of resistance, determined in Fig. 5.11a, allows to translate the resistance increase into a temperature increase ΔT_{eff}. Microwaves at frequencies of 10 MHz, 200 MHz and 1000 MHz are applied and the top axis displays the transmitted RF-power. Note that the RF transmission S_{21} is approximately equal for all frequencies. The orange dashed line indicates the constant output power of +2 dBm that was mainly used in Fig. 5.15.

In summary, the present chapter demonstrated the self-propulsion of a magnetic DW, i.e. the unidirectional motion in the presence of a symmetric RF-excitation. Self-propulsion by either an RF-magnetic field or an RF-current have been demonstrated. Herein, the symmetry-breaking static field H_y determines the directionality of self-propulsion. While the self-propulsion by an RF-field occurs only at resonant frequencies, the effect of an RF-current is largest at low frequencies and does not exhibit a clear resonance. By confirming the linear increase of the DW displacement with the RF burst time t_burst, the independence of the self-propulsion from the previous SOT pulse is confirmed and the velocity during self-propulsion was determined to be of the order of a few meters per second. While the microscopic mechanism of self-propulsion has not yet been fully determined, these results suggest a complex interplay of (a) RF magnetic fields, (b) RF electrical currents, (c) a symmetry-breaking magnetic field H_y, (d) the influence of a DW resonance and (e) temperature-assistance by heating.

To comprehend the DW's response to an RF-excitation even further, the magnetic field configuration will be adjusted next. Instead of applying a static transverse field H_y that breaks the symmetry of DW motion along $+x$ and $-x$, a static longitudinal field H_x will be applied in the next chapter.

Chapter 6

Sustained RF-driven domain wall motion after ultrashort current trigger

6.1 Measurement setup

This chapter uses the same magnetic thin films as in the sections 4 and 5.1, i.e. the following stack was used: 20 TaN / 50 Pt / 1 Ta / 3 Co / [7 Ni / 3 Co]$_{N=1}$ / 30 TaN (the numbers indicate the thickness in Å) with an interfacial Tantalum thickness of $d_{Ta} = 1.0$ Å. The same device as in chapter 5.1 is used here, i.e. a CPW is used to generate an RF magnetic field at the magnetic conduit while the DW is simultaneously driven by an electrical current pulse (device design A, chapter 3.2). However, the orientation of the static magnetic field is different here: While the effect of a *transverse* field H_y was previously discussed, this section focuses on the interaction of an RF field with a magnetic DW when a *longitudinal* field H_x is applied.

The effect of a static H_x field on the current-induced DW motion is described in section 2.3.4. Due to the finite DMI of the magnetic system, the DWs are chiral Néel walls, i.e. their equilibrium magnetization is aligned along $\pm x$ and the rotation of the magnetization along the DW has a fixed chirality. The effective DMI magnetic field H_{DMI} points along $-x$ ($+x$) for an $\uparrow\downarrow$ ($\downarrow\uparrow$) DW and determines the DW's equilibrium IP magnetization. When an external H_x field is applied along (opposite to) H_{DMI}, this will result in an increased (decreased) DW displacement d_p during current-induced DW motion [10]. When H_x is oriented opposite to H_{DMI} and exceeds its magnitude, the DWs now move along the electron flow instead of the current flow, i.e. d_p reverses sign. Note that in contrast to the H_y field, the H_x field does not break the symmetry of DW motion, i.e. the DW motion is symmetric and there exists no preferential direction. For instance, a current pulse with positive polarity will move the DW by a distance d_p^+ and a pulse with negative polarity will move the DW by d_p^- with $|d_p^-| = |d_p^+|$.

Now, the combined effects of an initial SOT-pulse and an RF-burst on the DW motion will be investigated. The initial current pulse that exerts an SOT is typically a few nanoseconds long and initiates the DW motion. The RF-burst then lasts for up to a few microseconds and is chosen to start already a few tens of nanoseconds before the current

pulse. This is due to the technical limitations of the timing precision between both pulse and burst. The electronic circuitry is explained in section 3.3.2 and seen in Fig. 3.13a.

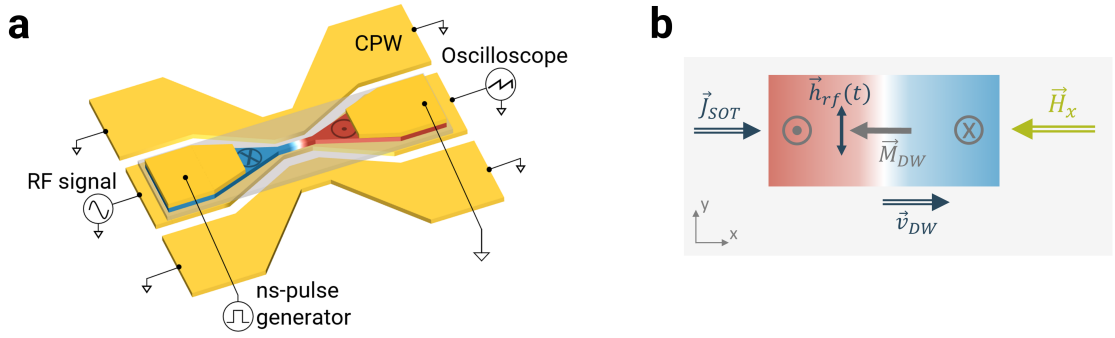

Figure 6.1: **Schematic of device geometry and measurement configuration using an RF-field and a longitudinal static field H_x. (a)** Schematic of the device geometry and electrical connections used in the DW motion measurements using the device design A. **(b)** Schematic illustration of the magnetic fields and currents acting on the magnetic DW.

6.2 Sustained DW motion

Figure 6.2a shows the current-density dependent displacement $d_p(j)$ for an ↑↓ DW with $\mu_0 H_x = -12$ mT that is applied along the H_{DMI} of the DW. In the absence of RF-fields and for off-resonant RF-fields ($f = 100$ MHz, $f = 1.0$ GHz) the results are similar and shows DW motion with increased speed compared to the zero-field case (open, gray symbols). Note that the DW motion is symmetric, i.e. $d_p^+ = |d_p^-|$, as explained earlier. However, as soon as the current-density of the pulse exceeds a certain threshold value of $j \geq 94$ MA/cm², the current-induced DW displacement d_p is significantly enhanced by a resonant RF-field at $f = 450$ MHz. Note that this enhanced DW displacement is still symmetric, i.e. d_p^+ and $|d_p^-|$ are almost equally increased. This RF-enhancement saturates for $|j| \geq 118$ MA/cm². Differential Kerr images of these effects are given in Fig. 6.4 at the end of this section.

However, the resonant RF-induced enhancement of d_p does not occur for $H_x = 0$, as seen in the H_x-field dependence of d_p in Fig. 6.2b. Without resonant microwaves present, $|d_p|$ is linearly proportional to H_x as theoretically expected. The crossing field where d_p reverses sign corresponds to $\mu_0 H_x = 20$ mT $= -\mu_0 H_{DMI}$ for the measured ↑↓ DW. When resonant microwaves at $f = 450$ MHz are applied, $|d_p|$ exhibits a significant increase once $\mu_0 H_x < -4$ mT. This shows that a threshold H_x field is also required to achieve RF-enhanced DW motion, alongside with the threshold in the current density j.

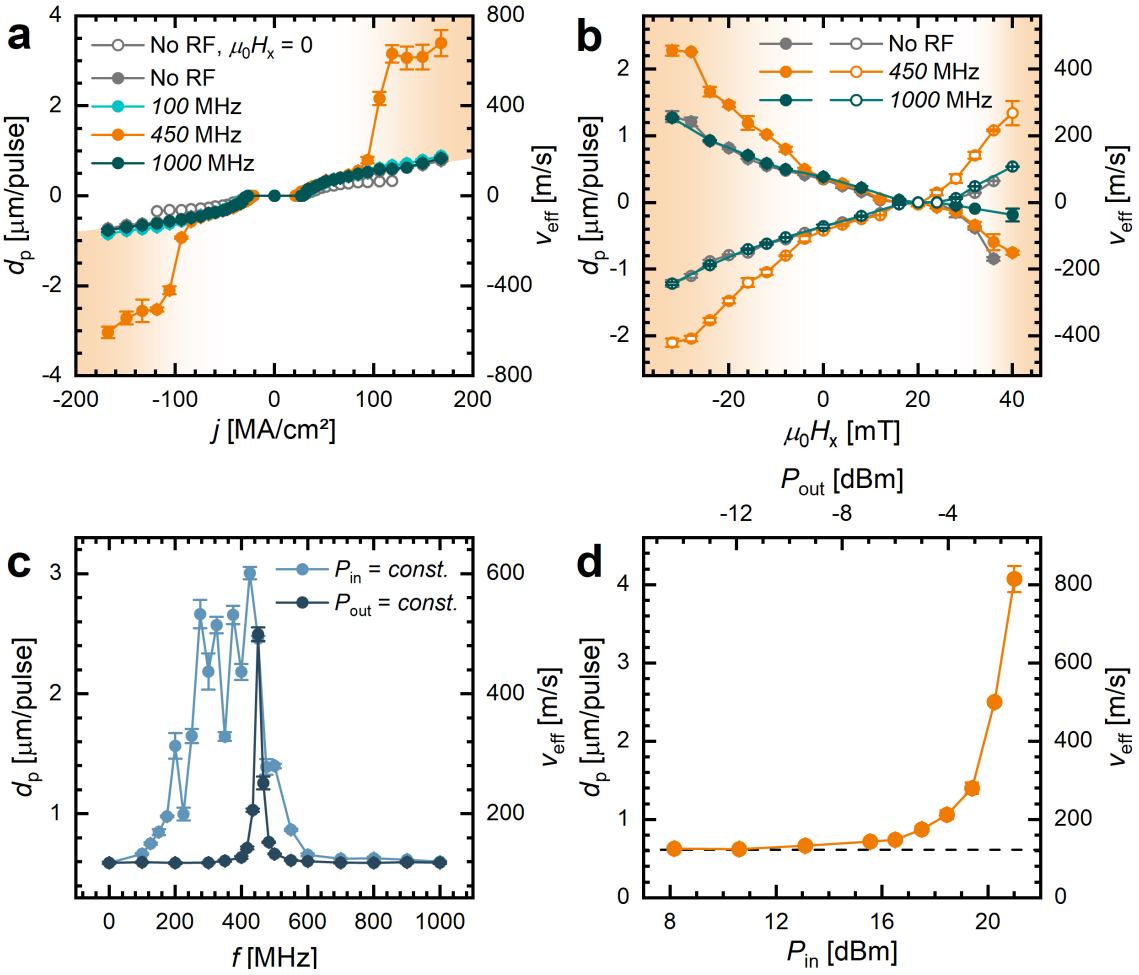

Figure 6.2: **Symmetrically enhanced DW displacement by the combined action of a resonant RF-field and a static H_x field.** Current-induced DW motion is measured in the presence of an H_x field and RF-fields. Current pulses with $t_{pulse} = 5$ ns are applied at the beginning of an RF burst. (**a**) d_p vs. j for $\mu_0 H_x = -12$ mT and $t_{burst} = 5$ µs. Only for the resonant frequency of 450 MHz, the DW displacement significantly exceeds its normal value, i.e. its value in the absence of RF-fields. For this enhancement, a threshold current density of $|j| = 94$ MA/cm² has to be surpassed. The effect saturates for $|j| \geq 118$ MA/cm². In (**a-b**), an RF power $P_{RF}^{in} = 21.6$ dBm is applied at all frequencies. This corresponds to a transmitted power of $P_{RF}^{out}(f = 450\ \text{MHz}) \approx -2$ dBm. (**b**) d_p vs. H_x at $j = 118$ MA/cm² and $t_{burst} = 1$ µs. The filled (open) symbols represent the DW displacement due to a positive (negative) current pulse. The resonant enhancement of d_p arises only once a threshold field is exceeded, e.g. for $\mu_0 H_x < -4$ mT. (**c**) d_p vs. frequency at $\mu_0 H_x = -12$ mT and $j_p = 118$ MA/cm². RF bursts with $t_{burst} = 5$ µs were applied. Both curves for a constant input power ($P_{RF}^{in} = 21.6$ dBm) and a constant transmitted power ($P_{RF}^{out} = -2.2$ dBm) are shown. **(d)** Power dependence of the enhanced DW displacement for $f = 450$ MHz and $t_{burst} = 5$µs. Current pulses with $j_p = 118$ MA/cm² are applied and a static field $\mu_0 H_x = -12$ mT is present. The dashed, horizontal line shows the DW displacement without applied RF-field. The bottom (top) axis show the input (transmitted) RF-power through the CPW. The results for an ↑↓ DW are shown in all figures.

The frequency dependence of the RF-enhanced DW motion in Fig. 6.2c shows that the resonant enhancement of d_p only occurs within a narrow frequency window. While $d_\mathrm{p} \approx 0.59$ µm/pulse holds for off-resonant frequencies, a peak value of $|d_\mathrm{p}| = 2.50(6)$ µm/pulse is achieved at $f = 450$ MHz when the transmitted RF-power $P_\mathrm{RF}^\mathrm{out}$ is kept constant (dark blue data). The resonance for constant $P_\mathrm{RF}^\mathrm{out}$ is very narrow and maximum at $f = 450$. In contrast, when the input RF-power $P_\mathrm{RF}^\mathrm{in}$ is kept constant (light blue data), the d_p enhancement occurs in a much broader frequency range but the data points are significantly more scattered at the resonance. The shape of these resonances is qualitatively in good agreement with the resonances for self-propulsion in Fig. 5.6a. These differences between the different power modes have extensively been discussed in section 5.1.4. This suggests that a similar underlying mechanism, i.e. an RF-induced torque, that induces self-propulsion when an H_y-field is applied, is also involved in the symmetrically enhanced DW displacement with H_x-field.

RF-bursts with well-defined durations are applied in the range 100 ns $< t_\mathrm{burst} <$ 15 µs to precisely gauge the RF-effect on the DW displacement. By adjusting the timing between nanosecond-long current pulse and RF-burst, it was observed that arbitrarily long RF-bursts *before* the arrival of the current pulse have no effect on the DW motion. However, the burst duration *after* the current pulse enhances the DW displacement. Because of this, t_burst corresponds to the burst time *after* an initial current pulse. d_p increases linearly with t_burst as shown in Figs. 6.3a, 6.4d. Both the timing and the duration of the RF-burst are thus crucial. This suggests that the current pulse initiates the current-induced DW motion and that this motion is subsequently ongoing in the presence of the RF excitation - though at slower speed. This ongoing DW motion after the end of the current pulse will be called *sustained* DW motion in the following. The linear fit in Fig. 6.3a yields the effective DW velocity arising from the RF field as $v_\mathrm{RF} = 0.41(2)$ m/s. Note that in addition to t_burst, the applied RF-power also effects the magnitude of the RF-induced displacement (see Fig. 6.2d).

In order to trigger this sustained DW motion, a sufficiently long current pulse is required. Fig. 6.3b shows the dependence of d_p on the current pulse duration t_pulse. As expected, d_p increases linearly with t_pulse when no RF-field is applied (teal-colored data). The linear slope corresponds to the speed of SOT-driven DW motion. However, in the presence of an RF-field (orange-colored data), d_p starts to increase and deviates from this linear slope as soon as current pulses with $t_\mathrm{pulse} > 3.5$ ns are applied. For $t_\mathrm{pulse} > 5$ ns, this increase saturates and d_p scales linearly with t_pulse again (cf. orange dashed lines). The vertical data offset is ascribed to the RF-induced sustained motion. This behavior is qualitatively equal for different burst times, but the vertical displacement d_RF increases with t_burst as expected from Fig. 6.3a.

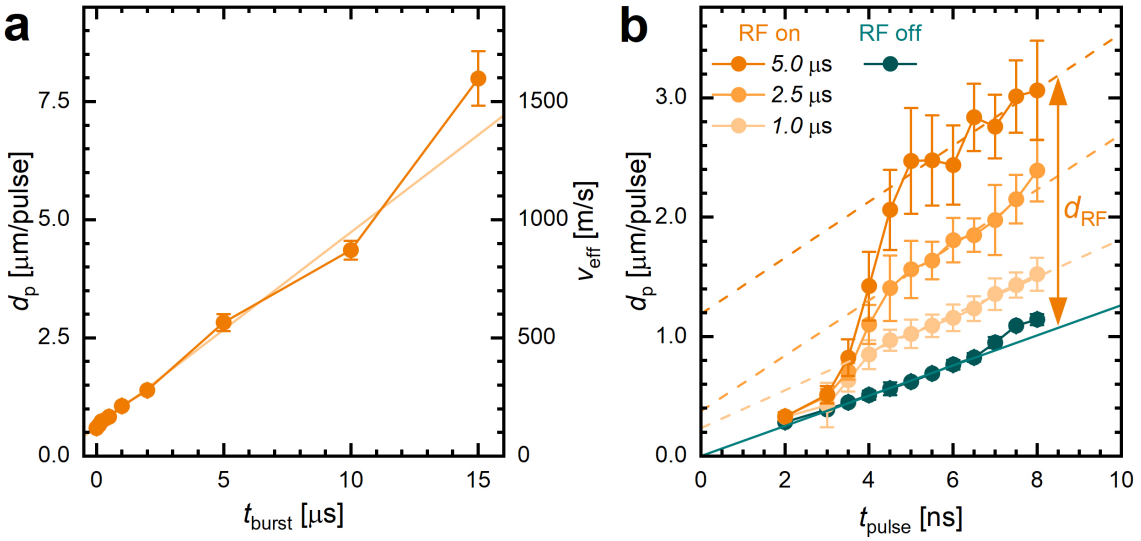

Figure 6.3: **Self-sustained domain wall propagation.** The mean absolute displacement $|d_p|$ of an $\uparrow\downarrow$ DW is measured using an initial trigger pulse with $j_p = \pm 118$ MA/cm² while a longitudinal magnetic field $\mu_0 H_x = -12$ mT is present. A resonant RF-field at $f = 450$ MHz is applied with a burst time t_{burst} *after* an initial current pulse trigger with duration t_{pulse}. (**a**) t_{burst} dependence of the sustained DW motion. The trigger pulse width amounts to $t_{pulse} = 5$ ns. The DW displacement increases linearly as shown by the linear fit. (**b**) The t_{pulse} dependence of the RF-driven DW displacement is shown. Resonant microwaves with $t_{burst} = 1.0$, 2.5 and 5.0 µs are applied. At short t_{pulse}, no RF-driven DW motion is triggered whereas the additional RF-induced displacement d_{RF} saturates at $t_{pulse} > 5$ ns. Herein, t_{burst} determines the magnitude of the RF-induced displacement, i.e. the vertical shift of the curves. The dashed lines serve as guides to the eye and correspond to linear fits to the saturated region of the respective data. In (**a-b**), the RF power $P_{RF}^{out} \approx -2$ dBm transmits the CPW.

Finally, it needs to be stressed that this RF-enhanced DW displacement is not caused by a self-propulsion of the DW (cf. chapter 5). The term *self-propulsion* was defined as the ability of the DW to propagate by the action of a sinusoidal RF-field but without any applied current-pulses through the magnetic conduit. In contrast, the results in this chapter show an RF-enhanced DW displacement, but only in combination with a sufficiently strong current pulse through the conduit that initiates the DW motion and defines a preferential direction. Hence, the initial current pulse acts as a trigger to the sustained motion. Fig. 6.2a and Fig. 6.3b clearly show that the trigger pulse requires a threshold in the current-density j and pulse length t_{pulse} to initiate the sustained motion.

During self-propulsion, the polarity of the transverse field H_y determines the direction of motion. In contrast, the sustained motion discussed here follows the direction of the triggering current pulse. This behavior suggests that the DW's inertia and momentum play a key role to enable its sustained motion. Indeed, magnetic DWs have been shown to exhibit acceleration and deceleration times of the order of approximately 2 ns to 10 ns due to their finite inertia [101, 102]. For SOT-driven DW motion in FM with DMI, this inertia during deceleration mainly arises due to the relaxation of a DW tilt, i.e. the re-orientation of the DW magnetization and the DW tilt to their equilibrium values. Herein, the DMI strength is closely related to both the build-up of this DW tilt during steady-state

DW motion and the tilt relaxation [102]. By the end of the triggering current pulse, the DW has acquired a certain momentum and does not instantly, but gradually slow down its speed. During this time, the DW is still moving and the resonant RF-excitation seems to compensate for its energy dissipation by magnetic damping and extrinsic pinning, thereby sustaining its momentum. The low velocity of the DW during its sustained motion thus represents the balance between the DW's power dissipation during motion and the power by the RF-field that is pumped to the DW.

It needs to be addressed that the requirement of a finite longitudinal magnetic field H_x for the sustained DW motion is not explained by the previous reasoning. Neither does H_x break symmetry of the DW, nor does it directly lead to ongoing DW motion. However, it facilitates the initial DW acceleration that is required for the sustained motion. Moreover, H_x affects the DW tilt and additionally affects the magnetization dynamics in the LLG equations. Which of the aforementioned aspects are relevant to induce the sustained motion is currently unknown.

In conclusion, this chapter demonstrates that the motion of a magnetic DW can be sustained by the action of a resonant RF-field over very long times of up to 15 µs. The resonant RF-field here serves to re-supply power to the moving DW to compensate energy losses due to magnetic damping. Key requirements of the effect are (a) resonant frequencies of the RF-excitation, (b) a static, longitudinal magnetic field and (c) a sufficiently strong current pulse through the magnetic conduit. The latter is required to induce sufficient momentum to the DW and thereby trigger the subsequent sustained motion. It also serves to break the symmetry of the DW and induce a directional motion. The sustained DW motion consequently represents a counterpart to the self-propulsion in chapter 5. For the former, the initial current pulse determines the propagation direction while for the latter, the transverse field H_y does so.

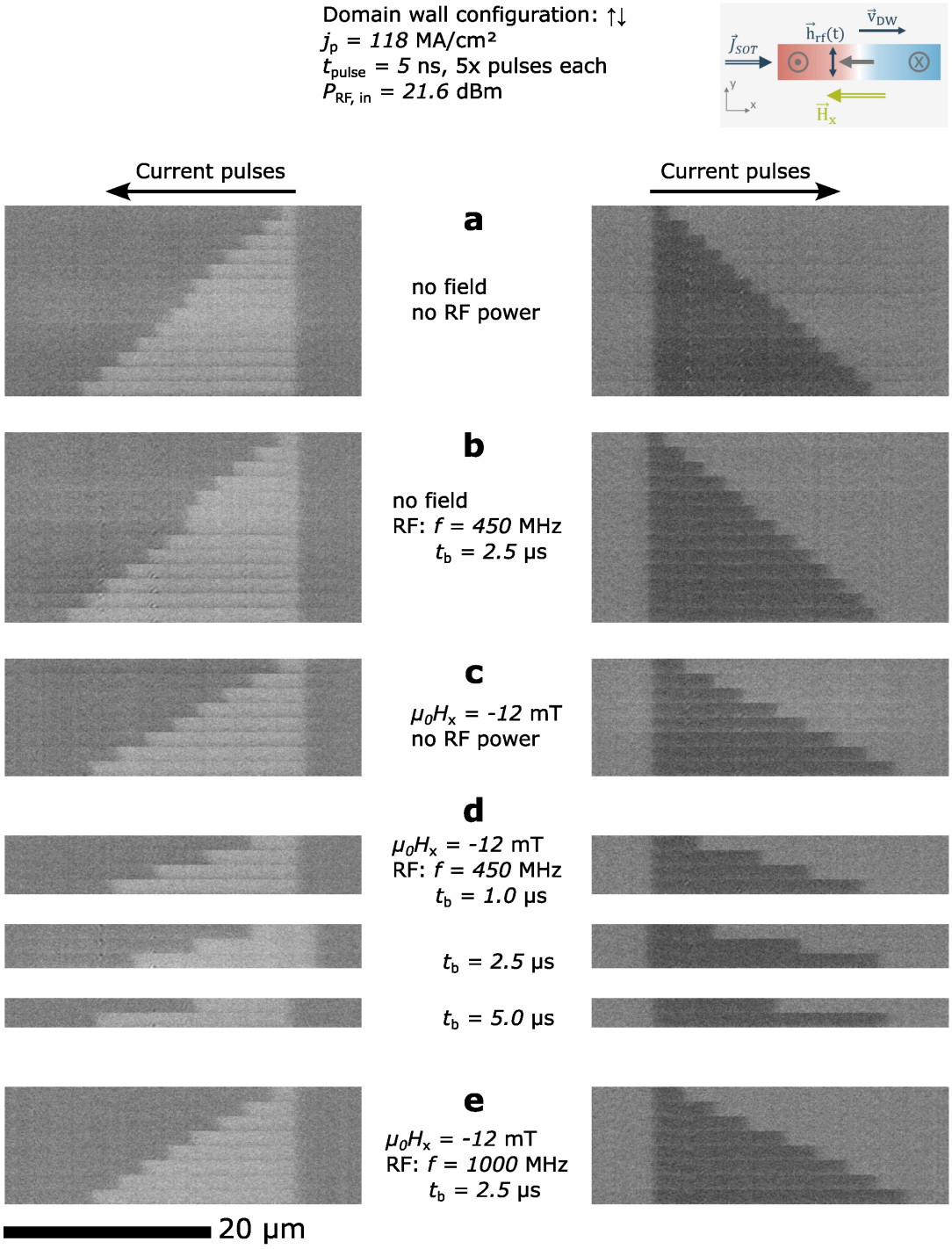

Figure 6.4: **DW motion in the presence of a static H_x fields and (off-)resonant RF fields.** Subsequent snapshots of the differential Kerr image, showing the current-induced DW propagation along the electrical current flow, are recorded in various configurations. White (black) contrast indicates that the up-down DW is moving to the left (right). A static, longitudinal H_x field is present during the measurement. (**a**) Zero static field and no RF-power. (**b**) Zero static field and resonant RF-bursts with $t_{burst} = 2.5$ µs. (**c**) $\mu_0 H_x = -12$ mT but no RF-power. (**d**) $\mu_0 H_x = -12$ mT and resonant RF-bursts are applied. The DW displacement per pulse increases with the burst time t_{burst}. (**e**) An off-resonant RF-field at $f = 1000$ MHz shows no enhanced DW motion at $\mu_0 H_x = -12$ mT compared to (**c**).

Part III

Microwave-assisted switching (MAS)

The previous part of this thesis investigated the dynamic excitation of magnetic DWs using RF magnetic fields and RF electrical currents. The DW's (resonant) susceptibility to an RF excitation enables phenomena such as the self-propulsion of the DW or the sustained DW motion after an initial current trigger.

Nevertheless, in addition to the importance of magnetic DW motion in proposed data storage devices such as racetrack memory [3], the magnetization switching is an essential aspect in both established and proposed spintronic applications. Magnetic HDDs and magnetic random access memory (MRAM) represent two major examples of such applications. Firstly, HDDs are ubiquitous in modern mass data storage and they use a local magnetic field for the reversal of magnetic bits [1]. Secondly, MRAM is made out of magnetic tunnel junctions where the current induced STT or SOT is used to switch the magnetization [4, 103, 104].

In order to achieve both a high thermal stability and a low switching energy of the magnetic element, the concept of microwave-assisted switching (MAS) was developed [21, 22, 66]. The latter uses a microwave excitation of the magnetic element to reduce the required switching power, e.g. by reducing the switching field or the switching current (see chapter 2.4.2 for the theory of MAS).

In the following, MAS will be discussed for two different switching configurations. Firstly, microwave-assisted SOT switching will be demonstrated in the same ultra-thin magnetic layers that were previously studied for DW motion. Interestingly, this switching assistance is related to the DW resonance and *not* to the FMR mode as for conventional MAS. Secondly, MAS will be presented for field-induced switching where the FMR mode or close-by standing spin-wave modes are excited. Herein, thicker FM multilayers are used to match the FMR frequency to the easily accessible frequency range of the experiment. Furthermore, a comparison of MAS by RF magnetic fields and RF electrical currents will be provided. Finally, a $\sim$100% reduction of the switching field by MAS and the corresponding destabilization of the magnetic state will be demonstrated.

Chapter 7

Microwave-assisted spin-orbit torque switching

7.1 Conventional SOT switching

It has been theoretically outlined in chapter 2.4.3 that current-induced SOT switching requires a static H_x field and a damping-like SOT. For small FMs with a spatial extension below the single-domain critical diameter [25], a multi-domain state is unfavorable and their switching may be described by a macrospin description. However, the switching of micron-sized magnets, that may host multiple domains, is investigated here. Their switching can occur incoherently by domain nucleation and expansion which is schematically displayed in Figs. 7.1a-e:

The magnetic conduit is initially saturated along $-z$ (Fig. 7.1a). Due to the finite DMI, the magnetization at the edges tilts away from the conduit (little gray arrows) [68]. When both H_x and an SOT current pulse are applied, a region with $+z$ magnetization is nucleated at one of the edges which will be named a magnetic *bubble* from now on. This nucleation is asymmetric and preferentially appears at the lower (upper) edge when starting with an initial magnetization along $-z$ ($+z$). Such asymmetric nucleation behavior is typical for systems with finite DMI and has been observed for both field-switching [68] and SOT switching [80]. In Fig. 7.1b, the nucleation appears at the lower edge since the current-induced SOT and the DMI-induced magnetization tilting at the edge are parallel to each other at the bottom edge, thereby favoring the bubble formation [80]. Once the bubble is formed, it expands due to the SOT-driven motion of the bubble DWs (Fig. 7.1c-d). This expansion is generally asymmetric due to the different impact of H_x on the left and right bubble DW. Finally, the bubble's DWs have expanded throughout the full conduit and the switching is complete (Fig. 7.1e). In summary, the SOT switching in extended magnetic structures is mostly a two-step process and composes of bubble nucleation and subsequent expansion.

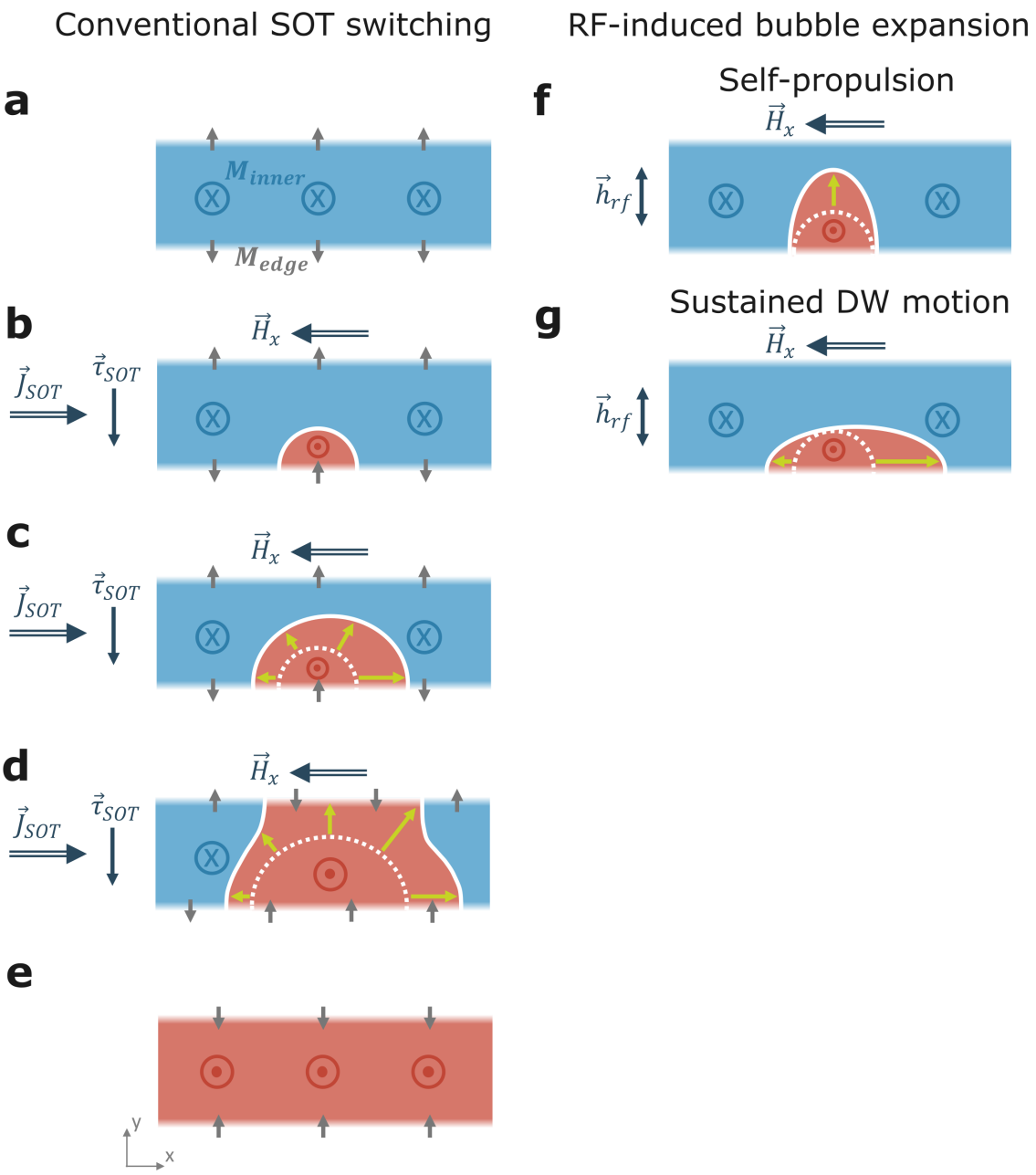

Figure 7.1: **Schematic of conventional and RF-assisted SOT switching. (a-e)** Conventional SOT switching sequence (chronologically ordered from top to bottom): Starting from a down-magnetized state **(a)**, the application of a longitudinal H_x field and an electrical current J_{SOT} (and the corresponding torque τ_{SOT}) leads to the nucleation of an up-magnetized bubble at the bottom edge **(b)**. This bubble expands due to the SOT τ_{SOT} **(c-d)** until finally the magnetic conduit is fully magnetized along $+z$ **(e)**. The green arrows indicate the expansion of the bubble compared to the previous image. Note that the magnetization at the edge (grey arrows) is tilted from the inner magnetization (blue or red areas) due to the DMI. The effects of an RF magnetic field h_{rf} on the bubble expansion is schematically shown in the following: **(f)** The presence of H_x breaks the symmetry of the upper part of the bubble. In line with chapter 5, this generally allows for self-propulsion of this part such that the bubble expands along $+y$. **(g)** After the end of a sufficiently strong SOT pulse, sustained DW motion (cf. chapter 6) enables the bubble to expand along $\pm x$. This expansion is asymmetric due to the combined or opposed action of H_x and the effective DMI field at the left and right bubble walls.

7.2 Measurement setup

This chapter uses the same magnetic film and device design as in the chapters 4, 5.1 and 6. The following film stack is used: 20 TaN / 50 Pt / 1 Ta / 3 Co / [7 Ni / 3 Co]$_{N=1}$ / 30 TaN (the numbers indicate the thickness in Å) with an interfacial Tantalum thickness of $d_{Ta} = 1.0$ Å. This allows to apply an RF-magnetic field while simultaneously passing an electrical current pulse through the magnetic conduit (Fig. 6.1a). In addition, a static, longitudinal magnetic field H_x is applied to enable deterministic SOT switching. This device geometry thus allows to investigate the impact of an RF magnetic field on SOT switching. In contrast to the previous chapters, the magnetic conduit is initially fully saturated, i.e. it hosts no magnetic DWs.

The switching is initiated by an electrical current pulse with adjustable pulse length 2 ns $\leq t_{pulse} \leq$ 100 ns. Starting almost synchronously with the current pulse, an RF burst with length t_{burst} is applied to the CPW. The switching is considered successful if a significant part of the 3×30 µm^2 magnetic conduit reverses its magnetic orientation. Note that the pulse generator that is used here to send the SOT pulses to the magnetic conduit, only allows for discrete current densities of the pulse. As will be seen in the experimental results of the following section, this leads to step-like changes of the switching current density j_{sw} and is a purely technical artifact.

Because SOT switching is often a two-step process, an incomplete switching may occur if the SOT pulse is too short or if H_x is too small, i.e. a magnetic bubble has nucleated but it has not yet expanded throughout the sample. Hence, two switching regimes will be differentiated experimentally: In the first regime, a complete switching occurs after passing a *single* current pulse through the magnetic conduit. In the second regime, although no switching is visible after a single pulse, *multiple* pulses eventually lead to a successful switching. A waiting time of typically 100 ms or more is chosen between subsequent current pulses to reduce Joule heating.

In line with the previous elaborations on the two-step nature of SOT switching, the switching by multiple pulses most likely originates from the fact that the initial current pulse successfully nucleates bubbles, but is too short to fully expand them. Consequently, multiple current pulses are required to complete the bubble expansion, i.e. switch the whole sample. Note that the switching is detected by an optical Kerr microscope whose resolution does not allow to detect tiny bubbles with nanometer size. It only allows to detect expanded bubbles once they grow to a size of ~ 1 µm. In conclusion, the measured threshold current density for successful SOT switching will thus differentiate between switching due to *single* and *multiple* pulses, where the latter situation exhibits a lower j_{sw} than the former one.

7.3 MAS by RF magnetic fields

This section investigates the SOT switching in the presence of RF magnetic fields. Based on the chapters 5 and 6, the magnetic DWs are significantly impacted by RF fields at frequencies around $f \sim 450$ MHz, whereas lower ($f = 100$ MHz) or higher ($f = 1000$ MHz) frequencies showed no effect on the DW. Since SOT switching is expected to involve the expansion of a magnetic bubble, i.e. the motion of the bubble's DWs, an RF-excitation of the DW is generally expected to impact the SOT switching.

Fig. 7.2a displays the H_x-dependence of the threshold current density j_{sw} for SOT switching. It was theoretically shown in section 2.4.3 that j_{sw} reduces linearly with H_x according to eq. (2.39). This linear j_{sw} decrease is seen in Fig. 7.2a when no RF-fields are applied (gray symbols). For single pulse switching (filled triangles), j_{sw} decreases from 210 MA/cm² at $\mu_0 H_x = 4$ mT to 149 MA/cm² at $\mu_0 H_x = 80$ mT. In contrast, for multiple pulse switching (open triangles), j_{sw} decreases from 210 MA/cm² to 67 MA/cm² in the same field range. The difference in j_{sw} between the two switching regimes suggests that the bubble nucleation takes place at lower current densities than the full bubble expansion into macroscopic regions.

When off-resonant RF-fields at a frequency $f = 1000$ MHz are applied (turquoise curves), j_{sw} is barely lowered. In contrast, j_{sw} significantly decreases for $f = 450$ MHz (orange curves). For instance, at $\mu_0 H_x = 12$ mT, the single pulse switching threshold decreases from $j_{sw} = 210$ MA/cm² when no RF-field is applied to $j_{sw} = 115$ MA/cm² when an RF-field at $f = 450$ MHz is applied. Interestingly, j_{sw} for both single and multiple pulse switching lie very close together now. The lowered j_{sw} for multiple pulses suggests that the bubble nucleation now occurs at lower current density. Moreover, the vicinity of the threshold for single and multiple pulses implies that the bubble expansion is facilitated and occurs at almost the same current density as the nucleation. In summary, the facilitation of the SOT switching by RF magnetic fields apparently occurs through a two-fold effect: Firstly, the RF-field assists the bubble nucleation and secondly, it aids its subsequent expansion. However it should be noted that the j_{sw} decrease with H_x is now non-linear and seems to converge towards a lower bound at $j_{sw} \approx 44$ MA/cm² for $H_x \geq 50$ mT. Hence, the RF-assisted switching deviates from of a linear j_{sw} decrease with H_x (eq. (2.39)) and implies that the conventional picture of SOT switching is not fully adequate anymore to describe the observed effects.

Note that very long RF-bursts with $t_{burst} = 100$ µs were applied in Fig. 7.2a. The RF-induced reduction of j_{sw} depends strongly on the duration t_{burst} of the applied RF-burst. Fig. 7.2c shows that the j_{sw} reduction sets in for $t_{burst} \geq 5$ µs and saturates for $t_{burst} \geq 20$ µs.

Fig. 7.2b displays the decrease of j_{sw} with the current pulse time t_{pulse}. Herein, a $1/t_{pulse}$ scaling of the switching threshold is usually expected for SOT switching in the short pulse regime [19]. However, such an $1/t_{pulse}$ scaling throughout the whole t_{pulse} range is only observed for the $f = 450$ MHz data (orange curve) as shown by the dashed

line. This can easily be seen in Fig. 7.2d, where j_{sw} is plotted against the inverse pulse time. Only the $f = 450$ MHz data fits a straight line while all other measurements change their slope at $t_{pulse} \approx 7.5$ ns so that a $1/t_{pulse}$ fit can only be applied for either short (≤ 7.5 ns) or long pulses (≥ 7.5 ns).

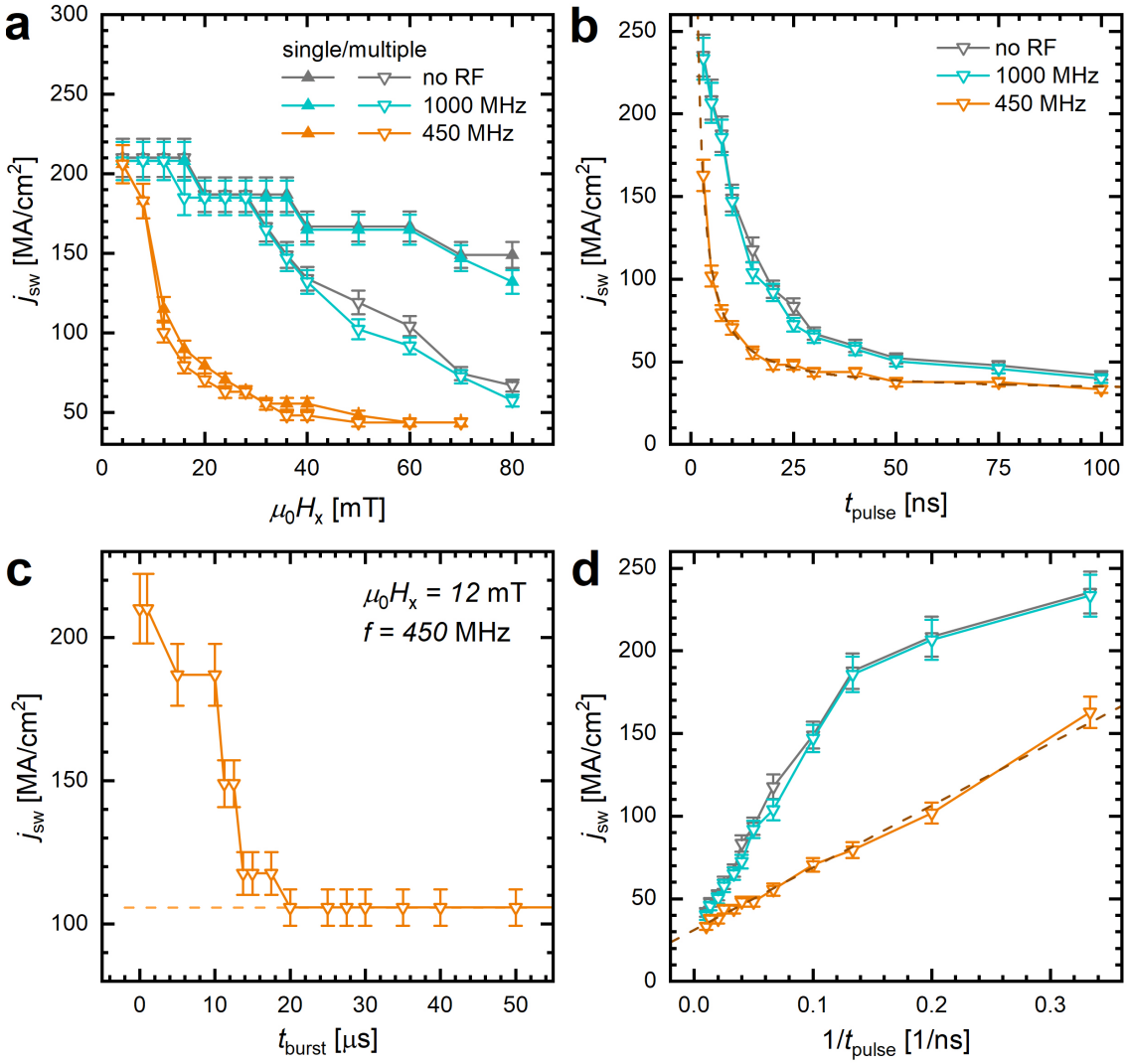

Figure 7.2: **Microwave-assisted SOT switching.** The current-induced magnetization reversal by SOT is investigated in the presence of RF magnetic fields at different frequencies. This graphs differentiates if SOT-switching was successful after a single current pulse (filled symbols) or if multiple pulses were required (open symbols). The electrical current density in the graphs exhibits clear steps and plateaus because of the discrete pulse amplitudes of the pulse generator. **(a)** Reduction of the switching threshold j_{sw} with H_x. In **(a), (b), (d)**, RF-bursts with $t_{burst} = 100$ µs were applied. **(c)** The RF-induced j_{sw} reduction requires the RF-burst to be sufficiently long. At $\mu_0 H_x = 12$ mT, the RF-enhanced switching effect sets in for $t_{burst} \geq 5$ µs and saturates for $t_{burst} \geq 20$ µs. Pulses with $t_{pulse} = 5$ ns were used in **(a, c)**. **(b)** Pulse time dependence of j_{sw} for $\mu_0 H_x = 12$ mT. The data for $f = 450$ MHz fits well to a $1/t_{pulse}$ function with constant offset throughout the t_{pulse} range (dashed line). **(d)** Plotting of j_{sw} vs. $1/t_{pulse}$ confirms that only the data for $f = 450$ MHz fits well to a $1/t_{pulse}$ function in the full t_{pulse} range (dashed line). A constant input power of $P_{RF}^{in} = 21.6$ dBm is used in all plots and at all frequencies. To improve the data visibility, the turquoise and orange lines in **(a), (b), (d)** are vertically shifted by -2 MA/cm² and -4 MA/cm², respectively, with respect to the grey data.

In summary, the experiment shows the presence of two separate j_{sw} thresholds for single and multiple pulse switching. These can be connected to the two steps of SOT switching: namely bubble nucleation and subsequent expansion (Fig. 7.1b-e). The separation of the two thresholds implies that the nucleation of reverse domains can already take place at lower current densities than required for a bubble expansion throughout the sample. Nevertheless, these nucleated bubbles are initially below the resolution limit of the optical microscope and only become visible upon the application of further pulses. While the RF magnetic field does not have a large impact on the switching efficiency for $f = 1000$ MHz, a large reduction in j_{sw} is observed when resonant RF-fields at $f = 450$ MHz are applied at sufficiently large times t_{burst}. Strikingly, the switching thresholds for both single pulse and multiple pulses now lie close together. Altogether, this suggests that the both nucleation and expansion of the reversed domains are facilitated by the RF-field at $f = 450$ MHz.

Note that the frequency dependence of the RF-enhanced SOT switching matches with the one for RF-induced self-propulsion and sustained DW motion (cf. chapters 5, 6). This is consistent with the initial hypothesis that an RF-excitation is expected to impact SOT switching by modifying the bubble expansion. In the following, two possible mechanisms are provided of how the RF-field assists to expand the bubble:

Firstly, an RF field can induce self-propulsion of a DW when a symmetry-breaking field is present that is transverse to the DW (cf. chapter 5). For the nucleated bubble in Fig. 7.1f, the H_x field is longitudinal to the bubble's DW (white line) at its left and right boundary and will not induce self-propulsion there. At the upper boundary of the bubble, however, H_x is transverse to the DW and enables self-propulsion along $+y$ by symmetry considerations. Secondly, after the end of the SOT current pulse, the RF-field can sustain the motion of the bubble's DWs (cf. chapter 6). This sustained DW motion requires a longitudinal H_x which is fulfilled at the left and right part of the nucleated bubble. The sustained DW motion would thus lead to the bubble expansion along $\pm x$ as seen in Fig. 7.1g. Both self-propulsion and sustained motion consequently contribute to the growth of nucleated bubbles and thereby assist the switching.

In addition to the RF-assisted bubble expansion, the nucleation process seems to be assisted by the RF-field. In this context, the conduits temperature increase (cf. Fig. 5.11b) due to the RF application to the CPW is likely to facilitate the nucleation process. Moreover, the conduit's edge magnetization is tilted in-plane (gray arrows in Figs. 7.1a-e) due to the DMI and plays a pivotal role in the nucleation process [68, 80]. This edge magnetization shares many similarities to Néel DWs and may be similarly susceptible to the RF-fields which in turn could facilitate the nucleation that occurs at the conduit edge.

The RF-assistance to SOT switching that is observed here, occurs at low RF-frequencies that are generally associated to a DW excitation. However, the excitation of uniform magnetization precessions, i.e. FMR, has not been observed to assist SOT

switching in this measurement setup. Nevertheless, the RF power transmission at the FMR frequencies of ~ 10 GHz is significantly lower than for $f < 5$ GHz (cf. Fig. 4.4). It is therefore not possible in the current device and film structure to exclude an RF-assisted SOT switching at FMR frequencies. Nevertheless, the strong excitation of the FMR mode is generally expected to have strong effects on switching (cf. chapter 2.4.2). The next chapter will focus on thicker magnetic multilayers that allow for a stronger FMR excitation and exhibit microwave-assisted field switching.

Chapter 8

Microwave-assisted field switching

So far, the field of MAS focuses mainly on reducing the switching field of high PMA materials such as such as Co-Cr-Pt granular films [105] or Co/Pt multilayers [22] for the next generation of HDDs with ultra-high recording densities. While these efforts particularly focus on thick magnetic layers with very high anisotropy, the investigation of MAS in ultra-thin magnetic multiayers that are suitable for current-induced DW motion or SOT switching is still overdue. Moreover, MAS is currently only induced by RF magnetic fields and the equivalent MAS by RF spin torques such as STT or SOT remains to be shown as well. This chapter hence serves as a first step to achieve MAS also in thinner magnetic layers with thicknesses of only a few nanometers and secondly addresses the MAS that is induced by an RF SOT.

In this chapter, the MAS of magnetic multilayers with PMA will be investigated. In contrast to the previous chapter, the microwaves facilitate the switching by strongly exciting the *ferromagnetic resonance* of the magnetic thin film and not by excitation of the magnetic DWs. Moreover, the magnetic film is now deterministically switched by the application of a static magnetic field along z and not mainly by an SOT.

The chapter is structured as follows: First, the properties of the magnetic thin films will be shown. Second, the measurement setup and the two measured device designs will be introduced. Both designs achieve MAS but they either apply an RF magnetic field or an RF electrical current to the magnetic conduit. Afterwards, the experimental results for both device designs are shown. Starting with MAS by an RF-field, the frequency- and power-dependence of MAS will be demonstrated and linked to the excitation of the FMR. The results are further complemented by an investigation of the switching field distribution for different burst time and RF power. Moreover, the use of RF electrical currents for MAS is compared to the previous measurements. Particularly, RF currents allow for even stronger MAS and exhibit a broad frequency region where the switching fields are close to zero.

8.1 Thin film characterization

In this chapter, films with the following multilayer structure have been used: 20 TaN / 30 Pt / 1.25 Ta / 3 Co / [7 Ni / 3 Co]$_{N=4}$ / 30 TaN (the numbers indicate the thickness in Å). In contrast to the previous chapters, the Pt thickness is decreased to 30 Å, the ultra-thin Tantalum thickness at the Pt/Co interface was slightly increased to 1.25 Å and a multilayer repetition $N = 4$ is used. Fig. 8.1 shows the static magnetic properties of the film stack that were measured by VSM. The OOP-field loop (Fig. 8.1a) reveals that the $N = 4$ multilayer shows good PMA, even though the switching loop is not rectangular anymore as for the $N = 1$ films in Fig. 4.1a. The latter implies that the magnetic field required for the nucleation of reverse domains is not sufficient for the expansion of these domains throughout the whole sample. Higher fields are required to expand the domains and achieve a saturated, reverse state. The IP-field scan (Fig.8.1b) shows that the effective anisotropy field, i.e. where the magnetization saturates, lies at approximately $\mu_0 H_{\text{ani,eff}} = 130 \pm 20$ mT and is thus significantly lower than for the films used in the previous chapters. Extended VSM data on the effect of Tantalum-thickness and multilayer repetition number is shown in the appendix (Figs. B.1, B.3).

Furthermore, the dynamic magnetic properties were measured by FMR. Fig. 8.2a shows the OOP-field dependence of the FMR frequency. The zero-field FMR frequency $f_0 = f_{\text{FMR}}(H = 0)$ and the corresponding anisotropy field $\mu_0 H_{\text{ani,eff}}^{\text{FMR}} = \frac{2\pi}{\gamma} f_0$ are summarized in table 8.1. The frequency dependence of the FMR linewidth in Fig. 8.2b allows to extract the damping constant α. Both the minimum, zero-field linewidth $\mu_0 \Delta H(f_0)$ and α are displayed in table 8.1. Note that both the minimum linewidth and the damping constant are significantly lower than for the $N = 1$ films used in the previous chapters.

VSM	**FMR**			
$\mu_0 H_{\text{ani,eff}}$ [mT]	f_0 [GHz]	$\mu_0 H_{\text{ani,eff}}$ [mT]	$\mu_0 \Delta H(f_0)$ [mT]	α
130 ± 20	3.567 ± 0.004	110.8 ± 0.1	4.8 ± 0.1	0.0203 ± 0.002

Table 8.1: **VSM and FMR results of the thin films used for MAS.**

This specific film structure was selected for MAS measurements mainly because of its low FMR frequency. This generally allows for low RF-losses in the waveguide and thus enables the strong excitation of FMR which will be shown to facilitate switching. However, for such a thick film, reliable and deterministic switching only by SOT is not possible anymore. Firstly, this is because the SOT arises from the Pt/Co interface and thus its impact on the total magnetic volume weakens with increasing FM thickness. Secondly, with weakening SOT, the STT becomes comparable with SOT and complicates the magnetization dynamics. Hence, to investigate MAS, an alternative switching mechanism to SOT switching is required. For this reason, the switching by a magnetic field H_z will be investigated in this chapter.

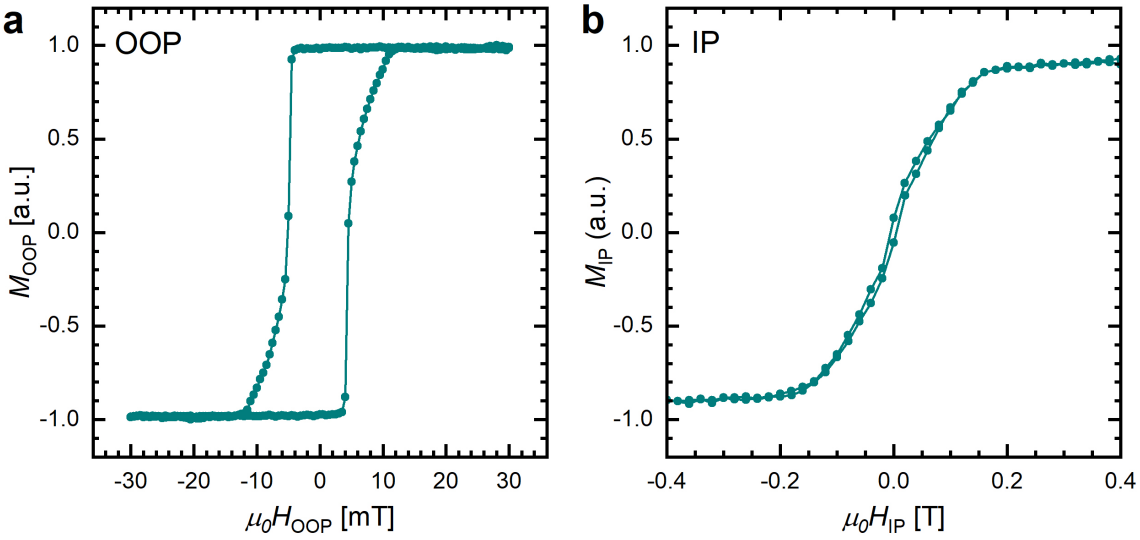

Figure 8.1: **Vibrating sample magnetometry.** **(a)** Out-of-plane and **(b)** in-plane magnetization of the magnetic multilayers with $N = 4$ Co/Ni repetitions and a Ta-dusting thickness of $d_{\mathrm{Ta}} = 1.25$ Å. The data is normalized to the saturation value. The OOP-scan confirms the stable PMA. The IP-scan allows to estimate the effective anisotropy field at $\sim 130 \pm 20$ mT.

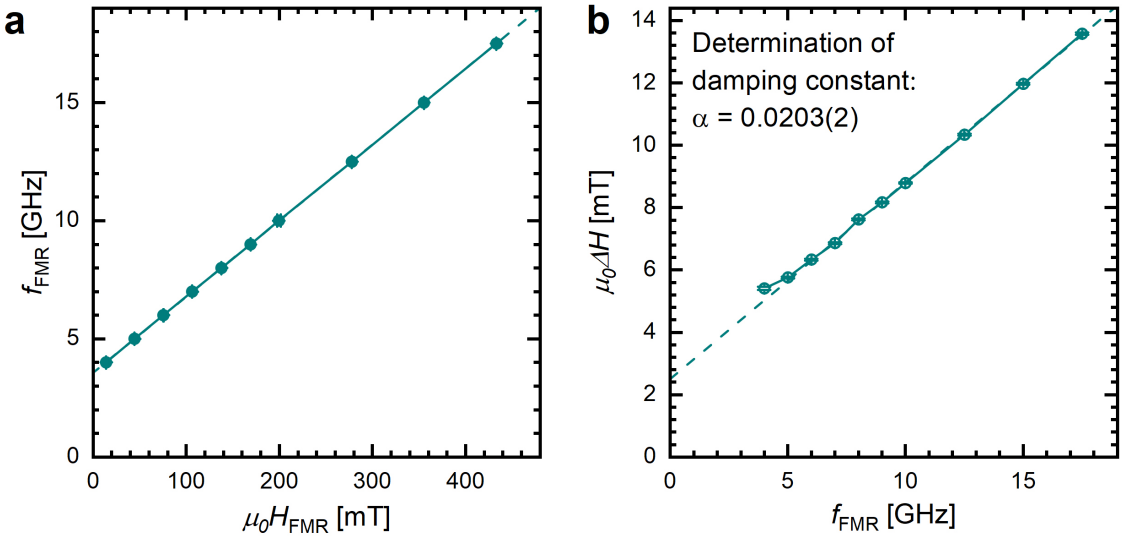

Figure 8.2: **Ferromagnetic resonance.** FMR measurements for magnetic multilayers with $N = 4$ Co/Ni repetitions and a Ta-dusting thickness of $d_{\mathrm{Ta}} = 1.25$ Å are shown. The linear dependence of the FMR frequency with an OOP-field is seen in **(a)**. The extrapolated frequency $f_{\mathrm{FMR}}(H = 0)$ is the FMR frequency in zero field and is a measure of the effective anisotropy of the magnetic film. **(b)** The resonance linewidth as a function of f_{FMR} reveals the damping constant α and the inhomogeneous broadening. The dashed lines in **(a), (b)** are linear fits to the data.

8.2 Measurement setup

In this chapter, the RF-power will be applied to the magnetic element by two alternative means: by an RF magnetic field or by an RF electrical current. Regarding the first approach, Fig. 8.3a schematically shows a circular FM (blue) on top of the center conductor of a CPW (yellow). Applying an RF current I_{rf} to the CPW will generate an in-plane RF-field h_{rf} at the FM that in turn can excite the FMR of the FM. Simultaneously a static out-of-plane field H_{z} is applied to deterministically reverse the FM's magnetization. The second approach in Fig. 8.3b uses an RF-current that is directly flowing through the FM and exerts a time-varying SOT $\tau_{\mathrm{rf,SOT}}$ to the FM to excite the FMR.

The details of device fabrication are given in chapter 3.2. The device for RF-field application consists of a circular magnetic element with a diameter of 8 µm that is placed on top of a CPW with a width of 10 µm. The schematic and the microscope pictures of the final devices are shown in Fig. 8.4a-b. The VNA data of the CPW reveals a high microwave transmission $S_{21} \geq -8$ dBm for $f \leq 6$ GHz without any pronounced dips in S_{21} (Fig. 8.4c).

Moreover, the device for RF-current application consists of a 10 µm wide stripe that is laterally contacted by gold pads as shown in Fig. 8.5a-b. In an area of 10×10 µm^2 the electrical current flows exclusively through the FM. The corresponding VNA data in Fig. 8.5c shows a microwave transmission of $S_{21} \geq -10$ dBm for $f \leq 6$ GHz.

The general measurement procedure to determine the magnetic switching field H_{sw} is provided in the methods section 3.3.4 and is shortly summarized here: A static magnetic H_{z} field along the FM's easy-axis is applied and the magnetic state is simultaneously monitored by Kerr microscopy. Initially, the FM is saturated by a large, negative H_{z}. The field is then increased in small steps of $0.1 - 0.2$ mT with a waiting time of ~ 500 ms between the steps. At each field step, a single burst of RF-power with duration t_{burst} is applied and the Kerr intensity of the magnetic element is subsequently recorded. The switching field H_{sw} is generally defined as the coercive field of the FM here, i.e. when the Kerr contrast exhibits as abrupt change at a certain field, this is considered as the switching field H_{sw}.

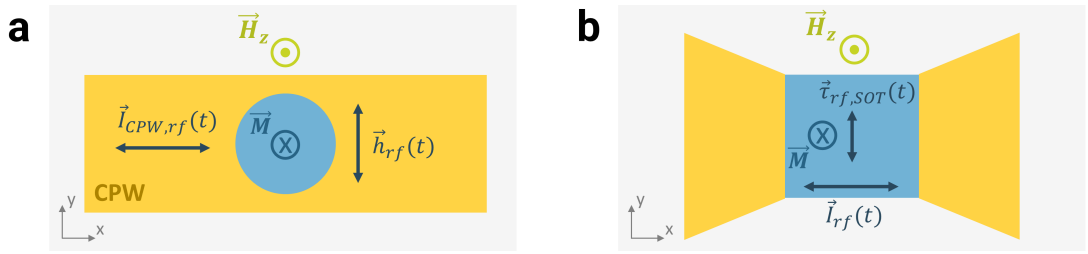

Figure 8.3: **Schematic of different MAS measurements. (a)** An RF-current $I_{\mathrm{CPW,rf}}$ flows through the CPW (yellow) and creates an RF-field h_{rf} at the magnetic dot (blue) sitting on the CPW. **(b)** The RF-current flows directly from the contact pads (yellow) through a magnetic stripe (blue) and exerts an RF spin-orbit torque $\tau_{\mathrm{rf,SOT}}$ there. The RF field or RF torque assists the reversal of the magnetization M by the action of a magnetic field H_{z}.

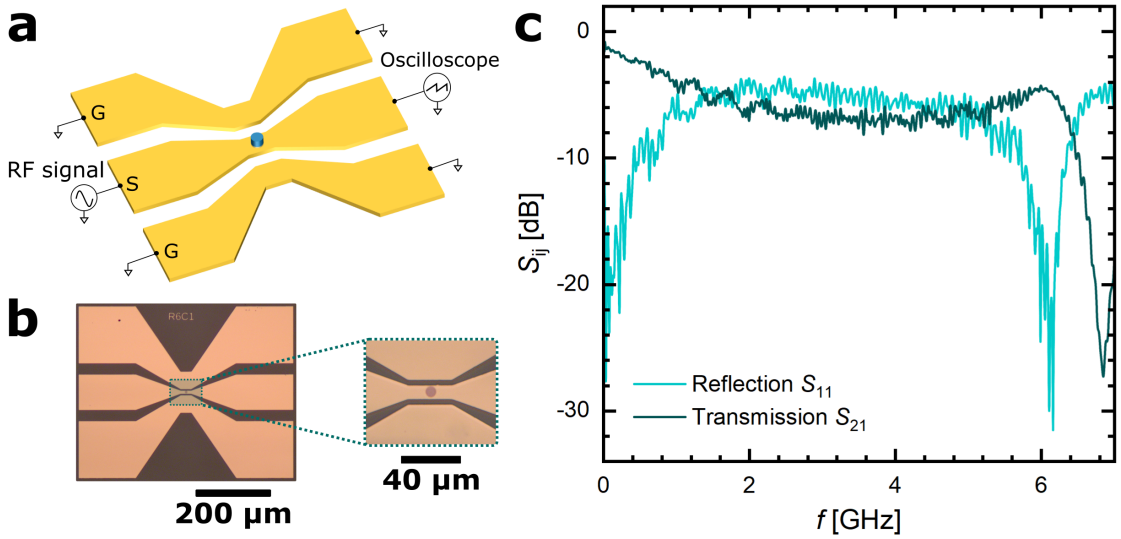

Figure 8.4: **Device schematic and VNA data of CPW. (a)** Device schematic of a magnetic dot (blue) sitting on top of a CPW (yellow). The CPW input is connected to a signal-generator and its output feeds into an oscilloscope. **(b)** Microscopy pictures of the actual device. A dot with 8 µm in diameter sits on a CPW with 10 µm width. **(c)** VNA data of the CPW. Both reflection coefficient S_{11} and transmission coefficient S_{21} are shown.

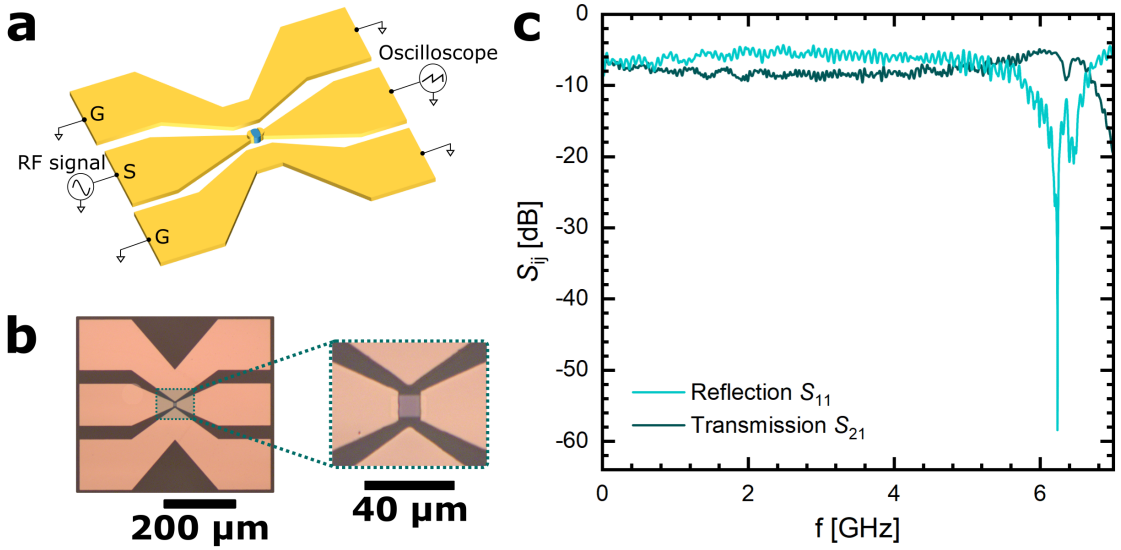

Figure 8.5: **Device schematic and VNA data of the device for RF-current injection. (a)** Device schematic of a magnetic element (blue) being contacted by electrical leads (golden) from both sides. The RF-current flows directly through the magnet. **(b)** Microscopy pictures of the actual device. A square stripe with 10 µm in edge length is visible between the lateral gold contacts. **(c)** VNA data of the device. Both reflection coefficient S_{11} and transmission coefficient S_{21} are shown.

8.3 MAS by RF magnetic fields

Fig. 8.6 displays the reduction of the switching field H_{sw} in the presence of an RF magnetic field with frequency f and burst length $t_{burst} = 50$ µs. The frequency-dependence of H_{sw} is shown for different RF-powers P_{RF}^{out} transmitting through the CPW that correspond to different strengths of the RF field. Without any RF-field present, the FM switches at $\mu_0 H_{sw} = 76$ mT (dashed line). When an RF-power $P_{RF}^{out} = 5.1$ dBm is transmitting through the CPW, it generates an in-plane RF field with a peak amplitude of $\mu_0 h_{RF} = 1.86$ mT. This causes H_{sw} to decrease linearly in the range from $f = 1.0$ GHz to $f = 2.375$ GHz, reaching a minimum $\mu_0 H_{sw} = 41.4$ mT that corresponds to a reduction of the switching field by 46%. Above a critical frequency $f_{crit} = 2.5$ GHz, H_{sw} returns to its initial value. For higher RF powers, H_{sw} further decreases in the MAS range for $f < f_{crit}$ and additionally f_{crit} increases. The results are summarized in table 8.2. For $P_{RF}^{out} = 10.1$ dBm, a secondary MAS region becomes visible for $2.75 \leq f \leq 3.08$ GHz, where H_{sw} still decreases linearly but is vertically displaced towards slightly higher fields. Such a secondary region is also visible for $P_{RF}^{out} = 15.1$ dBm. According to macroscopin simulations that were reported in literature [73], these regions could correspond to MAS with a different switching speed.

P_{RF}^{out} [dBm]	$\mu_0 h_{RF}$ [mT]	$\mu_0 H_{sw,min}$ [mT]	f_{crit} [GHz]
5.1	1.86	41.4	2.5
10.1	3.30	27.4	3.08
15.1	5.87	15.7	3.42

Table 8.2: **MAS results for frequency scans at different RF power.**

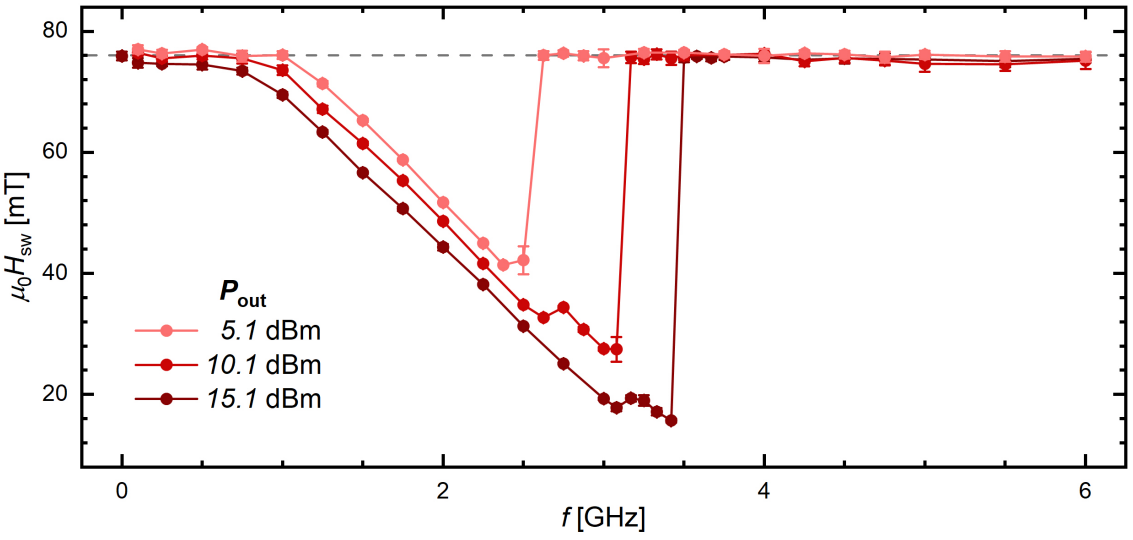

Figure 8.6: **Power- and frequency-dependence of MAS.** Frequency-dependence of the switching field H_{sw} for a magnetic multilayer structures with $N = 4$ repetitions of Co/Ni. RF bursts with $t_{burst} = 50$ µs are applied to the CPW and the transmitted RF-power P_{RF}^{out} is kept constant at each frequency. Each frequency scan is repeated for different levels of P_{RF}^{out}.

In the following the connection of MAS and FMR will be discussed. Fig. 8.7 shows the reduction of H_{sw} with the applied RF-frequency (left) together with the field-dependence of the FMR of the magnetic film (right). It is important to note that the FMR is measured using an H_z field that saturates the FM and is aligned along the equilibrium magnetization. The field magnitude is thus considered positive and increases the FMR frequency. In contrast, during MAS, H_z is aligned opposite to the magnetization. As long as the FM does *not* switch, the H_z field consequently reduces the FMR frequency (see dashed line in left part of Fig. 8.7). Noticeably, the H_{sw} reduction due to MAS aligns very well with this dashed line, i.e. the extrapolated FMR data. Hence, the MAS occurs once the RF-frequency of the RF-field matches with the frequency of the FMR. And since the latter scales linearly with H_z, the MAS curve $H_{sw}(f)$ scales linearly with H_z as well. Moreover, this picture allows to explain the emergence of a critical frequency f_{crit}, above which no MAS is observed. The maximum frequency for MAS corresponds to the zero-field FMR frequency f_0. For an RF-field with $f > f_0$, a magnetic field *along* the initial magnetization is required to match the FMR condition and thus H_z would reinforce the initial state and not switch it.

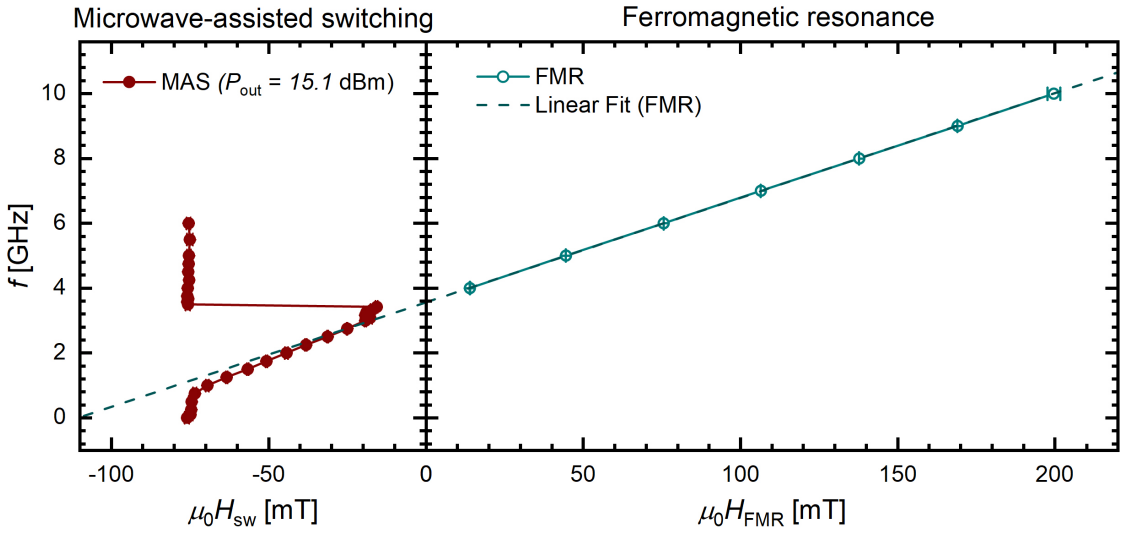

Figure 8.7: **Comparison of MAS with FMR.** The out-of-plane field-dependence of the FMR resonance frequency (right) is compared to the reduction of H_{sw} due to MAS (left). Note that the MAS data is rotated by 90° compared to Fig. 8.6. The dashed line displays a linear fit to the FMR data and is extrapolated to negative fields (left).

Nevertheless, this picture that connects the FMR excitation to MAS does not yet explain the power dependence of either H_{sw} or f_{crit} that has previously been shown in Fig. 8.6. However, it has been reported that the experimental observations of MAS can only be numerically reproduced by taking non-uniform excitations of the FM into account [22]. For example, numerical simulations have shown that the RF-field may excite standing spin waves (SWs) that cause MAS. Such standing SWs are non-uniform excitations of the magnetization that depend on the shape of the FM. Because of their non-uniformity (dispersion), their resonance field is below the resonance field for FMR [74]. The exci-

tation of higher order standing SW modes with increasing RF-power is likely to reduce H_{sw} at the same frequency. Additionally, for high RF driving fields, non-linear magnetization dynamics might arise that modify the previous picture of the FMR and SWs [26] and thereby modify the resonance condition where MAS occurs.

In the following, the dependence of MAS on the length of the RF-burst t_{burst} will be investigated: Fig. 8.8 shows the t_{burst} dependence of H_{sw} at $f = 3.0$ GHz. The switching field decreases by several mT when t_{burst} increases from 2 ns to 100 µs. This decrease proceeds in an approximately logarithmic fashion. Remarkably, an RF-field with a duration of only 2 ns is still sufficient to induce MAS. Note that this only corresponds to $t_{burst} \cdot f = 6$ periods of the RF-field. A critical discussion of the time dependence of H_{sw} is given in the appendix B.3.

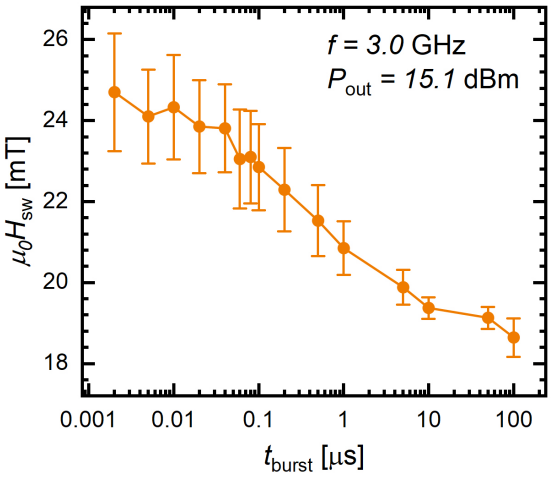

Figure 8.8: **Burst time dependence of MAS.** Reduction of H_{sw} with increasing burst time t_{burst} for $f = 3.0$ GHz. The transmitted RF-power is kept constant at $P_{RF}^{out} = 15.1$ dBm. The error bars correspond to the standard deviation of the switching field distribution.

In addition to the H_{sw} decrease, the standard deviation σ_{sw} of the switching field distribution (error bars in Fig. 8.8) decreases with increasing t_{burst}. For instance, the switching fields for t_{burst}= 500 ns spread over a distribution with $\sigma_{sw} = 0.88$ mT while for t_{burst}= 50 µs, the switching events occur in a much narrower range with $\sigma_{sw} = 0.27$ mT. This is directly visualized in Fig. 8.9a which shows the histograms of the switching field distributions. A longer burst time clearly narrows the switching distribution (cf. dark red and green histograms). In addition to the t_{burst} dependence, the histograms for different RF-powers are shown, i.e. for $P_{RF}^{out} = 10.1, 15.1, 20.1$ dBm. Interestingly, with increasing power, the standard deviation σ_{sw} of H_{sw} does not decrease monotonously but is lowest at intermediate powers $P_{RF}^{out} = 15.1$ dBm.

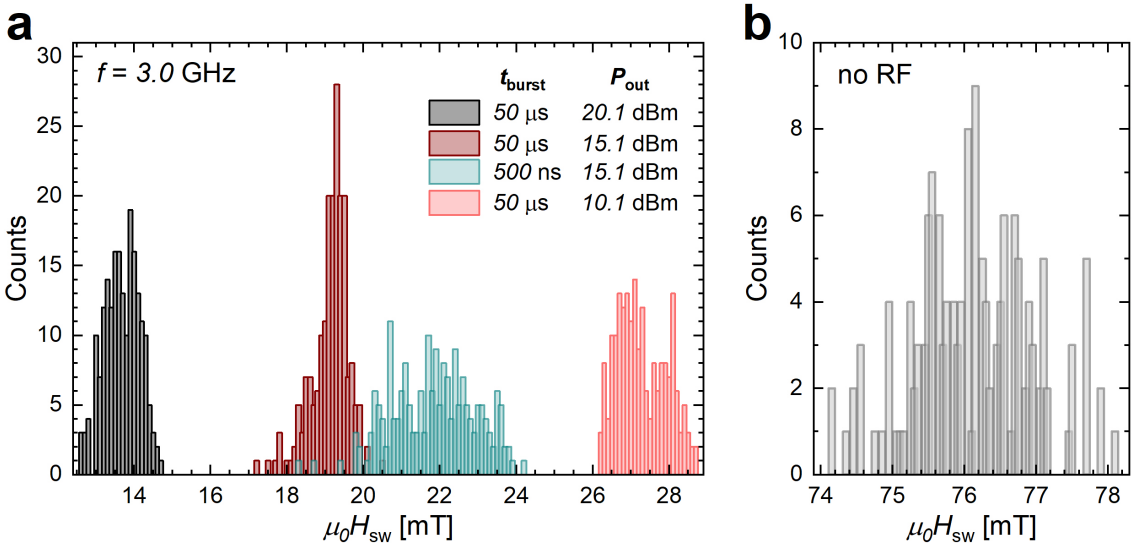

Figure 8.9: **Switching statistics.** Distribution of switching fields during MAS **(a)** and during conventional field-switching without RF-fields **(b)**. For **(a)**, 200 switching events are shown for each setting while for **(b)**, 150 events are shown. In **(a)**, the statistics for different combinations of burst time t_{burst} and RF-power $P_{\mathrm{RF}}^{\mathrm{out}}$ are displayed.

8.4 MAS by RF spin-orbit torques

In contrast to the previous section, an RF electrical current is directly flowing through a magnetic stripe here. This exerts an RF spin-orbit torque on the FM that could similarly excite magnetic resonances and induce MAS. While the symmetries of the damping-like RF SOT and the RF magnetic field are very similar, the RF SOT is expected to have a larger impact than the RF field when the same RF-power is transmitted to the FM and CPW, respectively.

The frequency dependence of MAS for several RF powers is shown in Fig. 8.10. For low RF powers $P_{\mathrm{RF}}^{\mathrm{out}} \leq 7$ dBm, the MAS is very similar to the data shown in Fig. 8.6, i.e. H_{sw} decreases linearly with f until the critical frequency is reached. With increasing RF power, the minimum attainable switching field lowers and f_{crit} increases (see table 8.3). Remarkably, when the RF power increases to $P_{\mathrm{RF}}^{\mathrm{out}} = 17$ dBm, a very broad frequency range 0.5 GHz $< f <$ 3.75 GHz now exhibits low switching fields with $\mu_0 H_{\mathrm{sw}} < 5$ mT. Herein, at $f = 1.0$ GHz, the switching field reaches its minimum at $\mu_0 H_{\mathrm{sw}} = 0.3$ mT. In other words, the RF burst assists the FM stripe to switch its magnetization by only a tiny magnetic field that corresponds to 0.38% of the required field for simple field switching without MAS. Lastly, for $f > f_{\mathrm{crit}}$ and $P_{\mathrm{RF}}^{\mathrm{out}} \geq 14.5$ dBm, the switching field does not increase immediately to its high value but exhibits intermediate frequencies where the RF current still significantly assists the switching. Altogether, this MAS behavior is thus qualitatively and quantitatively different from the reported MAS behavior in literature and from the MAS shown in the previous section 8.3.

In the following the very low switching fields during MAS for $P_{\mathrm{RF}}^{\mathrm{out}} = 17$ dBm (black data in Fig. 8.10) will be investigated in more detail. Fig. 8.11a shows the switching loops

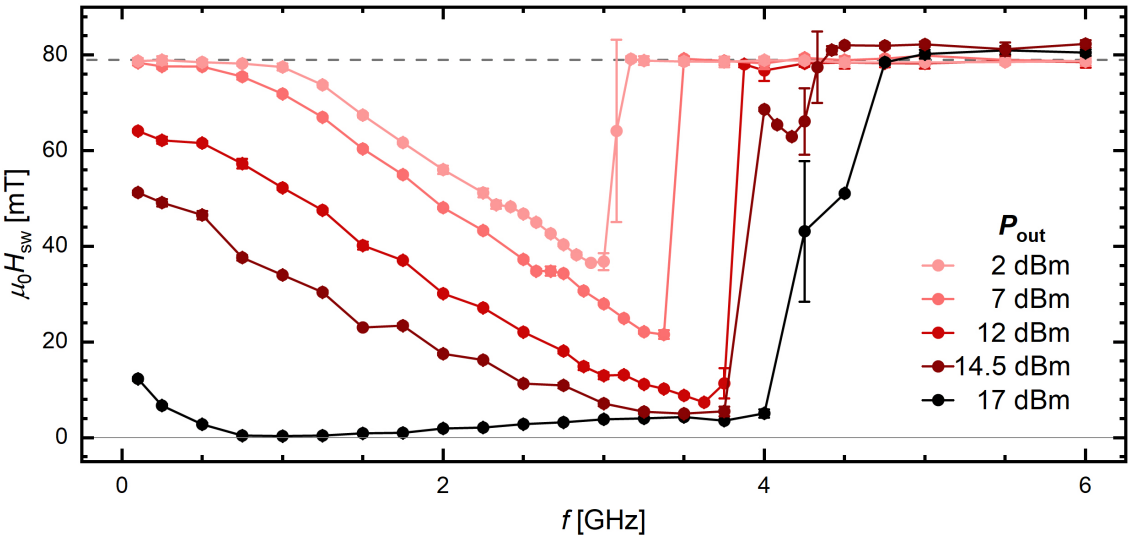

Figure 8.10: **Frequency scan of MAS for different RF-powers.** MAS during application of an RF electrical current: Frequency-dependence of MAS when RF-bursts with $t_{burst} = 50$ µs are applied. The transmitted RF-power P_{RF}^{out} is kept constant at each frequency. Each frequency scan is repeated for different levels of P_{RF}^{out}. Note that the shown H_{sw} corresponds to the coercive field of the switching loops.

P_{RF}^{out} [dBm]	$\mu_0 H_{sw,min}$ [mT]	f_{crit} [GHz]
2	36.5	3.0
7	21.6	3.375
12	7.3	3.625
14.5	5.0	3.75
17	0.3	4.0

Table 8.3: **MAS results for frequency scans at different RF power.**

at $f = 2.0$ GHz and $t_{burst} = 50$ µs when the RF power is gradually increased. Without MAS, the FM switches at 83.5 mT (gray curve) and the loop has a rectangular shape, i.e. the switching occurs very abruptly. An increasing RF-power then reduces H_{sw} but the loop remains rectangular for $P_{RF}^{out} < 17$ dBm. For $P_{RF}^{out} = 17$ dBm, the loop has a very low coercive field of only 1.9 mT (central, orange curve). However, the loop shape is not rectangular anymore but instead the magnetization switches via many intermediate steps.

The close-up view of such non-rectangular switching loops with low H_{sw} is shown in more detail in Fig. 8.11b for different frequencies. For low frequencies $f \leq 0.5$ GHz, the switching loops are still rectangular. In contrast, for $f \geq 1.0$ GHz, the loops become non-rectangular and in particular their remanence decreases, i.e. the magnetization already decreases when H_z is still aligned parallel to the initial magnetization. This implies that the RF SOT is effectively destabilizing the perpendicular magnetization of the FM and does so even without the assistance of an H_z field. This RF-induced destabilization of the FM seems most effective at $f = 1.0$ GHz where the switching loop exhibits almost no hysteresis and the remanence and coercive field are close to zero. For $f > 1.0$ GHz, the loops become more hysteretic and thus increase their remanence and coercivity.

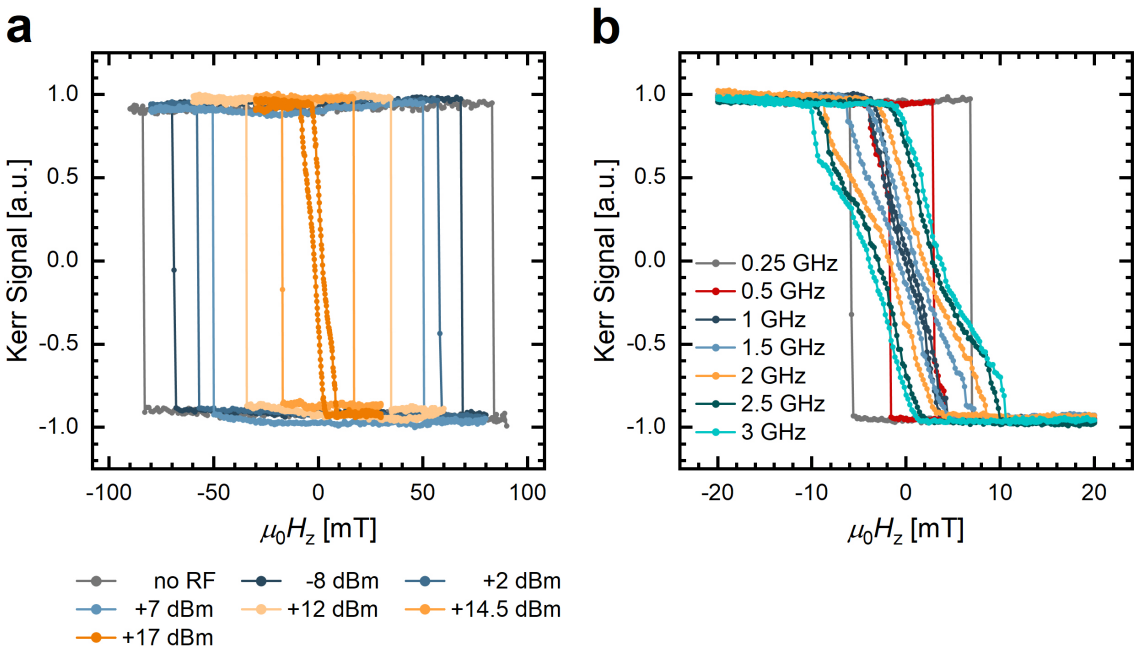

Figure 8.11: **Switching loops during MAS.** The Kerr signal during a field loop shows the magnetic switching events. Note that a linear background, originating from the Faraday rotation, has been corrected in the displayed Kerr signal. **(a)** RF-power dependence of the loops: For a frequency of $f = 2.0$ GHz, the transmitted RF-power $P_{\mathrm{RF}}^{\mathrm{out}}$ is gradually increased and facilitates the switching, i.e. reduces H_{sw}. For the highest power of $P_{\mathrm{RF}}^{\mathrm{out}} = 17$ dBm, the loop is not rectangular anymore but shows a strongly reduced remanence. **(b)** Frequency-dependence of loops for $P_{\mathrm{RF}}^{\mathrm{out}} = 17$ dBm. The close-up on the loop shape for low switching fields is still rectangular for $f = 0.25$ GHz and $f = 0.5$ GHz and the switching occurs abruptly. For $f \geq 1.0$ GHz, the loop shape changes significantly and exhibits a gradual switching process, i.e. a roughly linear decrease in the Kerr signal with field. Herein, the remanence and coercivity are minimal and close to zero for $f = 1.0$ GHz, whereas they gradually increase for $f > 1.0$ GHz. A burst time of $t_{\mathrm{burst}} = 50$ µs is used in **(a), (b)**.

In order to understand the switching mechanism during these non-rectangular switching loops, differential Kerr images at $f = 1.0$ GHz have been recorded during a switching loop as shown in Fig. 8.12. After an initial saturation at $\mu_0 H_z = -100$ mT, $\mu_0 H_z$ is stepped from -5 mT to $+5$ mT and at each field a single RF-burst is applied before the image is taken. Here, a black image contrast corresponds to a switching from $-z$ to $+z$. The figure shows that at $\mu_0 H_z = -4$ mT, two switched dots appear in the center of the FM stripe. For $\mu_0 H_z \geq -3$ mT, these dots enlarge into a network of stripe domains. With increasing H_z, this stripe network extends throughout the whole stripe and additionally the density of the stripes increases. For $\mu_0 H_z \geq 3$ mT, the FM seems to be completely saturated along $+z$.

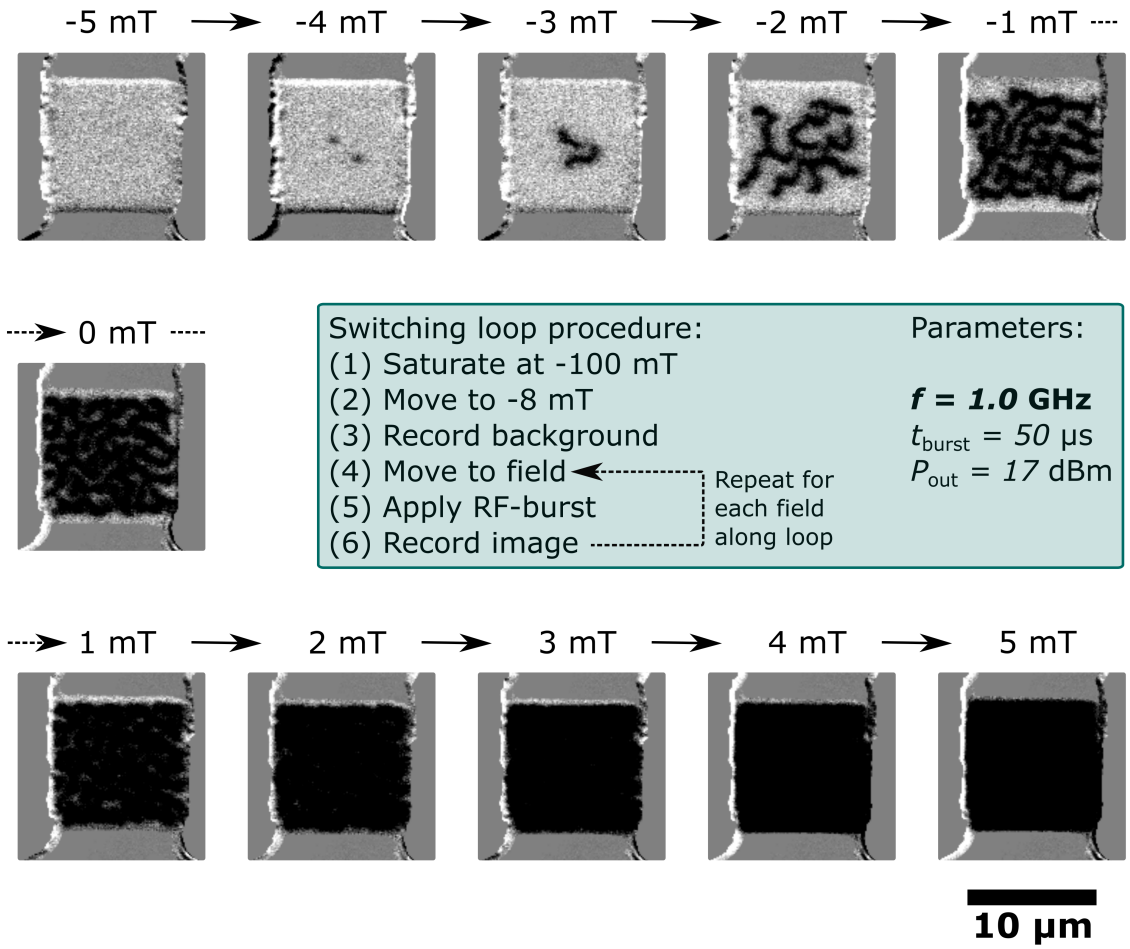

Figure 8.12: **Kerr microscopy snapshots during a switching loop.** The differential Kerr images of the magnetic stripe are recorded at various magnetic fields H_z during a field loop. The stripe has a square shape and is electrically contacted at the left and right (non-pixelated, gray areas). The details on measurement procedure and image acquisition are given in the teal box: The device is first saturated along $-z$ and the field is then increased to $\mu_0 H_z = -8$ mT where a background image is recorded. The latter is subtracted from all subsequently acquired images. The magnetic field is then increased in steps of 1 mT and a single burst with t_{burst} is applied before the Kerr image is recorded. The MAS process for $f = 1.0$ GHz occurs by gradual switching from $-z$ (initially gray) to $+z$ (black). The switching does not occur abruptly but instead starts by the reversal of small dots and stripes. At increasing field, the stripe pattern grows due to the RF-burst and the stripes begin to merge until the switching is almost complete at $+5$ mT.

It is important to point out, that in the time between the image acquisition, the domain patterns do not visibly change by growing or moving. Apparently, the applied H_z field is too small to cause DW motion in this field range. All changes to the patterns occur after the application of the RF-burst. To unequivocally prove that the growth of the stripe network are not a direct result of the H_z field alone, a new set of Kerr images were acquired with a different measurement procedure. After initially saturating the FM, the new images in Fig. 8.13 are *not* successively recorded along a switching loop but instead recorded after directly moving to the target field and applying a *single* RF burst. Each image is thus independent of each other. The fact that Fig. 8.13 shows very similar domain patterns than Fig. 8.12 thereby confirms that the emerging patterns are not caused by DW motion under H_z field. Instead, the RF-burst itself seems to strongly destabilize the FM state and the applied H_z field then determines the final magnetization state that emerges once the FM relaxes after the end of the RF burst.

In comparison to the previous switching process at $f = 1.0$ GHz, Fig. 8.14a displays the Kerr images for the slightly weaker MAS process at $f = 2.0$ GHz. Also here the nucleation of reversed dots starts at negative fields of $\mu_0 H_z = -3$ mT. In contrast, the switched dots first remain isolated and only merge into larger stripes for larger fields of $\mu_0 H_z \geq +1$ mT. Additionally, a higher field is required to fully switch the complete FM stripe. As a final reference, Fig. 8.14b displays the Kerr images for the switching process at $f = 4.0$ GHz. Here, the switching abruptly occurs at $\mu_0 H_{sw} = 7$ mT and does not exhibit intermediate switching states with stripe domains.

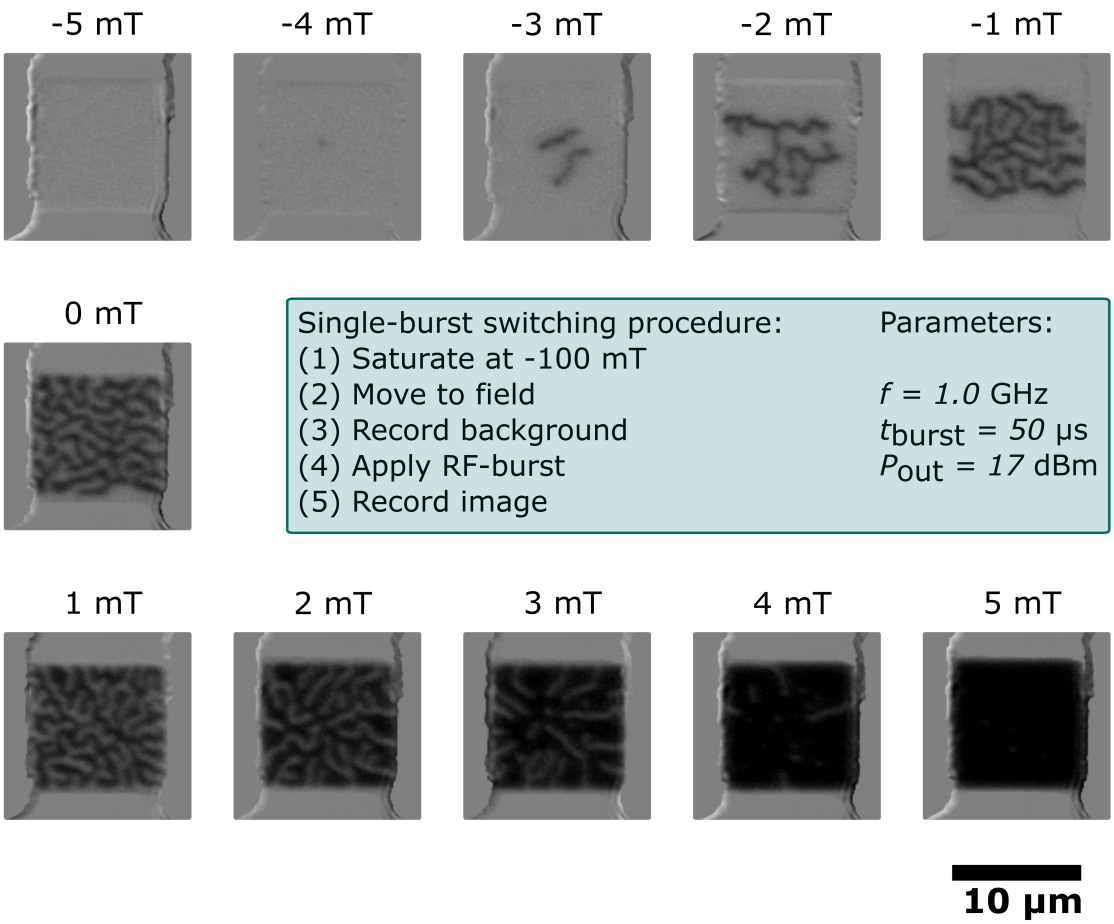

Figure 8.13: **Kerr microscopy snapshots after the application of a single RF-burst.** Differential Kerr images of the magnetic stripe are recorded after a single RF-burst at $f = 1.0$ GHz is applied to the stripe while a magnetic field H_z at various amplitude is simultaneously applied. The procedure is outlined in the teal box. In contrast to Figs. 8.12, 8.14, the images displayed here are independent of each other and not part of a gradual switching loop. In particular, the magnetic stripe is first saturated at -100 mT and H_z is then directly moved to the target field before a single RF-burst is applied. The observed nucleation of reversed dots and stripes closely resembles the results in Fig. 8.12. This measurement mode allows for a better image quality since it eliminates any contrast from the Faraday rotation during a switching loop. Moreover, it confirms that the stripe patterns directly emerge through the RF-burst application and are not an artifact due to gradual domain growth with increasing field. Note that the image acquisition settings of the Kerr microscope are changed compared to Fig. 8.12 to allow for a better resolution, albeit lowering the contrast.

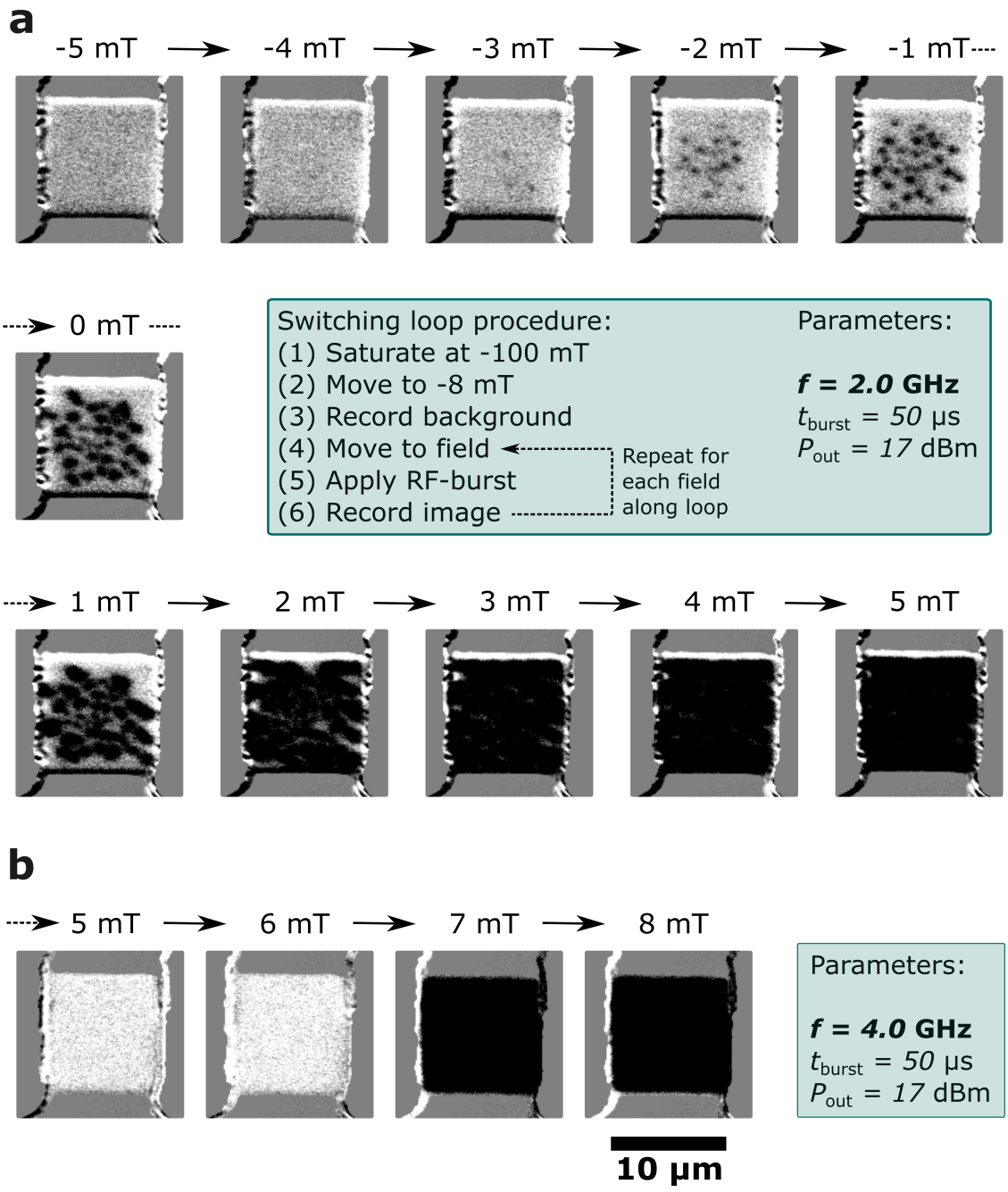

Figure 8.14: **Kerr microscopy snapshots during a switching loop.** The same procedure as in Fig. 8.12 is used in this figure. **(a)** In contrast, the RF frequency is changed to $f = 2.0$ GHz for the displayed MAS switching loop. The burst of RF-current leads to the nucleation of small reverse dots already at negative fields. With increasing field, more and larger dots appear and start to merge. In contrast to Fig. 8.12, this MAS effect nucleates seperate bubbles rather than interconnected stripe domains and sets in at higher fields. **(b)** For $f = 4.0$ GHz, however, the MAS does not show stable, reversed stripe or dot patterns along the switching loop, but abruptly switches the complete stripe at $+7$ mT.

Part IV

Summary and perspective

The effect of a microwave excitation on key spintronic operations such as DW motion and magnetization switching is thoroughly investigated in this thesis. For this purpose, Pt/Ta/Co/$[Ni/Co]_N$ multilayers with perpendicular magnetic anisotropy were used for their reliability in DW motion and SOT switching. Moreover, varying the multilayer repetition number N and the interfacial Tantalum thickness at the Pt/Co interface allows to tune the film properties, for instance to adjust the zero-field FMR frequency. As the main experimental techniques, Super-Nyquist-Sampling magneto-optical Kerr effect (SNS-MOKE) and wide-field MOKE microscopy were used. Herein, the former directly measures the magnetization dynamics of either DWs or uniform domains, whereas the latter visualizes DW motion and switching experiments.

To simultaneously excite a magnetic DW by RF fields and optically investigate its motion, a novel device geometry was developed that places the magnetic conduit on top of a CPW. RF power that is applied to the CPW will generate an RF magnetic field at the conduit. SNS-MOKE measurements revealed that the dynamic susceptibility of the DWs exhibits an asymmetric resonance that peaks at $f \approx 640$ MHz. This DW resonance lies significantly lower than the FMR mode in the uniform domains which is centered at $f \approx 9.5$ GHz. At the resonance, the detected signal of two neighboring DWs is out-of-phase. This agrees well with their opposite in-plane magnetization which is defined by their chirality. Altogether, the SNS-MOKE signal at the DWs is interpreted as either a resonant DW precession or DW oscillation or a combination of both.

By exciting this DW resonance in a static, transverse magnetic field H_y, the field-induced asymmetry of the current-induced DW motion is significantly enhanced. Further increasing the RF power leads to the self-propulsion of the DW, i.e. the DW moves by itself without the need for electrical current pulses. Herein, the polarity of H_y determines the DW's direction during self-propulsion. The emergence of an optimum magnitude of H_y for self-propulsion is interpreted as follows: It emerges as a tradeoff between several effects such as the H_y-induced asymmetry of DW motion, the efficiency of RF field-coupling to the DW and the H_y-induced DW tilting. The precise timing of the RF duration allows to determine the DW speed during self-propulsion as $v \sim 1$ m/s which implies DW motion in the depinning regime. Moreover the data suggests that the self-propulsion is stable for several microseconds. A critical investigation of the results reveals that resonant self-propulsion of the DW might not only be induced by the sole action of an RF field but also by both a parasitic RF-current in the magnetic conduit and by resonant RF heating. The details of their frequency-dependence and the exact self-propulsion mechanism for each of these factors is still an open question.

Moreover, a purely RF current-driven self-propulsion is demonstrated which exhibits a qualitatively very similar behavior except for its frequency dependence. In contrast to the resonant character of self-propulsion using an RF-field, the effect of an RF-current diverges towards the lowest frequencies where an automotion speed of $v = 8.6$ m/s is observed at $f = 10$ MHz. The frequency-dependence of the threshold for current-induced DW motion qualitatively explains the frequency-dependence of self-propulsion. The lat-

ter is consequently interpreted as a rectification of the RF current-induced DW oscillation. Future SNS-MOKE experiments on DWs being excited by a pure RF current will complement the previous information on RF-driven DW dynamics.

It was further observed that an RF field-excited DW in a static, longitudinal magnetic field does not exhibit self-propulsion anymore. However, triggering DW motion with a sufficiently strong current pulse enables sustained DW motion when a resonant RF-field is present. This sustained motion is stable for several microseconds after the end of the current pulse, occurs at a speed of $v \sim 0.4$ m/s and follows the direction of the current pulse. The observations were interpreted in terms of the DW's inertia. The latter causes a finite DW deceleration time after the end of the current pulse and possibly enables the RF-field to resupply energy to the moving DW to compensate for energy losses due to magnetic damping. The role of the longitudinal magnetic field during sustained motion is still an open question. Further experiments with precise timing between the trigger pulse and the RF burst are required to determine the deceleration time and the decay time for sustained motion.

In addition to DW dynamics in the presence of microwaves, this thesis also investigates microwave-assisted magnetization switching where the switching is mainly induced by either an SOT or an externally applied magnetic field. It is shown that by exciting the previously discussed DW resonance with an RF magnetic field, the efficiency of SOT switching is significantly enhanced in terms of a lower threshold current density and a shorter pulse time. These observations are interpreted as follows: SOT switching in micron-sized conduits is typically a two-step process that is based on the nucleation of a reverse magnetic bubble and its subsequent expansion throughout the device. The bubble expansion thus involves the motion of DWs. As shown in the previous parts of this thesis, the RF-field induces both self-propulsion and sustained motion of DWs and can continue the bubble expansion and facilitate switching. The microscopic details of bubble nucleation, stability and expansion, especially during RF-excitation are however unclear. Further improvements of the CPW and modified magnetic films are required to complement the previous results with RF-assisted SOT switching by the strong excitation of the FMR.

Nevertheless, the last chapter of this thesis demonstrates the strong impact of the FMR excitation on the switching process, albeit not for SOT switching but for field-induced switching. Herein, the microwave-assistance to switching is compared for RF magnetic fields and RF electrical currents where the latter induces an RF SOT. A switching field reduction of almost 100% is demonstrated using a resonant RF SOT. The results show that a burst of resonant RF SOT is capable of fully demagnetizing a magnet. The MAS behavior is qualitatively in conformity with the reported literature, except for the highest applied RF powers. Possibly, the MAS theory needs to be extended by an RF SOT which differs from the established RF field.

In the last two decades, the research efforts in the field of DW motion and switching have mostly been directed to the exploration of novel material platforms to achieve for instance a higher spin-to-charge conversion efficiency [2, 84], a higher maximum DW velocity [63, 106] or field-free magnetization switching [107]. Herein, both the material characterization and the device operation mainly used direct-current or pulsed techniques or at least did not particularly focus on the *operation* of such spintronic devices in the microwave regime. Furthermore, the excitation of magnetization precession for DW motion has often been ignored or even avoided since the increasing energy losses were believed to outweigh any performance benefit.

Nevertheless, it is still necessary to investigate the operation of spintronic devices at microwave frequencies for the following reasons: At latest for the integration of a spintronic device into the framework of a memory chip, the device performance at clocking rates in the MHz or GHz regime needs to be studied. These clocking rates are easily in the frequency range to which the DW is susceptible and may be close to the FMR frequency as well. Consequently, even without deliberately exciting magnetic resonances, the high operation speed in the memory circuitry requires the study of RF magnetic excitations to ensure a regular operation. Moreover, this thesis shows that the RF excitation in spintronic devices significantly extends the established research field by novel effects such as self-propulsion or sustained motion of a magnetic DW. Despite the fact that these are currently rather slow and energy-inefficient compared to the current-induced DW motion by SOT, a continued development of these concepts is required to assess their future applicability in electronics. In perspective, the RF-excitation of spintronic devices might serve to *complement* the capabilities of state-of-the-art techniques, rather than surpassing it.

Part V

Appendices

Appendix A

Derivation of collective coordinate approach (q-ψ model of DW dynamics)

In this section the collective coordinate model (q-ψ model) for the DW dynamics is derived. The Landau-Lifshitz-Gilbert-Slonczewski (LLGS) equation in implicit form describes the magnetization dynamics by taking into account an effective field $\mathbf{H}_{\text{eff}}$, magnetic relaxation, adiabatic and non-adiabatic STT as well as DL-SOT and FL-SOT:

$$\begin{aligned}\frac{\partial \mathbf{M}}{\partial t} =& -\gamma \mathbf{M} \times \mathbf{H}_{\text{eff}} + \frac{\alpha_{\text{G}}}{M_{\text{S}}} \mathbf{M} \times \frac{\partial \mathbf{M}}{\partial t} - u \frac{\partial \mathbf{M}}{\partial x} + \frac{\beta u}{M_{\text{S}}} \mathbf{M} \times \frac{\partial \mathbf{M}}{\partial x} \\ & - \frac{\tau_{\text{DL}}}{M_{\text{S}}} \mathbf{M} \times (\mathbf{M} \times \sigma_{\text{SHE}}) - \tau_{\text{FL}} \mathbf{M} \times \sigma_{\text{SHE}} \end{aligned} \tag{A.1a}$$

The sign of u is negative for a positive current density (i.e. an electron flow along $-x$) and may be described by $u = -\frac{g\mu_{\text{B}} P j}{2eM_{\text{S}}}$ [50], where g is the g-factor, P is the spin polarization and j denotes the electrical current density. The spin polarization σ_{SHE} at the interface between HM and FM, that arises from the SHE, depends on both current polarity and the considered HM/FM system. At the Pt/Co interface that is investigated here, σ_{SHE} is aligned parallel to $-y$ ($+y$) for a positive (negative) current density. The torque amplitude is given by $\tau_{\text{DL}} = \frac{\gamma_e \hbar \theta_{\text{SH}} j}{2eM_{\text{S}} d}$, $\tau_{\text{FL}} = \beta_{\text{SOT}} \tau_{\text{DL}}$ [108], where θ_{SH} is the spin-hall angle, d is the FM thickness and β_{SOT} is a scaling factor [108]. Usually, for SOT-driven DW motion $\beta_{\text{SOT}} \ll 1$ [108, 109].

Next, the LLGS equation is expressed in spherical coordinates (θ, ϕ, M) that correspond to the polar and azimuthal angle and the length of the magnetization, respectively. The unit vectors $\mathbf{e}_\theta$, $\mathbf{e}_\phi$, $\mathbf{e}_{\text{M}}$ are orthonormal and span the rotated coordinate system as seen in fig. A.1. The spherical unit vectors in cartesian coordinates read as follows:

$$\mathbf{e}_\theta = \begin{pmatrix} \cos(\phi)\cos(\theta) \\ \sin(\phi)\cos(\theta) \\ -\sin(\theta) \end{pmatrix}; \; \mathbf{e}_\phi = \begin{pmatrix} -\sin(\phi) \\ \cos(\phi) \\ 0 \end{pmatrix}; \; \mathbf{e}_{\text{M}} = \begin{pmatrix} \cos(\phi)\sin(\theta) \\ \sin(\phi)\sin(\theta) \\ \cos(\theta) \end{pmatrix} \tag{A.2}$$

In the following, the vectors are expressed in the spherical coordinate system instead of the cartesian system. That means that the components of a vector $\mathbf{A}$ are given in terms

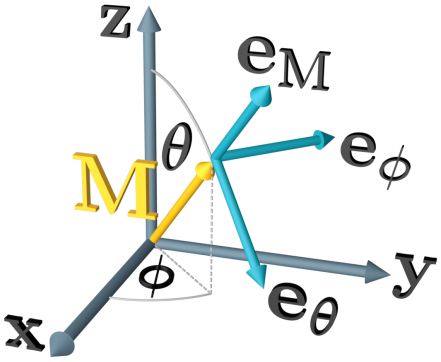

Figure A.1: **Cartesian and polar coordinate system.**

of the spherical unit vectors, i.e. $\mathbf{A} = A_\theta \mathbf{e}_\theta + A_\phi \mathbf{e}_\phi + A_\mathrm{M} \mathbf{e}_\mathrm{M} = \begin{pmatrix} A_\theta \\ A_\phi \\ A_\mathrm{M} \end{pmatrix}$. Furthermore, it is assumed that the saturation magnetization M_S does not change. The first two LLGS terms then transform as follows:

$$d\mathbf{M} = \begin{pmatrix} dM_\theta \\ dM_\phi \\ dM_M \end{pmatrix} = \begin{pmatrix} M_\mathrm{S}\, d\theta \\ M_\mathrm{S} \sin(\theta)\, d\phi \\ 0 \end{pmatrix} \quad \rightarrow \quad \frac{\partial \mathbf{M}}{\partial t} = \begin{pmatrix} M_\mathrm{S} \dot{\theta} \\ M_\mathrm{S} \sin(\theta) \dot{\phi} \\ 0 \end{pmatrix} \tag{A.3}$$

$$-\gamma \mathbf{M} \times \mathbf{H}_\mathrm{eff} = -\gamma \begin{pmatrix} M_\theta \\ M_\phi \\ M_\mathrm{M} \end{pmatrix} \times \begin{pmatrix} H_\theta \\ H_\phi \\ H_\mathrm{M} \end{pmatrix} = -\gamma \begin{pmatrix} 0 \\ 0 \\ M_\mathrm{S} \end{pmatrix} \times \begin{pmatrix} H_\theta \\ H_\phi \\ 0 \end{pmatrix} = -\gamma M_\mathrm{S} \begin{pmatrix} -H_\phi \\ H_\theta \\ 0 \end{pmatrix} \tag{A.4}$$

$$\text{with}: \quad \mu_0 \mathbf{H}_\mathrm{eff} = -\nabla_\mathbf{M} E; \quad H_{\mathrm{eff},\theta} = \frac{1}{\mu_0 M_\mathrm{S}} \frac{\partial E}{\partial \theta}; \quad H_{\mathrm{eff},\phi} = \frac{1}{\mu_0 M_\mathrm{S} \sin(\theta)} \frac{\partial E}{\partial \phi} \tag{A.5}$$

$$\tag{A.6}$$

To evaluate the STT-components, the following DW profile $\theta(x)$ is used where the sign in the exponent denotes the DW configuration, i.e. $+(-)$ stands for an $\uparrow\downarrow$ ($\downarrow\uparrow$) DW.

$$\theta(x) = 2 \arctan\left(\exp\left(\mp \frac{x - q(t)}{\Delta} \right) \right) \tag{A.7}$$

The resulting STT-terms in spherical coordinates then read as:

$$\frac{\partial \mathbf{M}}{\partial x} = \frac{\partial M_\theta}{\partial x} \mathbf{e}_\theta = \frac{\partial \theta}{\partial x} \frac{\partial M_\theta}{\partial \theta} \mathbf{e}_\theta = \mp \frac{\sin(\theta)}{\Delta} M_\mathrm{S} \mathbf{e}_\theta \tag{A.8}$$

$$\mathbf{M} \times \frac{\partial \mathbf{M}}{\partial x} = \begin{pmatrix} 0 \\ 0 \\ M_\mathrm{S} \end{pmatrix} \times \begin{pmatrix} \mp \frac{\sin(\theta) M_\mathrm{S}}{\Delta} \\ 0 \\ 0 \end{pmatrix} = \begin{pmatrix} 0 \\ \mp \frac{\sin(\theta) M_\mathrm{S}^2}{\Delta} \\ 0 \end{pmatrix} \tag{A.9}$$

In order to transform the SOT-terms to spherical coordinates, the orientation of the spin polarization $\sigma_{\mathrm{SHE}} \parallel -y$ needs to be transformed into spherical coordinates:

$$\sigma_{\mathrm{SHE}} = \begin{pmatrix} -\cos(\theta)\sin(\phi) \\ -\cos(\phi) \\ -\sin(\theta)\sin(\phi) \end{pmatrix} \tag{A.10}$$

$$\mathbf{M} \times \sigma_{\mathrm{SHE}} = M_{\mathrm{S}} \begin{pmatrix} \cos(\phi) \\ -\cos(\theta)\sin(\phi) \\ 0 \end{pmatrix} \tag{A.11}$$

$$\mathbf{M} \times (\mathbf{M} \times \sigma_{\mathrm{SHE}}) = M_{\mathrm{S}}^2 \begin{pmatrix} \cos(\theta)\sin(\phi) \\ \cos(\phi) \\ 0 \end{pmatrix} \tag{A.12}$$

Summarizing the previous transformation into spherical coordinates, the LLGS equation A.1a now reads as follows:

$$\dot{\theta} = -\frac{\gamma}{\mu_0 M_{\mathrm{S}} \sin(\theta)} \frac{\partial E}{\partial \phi} - \alpha \dot{\phi} \sin(\theta) \pm \frac{u \sin(\theta)}{\Delta} - \tau_{\mathrm{DL}} \cos(\theta)\sin(\phi) - \tau_{\mathrm{FL}} \cos(\phi) \tag{A.13}$$

$$\dot{\phi} \sin(\theta) = \frac{\gamma}{\mu_0 M_{\mathrm{S}}} \frac{\partial E}{\partial \theta} + \alpha \dot{\theta} \mp \frac{\beta u \sin(\theta)}{\Delta} - \tau_{\mathrm{DL}} \cos(\phi) + \tau_{\mathrm{FL}} \cos(\theta)\sin(\phi) \tag{A.14}$$

The collective coordinate approach aims at using a set of coordinates, the position q and the azimuthal DW angle ψ, to describe the DW dynamics. The following terms are useful to include the DW position q into the differential equations.

$$\frac{\partial \theta}{\partial x} = \mp \frac{\sin(\theta)}{\Delta} \tag{A.15}$$

$$d\theta = \frac{\partial \theta}{\partial x} dx = -\frac{\partial \theta}{\partial x} dq = \pm \frac{\sin(\theta)}{\Delta} dq \tag{A.16}$$

$$\dot{\theta} = \pm \frac{\sin(\theta)}{\Delta} \dot{q} \tag{A.17}$$

In order to describe the DW as a point-like object moving in a one-dimensional space, the equations A.13-A.14 need to be integrated accross the DW, i.e. along x.

$$\delta E = \frac{\partial E}{\partial \theta}\delta\theta + \frac{\partial E}{\partial \phi}\delta\phi \tag{A.18}$$

$$\begin{aligned}\delta\sigma &= \int_{-\infty}^{+\infty} \delta E dx = \int_{\theta(-\infty)}^{\theta(+\infty)} \delta E \frac{\partial x}{\partial \theta} d\theta = \int_0^{\pi} \delta E \frac{\Delta}{\sin(\theta)} d\theta \\ &= \int_0^{\pi} \frac{\Delta}{\sin(\theta)} \left[\frac{\partial E}{\partial \theta}\delta\theta + \frac{\partial E}{\partial \phi}\delta\phi\right] d\theta \\ &= \int_0^{\pi} \frac{\Delta}{\sin(\theta)} \left[\pm\frac{\partial E}{\partial \theta}\frac{\sin(\theta)}{\Delta}\delta q + \frac{\partial E}{\partial \phi}\delta\phi\right] d\theta \end{aligned} \tag{A.19}$$

By inserting equations A.13-A.14, the first and second terms in A.19 become:

$$\begin{aligned}\delta\sigma_{\mathrm{q}} &= \pm\int_0^{\pi} \frac{\partial E}{\partial \theta}\delta q d\theta \\ &= \pm\int_0^{\pi} \frac{\mu_0 M_{\mathrm{S}}}{\gamma}\left[\sin(\theta)\left(\dot{\phi} \mp \frac{\alpha\dot{q}}{\Delta} \pm \frac{\beta u}{\Delta}\right) + \tau_{\mathrm{DL}}\cos(\phi) - \tau_{\mathrm{FL}}\cos(\theta)\sin(\phi)\right]\delta q d\theta \\ &= \pm\frac{2\mu_0 M_{\mathrm{S}}}{\gamma}\left[\left(\dot{\phi} \mp \frac{\alpha\dot{q}}{\Delta} \pm \frac{\beta u}{\Delta}\right) + \frac{\pi\tau_{\mathrm{DL}}\cos(\phi)}{2}\right]\delta q \end{aligned} \tag{A.20}$$

$$\begin{aligned}\delta\sigma_{\psi} &= \int_0^{\pi} \frac{\Delta}{\sin(\theta)}\frac{\partial E}{\partial \phi}\delta\phi d\theta \\ &= \int_0^{\pi} \frac{\mu_0 M_{\mathrm{S}}}{\gamma}\left[\sin(\theta)\left(\mp\dot{q} - \alpha\Delta\dot{\phi} \pm u\right) - \tau_{\mathrm{DL}}\Delta\cos(\theta)\sin(\phi) - \tau_{\mathrm{FL}}\Delta\cos(\phi)\right]\delta\phi d\theta \\ &= \frac{2\mu_0 M_{\mathrm{S}}}{\gamma}\left[\left(\mp\dot{q} - \alpha\Delta\dot{\phi} \pm u\right) - \frac{\pi\tau_{\mathrm{FL}}\Delta\cos(\phi)}{2}\right]\delta q \end{aligned} \tag{A.21}$$

In the previous integration, it was assumed that the coordinate ϕ does not vary along x. Hence, a collective angle ψ with $\psi = \phi$ will now be used instead of the coordinate ϕ. ψ denotes the azimuthal angle of the DW orientation. This results the following differential equations for the collective coordinates q, ψ that are determined by the DW area energy density σ:

$$\frac{\gamma}{2\mu_0 M_{\mathrm{S}}}\frac{\partial\sigma}{\partial q} = \pm\dot{\psi} - \frac{\alpha\dot{q}}{\Delta} + \frac{\beta u}{\Delta} \pm \frac{\pi\tau_{\mathrm{DL}}\cos(\psi)}{2} \tag{A.22}$$

$$\frac{\gamma}{2\mu_0 M_{\mathrm{S}}}\frac{\partial\sigma}{\partial \psi} = \mp\dot{q} - \alpha\Delta\dot{\psi} \pm u - \frac{\pi\tau_{\mathrm{FL}}\Delta\cos(\psi)}{2} \tag{A.23}$$

The following differential equations for the DW position q and DW angle ψ are obtained:

$$\dot{\psi} = \frac{1}{1+\alpha^2}\left[\frac{\gamma}{2\mu_0 M_S}\left(\pm\frac{\partial\sigma}{\partial q} - \frac{\alpha}{\Delta}\frac{\partial\sigma}{\partial\psi}\right) \pm \frac{\alpha u}{\Delta} \mp \frac{\beta u}{\Delta} + \frac{\pi\cos(\psi)}{2}\left(-\tau_{DL} - \alpha\tau_{FL}\right)\right] \tag{A.24}$$

$$\dot{q} = \frac{1}{1+\alpha^2}\left[\frac{\gamma}{2\mu_0 M_S}\left(-\alpha\Delta\frac{\partial\sigma}{\partial q} \mp \frac{\partial\sigma}{\partial\psi}\right) + u + \alpha\beta u + \frac{\Delta\pi\cos(\psi)}{2}\left(\pm\alpha\tau_{DL} \mp \tau_{FL}\right)\right] \tag{A.25}$$

In order to calculate the DW dynamics based on these differential equations, the DW area energy density $\sigma(q,\psi)$ has to be known. In the following, the energy density E and area energy density $\sigma = \int_{-\infty}^{+\infty} E dx$ will be calculated based on the magnetic exchange, uniaxial anisotropy, demagnetization, Zeeman effect and Dzyaloshinskii-Moriya interaction.

$$E_{ex} = A\left[\left(\frac{\partial\theta}{\partial x}\right)^2 + \sin^2(\theta)\left(\frac{\partial\phi}{\partial x}\right)^2\right] \tag{A.26}$$

$$E_{anis} = K_u \sin^2(\theta) \tag{A.27}$$

$$E_{demag} = -\mu_0 \mathbf{M}\cdot\mathbf{H}_d = \mu_0 M_S^2 \sin^2(\theta)\left[\left(N_x - N_y\right)\cos^2(\phi) - N_z\right] + \text{const.} \tag{A.28}$$

$$E_{Zeeman} = -\mu_0 M_S\left[H_a\cos(\theta) + H_{ip}\sin(\theta)\cos\left(\phi - \psi_{ip}\right)\right] \tag{A.29}$$

$$\begin{aligned} E_{DMI} &= \frac{D}{M_S^2}\left[M_x\frac{\partial M_z}{\partial x} - M_z\frac{\partial M_x}{\partial x}\right] \\ &= D\left[\left(\cos(\phi)\sin(\theta)\right)\left(-\sin(\theta)\frac{\partial\theta}{\partial x}\right) - \cos(\theta)\left(\cos(\phi)\cos(\theta)\frac{\partial\theta}{\partial x}\right)\right] \end{aligned} \tag{A.30}$$

Using $\sigma = \int_{-\infty}^{+\infty} E dx = \int_0^{\pi} E\frac{\Delta}{\sin(\theta)} d\theta$, one obtains:

$$\sigma_{ex} = \frac{2A}{\Delta} \tag{A.31}$$

$$\sigma_{K_u} = 2K_u\Delta \tag{A.32}$$

$$\sigma_{demag} = 2\mu_0 M_S^2\Delta\left[\left(N_x - N_y\right)\cos^2(\psi) - N_z\right] \tag{A.33}$$

$$\sigma_{Zeeman} = \mu_0 M_S\left[\pm 2qH_a - \pi\Delta\cos\left(\psi - \psi_{ip}\right)H_{ip}\right] \tag{A.34}$$

$$\sigma_{DMI} = \pm\pi D\cos(\psi) \tag{A.35}$$

$$\rightarrow \frac{\partial\sigma}{\partial q} = \pm 2\mu_0 M_S H_a \tag{A.36}$$

$$\rightarrow \frac{\partial\sigma}{\partial\psi} = -2\mu_0 M_S^2\left(N_x - N_y\right)\Delta\sin(2\psi) + \mu_0 M_S H_{ip}\pi\Delta\sin\left(\psi - \psi_{ip}\right) \mp D\pi\sin(\psi) \tag{A.37}$$

Inserting A.36, A.37 into A.24, A.25 returns the final expression for $\dot{\psi}$, $\dot{q}$.

$$\dot{\psi} = \frac{1}{1+\alpha^2}\left[\gamma H_\mathrm{a} + \alpha\gamma M_\mathrm{S}\left(N_\mathrm{x}-N_\mathrm{y}\right)\sin(2\psi) - \frac{1}{2}\alpha\gamma H_\mathrm{ip}\pi\sin\left(\psi-\psi_\mathrm{ip}\right) \pm\frac{\alpha\gamma D\pi\sin(\psi)}{2\Delta\mu_0 M_\mathrm{S}} \pm\frac{\alpha u}{\Delta} \mp\frac{\beta u}{\Delta} + \frac{\pi\cos(\psi)}{2}\left(-\tau_\mathrm{DL}-\alpha\tau_\mathrm{FL}\right)\right] \tag{A.38}$$

$$\dot{q} = \frac{1}{1+\alpha^2}\left[\mp\alpha\Delta\gamma H_\mathrm{a} \pm \gamma M_\mathrm{S}\left(N_\mathrm{x}-N_\mathrm{y}\right)\Delta\sin(2\psi) \mp\frac{1}{2}\gamma H_\mathrm{ip}\pi\Delta\sin\left(\psi-\psi_\mathrm{ip}\right) +\frac{\gamma D\pi\sin(\psi)}{2\mu_0 M_\mathrm{S}} + u + \alpha\beta u + \frac{\Delta\pi\cos(\psi)}{2}\left(\pm\alpha\tau_\mathrm{DL}\mp\tau_\mathrm{FL}\right)\right] \tag{A.39}$$

Appendix B

Supplementary Materials

B.1 Scattering parameters

A *vector network analyzer* (VNA) is a device that measures the microwave properties of electronic circuitry. A two-terminal VNA, i.e. with two microwave ports, was used here. It allows to measure the transmission of microwave power between both ports as well as the reflection of microwave power from either of the ports. These properties are summarized in the complex *scattering matrix* $\widehat{S}$ that relate the voltage amplitude V_{i}^{+} of the incoming RF wave at port i with the amplitude V_{j}^{-} of the reflected RF wave at port j [110].

$$\begin{pmatrix} V_1^- \\ V_2^- \end{pmatrix} = \widehat{S} \cdot \begin{pmatrix} V_1^+ \\ V_2^+ \end{pmatrix} \tag{B.1}$$

$$\widehat{S} = \begin{pmatrix} S_{11} & S_{12} \\ S_{21} & S_{22} \end{pmatrix} \tag{B.2}$$

The diagonal matrix components S_{11}, S_{22} correspond to the reflection coefficient from port 1 or port 2, respectively. In contrast, the off-diagonal components S_{21}, S_{12} correspond to the transmission coefficient from port 1 to port 2 and vice versa.

The magnitude of the scattering parameters are often expressed in units of dB [111]:

$$S_{\mathrm{ij}}[\mathrm{dB}] = 20\log\left(S_{\mathrm{ij}}\right) \tag{B.3}$$

B.2 Magnetic thin film characterization

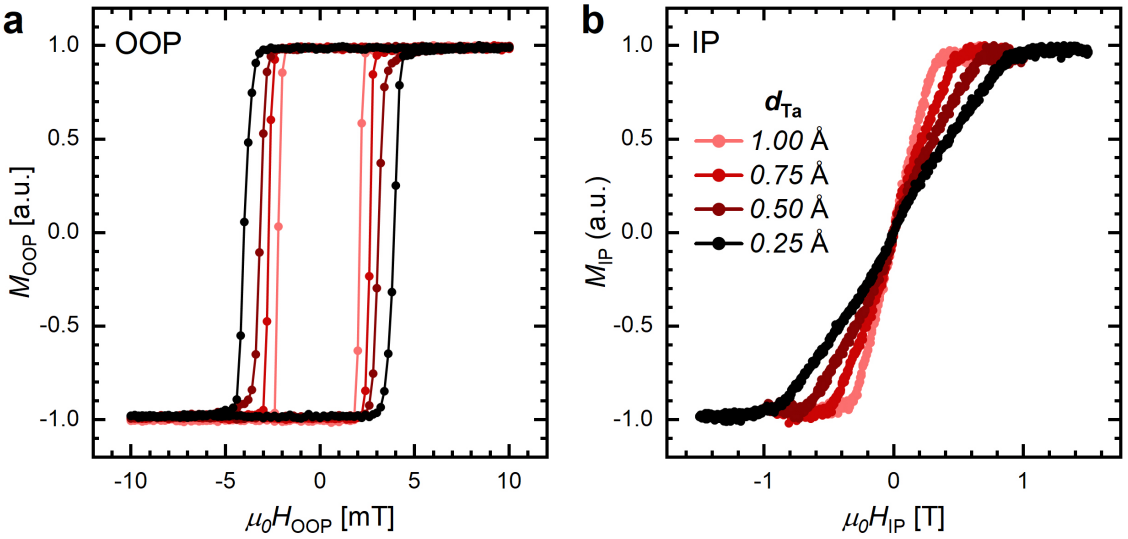

Figure B.1: **VSM data of magnetic thin films with Ta-dusting variation.** The static magnetic properties of magnetic thin films are measured by VSM. The films have the structure 20 TaN / 50 Pt / d_{Ta} / 3 Co / 7 Ni / 3 Co / 30 TaN (the numbers indicate the thickness in Å) and the interfacial Tantalum thickness d_{Ta} is varied. **(a)** Out-of-plane and **(b)** in-plane magnetization of the magnetic film. Both the coercive field in **(a)** and the effective anisotropy field (seen in **(b)**) decrease with increasing d_{Ta}.

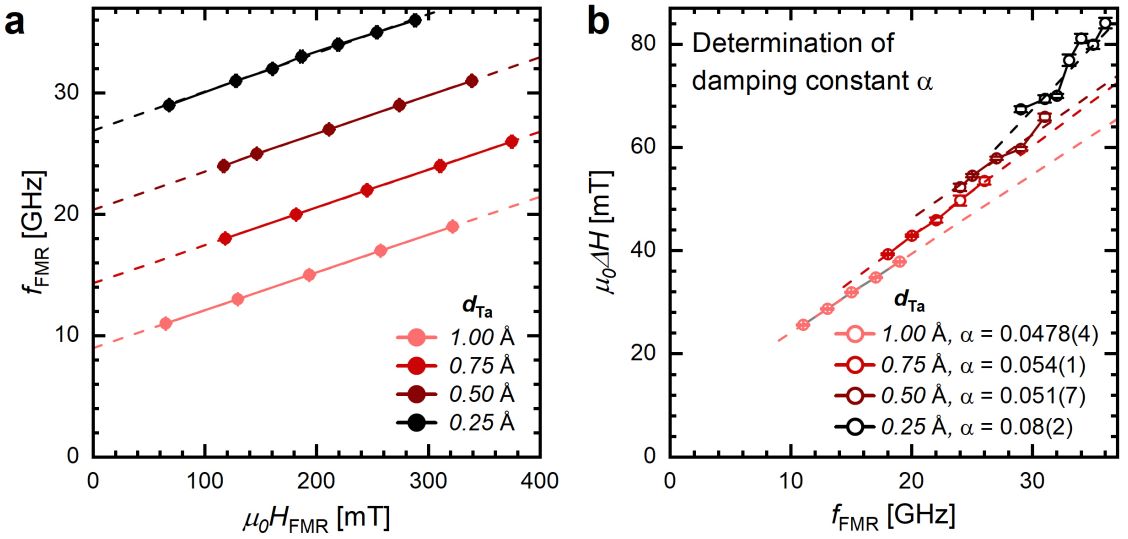

Figure B.2: **FMR data of magnetic thin films with Ta-dusting variation.** FMR measurements on magnetic film with the structure 20 TaN / 50 Pt / d_{Ta} / 3 Co / 7 Ni / 3 Co / 30 TaN (the numbers indicate the thickness in Å) where the interfacial Tantalum thickness d_{Ta} is varied. **(a)** Linear increase of FMR resonance frequency with an out-of-plane magnetic field. A larger d_{Ta} decreases the zero-field FMR frequency, i.e. decreases the perpendicular magnetic anisotropy. **(b)** The resonance linewidth ΔH as a function of the FMR frequency reveals the damping constant α and the inhomogeneous broadening. The damping decreases with larger d_{Ta}. The dashed lines are linear fits to the data.

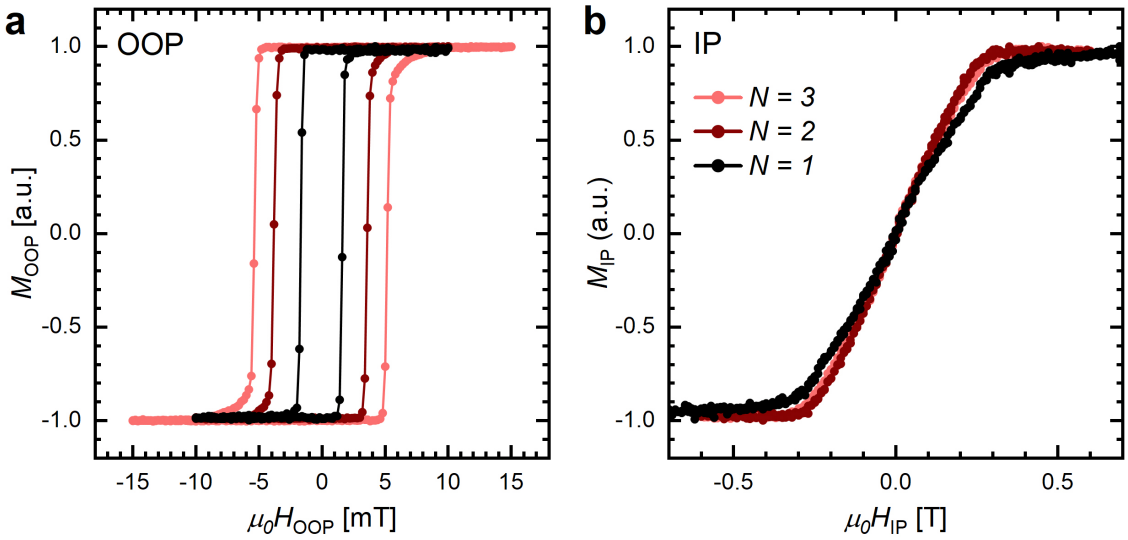

Figure B.3: **VSM data of magnetic thin films with different number of multilayer repetitions.** The static magnetic properties of magnetic thin films are measured by VSM. The films have the structure 20 TaN / 50 Pt / 1 Ta / 3 Co / [7 Ni / 3 Co]$_N$ / 30 TaN where the number N of multilayer repetitions is varied. **(a)** Out-of-plane and **(b)** in-plane magnetization of the magnetic film. With increasing repetitions N, the coercive field in **(a)** increases while the effective anisotropy field (seen in **(b)**) slightly decreases.

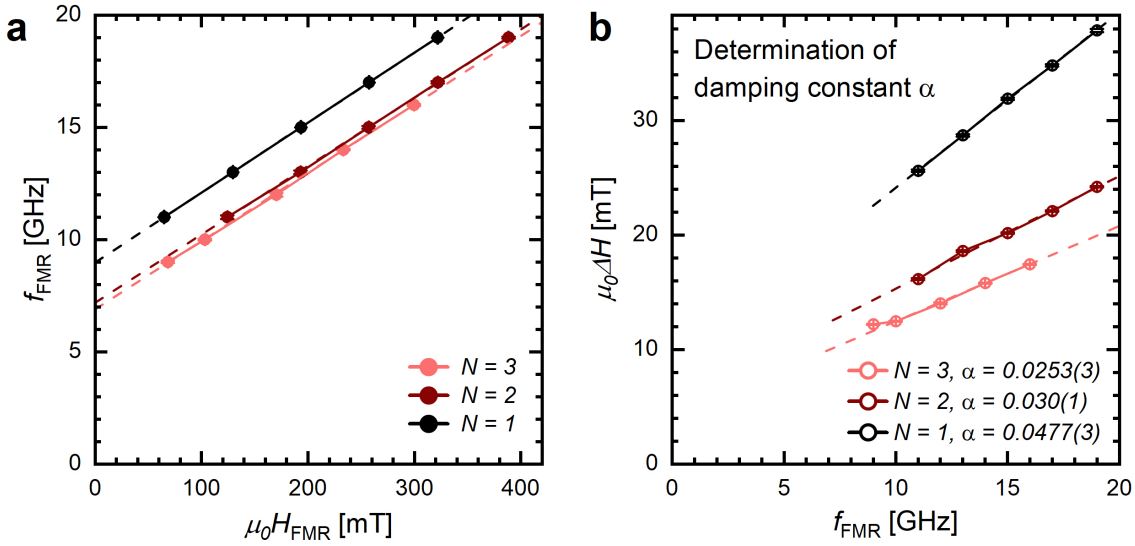

Figure B.4: **FMR data of magnetic thin films with different number of multilayer repetitions.** FMR measurements on magnetic film with the structure 20 TaN / 50 Pt / 1 Ta / 3 Co / [7 Ni / 3 Co]$_N$ / 30 TaN where the number N of multilayer repetitions is varied. **(a)** Linear increase of FMR resonance frequency with an out-of-plane magnetic field. A higher N decreases the zero-field FMR frequency, i.e. decreases the perpendicular magnetic anisotropy. **(b)** The resonance linewidth ΔH as a function of the FMR frequency reveals the damping constant α and the inhomogeneous broadening. The damping decreases with N. The dashed lines are linear fits to the data.

B.3 Discussion of time dependence of the MAS

In general, during field-induced magnetization switching, the switching field H_{sw} differs considerably depending on the time span t_{field} where the magnetic field H_{z} is applied. This time dependence is caused by the thermally assisted crossing of the switching energy barrier and may be described by the Sharrock equation [105, 112].

$$H_{\mathrm{sw}}(t_{\mathrm{field}}) = H_0 \left[1 - \left(\frac{1}{\beta} \ln\left(\frac{t_{\mathrm{field}} f_0}{\ln(2)} \right) \right)^{1/n} \right] \tag{B.4}$$

Herein, H_0 is the intrinsic switching field without thermal agitation, $\beta = K_{\mathrm{an,eff}} V / (k_{\mathrm{B}} T)$ is the thermal stability factor that relates the anisotropy energy barrier of a magnetic volume V to the thermal energy $k_{\mathrm{B}}T$, $f_0 = 10^{10}$ Hz is the attempt frequency. The exponent n depends on the alignment of the magnetic field to the magnet's easy-axis during switching. While $n = 2$ is only valid when the magnetic field is perfectly aligned along the FM's easy axis, a value of $n = 3/2$ should be chosen for general fields or easy axis distributions [105, 112, 113].

The situation becomes more complicated during MAS because the applied H_{z} field alone is usually insufficient to switch the FM but the simultaneous application of the RF-field induces the switching. Hence, the burst time t_{burst} of the RF-field would now be the time scale of interest that reduces H_{sw}. Indeed, a modified Sharrock equation has been proposed [66, 105] that includes the in-plane RF-field h_{RF} and a fictitious magnetic field $H_\omega = \frac{2\pi f}{\gamma}$ along z that emerges in the rotating frame approach (cf. chapter 2.4.2).

$$H_{\mathrm{sw}}(t_{\mathrm{burst}}) = \sqrt{{H_0}^2 \left[1 - \left(\frac{1}{\beta} \ln\left(\frac{t_{\mathrm{burst}} f_0}{\ln(2)} \right) \right)^{1/n} \right]^2 - \left(\frac{h_{\mathrm{RF}}}{2} \right)^2} - H_\omega \tag{B.5}$$

As will be outlined in the following, the previous equation is neglecting an important aspect of MAS, namely its resonant character. Firstly, to achieve MAS, the frequency f_{RF} of the applied RF-field needs to match the frequency of FMR or other magnetic resonances such as standing spin waves. Since f_{FMR} is governed by the H_{z} field (cf. eq. (2.13)), each applied frequency f_{RF} corresponds to a field H_{z} where the RF field is at resonance and can induce MAS. Consequently, for a fixed frequency, the occurrence of MAS is limited to a fixed H_{z} field range that is defined by the distribution of magnetic resonances and their linewidth. The occurrence of MAS outside such a limited field range seems unreasonable. As an example, the FMR linewidth in table 8.1 reads as $\mu_0 \Delta H(f_0) = 4.8$ mT.

Indeed, the suggested decrease of $H_{\mathrm{sw}}$with t_{burst} in eq. (B.5) seems unrealistic as soon as H_{sw} decreases below the field range where magnetic resonances occur. In the latter case, no MAS could occur and H_{sw} would be significantly increased. Since the modified Sharrock equation neither takes the resonant character of MAS nor the resonance distribution or linewidth into account, it seems unlikely that it can adequately describe the

time dependence of H_{sw} and e.g. allow to deduce the thermal stability constant from the experimental data in Fig. 8.8.

List of Figures

List of Tables

Curriculum Vitae

Lukas Fischer

Education

2021-2025	Doctoral researcher, Max-Planck Institute of Microstructure Physics
2018-2021	Master studies in Physics, University Heidelberg
2015-2018	Bachelor studies in Physics, University Heidelberg
2007-2015	Friedrich-Dessauer Gymnasium, Aschaffenburg

Bibliography

[1] J. M. D. Coey, S. Parkin, *Handbook of Magnetism and Magnetic Materials* (Springer, Cham) (2021).

[2] A. Hirohata, K. Yamada, Y. Nakatani, B. Hillebrands, Review on spintronics: Principles and device applications. *J. Magn. Magn. Mater.* **509** (166711) (2020).

[3] S. Parkin, M. Hayashi, L. Thomas, Magnetic domain-wall racetrack memory. *Science* **320** (5873), 190–194 (2008).

[4] Q. Shao, *et al.*, Roadmap of spin–orbit torques. *IEEE Trans. Magn.* **57** (7), 1–39 (2021).

[5] D. Kumar, T. Jin, R. Sbiaa, M. Kläui, S. Bedanta, Domain wall memory: Physics, materials, and devices. *Phys. Rep.* **958**, 1–35 (2022).

[6] G. Venkat, D. A. Allwood, T. J. Hayward, Magnetic domain walls: types, processes and applications. *J. Phys. D: Appl. Phys.* **57** (6), 063001 (2023).

[7] I. M. Miron, *et al.*, Fast current-induced domain-wall motion controlled by the Rashba effect. *Nat. Mater.* **10** (6), 419–423 (2011).

[8] K.-S. Ryu, L. Thomas, S.-H. Yang, S. Parkin, Current induced tilting of domain walls in high velocity motion along perpendicularly magnetized micron-sized Co/Ni/Co racetracks. *Appl. Phys. Expr.* **5** (9), 093006 (2012).

[9] S. Emori, U. Bauer, S.-M. Ahn, E. Martinez, G. Beach, Current-driven dynamics of chiral ferromagnetic domain walls. *Nat. Mater.* **12** (7), 611–616 (2013).

[10] K.-S. Ryu, L. Thomas, S.-H. Yang, S. Parkin, Chiral spin torque at magnetic domain walls. *Nat. Nanotechnol.* **8** (7), 527–533 (2013).

[11] S. Vélez, *et al.*, High-speed domain wall racetracks in a magnetic insulator. *Nat. Commun.* **10** (1) (2019).

[12] N. L. Schryer, L. R. Walker, The motion of 180° domain walls in uniform dc magnetic fields. *J. Appl. Phys.* **45** (12), 5406–5421 (1974).

[13] A. Thiaville, S. Rohart, E. Jué, V. Cros, A. Fert, Dynamics of Dzyaloshinskii domain walls in ultrathin magnetic films. *Europhys. Lett.* **100** (5), 57002 (2012).

[14] A. P. Malozemoff, J. C. Slonczewski, Magnetic domain walls in bubble materials: advances in materials and device research. *Academic Press* (1979).

[15] A. Thiaville, J. M. Garcia, J. Miltat, Domain wall dynamics in nanowires. *J. Magn. Magn. Mater.* **242**, 1061–1063 (2002).

[16] K. Wagner, *et al.*, Magnetic domain walls as reconfigurable spin-wave nanochannels. *Nat. Nanotechnol.* **11** (5), 432–436 (2016).

[17] I. M. Miron, *et al.*, Perpendicular switching of a single ferromagnetic layer induced by in-plane current injection. *Nature* **476** (7359), 189–193 (2011).

[18] L. Liu, *et al.*, Spin-torque switching with the giant spin Hall effect of tantalum. *Science* **336** (6081), 555–558 (2012).

[19] K. Garello, *et al.*, Ultrafast magnetization switching by spin-orbit torques. *Appl. Phys. Lett.* **105** (21), 212402 (2014).

[20] M. Baumgartner, *et al.*, Spatially and time-resolved magnetization dynamics driven by spin–orbit torques. *Nat. Nanotechnol.* **12** (10), 980–986 (2017).

[21] J.-G. Zhu, X. Zhu, Y. Tang, Microwave assisted magnetic recording. *IEEE Trans. Magn.* **44** (1), 125–131 (2008).

[22] S. Okamoto, N. Kikuchi, M. Furuta, O. Kitakami, T. Shimatsu, Switching behaviors and its dynamics of a Co/Pt nanodot under the assistance of rf fields. *Phys. Rev. Lett.* **109** (23), 237209 (2012).

[23] J. Stöhr, H. C. Siegmann, *Magnetism: From Fundamentals to Nanoscale Dynamics*, vol. 152 of *Solid-State Sciences* (Springer, Berlin, Heidelberg) (2006).

[24] R. Gross, A. Marx, *Magnetismus* (Walter de Gruyter GmbH, Berlin, Boston) (2018).

[25] A. P. Guimaraes, *Principles of Nanomagnetism* (Springer, Berlin) (2009).

[26] A. G. Gurevich, G. A. Melkov, *Magnetization Oscillation and Waves* (CRC Press, Boca Raton, New York, London, Tokyo) (1996).

[27] N. Nakajama, T. Koide, T. Shidara, Y. Suzuki, Perpendicular magnetic anisotropy caused by interfacial hybridization via enhanced orbital moment in Co/Pt multilayers: Magnetic circular x-ray dichroism study. *Phys. Rev. Lett.* **81** (23), 5229 (1998).

[28] G. H. O. Daalderop, P. J. Kelly, F. J. A. Den Broeder, Prediction and confirmation of perpendicular magnetic anisotropy in Co/Ni multilayers. *Phys. Rev. Lett.* **68** (5), 682 (1992).

[29] M. T. Johnson, J. J. De Vries, N. W. E. McGee, F. J. A. Den Broeder, Orientational dependence of the interface magnetic anisotropy in epitaxial Ni/Co/Ni sandwiches. *Phys. Rev. Lett.* **69** (24), 3575 (1992).

[30] G. H. O. Daalderop, P. J. Kelly, M. F. H. Schuurmans, Magnetic anisotropy of a free-standing Co monolayer and of multilayers which contain Co monolayers. *Phys. Rev. B* **50** (14), 9989 (1994).

[31] M. T. Johnson, P. J. H. Bloemen, F. J. A. Den Broeder, J. J. De Vries, Magnetic anisotropy in metallic multilayers. *Rep. Prog. Phys.* **59** (11), 1409 (1996).

[32] D. Sander, The magnetic anisotropy and spin reorientation of nanostructures and nanoscale films. *J. Phys.: Condens. Matter* **16** (20), R603–636 (2004).

[33] I. Dzyaloshinksy, A thermodynamic theory of "weak" ferromagnetism of antiferromagnetics. *J. Phys. Chem. Sol.* **4** (4), 241–255 (1958).

[34] T. Moriya, New mechanism of anisotropic superexchange interaction. *Phys. Rev. Lett.* **4** (5), 228 (1960).

[35] T. Moriya, Anisotropic superexchange interaction and weak ferromagnetism. *Phys. Rev.* **120** (1), 91 (1960).

[36] A. Fert, P. M. Levy, Role of Anisotropic Exchange Interactions in Determining the Propertiesof Spin-Glasses. *Phys. Rev. Lett.* **44** (23), 1538–1541 (1980).

[37] A. Fert, M. Chshiev, A. Thiaville, H. Yang, From Early Theories of Dzyaloshinskii–Moriya Interactions in Metallic Systems to Today's Novel Roads. *J. Phys. Soc. Jpn.* **92** (8), 081001 (2023).

[38] S. Rohart, A. Thiaville, Skyrmion confinement in ultrathin film nanostructures in the presence of Dzyaloshinskii-Moriya interaction. *Phys. Rev. B* **88** (18), 184422 (2013).

[39] S. M. Rezende, *Fundamentals of magnonics*, vol. 969 of *The Lecture Notes in Physics* (Springer, Cham) (2020).

[40] M. Härtinger, *Untersuchung magnetischer Materialien mit Methoden der ferromagnetischen Resonanz*, Thesis (2016).

[41] Y. Nakatani, A. Thiaville, J. Miltat, Faster magnetic walls in rough wires. *Nat. Mater.* **2** (8), 521–523 (2003).

[42] Y. Yoshimura, K. J. Kim, T. Taniguchi, T. Ono, Soliton-like magnetic domain wall motion induced by the interfacial Dzyaloshinskii–Moriya interaction. *Nat. Phys.* **12** (2), 157–161 (2016).

[43] L. Berger, Exchange interaction between ferromagnetic domain wall and electric current in very thin metallic films. *J. Appl. Phys.* **55** (6), 1954–1956 (1984).

[44] L. Berger, Emission of spin waves by a magnetic multilayer traversed by a current. *Phys. Rev. B* **54** (13), 9353 (1996).

[45] J. C. Slonczewski, Current-driven excitation of magnetic multilayers. *J. Magn. Magn. Mater.* **159** (1-2), L1–L7 (1996).

[46] Z. Li, S. Zhang, Magnetization dynamics with a spin-transfer torque. *Phys. Rev. B* **68** (2), 024404 (2003).

[47] Z. Li, S. Zhang, Domain-wall dynamics and spin-wave excitations with spin-transfer torques. *Phys. Rev. Lett.* **92** (20), 207203 (2004).

[48] A. Thiaville, Y. Nakatani, J. Miltat, N. Vernier, Domain wall motion by spin-polarized current: a micromagnetic study. *J. Appl. Phys.* **95** (11), 7049–7051 (2004).

[49] Z. Li, S. Zhang, Roles of Nonequilibrium Conduction Electrons on the Magnetization Dynamics of Ferromagnets. *Phys. Rev. Lett.* **93** (12), 127204 (2004).

[50] A. Thiaville, Y. Nakatani, J. Miltat, Y. Suzuki, Micromagnetic understanding of current-driven domain wall motion in patterned nanowires. *Europhys. Lett.* **69** (6), 990 (2005).

[51] J. E. Hirsch, Spin hall effect. *Phys. Rev. Lett.* **83** (9), 1834 (1999).

[52] J. Sinova, D. Culcer, Q. Niu, T. Sinitsyn, N. A. Jungwirth, A. H. MacDonald, Universal intrinsic spin Hall effect. *Phys. Rev. Lett.* **92** (12), 126603 (2004).

[53] J. Sinova, S. O. Valenzuela, J. Wunderlich, C. H. Back, T. Jungwirth, Spin hall effects. *Rev. Mod. Phys.* **87** (4), 1213–1260 (2015).

[54] M. I. Dyakonov, V. I. Perel, Current-induced spin orientation of electrons in semiconductors. *Phys. Lett. A* **35** (6), 459–560 (1971).

[55] F. T. Vas'ko, Spin splitting in the spectrum of two-dimensional electrons due to the surface potential. *Pis'ma Zh. Eksp. Teor. Fiz.* **30** (9), 574–577 (1979).

[56] Y. A. Bychkov, E. I. Rashba, Properties of a 2D electron gas with lifted spectral degeneracy. *JETP Lett.* **39** (2), 78–81 (1984).

[57] V. M. Edelstein, Spin polarization of conduction electrons induced by electric current in two-dimensional asymmetric electron systems. *Solid State Commun.* **73** (3), 233–235 (1990).

[58] E. L. Ivchenko, S. D. Ganichev, *Spin-photogalvanics* (Springer, Berlin Heidelberg), pp. 245–277 (2008).

[59] V. P. Amin, M. D. Stiles, Spin transport at interfaces with spin-orbit coupling: Phenomenology. *Phys. Rev. B* **94** (10), 104420 (2016).

[60] A. Manchon, *et al.*, Current-induced spin-orbit torques in ferromagnetic and antiferromagnetic systems. *Rev. Mod. Phys.* **91** (3), 035004 (2019).

[61] W. Zhang, X. Han, W. Jiang, S. H. Yang, S. Parkin, Role of transparency of platinum–ferromagnet interfaces in determining the intrinsic magnitude of the spin Hall effect. *Nat. Phys.* **11** (6), 496–502 (2015).

[62] C. F. Pai, Y. Ou, V.-L. L. H., D. C. Ralpha, R. A. Buhrmann, Dependence of the efficiency of spin Hall torque on the transparency of Pt/ferromagnetic layer interfaces. *Phys. Rev. B* **92** (6), 064426 (2015).

[63] L. Caretta, *et al.*, Relativistic kinematics of a magnetic soliton. *Science* **370** (6523), 1438–1442 (2020).

[64] E. C. Stoner, E. P. Wohlfarth, A mechanism of magnetic hysteresis in heterogeneous alloys. *Philos. Trans. R. Soc. A* **240** (826), 599–642 (1948).

[65] A. Thiaville, Extensions of the geometric solution of the two dimensional coherent magnetization rotation model. *J. Magn. Magn. Mater.* **182** (1-2), 5–18 (1998).

[66] S. Okamoto, M. Igarashi, N. Kikuchi, O. Kitakami, Microwave assisted switching mechanism and its stable switching limit. *J. Appl. Phys.* **107** (12), 123914 (2010).

[67] A. Aharoni, Theoretical search for domain nucleation. *Rev. Mod. Phys.* **34** (2), 227 (1962).

[68] S. Pizzini, J. Vogel, S. Rohart, A. Thiaville, Chirality-induced asymmetric magnetic nucleation in Pt/Co/AlO x ultrathin microstructures. *Phys. Rev. Lett.* **113** (4), 047203 (2014).

[69] C. Thirion, W. Wernsdorfer, D. Mailly, Switching of magnetization by nonlinear resonance studied in single nanoparticles. *Nat. Mater.* **2** (8), 524–527 (2003).

[70] G. Woltersdorf, C. H. Back, Microwave assisted switching of single domain Ni 80 Fe 20 elements. *Phys. Rev. Lett.* **99** (22), 227207 (2007).

[71] G. Bertotti, I. D. Mayergoyz, C. Serpico, M. d'Aquino, R. Bonin, Nonlinear-dynamical-system approach to microwave-assisted magnetization dynamics. *J. Appl. Phys.* **105** (7) (2009).

[72] M. Furuta, S. Okamoto, N. Kikuchi, O. Kitakami, T. Shimatsu, Stoner–Wohlfarth Like Magnetization Switching in Very Small Co/Pt Nanodots under the Assistance of Radio Frequency Magnetic Field. *Appl. Phys. Expr.* **6** (5), 053006 (2013).

[73] S. Okamoto, M. Furuta, N. Kikuchi, O. Kitakami, T. Shimatsu, Theory and Experiment of Microwave-Assisted Magnetization Switching in Perpendicular Magnetic Nanodots. *IEEE Trans. Magn.* **50** (3), 83–88 (2014).

[74] G. N. Kakazei, *et al.*, Spin-wave spectra of perpendicularly magnetized circular submicron dot arrays. *Appl. Phys. Lett.* **85** (5), 443–445 (2004).

[75] L. Liu, O. J. Lee, T. J. Gudmundsen, D. C. Ralpha, R. A. Buhrman, Current-Induced Switching of Perpendicularly Magnetized Magnetic Layers Using Spin Torque from the Spin Hall Effect. *Phys. Rev. Lett.* **109** (9), 096602 (2012).

[76] C. Zhang, S. Fukami, H. Sato, F. Matsukura, H. Ohno, Spin-orbit torque induced magnetization switching in nano-scale Ta/CoFeB/MgO. *Appl. Phys. Lett.* **107** (1) (2015).

[77] K. S. Lee, S. W. Lee, B. C. Min, K. J. Lee, Threshold current for switching of a perpendicular magnetic layer induced by spin Hall effect. *Appl. Phys. Lett.* **102** (11) (2013).

[78] A. Vansteenkiste, *et al.*, The design and verification of MuMax3. *AIP advances* **4** (10) (2014).

[79] G. Finocchio, M. Carpentieri, E. Martinez, B. Azzerboni, Switching of a single ferromagnetic layer driven by spin Hall effect. *Appl. Phys. Lett.* **102** (21), 212410 (2013).

[80] N. Mikuszeit, O. Boulle, I. M. Miron, L. D. Buda-Prejbeanu, Spin-orbit torque driven chiral magnetization reversal in ultrathin nanostructures. *Phys. Rev. B* **92** (14), 144424 (2015).

[81] E. Martinez, L. Torres, N. Perez, S. Moretti, Universal chiral-triggered magnetization switching in confined nanodots. *Sci. Rep.* **5** (1), 10156 (2015).

[82] G. Franz, *Low Pressure Plasmas and Microstructuring Technology* (Springer) (2009).

[83] K. S. Ryu, S. H. Yang, L. Thomas, S. Parkin, Chiral spin torque arising from proximity-induced magnetization. *Nat. Commun.* **5** (1), 3910 (2014).

[84] Y. Guan, *et al.*, Increased efficiency of current-induced motion of chiral domain walls by interface engineering. *Adv. Mater.* **33** (10), 2007991 (2021).

[85] G. Woltersdorf, *Spin-pumping and two-magnon scattering in magnetic multilayers*, Thesis (2004).

[86] Z. Q. Qiu, S. D. Bader, Surface magneto-optic Kerr effect. *Rev. Sci. Instrum.* **71** (3), 1243–1255 (2000).

[87] A. Hubert, R. Schäfer, *Magnetic domains: the analysis of magnetic microstructures* (Springer, Berlin, Heidelberg, New York) (2009).

[88] A. K. Zvezdin, V. A. Kotov, *Modern magnetooptics and magnetooptical materials* (CRC Press) (1997).

[89] P. N. Argyres, Theory of the Faraday and Kerr effects in ferromagnetics. *Phys. Rev.* **97** (2), 334 (1955).

[90] W. Kuch, R. Schäfer, P. Fischer, F. U. Hillebrecht, *Magnetic Microscopy of Layered Structures* (Springer, Heidelberg New York Dordrecht London) (2015).

[91] R. Dreyer, N. Liebing, E. R. Edwards, A. Müller, G. Woltersdorf, Spin-wave localization and guiding by magnon band structure engineering in yttrium iron garnet. *Physical Review Materials* **5** (6), 064411 (2021).

[92] S. O. Demokritov, A. N. Slavin, Spin waves, in *Handbook of Magnetism and Magnetic Materials*, J. Coey, S. Parkin, Eds. (Springer International Publishing, Cham), pp. 281–346 (2021).

[93] O. Boulle, *et al.*, Domain Wall Tilting in the Presence of the Dzyaloshinskii-Moriya Interaction in Out-of-Plane Magnetized Magnetic Nanotracks. *Phys. Rev. Lett.* **111** (21), 217203 (2013).

[94] P. Chauve, T. Giamarchi, P. Le Doussal, Creep and depinning in disordered media. *Phys. Rev. B* **62** (10), 6241 (2000).

[95] B. E. Argyle, S. Maekawa, P. Dekker, J. C. Slonczewski, Gradientless propulsion and state switching of bubble domains. *AIP Conf. Proc.* (1976).

[96] G. Tatara, N. Vernier, J. Ferré, Universality of thermally assisted magnetic domain-wall motion under spin torque. *Appl. Phys. Lett.* **86** (25) (2005).

[97] J. Yoon, S.-H. Yang, J.-C. Jeon, S. Parkin, Local and global energy barriers for chiral domain walls in synthetic antiferromagnet–ferromagnet lateral junctions. *Nat. Nanotechnol.* **17** (11), 1183–1191 (2022).

[98] K.-J. Kim, R. Hiramatsu, T. Koyama, T. Ono, Two-barrier stability that allows low-power operation in current-induced domain-wall motion. *Nat. Commun.* **4** (1), 2011 (2013).

[99] P. Bruno, *et al.*, Hysteresis properties of ultrathin ferromagnetic films. *J. Appl. Phys.* **68** (11), 5759–5766 (1990).

[100] B. Raquet, M. D. Ortega, M. Goiran, A. Fert, A. Khmou, Dynamical properties of magnetization reversal in an ultrathin AuCo film. *J. Magn. Magn. Mater.* **150** (1), L5–L12 (1995).

[101] L. Thomas, R. Moriya, C. Rettner, S. Parkin, Dynamics of Magnetic Domain Walls Under Their Own Inertia. *Science* **330** (6012), 1810–1813 (2010).

[102] J. Torrejon, E. Martinez, M. Hayashi, Tunable inertia of chiral magnetic domain walls. *Nat. Commun.* **7** (1), 13533 (2016).

[103] S. Jung, H. Lee, S. Myung, S. J. Kim, A crossbar array of magnetoresistive memory devices for in-memory computing. *Nature* **601** (7892), 211–216 (2022).

[104] A. Yusuf, T. Adegbija, D. Gajaria, Domain-specific STT-MRAM-based in-memory computing: A survey. *IEEE Access* **12**, 28036–28056 (2024).

[105] S. Okamoto, N. Kikuchi, A. Hotta, T. Shimatsu, Microwave assistance effect on magnetization switching in Co-Cr-Pt granular films. *Appl. Phys. Lett.* **103** (20), 202405 (2013).

[106] S.-H. Yang, K.-S. Ryu, S. Parkin, Domain-wall velocities of up to 750 m s-1 driven by exchange-coupling torque in synthetic antiferromagnets. *Nat. Nanotechnol.* **10** (3), 221–226 (2015).

[107] M.-G. Kang, S. Lee, B.-G. Park, Field-free spin-orbit torques switching and its applications. *npj Spintronics* **3** (1), 8 (2025).

[108] A. Meo, C. E. Cronshaw, S. Jenkins, R. F. Evans, Spin-transfer and spin-orbit torques in the Landau–Lifshitz–Gilbert equation. *J. Condens. Matter Phys.* **35** (2), 025801 (2022).

[109] A. V. Khvalkovskiy, V. Cros, D. Apalkov, A. Fert, Matching domain-wall configuration and spin-orbit torques for efficient domain-wall motion. *Phys. Rev. B* **87** (2), 020402 (2013).

[110] D. M. Pozar, *Microwave Engineering* (John wiley and sons) (2012).

[111] A. Razavi, *RF Microelectronics* (Prentice Hall, New York) (2012).

[112] M. P. Sharrock, Time dependence of switching fields in magnetic recording media (invited). *J. Appl. Phys.* **76** (10), 6413 (1994).

[113] R. H. Victora, Predicted time dependence of the switching field for magnetic materials. *Phys. Rev. Lett.* **63** (4), 457 (1989).